UNIVERSITÀ DEGLI STUDI DI PALERMO

Dottorato in ingegneria dell'innovazione tecnologica
Dipartimento di ingegneria
ING-IND/26 Teoria dello Sviluppo dei Processi Chimici

ELECTRODIALYSIS MODELLING FOR LOW ENERGY DESALINATION

IL DOTTORE
ING. ANTONINO CAMPIONE

IL COORDINATORE
PROF. SALVATORE GAGLIO

IL TUTOR
PROF. GIORGIO MICALE

I CO TUTOR
PROF. A. CIPOLLINA
PROF. I. DAVID L. BOGLE

CICLO XXXII
ANNO CONSEGUIMENTO TITOLO 2020

Electrodialysis modelling for low energy desalination

Table of contents

Introduction

Water desalination is the main non-conventional source of fresh water in many countries all around the world. In some specific areas, facing severe water scarcity conditions, it is indeed the first source of fresh water for the local population. Recent figures about desalination industry indicate a cumulative contracted capacity of desalination plants in 2016 of almost 100 Mm^3/day, with an average contracted capacity per year between 3 and 5 Mm^3/day in the last 5 years [1], and a continuous increasing trend is expected in the next decades. Interestingly, seawater desalination led the desalination market in the first decade of the third millennium, with a dramatic capacity increase for SW-desalination plants in those years. Conversely, during the second decade the desalination industry experienced a growth of the applications to the desalination of brackish water and other types of water streams (e.g. tertiary waste waters, surface saline waters, etc.), where the typical capacities are small or medium (below 50.000 m^3/day) [1].

Among several different technologies, membrane processes nowadays have the leading role. In particular, looking at the new contracted plants (2010-2016), Reverse Osmosis now holds by far the majority of the global market share, ranging from 60% to 90% depending on the geographical areas. Thermal evaporative processes (mainly Multiple Effects Distillation and Multiple Stage Flash technologies) are still keeping an important role in Gulf countries, historically characterized by the operation of huge thermal desalination plants, thanks to their robustness, small sensitivity to low quality seawater feed and salt concentration and to the large availability of low-temperature waste heat for powering the thermal evaporative plants.

Within this context, electromembrane processes, e.g. electrodialysis (ED), electrodialysis reversal (EDR) and electrodeionization (EDI), have a small, yet stable share in low-salinity desalination applications. New ED/EDR and EDI contracted plants in 2015-2016 covered between 1 and 2% of the total desalination installed capacity, with the majority of plants processing brackish water and with a size ranging between few tens of m^3/day up to a maximum of 10,000m^3/day, reached by an EDR plant installed in South Africa [1].

Such limitation in installed capacity and type of treated feed is mainly due to the relatively higher cost of ion exchange membranes (IEMs) compared to RO membranes, and to the significant reduction of membrane selectivity when seawater is used as the feed solution.

A very recent development in the field of electromembrane processes has been the launching of reverse electrodialysis (RED) for energy generation from salinity gradients. In this new application, the salinity difference between two streams (e.g. seawater and river water, or concentrated brines and brackish water) is converted into electricity by means of a controlled mixing of the two solutions. RED significantly promoted the development of new membranes and new plant configurations suitable for operations at high salinity, with optimized process efficiencies [2–8].

Electromembrane processes are thus experiencing a very promising revival era, pushed by R&D and industrial developments carried out by research institutions and major industrial stakeholders in the US, Europe and Japan [9].

In addition to that, a number of novel applications have been proposed in other industrial sectors, where the features of ED (or EDI) are more suitable than RO. Examples of these applications are the use of ED for brine concentration in sea-salt production facilities in Japan [10,11]; in food industry (e.g. for juice de-acidification) [12–14]; in electronics (e.g. for ultrapure water production) and wastewater treatment, especially for heavy metals removal [15–17]. Moreover, the recent trends in the field of renewable energy desalination have also highlighted the promising features of photovoltaic (PV)-ED coupling, made possible by the extreme flexibility of the ED process, which can follow the oscillating behaviour of PV power production [18]. The same features make ED extremely suitable also for coupling with other off-grid sources, such as wind energy [19].

Finally, several special applications of electromembrane processes are gaining room in the scientific-technological community, which is more and more engaged in developing new IEMs and devices, enlarging the potential for the application of this flexible and multi-faceted class of technologies. Among these, it is worth to mention the growing field of bipolar membranes for acid and alkali production and electrochemistry applications [20–26], the development of selective-electrodialysis for selective salt separation from saline streams [26–29], and the application of the electrodialysis metathesis (EDM) in Zero Liquid Discharge (ZLD) desalination [30–33].

The objective of this thesis was therefore to explore a number of challenges related to the process development of ED. In particular, these challenges are addressed by means of process modelling and experimental investigations, playing a central role throughout the thesis as fundamental analytical tools.

The first chapter presents a critical review on process fundamentals and applications, covering the basics of ED equipment as well as describing the most promising processes directly derived from ED. Some of the most relevant gaps in the literature are also identified.

The next chapter focuses on steady-state ED modelling. After presenting a novel semi-empirical model, some simulative case studies are presented, highlighting the peculiarities of batch and multistage operations.

Dynamic operations are explored in chapter 3. In the first part of the chapter, a model for capacitive electrodialysis (CED) is presented and used to study the process that is, by nature, cyclical. Then, dynamic simulations are used to analyse the coupling of ED with renewable energy sources, describing the performances of a controlled process powered by PV and wind turbines.

Chapter 4 is focused on one of the biggest challenges of ED modelling: multi-ionic systems. A novel multicomponent model is therefore presented. The main parameters required to characterise the model are discussed and experimentally estimated. The model is also validated against experimental data.

Finally, the last chapter presents optimisation studies of commercially relevant schemes for seawater desalination, showing how the model can be successfully used for exploring the energetic and cost potential in ED.

1 Electrodialysis fundamentals and applications

The need for unconventional sources of fresh water is pushing a fast development of desalination technologies, which proved to be able to face and solve the problem of water scarcity in many dry areas of the planet. Membrane desalination technologies are nowadays leading the market and, among these, electrodialysis (ED) plays an important role, especially for brackish water desalination, thanks to its robustness, extreme flexibility and broad range of applications. In fact, many ED-related processes have been presented, based on the use of Ion Exchange Membranes (IEMs), which are significantly boosting the development of ED-related technologies. In this section, the fundamentals of the ED process and its main features are presented. Starting from a brief historical perspective, an important outlook is given to operational aspects and process equipment. Finally, the most recent applications of ED-related processes are presented, highlighting limitations and potentialities in the water and energy industry.

1.1 Historical development and working principle

1.1.1 From early steps to commercialisation

ED was proposed for the first time in 1890 by Maigrot and Sabates [34]. They built an early concept unit to demineralize sugar syrup by using carbon as electrodes and permanganate paper as membrane. A dynamo served as current supply.

However, Maigrot and Sabates never used the term electrodialysis, which can be officially found for the first time in a patent in 1900 [35]. In this patent, Schollmeyer aimed to purify sugar syrup using the same technology as in [34], but with soluble zinc or iron anodes. Despite this, it is generally argued that ED was not actually theorised until 1911 [35–37], when Donnan presented his exclusion principle, experimentally confirmed by Teorell few years later. According to this principle, it is possible to manufacture membranes selective to cations using fixed negative charges and membranes selective to anions using fixed positive charges.

The theorisation of electrochemical principles governing the behaviour of IEMs opened the way to the development of new membranes and to the conceptualisation of an electrodialyzer with multiple compartments [34]. However, the actual concept of multi-compartment ED where anion and cation exchange membranes are alternated could be only realised in 1950, when W. Juda and W. A. McRay manufactured the first synthetic ion-exchange membranes from ion exchange resins [35]. These membranes were used by Ionics (US) in 1954 to build the first ED desalination plant for Aramco (Saudi Arabia) [35]. Since that year, many other ED units were built.

In 1974, ED faced the main breakthrough with the development of the electrodialysis reversal concept (EDR) [35,38]. This new operational strategy allowed ED to work by periodically inverting the current, offering the main advantage of membrane

fouling control and generating a breakthrough in the implementation of ED at the larger industrial scale.

By then, a number of "ED-derived" alternatives, applications and processes have been developed and presented in the literature, providing a further booster to the development of electromembrane technologies in general. Figure 1 represents a synthetic timeline of the most critical development steps for ED and related technologies, indicating from the first important milestones to the more recent and very differentiated applications presented so far, including the first laboratory- or pilot-scale experiences and the first commercialisation attempts of the most recent ED derived processes. A deeper insight on these special applications will be given in Section 1.4.

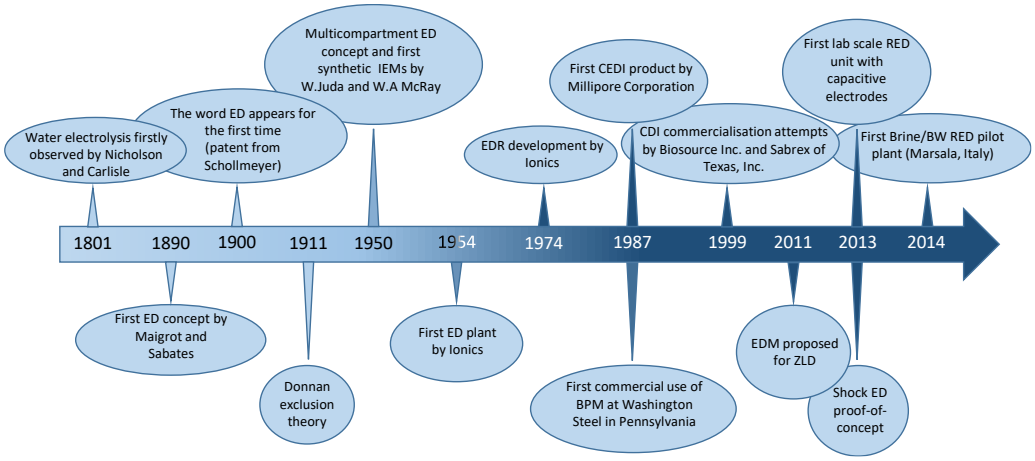

Figure 1. Timeline of the most important developments for ED and related processes [39].

1.1.2 ED devices: cell pair and stack

Electrodialysis (ED) is an electrically driven process. An ED unit is typically constituted by a train of ion-selective anion and cation exchange membranes (AEMs, CEMs), interleaved with alternating concentrate and dilute solution compartments and ending at both sides with an electrode compartment (Figure 2).

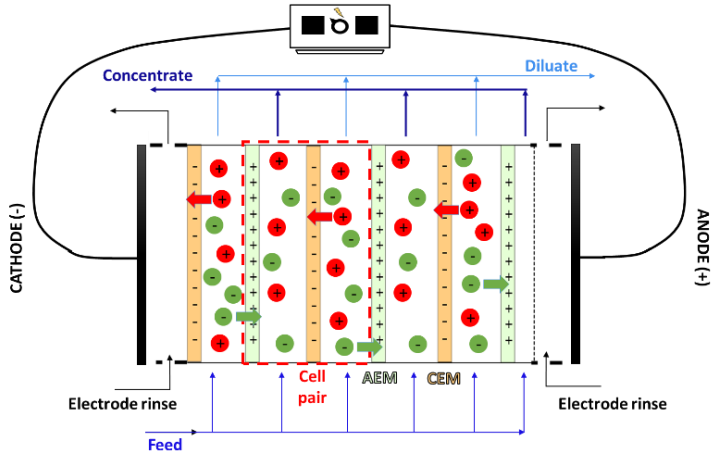

Figure 2. Schematics of an electrodialysis system, identifying the repeating unit (cell pair).

When the electrodes are electrically charged (by connecting them to a power source), an electrical current flows through the ED stack. As a consequence, electrically charged solutes are forced to move according to the electric field. In particular, anions migrate towards the anode (positively charged) and cations towards the cathode (negatively charged). The presence of IEMs, as ideally selective barriers to ions, ensures that anions move freely through the nearest AEM and are blocked by the nearest CEM. Conversely, cations move through CEMs and are blocked by AEMs, which leads to the depletion of salt content in the dilute compartments and the enrichment of the concentrate one (see Figure 2). The repeating unit of ED, namely the *cell pair*, consists of an AEM, a CEM, a dilute channel and a concentrate channel. An ED stack contains from a few cell pairs (in laboratory-scale units) up to several hundreds of cell pairs (values around 500 cell pairs or more are common in industrial units) and the two electrode compartments, which allow the current of electrons flowing through the external electrical circuit to be converted into a current of ions. The active area of a single membrane goes from ~0.01 to ~0.06 m^2 for laboratory scale units [40–44], reaching values around 1 m^2 for large industrial scale units [45,46].

In conventional electrodialyzers with the classical plate-and-frame equipment (see Figure 3), the feed channels are created by interposing between the membranes net spacers, maintaining a fixed inter-membrane distance and providing some mixing promotion in the channels. Spacers are provided with gaskets along the perimeter of the channels, which seal the channels and guide the solutions through them. Holes in spacers and membranes create special ducts for the two hydraulic circuits acting as manifolds for distributing/collecting the solutions to/from the channels. The ED device is closed with two end plates and compressed by bolts and nuts. ED stacks can be also built without spacers, by using profiled membranes (spacers and profiled membranes are discussed in detail in [39]). The inter-membrane distance in ED stacks typically ranges from ~0.3 to ~2 mm [10,40,42,45–51].

The electrode compartments are typically obtained from the end plates and contain the two electrodes and the electrode solution adopted for the conversion of ionic into electric current. NaCl has been used in the past as the electrode solution, although this causes the production of active Cl_2 [43] in the anodic compartment. For this reason, electrode rinse solutions containing SO_4^{2-} salts are now usually preferred in order to avoid damages to the anode [52].

Recently, the use of capacitive electrodes instead of conventional ones has been studied [53–55]. These electrodes are composed by an active carbon layer and a current collector. Ions are adsorbed/desorbed in the active layer; this releases/captures free electrons, which pass through the collector thus reaching the external electrical circuit. In this way, it is possible to convert the ionic current into an electronic one without the need for a redox reaction, thus providing advantages such as the absence of unstable or toxic products (i.e. Cl_2) and the reduction of the electrode potential drop [56]. On the other hand, capacitive electrodes suffer from saturation of the carbon layer, so that the electrical polarity needs to be periodically switched in order to operate the unit in a continuous way. For more insights on the topic, see section 3.1.

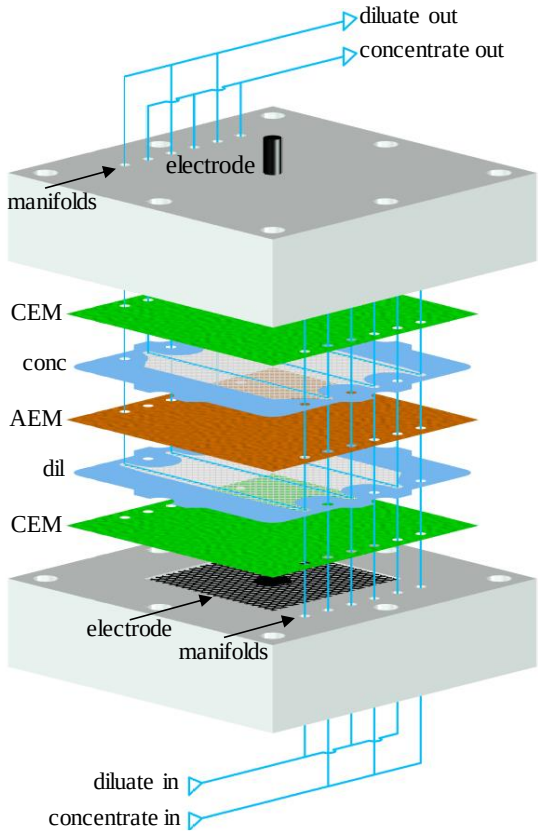

Figure 3. ED stack in the sheet flow arrangement of a laboratory scale unit with net spacers. A single cell pair and an additional CEM are represented [39].

The ED process can operate in batch or continuous mode. The first operating strategy is usually limited to small scale applications [43], while continuous operation is more common at industrial scale [50]. Typically, a single stack is not sufficient to reach the desired product specifications, and a multistage configuration is adopted. This configuration has also the potential to reduce the energy consumption and is particularly interesting for seawater desalination [50,57,58]. Alternatively, when a recovery higher than 50% is required, a feed and bleed operation mode can be adopted. In this case part of the concentrate, of the diluate or of both streams is recirculated back to the stack inlet, in order to independently control outlet brine and diluate concentrations [50]. Finally, an uncommon alternative configuration includes the presence of a circulation flow on the diluate side (as it happens in a batch process) and of segregated concentrate compartments, filled with non-circulating solution. This particular arrangement has been used at laboratory scale to obtain extremely concentrated solutions [59,60].

1.2 Overview of Ion Exchange Membranes

Ion exchange membranes (IEMs) represent the key components of all electromembrane processes. IEMs are typically thin polymeric films containing fixed charged groups which are ionisable in water [10,61]. On the basis of the presence of positive or negative charged groups, these membranes can be firstly classified into anion and cation exchange membranes, respectively.

A cation exchange membrane (CEM) is characterized by the presence of fixed negative charges. Thus it is able to let positive ions (counter-ions) move across it and to block anions (co-ions). Conversely, the anion exchange membrane (AEM) blocks cations allowing the transport of anions. This exclusion principle, firstly theorized by Donnan [62], represents the fundamental IEM feature that makes the operation of all electromembrane processes possible.

The following sections are intended to give a general overview of IEMs fundamental theory, manufacturing and characterisation. For a more detailed insight on these topics, readers can refer to some more specifically focused reviews [63–65].

1.2.1 Donnan equilibrium and membrane potential

When an IEM is in contact with an electrolyte solution, the fixed charges on the surface of the IEM attract counter-ions by Coulomb forces and generate an electrical field. The Donnan exclusion [50,66] causes a sharp change of concentration at the IEM-solution interface, thus generating a very thin charged region called electrical double layer (nanoscale, Debye length), where the counter-ions neutralize the fixed charges, and their concentration is much higher than the co-ions concentration (Figure 4). Therefore, counter-ions tend to diffuse from the IEM to the electrolyte solution while co-ions diffuse in the opposite direction. However, the large gradients of chemical potential are counter-balanced by a large gradient of electrical potential, the so-called Donnan potential, so that the electrochemical potential is conserved (Donnan equilibrium) and the net flux of ions is null.

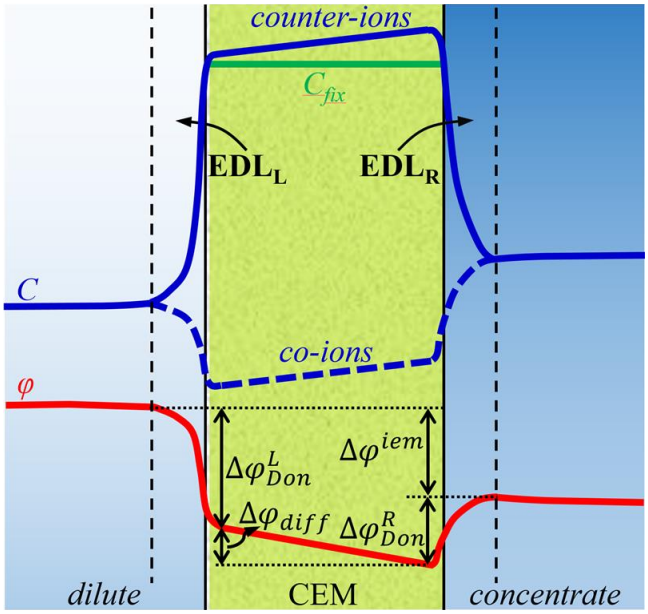

Figure 4. Schematic representation of ions concentration and electrical potential for a binary monovalent electrolyte solution in a cation exchange membrane immersed between a dilute and a concentrate solution [39].

By imposing the equivalence between the electrochemical potentials of ions in the electrolyte solution and in the IEM in equilibrium with it, the Donnan potential (η_{Don}) can be expressed [50,61] as

$$\eta_{Don} = \frac{1}{z_i F}\left[R_G T \ln\left(\frac{a_i^{SOL}}{a_i^{IEM}}\right) + \bar{V}_i \Delta\pi\right] \quad (1)$$

where F is the Faraday constant, z is the valence, R_G is the universal gas constant, T is the absolute temperature, a is the activity of the ion, $\bar{V}$ is the partial molar volume, $\Delta\pi$ is the osmotic pressure difference between the two phases, the subscript i refers to the salt ion i and the superscripts iem and SOL indicate the membrane and the solution, respectively. By equating the Donnan potentials for cation and anion, being the osmotic pressure term $\bar{V}_i\Delta\pi$ negligible with respect to the RT-logarithmic one [50] and by assuming that the activity coefficients are equal in both phases [66], the Donnan equilibrium for the concentration can be obtained as [62,66]

$$C_{co}^{IEM} = \sqrt{\left(\frac{C_{fix}}{2}\right)^2 + C^{SOL\,2}} - \frac{C_{fix}}{2} \quad (2)$$

where C_{co}^{IEM} is the co-ion concentration in the membrane, C_{fix} is the fixed charge concentration and C^{SOL} is the salt concentration in the solution.

An IEM immersed between two solutions at different concentrations is subject to a voltage difference over the two sides, referred to as “membrane potential”.

According to the well-known theory by Teorell-Meyer-Sievers (TMS), the membrane potential is [66–68]

$$\eta^{IEM} = \eta^{L}_{Don} - \eta^{R}_{Don} + \eta_{diff} \quad (3)$$

where $\eta^{L}_{Don}$is the Donnan potential on the left side, η^{R}_{Don} is the Donnan potential on the right side and η_{diff} is the diffusion potential arising from the concentration gradient within the membrane and from the different diffusivity of the two ions. The simplest expression of the membrane potential that can be derived from the TMS theory is [50,66,67]

$$\eta^{IEM} = (2\, t^{counter}_{IEM} - 1)\frac{R_G T}{z_i F} ln \frac{a^{SOL,R}}{a^{SOL,L}} \quad (4)$$

where $t^{counter}_{IEM}$ is the transport number of the counter-ion in the membrane, while $a^{SOL,R}$ and $a^{SOL,L}$ are the activities in the right and left solution, respectively.

The one-dimensional TMS model is based on several simplifying assumptions [67,68] and predicts well the membrane potential within a certain range of solutions concentration, while deviating from experimental data in other conditions, e.g. with large concentration ratios [68,69]. Models accounting for the effect of the membrane nano-pore radius have been developed, such as the “uniform potential” model and the “space charge” model [68,69]. The discussion of these models goes beyond the scope of this section; however, the simple mathematical formulation of the TMS theory makes it the most commonly adopted for practical uses. Therefore, in the following the membrane potential will be intended as derived from the TMS theory.

1.2.2 IEMs preparation and classification

Based on their morphology, IEMs can be classified into two main categories: homogenous and heterogeneous [61,70]. A more detailed classification based on the degree of homogeneity of the structure can be made [70,71], which is particularly useful for IEMs characterized by micro-inhomogeneities.

Homogeneous membranes are the most commonly used in ED and other electro-driven processes [70,72–76], especially in high salinity applications where membrane resistance is a key aspect. Such membranes appear homogeneous at the microscopic scale, but at the nanoscopic scale they can be observed as multiphase (i.e. microheterogeneous) systems composed by at least two phases: the polymer matrix with the fixed charges and the interstitial (electroneutral) salt solution. A more rigorous description, as given by Zabolotsky *et al.* [77], recalls the presence of a gel phase, generated by a thin layer of solution, and of fixed charges located at the internal walls of interstitial vescicles (Figure 5). This phase is also related to the formation of an electrical double layer (EDL), where electroneutrality is not maintained due to the split of anions and cations concentration profiles, which actually generates the Donnan potential at the interface [64,70,78,79]. The microheterogeneous model in [77] is particularly useful for the estimation of structural parameters as well as for the description of the peculiar behaviour (i.e.

dependence on electrolyte concentration) of fundamental properties such as permselectivity and electrical conductivity.

Nevertheless, Kamcev *et al.* [80] recently discarded the actual existence of such a microheterogeneous structure discussing data of membrane resistance measurements. Therefore, this is still an open issue which will require further research activities.

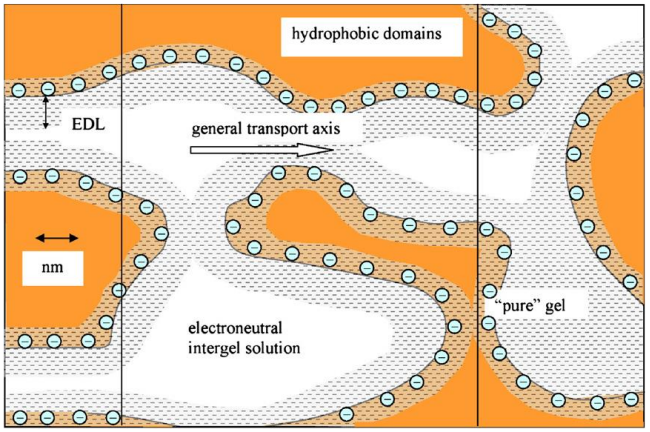

Figure 5. Representation of the structure of a homogeneous CEM, with the three different phases: polymeric hydrophobic, electroneutral solution and gel phase [78]**.**

For homogeneous membranes, three main manufacturing methods can be identified [61,70,81]:

- Polymerisation of monomers: at least one of these monomers must contain ionisable groups;
- Introduction of charged moieties into a polymeric film: this can be done by adding either a charged monomer or a non-functional monomer to be functionalized afterwards;
- Introduction of charged moieties into a polymer, followed by polymer melting (or solvation in a solvent) and casting into a film.

Styrene-divinylbenzene-based membranes represent one of the most remarkable examples of homogeneous structures produced starting from monomers. These membranes have been widely used in ED and are obtained from sulfonated or aminated styrene-divinylbenzene copolymers [74,75]. These IEMs have been also used in ED plants concentrating seawater in order to produce table salt, where it is essential to increase the monovalent ion selectivity [74].

Concerning the second class of manufacturing methods, polyethylene, polypropylene and fluorocarbon polymers are used for IEMs production from a preformed polymeric film [81]. In this case, films are commonly functionalized by grafting acrylic monomers to obtain weak acidic CEMs [82–86]. Alternatively, vinyl monomers such as styrene are grafted to the polymer film and subsequently sulfonated or aminated in order to produce strong acidic CEMs [87–90] or AEMs [91,92].

The third manufacturing method is commonly adopted for soluble polymers such as polyether ketone and sulfonated polymers [81,93]. These latter are particularly important as they represent a promising option for producing cheap membranes to be used for ED and other processes when working under severe conditions such as high temperature [70]. Production processes and properties of IEMs based on polysulfone block copolymers, polyether sulfone and polyarylene ether sulfone have been widely described in the literature [94–99].

Though still at a laboratory scale, electrospinning (coupled with hot-pressing) has recently been proposed for the production of nanoporous IEMs [63]. By this method it is possible to produce nanofibrous structures combining high porosity and large surface area with higher tensile modulus compared to the bulk material. In particular, very good performances of these new IEMs have been found for diffusion dialysis applications [63].

Heterogeneous membranes are characterized by ion-exchange particles (of macroscopic size, compared to the nano-scale of phase discontinuities of homogeneous membranes) incorporated in a continuous phase made of a binding polymer [61]. These membranes are usually thicker, with higher mechanical strength but poorer electrochemical properties. The use of cheap binding polymers allows for a significant reduction in the IEMs specific price, and the best trade-off is to be found between these aspects [70]. Heterogeneous membranes are usually manufactured by incorporating ion-exchange resins into polymer sheets (the binder polymer) with three main alternative procedures [70,100]:

- calendering the particles into the polymeric sheet;
- dry moulding of the inert polymer film and the resin particles followed by milling;
- dispersion of resin particles in a solution containing a film-forming binder followed by casting and solvent evaporation.

In addition, new preparation methods have been recently engineered with the aim of improving IEMs structure. In this context, polymer blending and pore filling methods represent recently proposed alternatives [63].

An important feature strongly affecting the mechanical behaviour of heterogeneous membranes is the particle size distribution. In particular, it was observed that the flexibility increases when decreasing the particle size, while the brittleness increases with the particle loading [101].

Special ion exchange membranes have also been developed through several research efforts focused on the optimal tuning of membrane properties. These efforts led to special membranes characterised by hybrid structures and particular manufacturing methods [70,81]. Interpenetrating (IPN) and semi-interpenetrating (sIPN) polymer network IEMs are examples [102–107]. IPN are prepared by mixing two polymers that cross-link due to permanent entanglement, while sIPN are composed by a linear or branched polyelectrolyte immobilised in a cross-linked polymer matrix. This particular structure allows electrochemical and mechanical properties to be tailored for specific applications [102,107]. Membranes prepared by radiation grafting represent another class of IEMs, in which this new technique allows incompatible polymers to be linked, thus combining their properties. In

addition, these properties can easily be tuned by choosing the degree of grafting [70]. Several works deal with the preparation and characterisation of IEMs through the grafting method, and the possibility of using them in ED has been assessed [108–112].

The last group of special membranes is represented by the hybrid organic-inorganic IEMs. Combining the properties of polymers with those of inorganic materials, chemical, mechanical and thermal stability can be significantly enhanced [81]. For this reason, these membranes are mainly used in fuel cell applications [113–121]. Hybrid structures are usually obtained through intercalation, blending, in situ polymerization, molecular self-assembling or sol–gel process, with this latter being the most widespread method [122,123].

A particular development has led to special membranes incorporating both positive and negative fixed charges within the same membrane [81].

Bipolar membranes (BPM) are the most remarkable example of this class. BPM are constituted of an anion exchange layer placed in contact with a cation exchange layer. These membranes are mainly used in a special application of electrodialysis, where water splitting is induced to produce acid and alkaline solutions [61,81]. Bipolar membranes can be manufactured by different methods such as casting a cation exchange polyelectrolyte solution on an anion exchange membrane (or *vice versa*) [124], adhering commercial cation and anion exchange membranes [23], or functionalizing the two sides of a standard membrane [125–128].

Two other interesting classes of membranes containing both type of charges are the amphoteric and the mosaic membranes [81]. The former present randomly distributed weak acid and weak basic groups. Their main feature is that charged groups respond to pH variations, thus modifying the cationic or anionic selective character of the membrane. This makes amphoteric membranes particularly useful in special applications such as in biomedical and industrial fields [81].

Mosaic membranes are characterised by anion and cation exchange areas arranged in a parallel way within a single membrane [129]. This allows individual current circulation in each layer, leading to negative osmosis and a salt permeability higher than that of neutral species. These special properties make mosaic membranes a promising candidate for the treatment of waste streams where salt should be separated from organic compounds. However, these membranes are not yet commercially available [81].

1.2.3 IEMs properties and characterisation

In order to evaluate the performance of a membrane it is necessary to estimate several properties which can be grouped into three main categories: mechanical, physicochemical and electrochemical properties.

Mechanical stability is essential for a membrane to be used in industrial applications such as ED. Several mechanical tests are performed for the mechanical characterization of membranes [130]. In particular:

Uniaxial tensile test. It is the most common test to evaluate Young's modulus, yield strength, elongation at break, strain-softening and strain-hardening.

Creep and relaxation tests[131].

Dynamical mechanical analysis. It is widely adopted to investigate the viscoelastic properties and the glass transition temperature.

Bursting test. During the test, a membrane is exposed to an increasing pressure (simulating the presence of a differential pressure between the two channels of a cell pair) until failure occurs.

The mechanical behaviour of IEMs is affected by several features of the membrane material, e.g. cross linking degree, water uptake, aging, and by operating conditions, e.g. temperature [72]. In particular, Young's modulus decreases as the temperature increases [132] and membranes become stiffer as the cross-linking degree increases On the contrary, membranes plasticize at high level of water uptake [133].

Physico-chemical properties to be characterised in IEMs are swelling, ion-exchange capacity (IEC), chemical stability and permeability to ions (conductivity and diffusive permeability) and neutral species (diffusive permeability).

The swelling degree can have a direct influence on the dimensional stability, permselectivity and specific electrical conductivity. The swelling degree can be evaluated by measuring the weight difference between dry and swollen membrane [134,135]. In order to calculate the volumetric swelling, the membrane material density is needed [70].

The IEC indicates the amount of fixed charges in the IEM. It is commonly expressed as milli-equivalent (meq) of functional groups per gram or cm^3 of dry membrane (though in some cases they can be expressed per gram or cm^3 of swollen membrane) and it is useful to estimate the fixed charges concentration. The main technique for the measurement of IEC is titration with NaOH for negative groups and with HCl for positive groups [93,134,135].

In ED and related processes, very large concentration differences can be achieved in the two compartments. For this reason, salt and water diffusion through IEMs can represent an important factor for determining process performance.

Salt diffusion can easily be measured using the time-lag method or a more advanced method adopting radioactive tracers [50].

Water moves across membranes by two main mechanisms: osmosis (water passage driven by an osmotic pressure difference) and electroosmosis (passage of water molecules entrained in the solvation shell of ions, thus proportional to the ions flux). In order to determine the water osmotic permeability it is possible to measure the water flux in an ED batch process by simply measuring the weight change in the reservoirs, periodically switching off the stack current to exclude the electroosmotic effect [43].

Electrochemical properties have the most important influence on the performance of IEMs. In particular, the two main electrochemical properties to be measured are permselectivity and electrical resistance.

Permselectivity indicates how selective the membrane is to the passage of counter-ions. A low perm-selective membrane will allow the passage of co-ions between compartments, thus negatively affecting the separation efficiency. The fastest method to estimate membrane permselectivity is by measurement of non-Ohmic membrane potential [70,136]. The real (measured) membrane potential in the case of a single electrolyte in solution can be written as [32]:

$$\eta_{measured}^{IEM} = \alpha_{IEM} \frac{RT}{z_i F} \, ln \frac{a^{SOL,R}}{a^{SOL,L}} \tag{5}$$

where $a^{SOL,R}$ and $a^{SOL,L}$ are the salt activities in the solutions at the two sides (right and left) of the membrane and α_{iem} is the membrane permselectivity, which can be seen as the ratio between the actual membrane potential and the theoretical one given by the Nernst equation (5) for α_{IEM} = 1, i.e. $\alpha_{IEM} = 2\, t_{counter}^{IEM} - 1$ (see eq. (4)).

It should be noted that the transport number (and thus the permselectivity) evaluated with this simple method is generally underestimated. In fact, this measurement leads to an apparent transport number that should be corrected by the water transport number. A more detailed discussion of this issue can be found in [65].

By a more rigorous definition, the permselectivity can be expressed as [50,70]:

$$\alpha_{IEM} = \frac{t_{IEM}^{counter} - t_{SOL}^{counter}}{t_{SOL}^{co}} \tag{6}$$

where $t^{counter}$ and t^{co} are the transport number of the same counter-ion and co-ion in solution, and the subscript IEM indicates that, using the relevant values, the expression is valid for both AEM and CEM. In particular, it is possible to experimentally estimate transport numbers using Hittorf's method [65,70,138,139] or by chronopotentiometric measurements [140–144]. One of the most critical aspects is that the concentration of electrolytes in solution affects permselectivity [5,145]. For this reason, multiple measurements at different concentrations are necessary in order to get the different permselectivity values in the whole operational range. It is worth noting that the definition of permselectivity has a physical meaning just in presence of single salt solutions. In the case of multi-ionic feeds, the expression of the membrane potential does not allow the definition of permselectivity as will be shown in chapter 4.

The membrane electrical resistance (ER), inversely related to the electrical conductivity, generates Ohmic potential drops when an electrical current passes through the membrane pile, thus dramatically affecting the process energy consumption. As in the case of permselectivity, electrical resistance is influenced by solutions concentration [64,79,146] as well as composition. This dependence can be explained with the typical multiphase structure of IEMs, widely reported in the literature [64,77,147]. In order to characterise membranes ER, direct current (DC) or alternating current (AC) measurements can be carried out.

The simplest method consists of estimating ER from the slope of an *I-V* (current-potential) curve in DC mode, limited to the region where a linear relationship between voltage and current is maintained. This curve can be obtained using a test-

cell with two chambers separated by one membrane [148] or by chronopotentiometry in a six-cell compartment device [79,144]. Another option involves the use of a *clip cell*, composed by two black graphite electrodes fixed on Plexiglas plates and used to "clip" a conditioned wet membrane [149,150]. ER can thus be measured by the previously mentioned DC method but also by means of AC methods (as described in the following lines).

It should be noted that *I-V* curves (and, more generally, the use of DC methods) give reliable results only when IEMs are placed in contact with a sufficiently concentrated solution. The reason is that this method is not suitable for low concentrations as it cannot separate the effects of electric double layer formation and concentration polarisation. In addition, the presence of DC leads to concentration polarisation in the internal pores even when the external diffusion layers are not present [151]. Finally, the blank resistance to be subtracted in order to separate the resistance of the membrane from that of the solution can be relatively very high for low concentration, thus affecting the accuracy of the method.

As an alternative to DC-based methods, AC-based measurements can be performed adopting the Electrical Impedance Spectroscopy (EIS) method, able to distinguish among the contributions due to Ohmic effects, electric double layer and diffusion boundary layer and, thus, to estimate the pure membrane resistance [79,146,152,153]. On the other hand, EIS is the most complex methodology, as it requires the identification and implementation of an "electrical model" fully describing all phenomena involved, in order to properly interpret the experimental data and convert them into the desired information.

1.2.4 Fouling and electrodialysis with polarity reversal (EDR)

Although ED is not generally affected by fouling and scaling phenomena as much as other desalination processes such as RO [154], IEMs fouling can still be a limiting factor for maintaining good process performances. In particular, this phenomenon can significantly enhance membrane resistance and pressure drops along the channel and, in some cases, even reduce membrane permselectivity [155]. *I-V* curves are often used to characterise membrane fouling, though this method does not provide information on the properties of fouling layers. EIS has been proposed as a supplementary investigation method in order to capture more details on interfacial layers [156].

Three main classes of fouling compounds can be identified: scalants, colloidal particles and organic materials [157].

Scaling is one of the most important problems in desalination, especially when the feed water is rich in low-solubility salts such as $CaCO_3$ and $CaSO_4$. The most common methods for reducing it include the use of lower recovery rate, the adjustment of pH and cleaning procedures with citric acid or EDTA [157]. In addition, the possibility of treating the concentrate stream (i.e. the one with highest scaling potential) of a batch ED unit by magnetic or ultrasonic field has been reported [158]. In particular, the magnetic field was applied to a part of the feeding line, while an ultrasonic bath

was used as the concentrate tank. Interestingly, the last method not only results in a scaling reduction but also in an improvement of ions transport.

Colloidal particles can be abundant in sea or brackish waters and they are often negatively charged. Their deposition on the membrane surface is driven by the electric field pushing the colloidal particles towards the positive electrode. Such migration is stopped by the presence of the membranes, acting as a mechanical barrier and being covered by a growing deposited layer of colloids on their surface. Similarly to scaling, colloidal-fouling prevention strategies include the reduction of recovery and pH adjustment. Besides, micro and ultrafiltration can be used as pre-treatments, while a higher fluid velocity inside the stack can help particles displacement from the membrane surface [157]. The most effective action for colloidal and organic foulants, however, is the use of a polarity reversal strategy, which will be presented in the following lines.

Fouling due to organic matter can be very severe when ED treats food industry streams [159,160] and in water reuse applications [155,161]. In these cases, the presence of organic compounds can dramatically affect fouling phenomena leading to a huge decline in process performances. For this reason, several research works have adopted model foulants such as bovine serum albumin, humate and sodium dodecylbenzene-sulfonate in order to investigate the phenomenon in depth [156,162].

The molecular size of organic particles can significantly affect their fouling behaviour. In fact, particles with a molecular weight of 200 - 700 Da can cause internal membrane fouling, being able to penetrate membrane pores. On the other side, larger molecules cannot enter inside pores, thus being blocked on the external surface, while, conversely, much smaller molecules pass freely through membrane pores, thus not generating any internal blocking and fouling in the IEM [161]. In order to reduce organic fouling pre-treatments such as microfiltration, ultrafiltration or activated carbon have been proposed and cleaning actions with NaOH solutions are also possible [157].

Regardless the different classes of materials, most foulants present in feed waters exhibit electrostatic features which enhance the fouling risk for AEMs [155,163]. In this respect, many efforts have been made through years in order to increase AEMs antifouling properties by surface modification processes [164–166]. Grebenyuk. *et al.* [164] modified AEMs by adding high molecular mass surfactants obtaining an increased resistance against organic deposition. Alternatively, modification with poly(sodium 4-styrene sulfonate) [165] or polydopamine [166] can also reduce fouling, while negligibly affecting other IEMs properties.

Despite the different strategies proposed for reducing fouling in IEMs, standard ED operation always require in-place-cleaning procedures, resulting in a cost increase for the process [157]. For this reason, the development of the electrodialysis reversal (EDR) concept represented one of the main breakthroughs for the ED technology, succeeding in dramatically reducing the fouling tendency of IEMs in ED stacks for very long lifetimes. The EDR concept is based on the idea of reversing the polarity of the electrodes at regular time intervals [167]. Consequently, diluate and concentrate channels are inverted and the reverse electric field promotes the periodic removal of electrically-charged foulants (e.g. colloids or organic matter)

deposited on membranes surface. In this way, detached particles are entrained by the flowing solutions and discharged with the exiting streams ("off-specification" outlet), which are therefore disposed back to the sea (or to another receiving body) for a time interval allowing the complete cleaning of the feed compartments, typically ranging from a few seconds up to 1-2 minutes [167]. EDR adds complexity to the process as it requires a triggering control unit, electric control systems to change polarity and automatic valves for compartments switching. In addition, some of the feed is wasted during the "off-spec transition", which leads to a reduction in the conversion rate of the process.

Nevertheless, EDR offers significant advantages in terms of minimisation of cleaning procedures and pre-treatments and avoids the presence of acids tanks, complexing agents tanks, dosing pumps and pH controllers inside the desalination plant [167]. Moreover, the polarity reversal technology is able to operate under extreme conditions, such as salt supersaturation, with examples of plants operating under a super-saturation level of $CaSO_4$ higher than 175% [168]. More importantly, EDR has allowed the operation of brackish water ED industrial plants for more than 30 years, with IEMs lifetime reaching up to 10-15 years.

More recently, a concept similar to polarity reversal has been investigated, namely the pulsed electrical field (PEF) [157,169,170]. The PEF operating mode consists of discontinuously applying the electric field and generating a constant current, leaving some time intervals without any electric field applied. This method is claimed to reduce membrane fouling, thus increasing process performances, by disturbing the deposition of charged species. In addition, a reduction of the polarisation layer has also been experienced [169,170]. PEF has been recently compared with EDR, showing similar performances or even lower energy consumption under certain conditions [171].

1.3 Concentration polarization and limiting current in electrodialysis

The role of hydrodynamics and associated phenomena of mass transport is crucial in determining the performance of ED stacks and the capital and operating costs of the process. It is well known that mass transfer limitations and non-Ohmic voltage drops arise because of the so called "*concentration polarization phenomena*" and can be mitigated by enhancing mixing. The energetic cost of the process may also be affected by the power consumption for pumping the solutions through the channels. Moreover, the channel features, which are essential for hydrodynamics and mass transport, also affect other aspects that may be critical, such as the Ohmic voltage drop. Finally, pressure drop in the manifolds, voltage losses caused by a non-uniform flow distribution among and in the channels, internal leakages due to pressure gradients across the membrane are additional phenomena depending on the stack hydrodynamics.

Clearly, the optimization of ED (or EDR, or other electromembrane processes) units is based on a very delicate equilibrium among the stack features (including the membranes properties) and the operating conditions. The following sections will

focus on the fundamentals of concentration polarisation and limiting current density (LCD) in ED and the way these affect the operation of ED and related processes.

1.3.1 Concentration polarization phenomena

In membrane separation processes, concentration polarization is a well-known phenomenon which manifests itself as a concentration gradient within the solution and perpendicular to the membrane surface. In the case of IEMs-based processes, the electrical current is carried roughly in the same amount by cations and anions migrating through the solution in opposite directions. On the contrary, inside the membrane current is carried mainly by counter-ions, while co-ions are (ideally) excluded. As a consequence, at the solution-membrane interface the migrative flux of co-ions (typically directed from the interface to the bulk of the solution) has to be counterbalanced by a diffusive flux in the opposite direction, intrinsically accompanied by a concentration gradient able to generate such diffusive flux according to Fick's law [10,172–174].

Concentration polarization and transport phenomena near interfaces have commonly been analysed by the Nernst film model [175,176]. The basic assumption of this theory is the existence of a "Nernst diffusion layer" between the membrane-solution interface and the fluid bulk with uniform composition. This is also known as "diffusion boundary layer" (DBL) and can be considered as a thin stagnant layer where no convection occurs and mass transfer is controlled by diffusion-migration, resulting in a linear concentration profile (Figure 6 (a)). The Nernstian idealization was improved by Levich [176], showing that the presence of convective transport within the DBL results in a smooth monotone concentration profile asymptotically approaching the bulk concentration.

Mass transport in IEMs and electrolyte solutions has been widely studied by the theoretical description given by the Nernst–Planck formalism [66,175], which can also lead to a more rigorous definition of the concentration polarisation gradient. In fact, under certain hypotheses the flux $\vec{J}_i$ of type-i ions can be expressed as

$$\vec{J}_i = -D_i\vec{\nabla}C_i - z_iFD_iC_i\vec{\nabla}\varphi + C_i\vec{u} \tag{7}$$

where D_i is the ionic diffusion coefficient, C_i is the concentration, z_i is the valence, F is Faraday's constant, φ is the electric potential, and $\vec{u}$ is the velocity vector. Hence, the total flux is given by the sum of diffusive, migrative and convective flux. The ion diffusion-migration flux can also be expressed as a chemical diffusion-Ohmic conduction flux [66], so that, for a strong binary electrolyte, it can be written as:

$$\vec{J}_i = -D\vec{\nabla}C_i + \frac{t_{SOL,i}\vec{\imath}}{z_iF} \tag{8}$$

where D is the electrolyte diffusion coefficient, $t_{SOL,i}$ is the migration transport number and $\vec{\imath}$ is the current density. At the membrane-solution interface, the mass balance under steady state conditions is obtained by equating the flux on the solution side (eq. (8)) with that on the membrane side. Considering only the component normal to the membrane surface (y coordinate) one has:

$$-D\frac{\partial C_i}{\partial y}+\frac{t_{SOL,i}i}{z_iF}=\frac{T_{IEM,i}i}{z_iF} \quad (9)$$

where T_i^{IEM} is the integral transport number within the membrane [66,177,178] accounting for both ionic diffusion and migration (i is positive if directed towards the positive y axis). Therefore, the following boundary condition can be written:

$$\frac{\partial C_i}{\partial y}=-\frac{i}{z_iFD}\left(T_{IEM,i}-t_{SOLi}\right) \quad (10)$$

In the literature, this boundary condition is often given by a less rigorous expression where $T_{IEM,i}$ is replaced by the migration transport number within the membrane $t_{IEM,i}$ [172–174,179–182], but the approximation is legitimated by the fact that diffusion inside the IEM is often negligible.

Moreover, commercial membranes normally have high permselectivity, i.e. the counter-ion transport number is close to 1 in the membrane, while being close to 0.5 in solution (NaCl). As a result, a diffusive flux roughly equal to 50% of the current density (i) divided by z_iF, i.e. equal to the conductive transport for each ion, is established at the IEM-solution interface. Thus, salt diffusion (of both co- and counter-ions due to electroneutrality) between the solution bulk and the interface takes place, in the same direction of migration for counter-ions and in the opposite direction for co-ions. Salt depletion occurs at the IEM-diluate channel interface, while salt enrichment occurs at the IEM-concentrate channel interface, affecting the electric potential profile as shown in Figure 6 (b). Typically, the electrolyte concentration profile in solution is slightly asymmetric, due to the difference in the transport number of cation and anion (e.g. $t_{Na+} \approx 0.4$ and $t_{Cl-} \approx 0.6$).

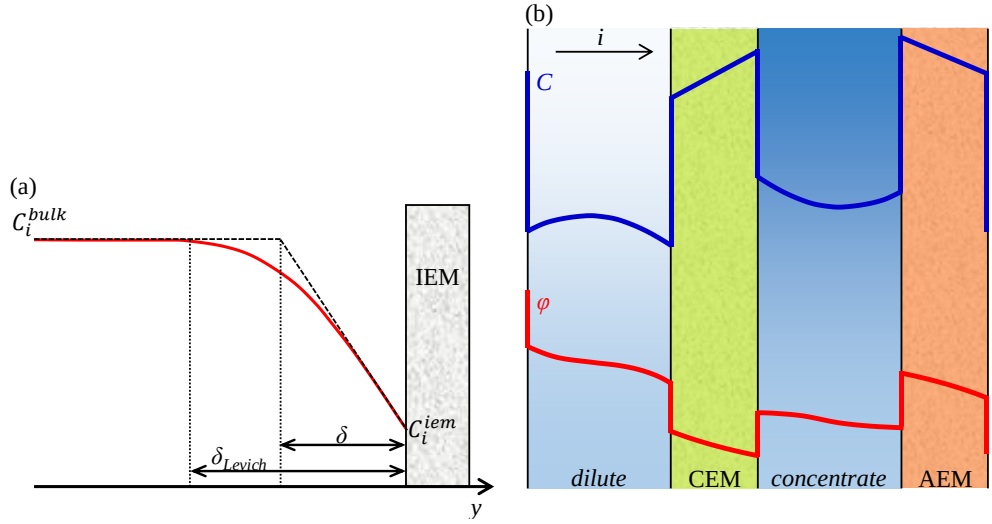

Figure 6. (a) Concentration profile within current-induced diffusion layer in steady-state conditions: Nernst's linear concentration profile (dashed line); Levich's profile taking into account convection contribution (solid line), where the concentration differs from the bulk concentration only by 1% at the distance δ_{Levich} from the IEM [78]. (b) Qualitative profiles of electrolyte concentration and electrical potential within an ED cell pair. Inside the IEMs the concentration of counter-ions is depicted. Electrical double layer phenomena are represented as sudden jumps at each IEM-solution interface.

Experimental observations of concentration polarization gradients have been carried out by several techniques. Choi *et al.* [183] measured the potential drop by a mobile micro-electrode at various distances from a CEM (two-compartment cell), obtaining the concentration profiles in the depleted side by letting the current vary. Tanaka [184,185] reported data on the electrolyte concentration profile obtained by the so-called Schlieren-diagonal method, based on the measurement of the refractive index in a three-compartment optical glass cell. Another method of visualization of the concentration profile is laser interferometry, firstly introduced by Forgacs *et al.* [186] and then applied in several works [187–191], some of which were used to validate models simulating ED stacks equipped with ion conducting spacers or profiled membranes [189,191], or analysing intensive current regimes ("overlimiting" region) [190]. Kwak *et al.* [192] fabricated a microfluidic ED device and applied a technique for the direct visualization of fluid flows and salt concentration profiles using charged fluorescent dyes over a wide range of voltage (0-100 V). Recently, the same research group [193] used the microscale ED system for studying the effects of floating spacers and validate their model for fluid dynamics and mass transport phenomena.

Regardless of the true concentration profile, the interfacial condition expressed in eq. (10) can also be written in Nernstian form, taking into account the DBL thickness (δ_{DBL}) [173,174,177,182,194,195] or the Sherwood number (Sh) [51,178,182,196]:

$$\frac{\partial C_i}{\partial y} = \pm \frac{C_i^{IEM} - C_i^{bulk}}{\delta_{DBL}} = \pm \frac{Sh\left(C_i^{IEM} - C_i^{bulk}\right)}{d^{eq}} \tag{11}$$

where C_i^{IEM} is the concentration at the IEM-solution interface (solution side), C_i^{bulk} is the bulk concentration, d^{eq} is the equivalent diameter. In eq. (11) the sign + has to be considered when moving from bulk to interface, while the sign – in the opposite case. For simplicity, the difference of the transport numbers is often assumed equal to 0.5 [6,196,197]. Eq. (11) identifies the most common expressions of mass transfer rate in these systems, also allowing an in depth comprehension of mass transport phenomena at the boundaries. In fact, under steady state conditions, both diffusion and convection in solution from bulk to interface or *vice versa* compensate for the difference between the migrative fluxes across solution and membrane.

The Sherwood number is defined as

$$Sh = \frac{k_m\, d^{eq}}{D} \tag{12}$$

where k_m is the mass transfer coefficient. From dimensional analysis, it can be found that the Sherwood number depends on the channel configuration (geometry of spacer or membrane profiles, but also active walls surface, depending on the presence of conductive spacers or profiles), the Reynolds number (*Re*) and the Schmidt number (*Sc*) [198–205].

Besides concentration polarization visualization techniques, some experimental methods for the measurement/estimation of δ_{DBL} (and thus *Sh*) have been developed and tuned up, e.g. based on chronopotentiometry [78,143,206,207] and EIS [208]. However, mass transfer characteristics are often evaluated by measurements of limiting current density, an important parameter controlling the operation of ED units.

1.3.2 Limiting current density in ED units

The increase of current density in a stack is always accompanied by an increase in diffusive transport of ions in solution, leading to a depletion of salt in the solution at the IEMs interface of the diluate channel. Such phenomenon is allowed only until the concentration at the wall in the depleted layer becomes zero. In this condition, the so-called "*limiting current density*" is achieved, which, from eq. (11), can be expressed as:

$$i_{lim} = \pm \frac{C_i^{bulk} z_i F D}{\delta_{DBL}\left(T_{IEM,i} - t_{SOL,i}\right)} = \pm \frac{Sh\, C_i^{bulk} z_i F D}{d^{eq}\left(T_{IEM,i} - t_{SOL,i}\right)} \tag{13}$$

According to the sign conventions cited above, i_{lim} will be positive if directed towards the positive y axis. Thus the limiting current density depends on hydrodynamic conditions, channel thickness and salt transport numbers. Interestingly, once the values of i_{lim} and $T_{IEM,i}$ are known, the DBL thickness and *Sh* could be easily calculated from eq. (13), but it should be noted that phenomena occurring in limiting current conditions, such as electroconvection, may significantly affect the value of *Sh* determined with this equation [143]. Therefore, if the hydrodynamics features

and mass transport coefficients have to be determined in the underlimiting range, where the above mentioned phenomena do not play a role, chronopotentiometric and EIS-based methods are more suitable.

From eqs. (11) and (13), it follows that, for a current density $i < i_{lim}$, the concentrations at the IEM-solution interface can be expressed as [173,181,183,194,209]

$$C_i^{IEM} = C_i^{bulk}\left(1 \mp \frac{i}{i_{lim}}\right) \tag{14}$$

Values of limiting current density can be obtained experimentally by current-voltage curves. As the voltage increases, the current increases more and more slowly due to the higher boundary layer effects that increase the resistance (see Section 1.3.3), until current increases only slightly with large voltage increments, indicating the achievement of limiting current condition. However, when the limiting current is approached, experimental observations deny the presence of the plateau theoretically postulated as a curve saturation (see Figure 7), so that the classical theory of concentration polarization is not anymore considered valid since the early 1970's [41,173,174]. Instead, only a narrow flat region or even an inflection point are found, along with a further increase of current (*overlimiting* current), due to the onset of further phenomena that were not observed at electrode-solution interfaces. Water splitting was considered responsible of the further charge transport, thus causing such deviation. However, many other mechanisms have been more recently theorized, discussed and experimentally proven [39].

Figure 7 shows a typical *S*-shaped current-voltage curve, exhibiting three regions [179,192,194,195,210–214]. Region I has been often defined as Ohmic, though this may be misleading due to the coexistence of both Ohmic and non-Ohmic phenomena. In the first small tract, the curve can be well approximated by a straight line; however, as the current increases, polarization (non-Ohmic) effects become more pronounced and cause a deviation from the linear trend. A much lower slope characterises region II, which can be regarded as a transition step following the achievement of the limiting current, conventionally identified by the intersection between the line tangent at the first tract of the current-voltage curve and the tangent of the plateau (or at the inflection point) in region II. Then, the slope increases again towards region III until reaching an asymptotic value leading to a stable linear increase of current *vs* voltage.

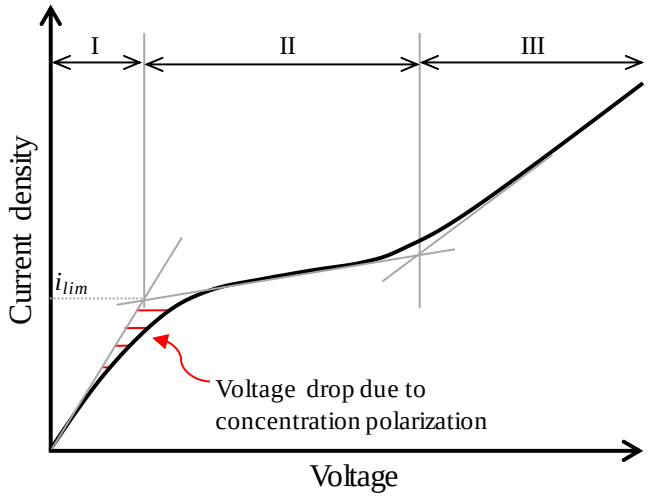

Figure 7. Sketch of a typical current-voltage curve for an IEM immersed in an electrolyte solution, showing a limiting current density and the presence of three distinct regions [39].

The behaviour of IEMs in current-voltage tests has been explained by the effects of the conductive heterogeneity of the membrane surface [142,211,212,215–220], which can be viewed as a mosaic of alternating conductive and insulating regions of size ranging from micrometers to tens of micrometers. Therefore, for any given average current density, the local current density on the conductive areas is larger. This results in a decrease in the average value of i_{lim} compared to a membrane having an electrically homogeneous surface, or to a metal plate electrode. Hence, region II of the current-voltage chart is due to a gradual achievement of the local i_{lim} in the non-conductive regions, at the cost of a much larger voltage drop. Another effect of the conductive heterogeneity is the alteration (elongation or shortening, depending on the distance between the surface heterogeneities) of the plateau length, i.e. of the onset of the overlimiting transport phenomena, namely electroconvection, associated to the generation of a non-uniform electric field with tangential components. Also geometrical heterogeneities of the membrane surface affect current-voltage curve features such as the i_{lim} value, the plateau length and the amount of overlimiting transport through electroconvection. Profiled membranes may enhance the mass transfer rate by the increase in the membrane active area, the promotion of fluid mixing and the increase of electroconvective mixing due to larger tangential components of driving force [221]. More recent studies [177,221–223] have proven that also other membrane properties, such as roughness, degree of hydrophobicity and surface charge density, affect the current-voltage curve characteristics.

Figure 8 (a) shows experimental current-voltage curves of a six-compartment stack with and without the central membrane. By subtracting these results, the current-voltage curve of the central membrane can be obtained [182]. The limiting current density is often identified as the point where the slope change occurs in the corresponding *Cowan plot* [173,182,195,213,224–230] reporting the apparent

resistance as a function of the reciprocal of current density (or, simply, of electrical current) as shown in

Figure 8 (b). Measurements of i_{lim} have been carried out in several works in order to assess the effect of spacers or profiled membranes on mass transfer. Values of i_{lim} are reported as functions of the fluid velocity [40,181,213,224,226,227,231] and fitted by power laws. Other works report *Sh* values determined from i_{lim} measurements according to eq. (13) [51,182,199,204,229,232–236] and correlations as power laws. Recently, La Cerva et al. measured the limiting current at different conditions, proposing a new definition for the limiting current density based on the current efficiency [237].

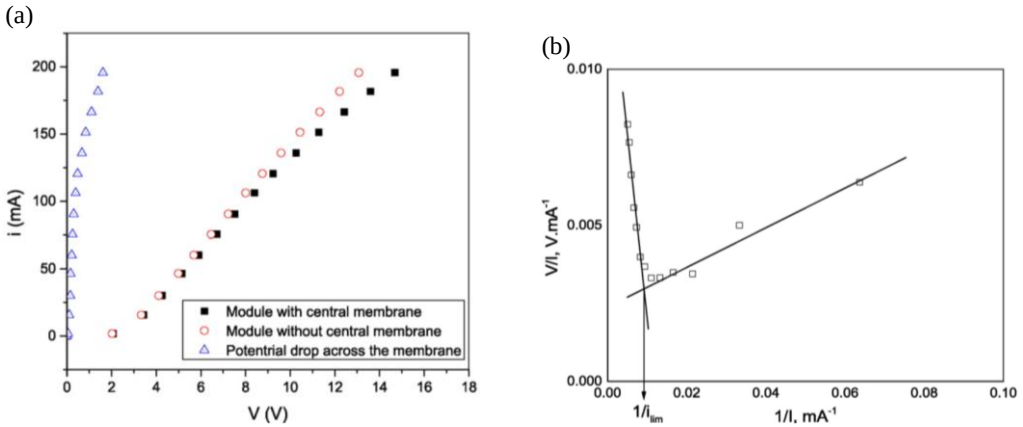

Figure 8. (a) Experimental current-voltage curve and (b) apparent resistance over the membrane as a function of the reciprocal of electrical current (*Cowan plot*) for the estimation of i_{lim} [182]**.**

Sh values have also been obtained by measurements of i_{lim} on electrodes of simple electrochemical cells without membranes [204,233–236]. However, these devices simulate only an ideal mass transfer of an IEM-based system, as membrane properties govern the mass transfer mechanisms. In fact, as claimed by Rubinstein and Maletzki [211], membranes with the same permselectivity may exhibit a markedly different behaviour even in the underlimiting region, significantly affecting polarisation phenomena.

Finally, when overlimiting conditions occur, mass transfer characteristics can be assessed by the approach proposed by Nikonenko *et al.* [196] and Larchet *et al.* [51] based on the experimental procedure described in [238].

1.3.3 Influence of polarization phenomena on the voltage drop

The limiting current density is only one of the aspects related to concentration polarization phenomena. However, several other effects caused by concentration polarisation have to be characterised, as they can significantly affect the total stack voltage drop. The total potential drop between two bathing solutions (left, *L*, and right, *R*) facing an interposed IEM can be analysed following the *segmentation modelling* approach by TMS (see Section 1.2.1) [68,206,239] in a multi-layer system taking into account the presence of the DBLs, as in Figure 9.

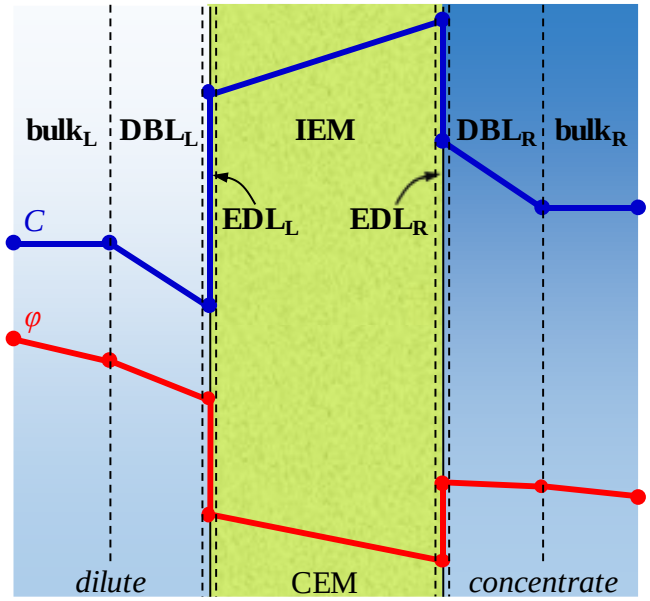

Figure 9. Segmentation of the system composed by a membrane and two bathing solutions, according to the TMS theory, showing concentration of counter-ions and electric potential changes in each layer. The example in the picture shows a CEM immersed between a dilute solution and a concentrate solution [39].

Some aspects related to the total voltage drop were treated in the first experimental and theoretical studies by Cooke [172] and Sonin and Probstein [240]. The topic was then treated more extensively by some authors in the early 1970s [173,174] and many further studies have been performed [178,203,206,209,239,241–247] since then. However, by pursuing the aim of a general discussion based on these works, the total voltage drop including all the possible contributions can be expressed as

$$V_{R-L} = V_{Ohm}^{bulk_L} + V_{Ohm}^{DBL_L} + \eta_{diff}^{DBL_L} + \eta_{IEM} + V_{Ohm}^{IEM} + \eta_{diff}^{DBL_R} + V_{Ohm}^{DBL_R} + V_{Ohm}^{bulk_R} \qquad (15)$$

where the different terms represent: Ohmic voltage drop within the left solution bulk, Ohmic voltage drop within the left DBL, (non-Ohmic) diffusion potential within the left DBL, (non-Ohmic) membrane potential, Ohmic voltage drop within the membrane, (non-Ohmic) diffusion potential within the right DBL, Ohmic voltage drop within the right DBL, Ohmic voltage drop within the right solution bulk.

In the case of a binary monovalent electrolyte, the membrane potential (eqs. (3)-(5)) acting as a back electromotive force [203,248–251] can be expressed as:

$$\eta_{IEM} = \alpha_{IEM} \frac{R_G T}{F} ln \left[\frac{\gamma_C^{int,IEM} \, C_C^{int,IEM}}{\gamma_D^{int,IEM} \, C_D^{int,IEM}} \right] \qquad (16)$$

where C_{SOL}^{int} and γ_{SOL}^{int} represent the electrolyte concentration and the electrolyte activity coefficient at the IEM-solution interface (solution side) and the subscripts C and D refer to the concentrate and the dilute channel, respectively. It is useful to

resort to polarization coefficients [6,197], whose values range from 0 (maximum polarization) to 1 (no polarization), defined as:

$$\theta_D^{IEM} = C_D^{int,IEM}/C_D^{bulk} \quad (17)$$

$$\theta_C^{IEM} = C_C^{bulk}/C_C^{int,IEM} \quad (18)$$

where C_{SOL}^{bulk} is the electrolyte concentration at the solution (dilute or concentrate) bulk. In a cell pair, there are four polarization coefficients, one for each IEM-solution interface. Values of θ_{SOL}^{IEM} can be derived from eq. (14), though a more rigorous approach relates them to eq. (11).

Interestingly, focusing on hydrodynamics-related features, the DBLs contribute to the total potential drop by means of both Ohmic and non-Ohmic phenomena, which can easily be calculated assuming a linear concentration profile. V_{Ohm}^{DBL} can be computed by Ohm's law integrating the resistivity over δ_{DBL} and multiplying by the current density (1-dimensional approach, where i = cost). η_{diff}^{DBL}, also called concentration potential or junction potential, is strictly non-Ohmic and originates from the difference in the ionic diffusion coefficients and the need to maintain the local electroneutrality [66]. Note that V_{Ohm}^{DBL} has a dissipative nature, i.e. it is caused by the irreversible process involving Joule's effect [66]; conversely, non-Ohmic phenomena are (at least ideally) reversible and, ultimately, convert the electrical energy into the chemical energy of a salinity gradient.

In very recent years, researchers have shown a wide interest on transport phenomena and DBL effects in IEMs-based systems. The resistance associated with the boundary layer has been measured by chronopotentiometry [3,4,143,207,252,253] and EIS [144,208,209,254–256]. Finally, Abu-Rjal *et al.* [257] have investigated the influence of the DBL on the membrane permselectivity, finding that concentration polarization may significantly affect counter-ions transport through the membrane, due to variation of the interface concentration and concentration profile across the membrane as the electric current changes.

1.4 Special applications of electrodialysis

Several ED-related processes, have been proposed and are still arousing interest among researchers around the world. These special technologies, expanding the application field of ED and promoting the development of system components and the optimization of devices, are discussed in this section.

1.4.1 Electrodialysis with bipolar membranes

Electrodialysis with BiPolar Membranes (EBPM) is a process based on the use of special IEMs, namely bipolar membranes (BPM, see Section 1.2.2) constituted by a double layer of adhering anion and cation exchange membranes, mostly used for the production of acids and bases from salt solutions. An EBPM stack is composed by alternating an AEM, a BPM and a CEM. These three membranes together with three channels represent the repeating unit of the EBPM stack (Figure 10). A salt solution flows in between the AEM and the CEM, while an acid and a basic solution flow in

the other two channels respectively [10]. When an electrical potential is applied to the electrodes, water trapped inside bipolar membranes is induced to split catalytically into H^+ and OH^- ions, which will pass through the cationic and anionic layer of the BPM, reaching the acidic and alkaline compartment, respectively. At the same time, anions and cations from the salt solution migrate through IEMs, electrically balancing the passage of H^+ and OH^-, thus restoring electroneutrality and generating the acid and base solutions. Although the three cells compartment is the most diffused configuration, sometimes a two compartment scheme is used, in which only one type of product (either acid or base solution) is obtained, while the salt solution absorbs also the excess H^+ or OH^- generated. This can happen especially when it is not possible or convenient to obtain a high purity for both acid and base [258].

EBPM is an industrial competitor of electrolysis for the production of acid and base compounds. Several works in the literature show how EBPM can reach very low energy consumptions, especially assuming ideally conductive and permselective membranes. Nevertheless, in practical applications energy consumption is considerably increased by the actual stack Ohmic resistance, diffusional losses and non-ideal permselectivity of homopolar and bipolar membranes [258].

A particularly interesting application of EBPM is the treatment and valorisation of waste brines from desalination plants [259–266]. The process is used to convert very concentrated NaCl (plus a number of additional minor elements) solutions into HCl and NaOH products. Through this novel application of EBPM, brine can be diluted to attenuate disposal issues and, at the same time, valuable products are obtained. Despite the clear environmental advantage, this application has to face a number of technical and economic barriers mainly related to membrane cost and performance (i.e. limited permselectivity and electroosmosis) and to the purity of the product streams due to the presence of minor elements in the feed brine. More details on potentials and limitations of this application can be found in [267].

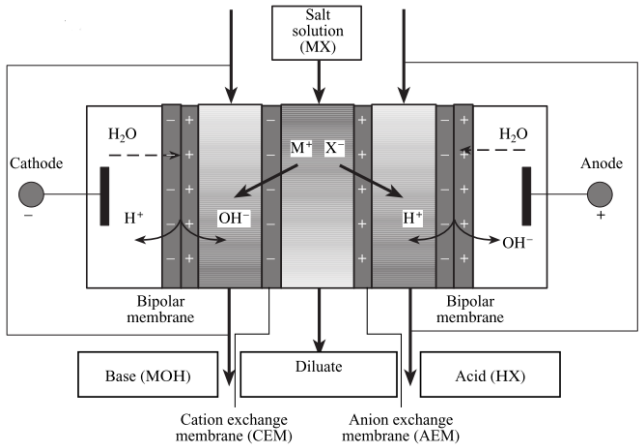

Figure 10. Electrodialysis with bipolar membranes in a conventional three cell compartment configuration [258]**.**

1.4.2 Continuous electrodeionisation

Continuous ElectroDeIonisation (CEDI) can be considered a hybrid process merging ion exchange deionisation and ED [268]. A typical CEDI unit has a similar configuration to ED, with alternating IEMs, concentrate and diluate compartments where feed solutions flow. Differently from ED, in CEDI at least one channel is filled with ion exchange resins.

CEDI has two possible layouts. In the first the diluate channel is filled with mixed anion and cation exchange resins (Figure 11 (a)), while in the second anionic and cationic resins are placed in two different channels separated by a bipolar membrane (Figure 11 (b)) [10]. The presence of ion exchange resin particles inside the diluate compartment allows for a fast migration of ions through the channel from one membrane to the other, avoiding the limitation of low conductivity of dilute solutions [269]. This makes CEDI also useful for the production of extremely dilute water solutions in small and medium scale applications. For example, CEDI is often adopted for the production of ultra-pure water in food, pharmaceutical and electronics industry [10,268,269]. Another proposed application of CEDI is the removal of heavy metals in wastewater treatment trains [269].

The main advantage of the mixed resins bed is that anions and cations are simultaneously removed, thus avoiding the need for a double passage of the solution (as in case b) and minimising its residence time inside the CEDI unit. However, two separated beds are much more efficient when the solution contains weakly dissociated electrolytes [10]; in this case, the feed solution undergoes the cation exchange step first, where cations are exchanged with the protons generated and released by the bipolar membrane. The resulting acidic solution then flows through the anion exchange channel where anions are exchanged with hydroxide ions from the bipolar membrane, restoring solution neutrality. Nowadays, both layouts (a) and (b) are widely used in the industry.

Interestingly, also novel configurations of CEDI have recently been proposed, based on the use of electrostatic shielding zones instead of membranes [270,271], though these have not yet reached an industrial applicability scale.

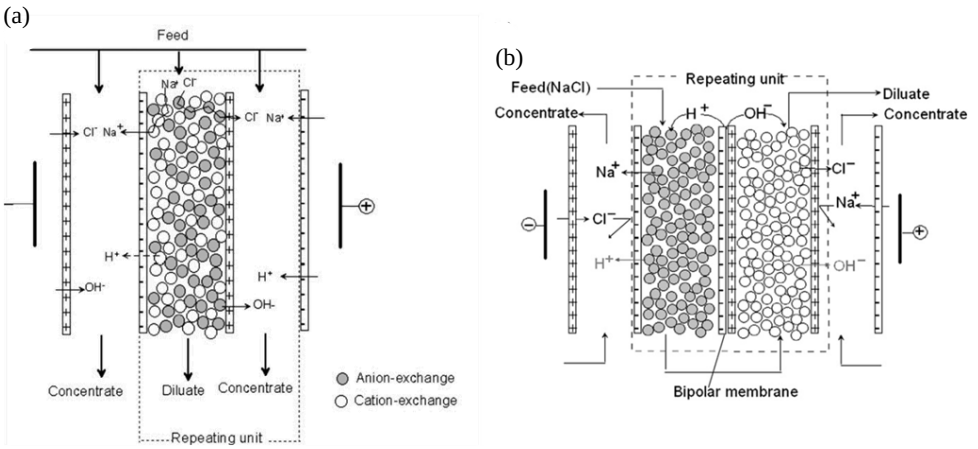

Figure 11. Schematics of the two different layouts of continuous electrodeionisation stacks (from [10]). (a) Conventional stack with diluate channel filled with mixed cation and anion exchange resins, (b) stack with anion and cation exchange resins in two different channels with a bipolar membrane in between.

1.4.3 Capacitive deionisation

Capacitive DeIonistation (CDI) is a desalination and ion transfer process based on the use of capacitive materials to remove/release ions from/into solutions in a cyclic way [10]. In CDI, a salt solution flows through a channel between the two capacitive electrodes, which are usually covered with an IEM (or, more generally, an ion selective layer) in order to enhance the current efficiency, thus increasing process performance [272]. Applying an electrical potential difference between the electrodes, ions move according to the generated electric field and are eventually absorbed on the capacitive electrodes surface (often consisting in a modified carbon-based matrix), removing salts from the feed water and producing desalinated water. When electrodes reach the saturation condition, polarity is reversed and ions are discharged from the electrodes into a purge stream flowing through the channel, thus regenerating the electrodes and producing a concentrated brine to be disposed. CDI is not yet a fully mature technology, but some commercial manufacturers already exist and some examples of real applications have been reported [273]. Nowadays, CDI suffers from market penetration issues mainly due to upscaling difficulties related to the large quantity and cost of the electrode material needed for large capacity plants [274].

1.4.4 Electrodialysis metathesis and selectrodialysis

Since the early ‘80s the possibility of using an ED stack to carry out a metathesis reaction has been assessed [30–33]. The metathesis reaction allows two salts to be produced by interchanging the anions and cations of two different initial salts:

$$MX + M'X' \rightarrow MX' + M'X \quad (19)$$

Differently from conventional ED, the repetitive unit of electrodialysis metathesis (EDM) is composed by 2 dilute compartments, 2 concentrate compartments, 2 CEMs and 2 AEMs (Figure 12) [33]. Feed channels are alternatively fed with two streams, one containing the first reactant (MX) and the other containing the second ($M'X'$), while a *"sink"* solution flows through the other two channels. The presence of the applied electrical field and of the selective IEMs leads to the passage of ions from feed to compartments containing sink solution and, as a result of this ion shift, product streams are generated in the sink channels. As an example, assuming that the feed solutions contain magnesium chloride and sodium sulphate, the product outlets will contain magnesium sulphate and sodium chloride, which may reach an over-saturation condition and precipitate out of the channel to form solid product salt [33]. In the past years, the possibility of using EDM for the production of different salts such as potassium carbonate, magnesium sulphate and potassium sulphate from more soluble and less valuable salts has been studied [30,275]. Recently, EDM was also used for the production of ionic liquids precursors [276]. Another important application of the EDM process is the treatment of RO concentrated brines in zero liquid discharge desalination [31]. In this case, the repeating cell is characterised by a conventional AEM, a conventional CEM, a monovalent selective AEM and a monovalent selective CEM. By feeding the unit with desalination brine and artificial NaCl solution two concentrate product streams are obtained: the first containing sodium with anions and the other containing chloride with cations [31,33]. In both cases, concentration in the outlet brines can be significantly increased thanks to the high solubility of the salts generated by the metathesis process, thus overtaking the main limitation of RO being the risk of scaling (mainly due to calcium and magnesium carbonates and sulphates) when a recovery ratio of 40-50% is exceeded.

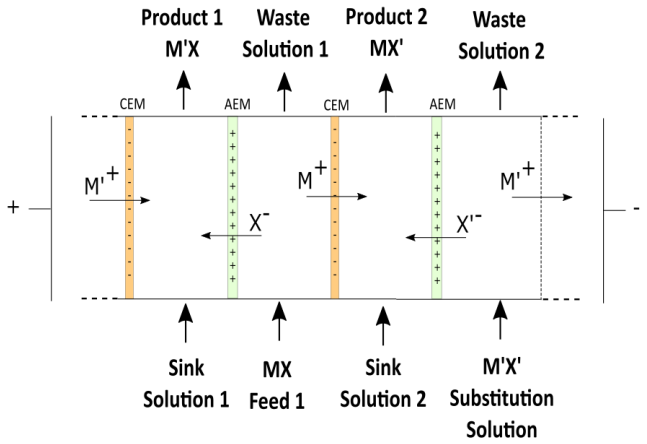

Figure 12. Schematic representation of the electrodialysis metathesis process.

Similarly to EDM in zero liquid discharge applications, selectrodialysis (SED) is a particular technology that makes use of monovalent selective IEMs. A typical SED repeating unit is constituted by 3 compartments with a central monovalent selective

IEM (MVA or MVC) between a conventional CEM and an AEM [277]. This configuration allows monovalent and divalent ions to be selectively separated from feed solutions. The scheme reported in Figure 13 refers to the case of separating monovalent and bivalent anions from a feed solution by adopting a monovalent selective anion membrane (MVA) in the centre of the SED repeating unit.

SED is a relatively novel process for which ion fractionation capabilities have generally been claimed [27], but have been practically demonstrated only in a few applications. Examples are the recovery of phosphate from waste streams [28,278] or the separation of chloride and sulphate compounds from a NaCl and Na_2SO_4 mixture to simulate the application of SED in brine treatment processes [26].

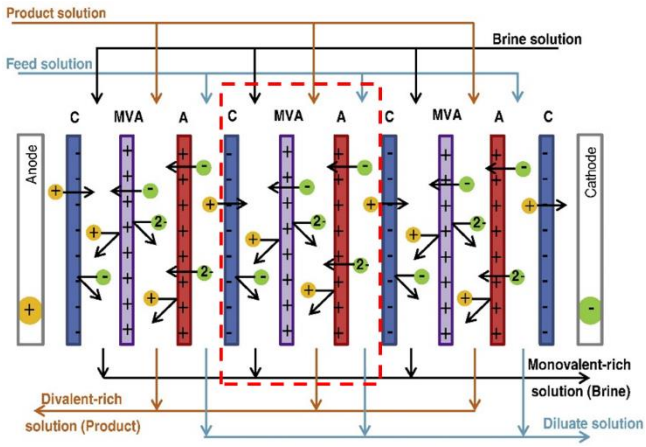

Figure 13. Scheme of a selectrodialysis stack for the separation of salts containing mono- and bi-valent anions (e.g. Cl^- and SO_4^{2-}) showing the functioning principle (adapted from [26]).

1.4.5 Shock electrodialysis

Limiting and overlimiting currents are possible operating conditions in ED, though they are generally avoided in standard operation [50]. However, the shock electrodialysis concept, recently proposed for water desalination purposes, operates under overlimiting current conditions [279–281]. A shock ED repeating unit is composed by a weakly charged porous medium placed in a channel between two equally-charged ion exchange membranes, such as two CEMs or AEMs (Figure 14). As in conventional ED, electrodes are placed at both ends of a pile comprising a number of repeating units, next to the IEMs. While salted water flows through the channel, a potential is applied at the electrodes. This causes a flux of anions and cations in the two opposite directions. If CEMs are chosen as selective layers (as shown in the example of Figure 14), sodium ions are removed from the channel, creating a depletion zone at one side of the compartment and a salt enriched zone at the opposite side. Conversely, anions move from the depletion to the enriched zone, being blocked in the upper part of the compartment by the CEM. As in ED, when the ion concentration at the membrane interface reaches zero, the limiting current is reached. However, applying an overlimiting current in the presence of the weakly

charged porous medium results in a transport of ions much faster than diffusion. The overlimiting current makes the edge of the depletion zone propagate through the pores as a shock wave creating a sharp boundary between the depleted and undepleted zones. Solutions flowing through the two zones are finally separated by a splitter placed in the last part of the channel so that a desalinated water and a brine streams are obtained [281]. Phenomena occurring in shock-ED at overlimiting current condition are still under debate [282–284]. So far, two main phenomena are believed to occur: surface migration and surface convection [282]. The first is typical of sub-micropores; the second is due to electroosmotic flow and is dominant in larger pores.

Shock ED is a very recent technology, still in an early development stage. Although there are no industrial applications, Schlumpberger *et al.* in 2015 showed a small scalable prototype able to remove over 99% of salt from a feed water with a salt concentration up to 100 mM [279]. Also, Deng *et al.* developed a small unit demonstrating the possibility to use shock ED in filtration, separation and disinfection [281].

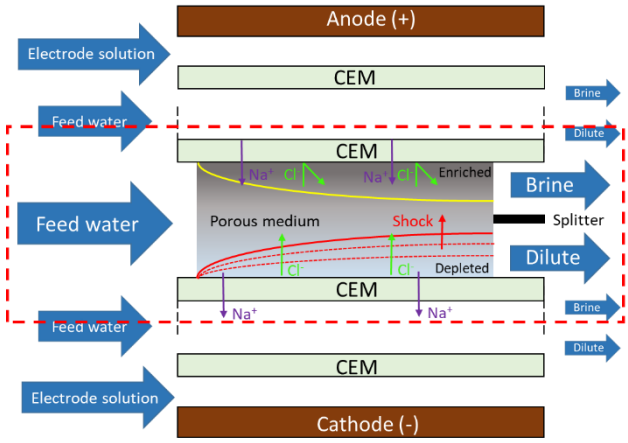

Figure 14. Schematic representation of the shock electrodialysis process with indication of the system repeating unit.

1.4.6 Reverse electrodialysis

Reverse ElectroDialysis (RED) can be considered as the opposite process of electrodialysis. The latter makes use of electric energy to remove salts from a solution: energy is used to generate a salinity difference between a dilute stream (i.e. the produced fresh water) and a concentrate stream (i.e. the generated brine). Conversely, RED is able to convert the salinity difference, i.e. the chemical potential difference existing between two solutions at different concentrations, into electric energy. RED is one of the most important among the so called Salinity Gradient Power (SGP) technologies, recently arousing the interest of scientists and

technologists in the field of water and energy generation from non-conventional sources.

As depicted in Figure 15, the repeating unit of a RED stack (called “cell pair”) consists of a CEM, a dilute compartment, an AEM, and a concentrate compartment. As in ED, anion and cation exchange membranes are also alternatively arranged, and the dilute and concentrate feed solutions flow within channels arranged in an alternate way. Under open circuit conditions (i.e. when the end electrodes are not connected to an external circuit) and assuming ideal membranes, nothing passes through the membranes and the chemical potential difference existing between two adjacent channels is counterbalanced by the electric potential difference generated in each membrane by the Donnan equilibrium (see Section 1.2.1). This potential difference is typically addressed as the *open circuit voltage* and represents the electromotive force of the RED generator. When the circuit is closed, ions start to move from the concentrate channels to the dilute ones oriented by the presence of selective IEMs. Thus, positive ions will move towards the cathode passing through CEMs and negative ions will move in the opposite direction, thus generating a net ionic current through the cell pairs. In analogy with ED, the net flux of charges is eventually converted into a flux of electrons in the final compartments of the stack, where electrodes are placed and redox reactions occur. The current of electrons generated at the electrodes can be used to supply an external load [285–288]. As in standard electric energy generators, also in a RED stack the increase in electric current (related to a reduction in the external load resistance) leads to internal voltage drops, which reduce the available voltage at the stack electrodes, leading to the extreme condition in which a short-cut circuit between electrodes generates the maximum current depleting completely the electromotive force generated in the pile.

It can be demonstrated that the maximum power density can be obtained when the resistance of the external load matches the internal resistance of the stack. Under this condition, only 50% of the available Gibbs free energy of mixing can be theoretically harvested.

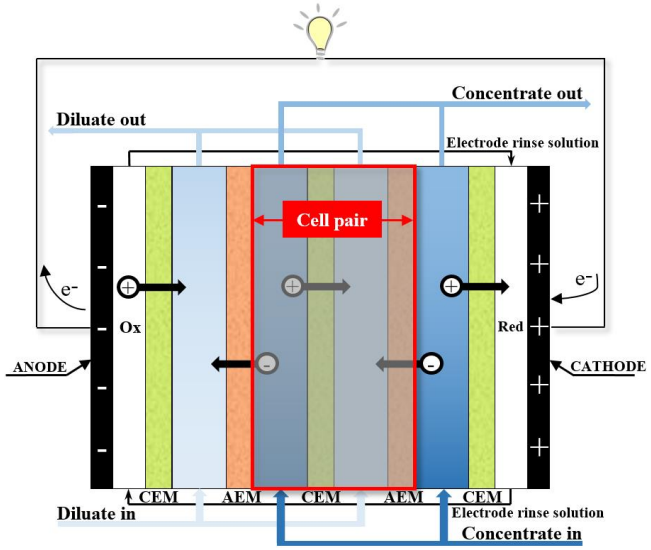

Figure 15. Scheme of Reverse Electrodialysis process.

It is worth mentioning that, under practical conditions, only a portion of this energy can actually be converted into electric energy. Thus, since the amount of electricity producible is not high, all detrimental effects as Ohmic and non-Ohmic resistances and pumping losses due to pressure drops represent matters of crucial importance. In particular, a maximum in the net power density (i.e. gross power density minus pumping power density) is typically found for streams velocity around or below 1 cm/s [289]. At these flow rates, the power output reduction due to pumping power normally amounts to about 10-20% for spacer-filled channels RED units [290] and to about 3-25% in RED systems where profiled membranes are used [4,252,253]]. The channel thickness is usually in the order of a few hundred microns to keep the channels' electrical resistance low. These aspects mark a difference from ED where thicker channels and larger stream velocities are adopted.

The performance of RED units has rapidly increased during the last years, moving from generated power densities of 0.05 W/m² reported in the early '50s by Pattle [291], who first conceptualised the RED process, to values of 1-2 W/m² recently obtained by Veerman *et al.* [292] and Veermaas *et al.* [3] mixing solutions simulating river and sea water (see Table 1). The highest values of power density, however, were recently achieved by mixing solutions simulating fresh or brackish water and concentrated brines at temperatures of 40 or 60°C, reaching values up to ~6.70 W/m² [5,293,294]. A more detailed chronology of the RED technology development is reported in Table 1.

Table 1: Chronological trend of increasing power densities achieved in laboratory scale RED systems. Experimental conditions are also reported (adapted from [294]).

Year	Authors	Power density (W/m^2)	Spacer Thickness (μm)	Solution concentrations (M)	Temperature (°C)
1955	Pattle [291]	0.05	1000	Not specified	39
1976	Weinstein and Leitz [295]	0.17	1000	0.02–0.57	Ambient
1983	Audinos [296]	0.40	1000	4.3	Ambient
1986	Jagur-Grodzinski and Kramer [297]	0.41	250	tap water and seawater	Ambient
2007	Turek and Bandura [298]	0.46	190	0.01–0.5	Ambient
2008	Turek *et al.* [299]	0.87	190	0.01–1.9	Ambient
2008	Veerman *et al.* [292]	0.93	200	0.017–0.5	Ambient
2011	Vermaas *et al.* [3]	2.20	60	0.017–0.5	Ambient
2014	Daniilidis *et al.* [5]	5.30	100	0.01–5	40
2015	Tedesco *et al.* [294]	6.04	270	0.1–5	40
2014	Daniilidis *et al.* [5]	6.70	100	0.01–5	60

During the last years, research achievements have pushed up the RED *Technological Readiness Level* (TRL), allowing the shift from lab-scale units to the first prototypes and pilot plants. Two different pilot plants have been built so far as outcomes of two different projects: Blue Energy and REAPower. Both plants are located in Europe.

The Blue Energy pilot plant is located in Breezanddijk at the Afsluitdijk closure dam (the Netherlands) where seawater and river water are available with an intake

capacity of 200 m^3/h. Assuming a technical potential of 1 MJ per m^3 of sea and river water [300], this flow rate has a potential for energy generation of 50 kW [301].

The REAPower pilot plant was installed in Marsala (Sicily, Italy) in 2014 within a saltworks area where solutions at different salinities were available such as: a concentrated brine from evaporating basins, seawater and brackish water from a shoreline well [293,302]. The concentration of the brine changes during the year ranging between 3 and 5 M (in terms of $NaCl_{equivalent}$ concentration), while the concentration of brackish water is quite constant and equal to 0.03 M (in terms of $NaCl_{equivalent}$ concentration). The pilot plant, consisting of 3 different RED stacks, had a nominal capacity of about 1 kW, reaching under real operation a power output of almost 700 W with artificial solutions and about 330 W with real brackish water and brine [8]. Interestingly, the plant was tested for several months without encountering any performance reduction [302].

Very recently, the RED technology has been also proposed in a closed loop arrangement as a promising way to convert low-temperature waste heat (below 100 °C) into electric energy [303–306]. Two artificial solutions at different salinities are used in a RED unit to produce electricity, exiting as partially mixed streams. These are fed to a regeneration unit powered with low-grade heat where the initial salinity gradient is restored, thereby closing the cycle. Perspective analyses have recently shown that conversion efficiencies up to 10-15% can potentially be achieved in these systems [307]. Closed-loop RED/ED systems have also been proposed for SGP-based energy storage applications, in which energy is stored in the form of salinity gradients. These are converted into electricity in peak demand hours, while, when surplus energy is available, this is used to regenerate the depleted salinity gradient [308,309].

1.4.7 RED-ED coupling for low-energy desalination

A very recent development in the field of ED for desalination is represented by the coupling with salinity gradient power or osmotic dilution devices for low-energy desalination [310].

Among the different alternatives that have been theorised, the coupling of RED with ED (or, more in general, with a desalination unit such as RO or even CDI [311]) may result in a technological breakthrough, especially for seawater desalination [9,312–316]. Figure 16 shows the two main coupling possibilities.

In the first configuration (coupling of unit I and II in the scheme) the RED unit is used as pre-treatment step. When a low-salinity solution (that, at least according to current regulations and due to the opposing public opinion, is not per se suitable for drinking water production [317]) is available (e.g. impaired water from a waste water treatment plant) this can be used as the dilute feed of a RED unit, while seawater can be used as the concentrate. In this way, energy is generated from the salinity gradient and seawater exiting the RED device is diluted thanks to the passage of salt into the impaired water, without directly mixing with it. Pre-diluted seawater can thus be fed to a desalination unit in which the energy required to reach the target

concentration will be significantly reduced. Additionally, the RED energy generation can be used further to reduce the overall process consumption.

In the second configuration (coupling of unit II and III), the RED unit can be used as a post-treatment in order to mix the brine with impaired water, mitigating disposal issues and recovering energy from the two waste streams. The two configurations can also be used together resulting in the complete scheme of Figure 16.

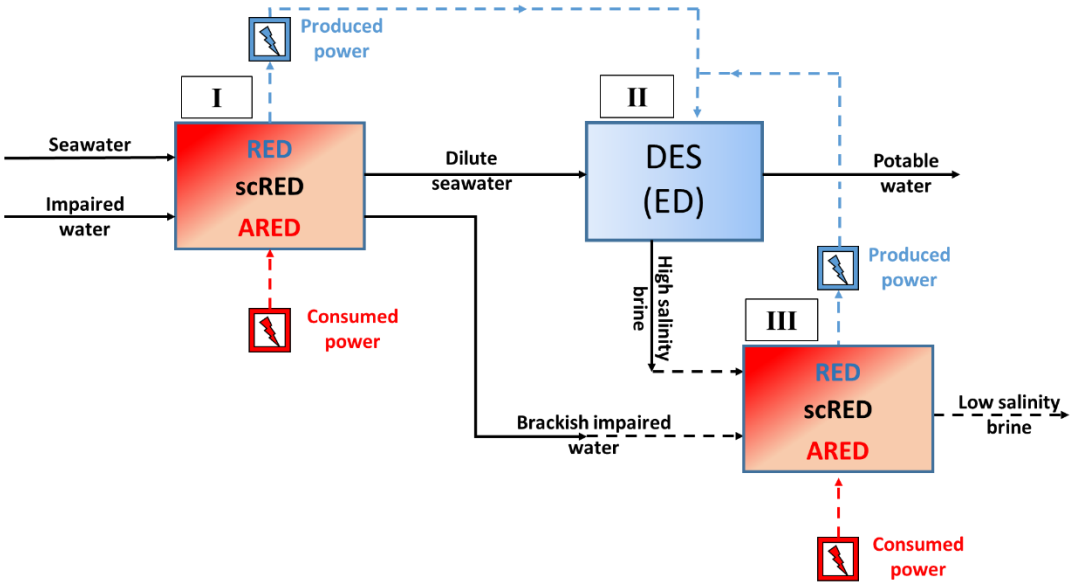

Figure 16. Possibilities of RED/ED integration. Unit I represents RED (or short-circuited RED or assisted RED) used as dilution pre-treatment before feeding the seawater inlet to ED (Unit II). Unit III represents RED used as post-treatment for the recovery of energy from waste brine and relevant dilution with impaired water stream. Coupling Unit I, II and III represents the most complete integration possibility.

Besides the classical SGP operation mode, the RED unit can be operated in two other different modes, thus serving as an enhanced osmotic dilution device [310]:

- Short-circuited Reverse Electrodialysis (scRED)
- Assisted Reverse Electrodialysis (ARED)

In scRED mode the RED unit external load is short-circuited, thus renouncing to energy production in order to maximise the salt transfer rate from the concentrate to the dilute compartment, thus enhancing the dilution effect.

In ARED mode the ionic current inside the scRED unit is further increased by applying an additional external electrical potential to the RED unit, consuming energy in order to "assist" the dilution process, exceeding the maximum achievable current in scRED.

In both cases, the arising benefits are more suitable for the first coupling configuration, where dilution plays a fundamental role in reducing the overall

energy consumption, rather than in the second, where dilution is considered beneficial only for environmental reasons.

Due to the complex nature of such processes, it is not possible to determine *a priori* which of the configurations or RED operation mode is the most convenient to achieve the overall minimum energy consumption. In addition to that, pushing the dilution process to high levels will significantly increase the capital costs, mainly depending on the amount of membrane area required. For this reason, optimisation studies are crucial for the development of such hybrid schemes.

In the current literature, the RED-RO coupling has been investigated by several authors, although still at a conceptual level [312–315,318]. In particular, Li *et al.* [312] explored the RED-RO process through a simple mathematical model, showing that the process can potentially achieve a ~50% lower energy consumption compared to state-of-the-art seawater RO. Vanoppen *et al.* [310] performed a comparative analysis of all RED operational modes coupled to RO, exploring the operational ranges and identifying the benefits in energy consumption reduction. Specific energy consumption below 1 kWh/m^3 were theoretically demonstrated to be feasible, although an important increase of overall membrane area required (including RED membranes) was found in these scenarios.

The RED-ED process has been much less studied, with only few recent publications as the one by Wang *et al.* [316] who focused on the very specific case of desalination of high salinity waste brine containing phenols. They demonstrated an overall reduction of energy consumption of about 30% compared to the stand-alone ED case, though such figures cannot be compared with RO, due to the much higher energy consumption of the base case (above 20 kWh/m^3). The RED-ED process was further analysed as possible scheme for SW desalination in section 5.2.

It should be noted that, as an alternative to the reverse electrodialysis dilution process, other osmotically-driven processes such as Pressure Retarded Osmosis [315,319] have been proposed in the literature. Similarly to the RED case, forward osmosis [320–323] and pressure-assisted osmosis [320] have also been proposed for further enhancing the dilution process in order to reduce the overall desalination energy consumption.

2 Electrodialysis steady-state process modelling

In this chapter, a new hierarchical model for the electrodialysis (ED) process is presented. The model has been implemented into *gPROMs Modelbuilder (PSE, UK),* allowing the development of a distributed-parameters simulation tool that combines the effectiveness of a semi-empirical modelling approach to the flexibility of a layered arrangement of modelling scales. Thanks to its structure, the tool makes possible the simulation of many different and complex layouts, requiring only membrane properties as input parameters (e.g. membrane resistance or salt and water permeability). The model has been validated against original experimental data obtained from a lab scale ED test rig. Simulation results concerning a 4-stage treatment of seawater and dynamic batch operations of brackish water desalination are presented, showing how the model can be effectively used for predictive purposes and for providing useful insights on design and optimisation.

2.1 State of the art of modelling of ED process

In order accurately to describe the ED process and develop effective process simulation tools it is necessary to implement mathematical models able to take into account a number of complex phenomena. These include solution-membrane equilibria, concentration polarisation and fluid flow behaviour along channels, mass transport phenomena and mass balances in the compartments, electrical phenomena, etc. Several different modelling approaches have been presented so far in the literature, each one addressing in a different way and to a different extent all these aspects. In most cases, the aim was to develop effective design and optimisation tools for ED processes. It is worth noting that the classification presented here is not intended as a strict rule. In fact, each model has unique properties that may place it in between two categories. Nevertheless, this classification can be taken as a general guideline for a systematic understanding of the possible modelling approaches, in order to be aware of the advantages and disadvantages of each one.

The first category includes all the **simplified models**, which are usually developed with the aim of performing preliminary design [224] or to study a very specific system relying on experimentally fitted parameters [324]. In this case, several assumptions are generally used and lumped parameters are considered. Typically, overall quantities, such as the required membrane area to perform a certain desalination or the total power consumption, can be estimated.

The second category is represented by the **advanced models**, which, differently from the previous ones, take into account several phenomena causing deviations from the ideal behaviour. Advanced models can be sub-classified in theoretical and semi-empirical.

Theoretical models for (reverse) electrodialysis are based on the solution of rigorous equations (i.e. Nernst-Planck [185,325–330], or even the more complex Stefan-Maxwell equations [331–333]) that mathematically describe local transport

phenomena. However, these models require a number of thermodynamic and electrochemical parameters that cannot always be easily determined. In addition, the large amount of computational power required to solve this kind of models makes them suitable only for simplified geometries [39].

Semi-empirical models for (reverse) electrodialysis are based on the use of mass balances and detailed transport equations accounting for salt and water fluxes through the membranes and on the calculation of the voltage drop by the segmentation approach (see section 1.3.3). They require (i) empirical information such as membrane properties, being available from manufacturers or easily measured by experiments (transport numbers, ohmic resistance, salt permeability, osmotic permeability, etc.), and (ii) a lower computational power. These features make this modelling approach suitable for faster and more reliable predictions than the theoretical models, especially in the simulation of realistic geometries of channels and stacks, which are more complicated than the simplified configurations typically assumed in theoretical models [39]. Semi-empirical models can be based on lumped parameters [178,203,334–339]. However, in this case they have limited prediction capabilities, providing accurate results only under some conditions [338]. On the contrary, distributed parameters models [6,145,237,242,340–343] are more accurate, but at the cost of a larger implementation effort. In summary, with respect to the theoretical models, 1-D semi-empirical models are preferable as process simulators thanks to their features of versatility, robustness and effectiveness.

Some advanced semi-empirical models use a "practical" current density calculated as a fraction of an experimentally determined limiting current density [336–338]. Many other models of this category, instead, adopt a multi-scale approach treating the lower scale mass transfer phenomena (Sherwood number and, thus, concentration polarization) for calculating the voltage drop with different approaches. In particular, the majority makes use of either empirical information [178,203,242,335,339,343,344] (e.g. limiting current density) or 3-D computational fluid dynamics (CFD) simulations [6,145,237,342]. Numerical simulations can also predict pressure drops and ohmic resistance [6].

Tedesco et al. [137,145]presented one of the first examples of 1-D semi-empirical process models (although it was developed for RED) that makes use of CFD simulation results to predict concentration polarisation and pressure drops. The approach adopted by Tedesco et al. is similar to what is reported in section 2.2. Salt transport across the IEMs is described considering both conductive as well as diffusive flux. However, conductive flux of co-ions (i.e. the term $1 - t_{AEM}^{counter}$ from eq. (20)) was not considered. Apart from this, the model contains a comprehensive collection of the most important phenomena [145]. Water transport across the membranes considers both electroosmosis and osmosis, including the presence of osmotic coefficients (as per eq. (23)). Electrical variables include both non-ohmic and ohmic voltage drops, accounting also for concentration polarisation phenomena. Finally, an electrical model for the estimation of parasitic currents through manifolds (particularly relevant for large RED stacks) was also incorporated.

The model recently proposed by Chehayeb and co-workers [334,340,341] represents a practical example of how the different approaches (i.e. theoretical and semi-

empirical) can be actually mixed together. In fact, the diffusion boundary layer thickness was calculated by experimental data on the Sherwood number, voltage drop is calculated according to eq. (31) (although membranes' ohmic resistance is not taken into account), while mass transport in the boundary layer was simulated by the Maxwell-Stefan approach in order to predict concentration and electrical potential profiles and ionic and water fluxes. With Maxwell-Stefan approach transport equations can be seen as force balances where the driving force is equated to the friction that is applied by one species to the others. These equations are thus defined for both the DBL as well as inside the membranes, where the equations are formally the same although a different value of the characterisation parameters is required [334]. As pointed out by the authors themselves [334], it is worth noting that this model was originally developed to perform entropy generation calculations, that are not affected by the difficult determination of fitting parameters typical of Maxwell-Stefan approach.

In a different work, Chehayeb et al. proposed the use of the aforementioned model to perform energy and cost optimisation for brackish water desalination, while using a simplified model for brine concentration (due to the lack of fitting parameters for this system) [340]. Interestingly, a comprehensive analysis of the main process parameters such as spacers' dimensions and channel velocity was provided, highlighting how the pumping energy becomes negligible compared to ED power consumption in the brine concentration scenario. More recently [341], the same models where used to analyse the effect of 2-stage ED for 3 different applications: brackish water desalination (from 3 to 0.35 g/kg), partial seawater desalination (from 35 to 1 g/kg) and brine concentration (from 70 to 200 g/kg). Moreover, counterflow arrangement was simulated. As a result, two-stage operations were shown to be effective in energy saving in all cases, while counterflow arrangement did not provide a significant reduction in the energy consumption.

Wright et al. [343] proposed another simple semi-empirical ED model, applicable to brackish water desalination and used it for a cost analysis for domestic applications of groundwater treatment [344]. Similarly to the model presented in section 2.2, channels are discretised in the direction of the flow (i.e. the model is 1-D). Salt transport across the membranes takes into account both conduction and diffusion, while water transport in the same direction was generally neglected in the simulations. Electrical variables are described according to eq. (45), including the contribution of the electrodes' voltage drop. Moreover, LCD and concentration polarisation are taken into account by means of empirical correlations, while pressure drops are estimated by means of the Darcy equation (eq. (47)), where the friction factor can be estimated by different correlations [343]. A series of assumptions characterises the model, such as counter-ion transport number in the IEMs considered equal to 1 (i.e. membranes are assumed perfectly selective). This assumption has implications in transport equations (i.e. the equivalent of eq. (20) does not contain any transport number), interfacial phenomena (i.e. the term $t_{IEM}^{counter}$ in eq. (43) is absent) and membrane potential (i.e. the permselectivity has a value of 1). In addition, membrane resistance was considered constant, neglecting the increase that can be experienced at low solution concentration (see section 2.2.1).

The model of Wright and co-workers was used to simulate batch systems via a quasi-steady state approach [343]. A sensitivity analysis accompanied by a comparison with experimental data on ED units operated in batch mode showed that the aforementioned simplifying assumptions are certainly acceptable when using the model under "conventional" operations and low feed concentrations (up to 3.5 g/l). However, in the case of high salinity feed solutions (e.g. seawater or concentrated brine) such assumptions are not valid and would lead to erroneous predictions.

More recently, an interesting application for this same model was presented by Shah and co-workers [345]. In this work, the authors proposed the use of simulations as a mean of improving brackish water batch ED performances. In particular, a feedforward controller was designed and experimentally applied with the aim of providing a variable voltage over time to the batch unit. The result was an increase of 37% in the production rate compared to the constant voltage case (i.e. the common practice in industrial applications).

The number of recently published works shows the current significant interest of the scientific community in the development of effective and reliable modelling tools for (reverse) electrodialysis. On the other hand, 1-D process simulators have been poorly devoted to study non-conventional ED applications, such as seawater desalination and multistage configurations. In this study, we propose a 1-D semi-empirical hierarchical model of the ED process, based on a robust and generalised approach developed for a wide range of operating conditions (from brackish to sea water feed solutions), and of any scale of application, spanning from bench stacks to industrial plants, and for both single and multistage configurations. The model takes into account the main phenomena involved in determining the process performance, with the aim to achieve reliable simulation results in different scenarios, thus providing a useful tool for process design and optimization. The model was validated against experimental data, and was used to study some specific applications, focusing on a 4-stage system of seawater desalination and on single-stage batch operations of brackish water desalination.

2.2 Model description

The process model is based on a hierarchical semi-empirical approach, schematically represented in Figure 17. The lowest scale is represented by the cell pair (I), the repeating unit of an ED unit composed by an AEM, a CEM and two adjacent channels. The higher scale of the stack (II) is modelled by considering a series of cell pairs and the electrodes. Finally, the stack model can be used in the highest scale of the overall plant (III), where the stacks can be variously arranged, thus simulating different process layouts (i.e. single stage, multistage, batch, feed and bleed etc.).

A number of assumptions characterises the model, in particular:

- A one-dimensional approach is adopted, in order to simulate distribution profiles along the channels, thus co- and counter-current arrangements can be simulated, while changes along the direction of the channel width are neglected:

- The presence of salt other than NaCl is neglected, thus a single salt solution is simulated;
- The unit operates below the limiting current;
- The effect of parasitic currents *via* manifolds is not taken into account;
- Transport numbers inside IEMs (and thus membrane permselectivity) are assumed independent of salt concentration in the solutions;
- The flow distribution is homogeneous among all cell pairs.

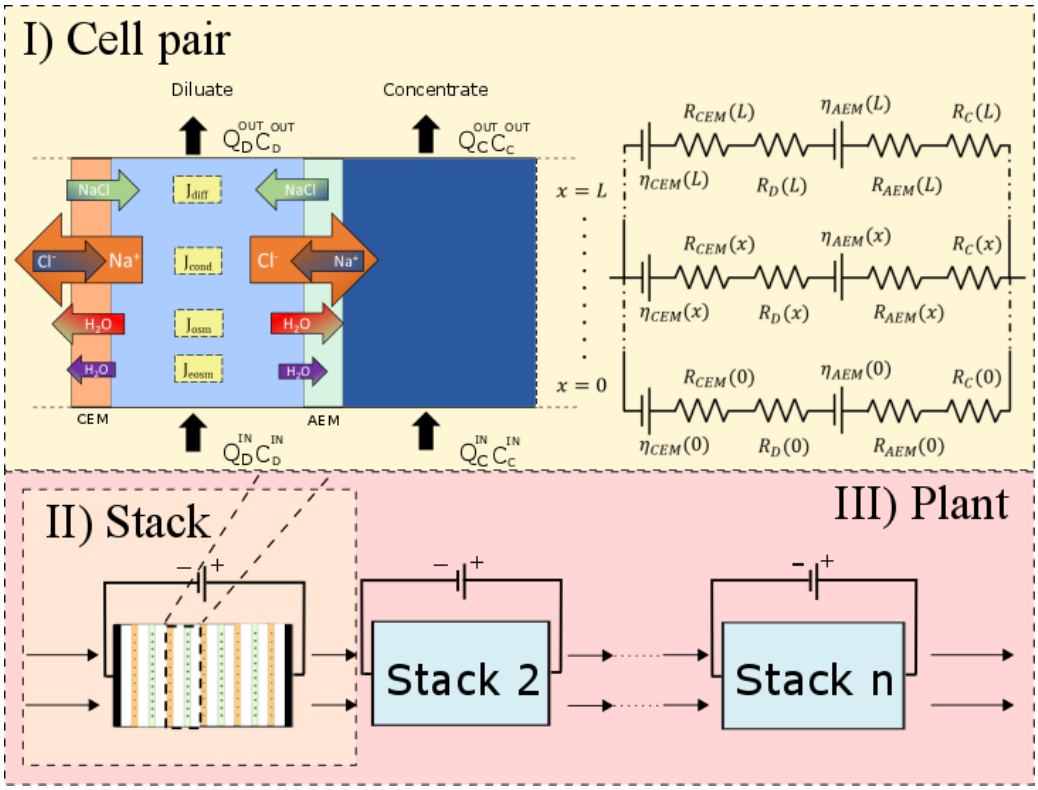

Figure 17. Schematic description of the hierarchical approach showing I) Cell pair, with the main transport mechanisms, II) Stack, III) Overall plant (i.e. multistage system).

2.2.1 Cell pair

At the scale of the cell pair (Figure 17 I), mass balances, transport phenomena, solutions thermodynamics and electrical parameters are described.

Different transport phenomena take place inside the cell pair, causing both salt and water to move through membranes. The main salt transport mechanism is the conductive flux, which is proportional to the generated ionic current and is

associated to the external applied voltage. In a general position along the length of the cell pair, it can be calculated as:

$$J_{cond}(x) = [t_{CEM}^{counter} - (1 - t_{AEM}^{counter})] \frac{i(x)}{F} \quad (20)$$

where i is the current density, F is the Faraday constant, and $t_{CEM}^{counter}$ and $t_{AEM}^{counter}$ are the transport numbers of the counter-ions inside the IEMs, directly linked with the membrane permselectivity according to eq. (6).

It is worth noting that the term $[t_{CEM}^{counter} - (1 - t_{AEM}^{counter})]$ in eq. (20) is representative of the non-ideal permselectivity of the membranes, as it accounts for the conductive co-ion transport through IEMs that in practice results in a drop of the salt removal efficiency of the system.

In addition to the effects on the conductive flux, another consequence of the non-perfect membrane selectivity is the occurrence of a back-diffusive salt flux driven by the salt concentration difference between the channels, which, for a single membrane, can be written as:

$$J_{diff}^{IEM}(x) = -\frac{D_{salt}^{IEM}}{\delta^{IEM}}(C_C{}^{int,IEM}(x) - C_D{}^{int,IEM}(x)) \quad (21)$$

where D_{salt} is the salt permeability coefficient through the IEMs, δ^{IEM} is the thickness of IEMs and C^{int} is the salt concentration in solution at the interface with the membrane. Subscripts C and D refer to concentrate and diluate respectively and the superscript IEM indicates that, using the relevant values, the expression is valid for both AEM and CEM. The overall diffusive flux can be written as the sum of the fluxes through the two membranes.

Also water molecules can move through the membranes. Water transport can be attributed to two phenomena: osmosis and electroosmosis. The first transport mechanism is caused by the interfacial concentration gradient between concentrate and diluate and can be expressed as:

$$q_{osm}^{IEM}(x) = L_p^{IEM}(\pi_C^{IEM} - \pi_D^{IEM}) \quad (22)$$

$$q_{osm}^{IEM}(x) = L_p^{IEM}\left[\nu R_G T\left(\varphi_C^{IEM} C_C{}^{int,IEM}(x) - \varphi_C^{IEM} C_D{}^{int,IEM}(x)\right)\right] \quad (23)$$

where L_p is the water permeability coefficient of IEMs and π is the osmotic pressure that can be related to the van 't Hoff coefficient (ν), the osmotic coefficient (φ) and the solution concentration. Pitzer's correlation is used to estimate osmotic coefficients [346,347]:

$$\varphi - 1 = -A_1 \frac{\sqrt{m}}{1 + b'\sqrt{m}} + mB^{\varphi} + m^2 C^{\varphi} \quad (24)$$

$$B^{\varphi} = \beta^{(0)} + \beta^{(1)} e^{-\alpha\sqrt{m}} \quad (25)$$

where A_1 is the modified Debye-Huckel constant (0.3915 at 25 °C), b' is a correlation constant equal to 1.2, m is the molality of the electrolyte, α is a fixed constant with a value of 2 $(kg/mol)^{1/2}$, $\beta^{(0)}$, $\beta^{(1)}$, C^{φ} are functions of the nature of the electrolyte and

amount to 0.06743, 0.3301 and 0.00263, respectively, for NaCl. As for the diffusive flux, the total osmotic flux is the sum of the fluxes on the two membranes.

The second transport mechanism, electroosmosis, is the water flux coupled with the ions movement due to two main contributions: the water molecules of the solvation shell and the water flux dragged by the momentum arising on the slip-plane between the solvation shell and the solvent [348,349]. Generally, electroosmosis can be expressed as a function of the overall salt flux:

$$q_{eosm}(x) = \frac{w\, J_{tot}(x) M_w}{\rho_w} \tag{26}$$

where $J_{tot}(x)$ is the sum of the diffusive (of both AEM and CEM) and the migrative salt flux and w is the total water transport number, defined as the sum of the water transport number relative to each ion. In [348], Wilson reports that for most membranes the ionic transport numbers are close to the primary hydration numbers. Thus, the simplifying assumption of a constant value of 12 moles per equivalent of transported salt was made. However, it should be noted that this parameter can change with the type of membrane and salt concentration [64].

The model computes distributions over the dimension of the channel length. Bulk concentration and flowrate distributions inside the channels are described through differential mass balance equations that, in the case of co-current flow and negligible changes in the solutions density, are:

$$\frac{d\, Q_D(x)\, C_D(x)}{dx} = -b\, J_{tot}(x) \tag{27}$$

$$\frac{d\, Q_C(x)\, C_C(x)}{dx} = b\, J_{tot}(x) \tag{28}$$

$$\frac{d\, Q_D(x)}{dx} = -b\, q_w(x) \tag{29}$$

$$\frac{d\, Q_C(x)}{dx} = b\, q_w(x) \tag{30}$$

where $Q(x)$ represents the local volumetric flow rate, b the channel width and $q_w(x)$ the local overall volumetric water flux (i.e. the sum of osmotic and electroosmotic fluxes).

A crucial aspect of ED process modelling is to relate the ionic current to the applied voltage. The voltage drop over a cell pair (V_{cp}) is calculated as:

$$V_{cp} = \eta\,(x) + R_{tot}(x) i(x) \tag{31}$$

where η is the non-ohmic voltage drop associated to the back electromotive force (diffusion potentials are not taken into account), i is the current density, R_{tot} is the total areal ohmic resistance of cell pair that can be calculated as the sum of the four components in series

$$R_{tot}(x) = R_{CEM}(x) + R_{AEM}(x) + R_C(x) + R_D(x) \tag{32}$$

where R_{CEM} and R_{AEM} represents the resistance of IEMs. R_C and R_D are the resistance of concentrate and diluate respectively, and, neglecting the ohmic (thus assuming to work in conditions far from the limiting current) contribution of the diffusion boundary layers, can be generally expressed as:

$$R_{SOL}(x) = f_{s_{SOL}} \frac{\delta_{SOL}}{\Lambda_{SOL}(x)\, C_{SOL}(x)} \tag{33}$$

with δ being the compartment thickness, f_s the shadow factor, which accounts for the resistance increase due to the presence of a non-conductive spacer [145] and Λ the equivalent conductivity. The subscript SOL refers to the generic solution, thus making the equation valid for both concentrate and diluate resistances by using the relevant parameters. For a NaCl salt solution, the equivalent conductivity can be estimated by the correlation of Islam et al. [350]:

$$\Lambda(x) = \left[\Lambda^0 - \frac{B'_1(C)\sqrt{C}}{1 + B'(C)\, a_1\sqrt{C}}\right]\left[1 - \frac{B'_2(C)\sqrt{C}}{1 + B'(C)\, a_1\sqrt{C}} F'(C)\right] \tag{34}$$

$$B'(C) = 50.29 \cdot 10^8/(\varepsilon T)^{1/2} \tag{35}$$

$$B'_1(C) = 82.5/\left[\psi(\varepsilon T)^{1/2}\right] \tag{36}$$

$$B'_2(C) = 8.204 \cdot 10^5/(\varepsilon T)^{3/2} \tag{37}$$

$$F'(C) = \frac{\left[exp\left(0.2929\, B'\, C^{1/2} a_1\right) - 1\right]}{\left(0.2929\, B'\, C^{1/2} a_1\right)} \tag{38}$$

where Λ^0 is the equivalent conductivity at infinite dilution, C is the molar concentration, η is the viscosity, ε the dielectric constant and T the electrolyte solution temperature and $a_1 = 3.79\ A^o$ for NaCl. The main advantage of using this correlation is that it can reliably predict the conductivity even at high ionic strength (i.e. with concentrated brines).

The shadow factor is generally a function of the geometrical characteristics of the spacer. Therefore, it is usually calculated as a function of the channel porosity [242,342], open area [145], or both [292,351]. The porosity represents the fraction of channel volume occupied by the liquid, while the open area represents the free fraction of membrane area projected in the direction perpendicular to membranes. Values for the open area typically range between 40-60% [145]. In this study, the shadow factor for the simulated spacer has been calculated by finite-volume simulations (solving the Laplace equation for the electric potential), resulting in a value that is close to the reciprocal of the average of porosity and open area, and is in agreement with experimental findings [352].

It is known that membrane resistance is influenced by solution concentration [146,353,354]. According to the experimental data by Galama et al. [146], membrane resistance appears to be generally influenced by diluate solution concentration. Based on those findings, the following trend can be attributed to membrane resistance:

$$R_{IEM}(x) = R_{IEM}^{HIGH} + \frac{n_1}{C(x)^{n_2}} \tag{39}$$

where R_{IEM}^{HIGH}, n_1 and n_2 and are constants o value 7×10^{-3} and 1.25 respectively. In this specific case, R_{IEM}^{HIGH} has been taken equal to the value of the resistance measured at the standard concentration of 0.5 M NaCl (see Table 2). The values of the other constants are obtained by assuming the same trend of membrane resistance against the diluate concentration reported in Galama's work [146].

The non-ohmic contribution of the voltage drop (η) is the sum of the membrane potentials that are established within all cell pairs due to the different salt

concentration between flowing solutions. As was discussed in section 1.3.3, taking also into account concentration polarisation effects, the non-ohmic drop at each IEM can be calculated as in eq. (16) with η being the sum of the two membranes' potential. Similarly to osmotic coefficients, in eq. (16) the Pitzer model can be used to estimate the average activity coefficient of salt in solution ($\gamma_{\pm}$) [346,347]:

$$ln\gamma_{\pm} = -A_1 \left[\frac{\sqrt{m}}{1+b'\sqrt{m}} + \frac{2}{b'}\ln\left(1+b'\sqrt{m}\right)\right] + mB^{\gamma} + m^2C^{\gamma} \quad (40)$$

$$B^{\gamma} = 2\beta^{(0)} + 2\beta^{(1)}\left[1-\left(1+\alpha\, m^{\frac{1}{2}} - \frac{\alpha^2 m}{2}\right) exp\left(-\alpha\, m^{\frac{1}{2}}\right)\right]/\alpha^2 m \quad (41)$$

$$C^{\gamma} = \frac{3}{2}\, C^{\varphi} \quad (42)$$

The salt concentrations at the solution-membrane interfaces are estimated as functions of the current density and the Sherwood number, the latter being calculated by CFD correlations. In particular, neglecting the salt back-diffusion, eq. (21), the interface salt concentrations (solution side) appearing in eq. (16) can be estimated by the following relations [6,39]:

$$C_C^{int,IEM}(x) = C_C(x) + \frac{(t_{IEM}^{counter} - t^{ion})\, i(x)}{F\, Sh_C^{IEM}(x)} \frac{d_C^{eq}}{D_C} \quad (43)$$

$$C_D^{int,IEM}(x) = C_D(x) - \frac{(t_{IEM}^{counter} - t^{ion})\, i(x)}{F Sh_D^{IEM}(x)} \frac{d_D^{eq}}{D_D} \quad (44)$$

where Sh is the Sherwood number, D is the salt diffusion in solution and d^{eq} is the equivalent diameter, here assumed equal to two times the channel thickness. Sherwood numbers, in turn, are computed through correlations obtained by 3-D CFD simulations for various spacer or profiled membrane geometries [197,290,355].

2.2.2 Stack

At the higher hierarchy level, overall quantities are estimated and the voltage drop within the electrode compartments is taken into account. Therefore, the overall voltage applied to the stack is calculated as:

$$V_{tot} = \frac{R_{blank} I}{A} + \sum_{i=1}^{N_{cp}} \Delta V_{cp_i} \quad (45)$$

where V_{tot} is the overall applied voltage, A is the area of a single membrane, R_{blank} is the blank resistance, accounting for electrode compartments, I is the overall current, calculated as the integral of the current density over the active area, and N_{cp} is the number of cell pairs in the stack.

In the stack model, most of the energetic parameters are also computed. The total power required to desalinate a certain amount of water is the sum of the electric

energy supplied to the stack, plus the energy needed for pumping the solutions. The total power consumption is:

$$P = V_{tot}\, I \; + \; \Delta p_C^{tot} Q_D^{av} + \; \Delta p_C^{tot} Q_D^{av} \tag{46}$$

where Q^{av} is the average solution flowrate and Δp^{tot} is the overall pressure drop through the stack, i.e. including hydraulic losses in the manifolds and in the channels. Pumping power is usually negligible compared to electric power consumed directly by the stack ($V_{tot}\, I$), especially when high salinity feeds (e.g. seawater) are treated. However, it may play a significant role, depending on stack features and operating conditions. CFD correlations are also used in order to calculate the pressure drop distributed along the channels [289] and, thus, the pumping power consumption in eq. (46). In particular:

$$\Delta p_{SOL} = \frac{1}{2} f_{SOL} \frac{\rho_{SOL} {u_{SOL}^{av}}^2}{d_{SOL}^{eq}} L \tag{47}$$

where Δp is the pressure drop, ρ is the density of solution, f is the Darcy friction coefficient that it is correlated to the Reynolds number [6,290] and u^{av} is the average superficial velocity, with the local superficial velocity being defined as:

$$u_{SOL}(x) = \frac{Q_{SOL}(x)}{b\, \delta_{SOL}} \tag{48}$$

In the calculation of the total pressure drop, the hydraulic losses through the manifolds may be included using empirical data or, again, simulation results. It is worth noting that, as the stack geometrical features vary, the relevance of this contribution on the total pressure drop may change significantly [39].

In addition, the energy consumption per unit volume of product (here represented by the diluate) can be defined as:

$$E_{spec} = \frac{P}{Q_D^{OUT,tot}} \tag{49}$$

where $Q_D^{OUT,tot}$ is the overall outlet diluate flowrate and E_{spec} is the specific energy consumption expressed in kWh/m^3. Moreover, the salt-specific energy consumption can be defined as:

$$E_{spec}^{salt} = \frac{P}{C_D^{IN} Q_D^{IN,tot} - C_D^{OUT} Q_D^{OUT,tot}} = \frac{P}{C_C^{OUT} Q_C^{OUT,tot} - C_C^{IN} Q_C^{IN,tot}} \tag{50}$$

where superscripts *IN* and *OUT* refer to inlet and outlet conditions. Eq. (17) is particularly useful when the separation target is related to salt removal rather than to the volume of diluate produced.

Other two figures of merit have been defined to analyse the process performance. The first one is the current efficiency, which can be expressed as:

$$\xi = \frac{(C_D^{IN} Q_D^{IN,tot} - C_D^{OUT} Q_D^{OUT,tot}) \cdot F}{I \cdot N_{cp}} \tag{51}$$

The current efficiency represents the amount of current that is actually converted into useful salt flux, thus expressing the efficiency of current utilisation of the process [348] .

The second parameter is the apparent product flux (or water productivity [356]) and it is defined as:

$$J_P = \frac{Q_D^{OUT,tot}}{2A\ N_{cp}} \tag{52}$$

This variable gives an indication of the area required to obtain a certain flowrate of desalinated water. This is very useful for comparison with other desalination processes such as reverse osmosis, where the flux is often used as performance indicator.

2.2.3 Overall plant

The main advantage of using a hierarchical approach is that the stack model can be inserted into higher hierarchy models in order to simulate complex plant layouts. In this work, multistage and batch operations have been analysed as examples of articulated flowsheeting.

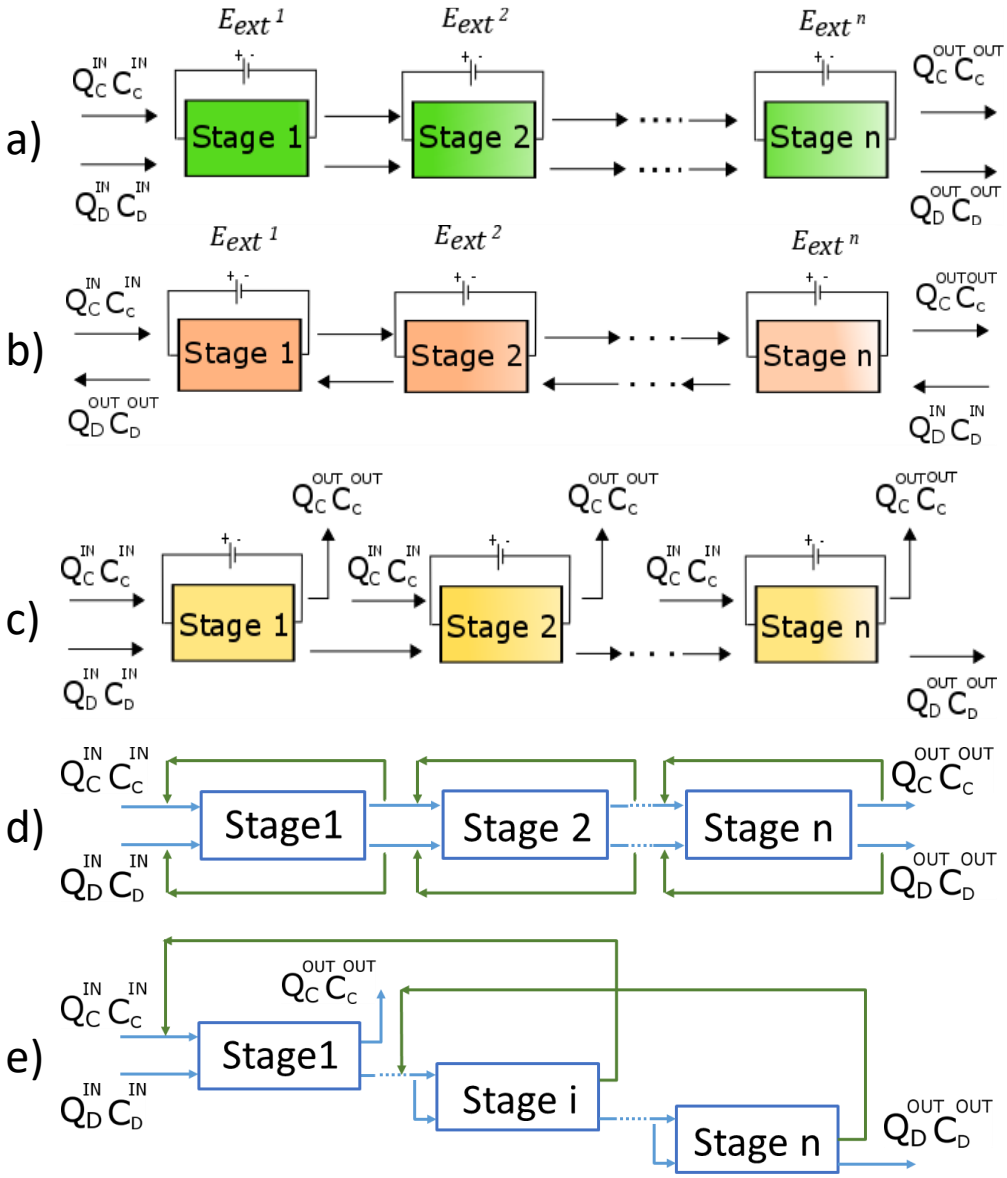

Figure 18. Block diagrams of multistage ED processes in series in the case of a) co-current, b) counter-current, c) stages with independent feed, useful in seawater desalination to reduce the concentration difference inside the stacks by feeding the concentrate compartments of each stage with fresh seawater. d) Concentrate and diluate feed & bleed, useful to either control the system recovery ratio or to increase the velocity inside the unit to reduce limiting current issues. e) Interstage recycles. Each stage can recirculate its outlet concentrate back to the feed concentrate of one previous stage, while the diluate in each stage is fed to both concentrate and diluate compartments of the next stage. In this way, it is possible to control and reduce the concentration difference inside each unit.

A multistage configuration requires a number of stacks that can be connected according to different schemes, some of which are reported as example schemes in Figure 18. As case study, a co-current multistage operation (Figure 18 a) was taken into account.

In a multistage system, it is more convenient to define the specific energy consumption of the overall system as follows:

$$E_{spec}^{TOT} = \frac{\sum_{i=1}^{N_s} P_i}{Q_{D,N_s}^{OUT,tot}} \tag{53}$$

where N_s is the number of stages and $Q_{D,N_s}^{OUT,tot}$ is the diluate flowrate coming out from the last stack.

In the same way, the water productivity for the overall system will contain the diluate flowrate coming out from the last stack

$$J_P = \frac{Q_{D,N_s}^{OUT,tot}}{\sum_{i=1}^{N_s} N_{cp,i}\, 2A_i} \tag{54}$$

Generally, a multistage system has the advantage to reduce the energy requirements of a certain desalination operations (e.g. seawater desalination) compared to a single stage operating at the same conditions. On the other hand, the system design and optimisation complexity increases with the number of stages, as it becomes necessary to deal with more variables. Therefore, it becomes crucial to support such design operations with simulations. A common issue can be the optimisation of the applied voltage per each stage in order to minimise the energy consumption. In addition, it is also possible to test the stages with more complex arrangements that may include recycles or splitting of the streams.

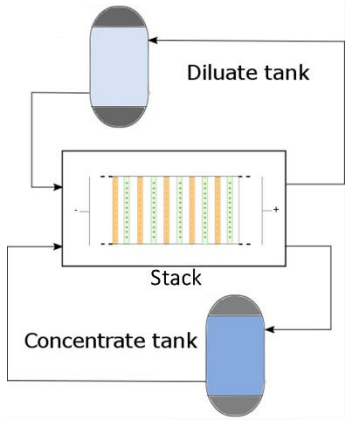

Figure 19. Batch ED block scheme including the ED unit and the recirculation tanks.

The model can also deal with the simulation of transient operations of batch ED systems (Figure 19). In this case, an additional model of lower hierarchy describing the tanks is defined, thus predicting the time variation of solutions concentration

and volume within the tanks. Assuming that the tanks are perfectly mixed, this model is characterised by time dependent differential equations (eqs. (55)-(56)):

$$\frac{d(V_{tank} \cdot C_{tank})}{dt} = Q_{tank}^{IN} C_{tank}^{IN}(t) - Q_{tank}^{OUT} C_{tank}(t) \quad (55)$$

$$\frac{dV_{tank}}{dt} = Q_{INtank}^{IN}(t) - Q_{tank}^{OUT}(t) \quad (56)$$

where V_{tank} is the solution volume inside the tank, C_{tank} is the salt concentration in the solution inside the tank (i.e. entering the stack), Q_{tank}^{IN} and C_{tank}^{IN} are the flowrate and salt concentration of the solution going into the tank (i.e. coming out from the stack) and Q_{tank}^{OUT} is the solution flowrate exiting the circulation tank. In addition, two initial conditions are required for volume and concentration. Using the relevant initial conditions, the aforementioned model is indistinctly applicable to the diluate and concentrate tanks. Assuming that stack dynamics is negligible compared to the time variation of concentrations in the tanks, a quasi-steady state approach can be adopted to combine the dynamic tank model to the steady state ED stack model.

2.3 Experimental model validation

An experimental campaign was carried out in order to validate the model. All the experiments were conducted in a single ED stack (*Deukum GmbH*, Germany). The ED unit was equipped with 10 cell pairs, with an active membrane area of 10×79 cm² and woven spacers 270 μm thick (*Deukum GmbH, Germany*). Homogeneous ion exchange membranes (*FUJIFILM Manufacturing Europe B.V., The Netherlands*) were used for all the tests. The relevant properties of both AEMs and CEMs (as provided by the membrane manufacturer) are reported in Table 2. The electrodialysis tests were performed under galvanostatic mode, using a power supply (*Elektro-Automatic GmbH, Germany).*

Table 2. Properties of the Fujifilm membranes (provided by the manufacturer).

Membrane	δ (μm)	α*	L_p (ml/(bar h m²))	R (Ω cm²)**
AEM	130	0.969	6.29	1.77
CEM	130	0.975	7.79	1.89

*Permselectivity measured in between 0.05M/0.5M KCl solutions

**Membrane resistance measured with 0.5 M NaCl solution

Artificial salt water at different concentrations was prepared by using re-crystallised NaCl with purity >99.5% (*Saline di Volterra s.r.l.*, Italy), and demineralized water. The electrode rinse solution was a 10 g/l Na_2SO_4 aqueous solution, operating at 700 ml/min. Feed and electrode rinse solutions were pumped by three peristaltic pumps

(*Lead Fluid Technology Co., Ltd., China*). Single pass experiments were performed. Conductivity measurements were performed at the concentrate and diluate outlets by conductivity meters (*XS instruments, Italy*), while glycerin-filled pressure gauges (*Cewal S.p.a., Italy*) were placed at the inlets to measure pressure drops.

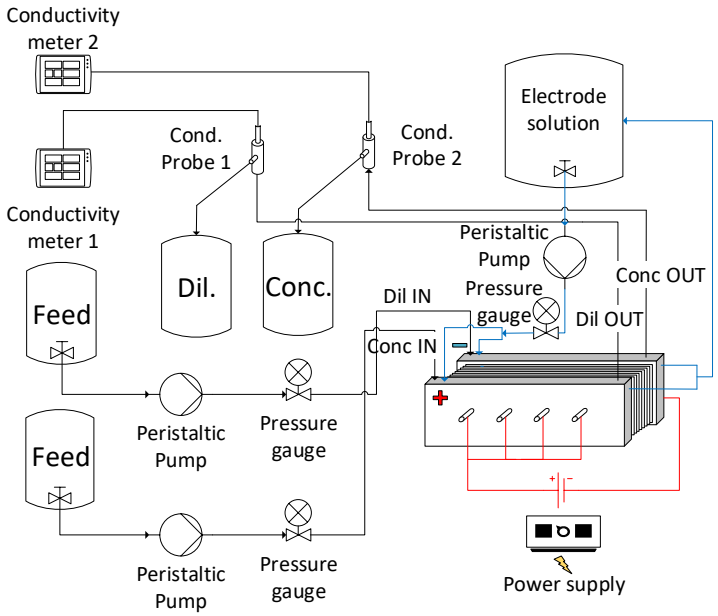

Figure 20. Schematic representation of the experimental set-up.

A schematic representation of the set-up is presented in Figure 20. For every experiment, the stack was operated with feed water (at the given flowrate and concentration) for at least 5 minutes, to ensure proper membrane conditioning and steady state conditions. Then, a constant current was applied, until a stable value of the outlet conductivity was reached. A summary of the main process conditions (i.e., inlet concentrations, velocities, and currents) is given in Table 3.

Table 3. Summary of the main process conditions of the experimental tests.

C^{IN} (g/l)	u (cm/s)	I (A)	i_{av} (A/m²)
1	0.7-2.5	0.2-0.5	2.5 - 6.25
3	0.7-2.5	0.2-1.5	2.5 - 18.75
6	0.5-2.2	0.2-4	2.5 - 50
10	0.5-2.25	0.2-7	2.5 - 87.5
30	0.45-2.25	0.2-10	2.5 - 125

Model predictions were compared with experimental results over a wide range of inlet concentrations (i.e. from 1 to 30 g/l), electrical currents and flow velocities. A representative part of the experimental points is depicted in Figure 21, reporting the comparison between model predictions and experimental values of outlet

conductivities for both concentrate and diluate. Model results fit very well experimental data of conductivities as functions of the current for all the investigated inlet concentration and flow velocity.

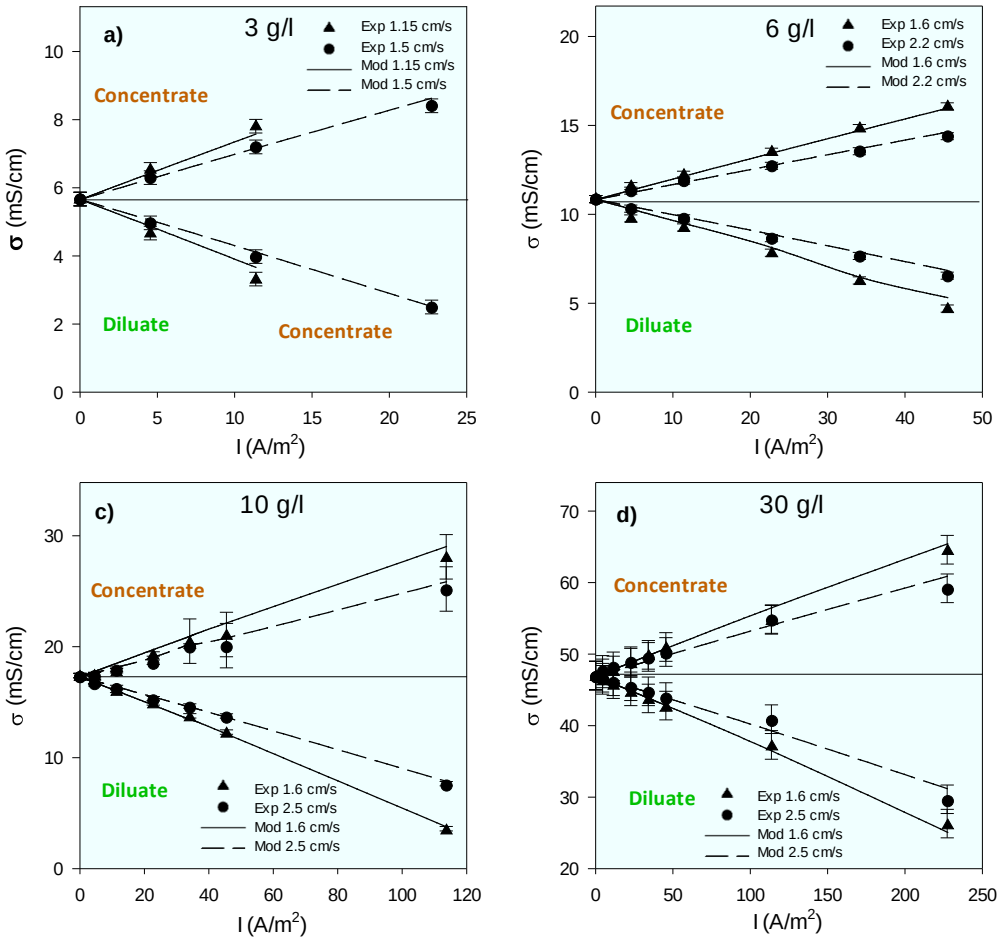

Figure 21. Comparison between model predictions (lines) and experimental data (symbols), for both concentrate and diluate outlet conductivity at different currents, velocities, and feed concentrations: a) 3 g/l, b) 6 g/l, c) 10 g/l, d) 30 g/l. Stack area:10×79 cm², spacer thickness: 270 µm.

A comprehensive overview on the model prediction accuracy for all experiments performed is reported in Figure 22, showing the parity plot for streams conductivity, i.e. the experimental outlet conductivity versus the conductivity calculated by the model for diluate and concentrate. Again, the model reliability is confirmed as most of the points are very close to the reference line $y = x$.

On this basis, it is worth noting that, compared to other literature works, the developed model has been validated in a much wider range of feed concentration (i.e., ranging from brackish water to seawater conditions), and is therefore suitable for a variety of possible applications. In the following sections, two examples of

application of the model predictive capability to complex operating schemes are reported.

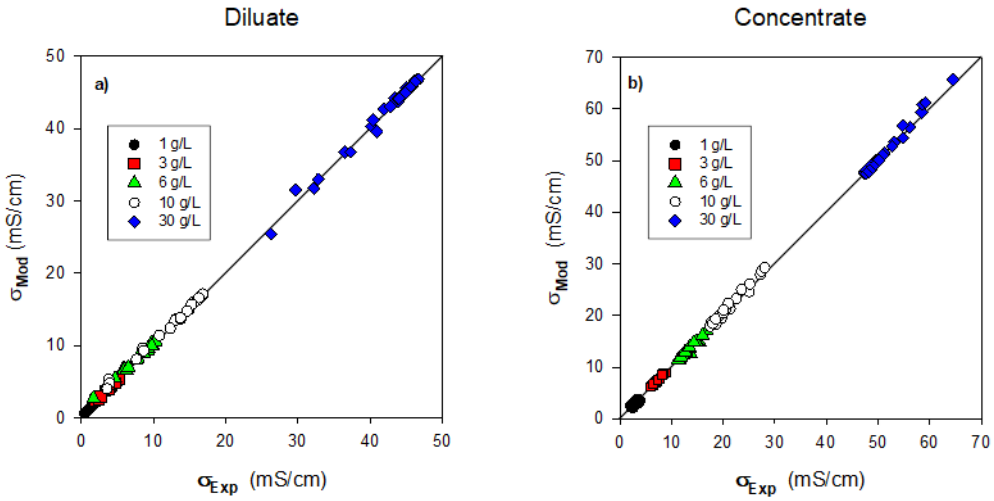

Figure 22. Predicted vs. experimental outlet conductivities for a) diluate and b) concentrate for all performed experiments (symbols). Stack area:10×79 cm², spacer thickness: 270μm.

2.4 Simulation analysis of alternative schemes

In this section, the model predictions for two representative cases (i.e. multistage ED for seawater and single-stage batch ED for brackish water) are presented and discussed.

2.4.1 Case I: Seawater multistage desalination

The model has been used to simulate a multistage ED system for seawater desalination, as this is a relatively newly explored application [9]. In fact, electrodialysis is not used nowadays for seawater desalination, mainly due to the high energy consumption compared to state-of-the-art desalination processes (e.g. reverse osmosis). However, the use of staging in ED is of importance, as this could lead to a reduction of the overall energy consumption. In this regard, the developed model has been used to assess the effect of different current/voltage distributions on the specific energy consumption, simulating a series of 4 ED stacks with fixed geometrical properties (active area, number of cell pairs, spacer type), and arranged in co-current mode (Figure 18a). Table 4 summarises the process conditions and geometric parameters simulated for the 4-stage ED system.

Table 4. Simulated geometric parameters and process conditions of a 4-stage ED system for seawater desalination. The flowrate refers to both the diluate and the concentrate separately. The co-current configuration is simulated and Fujifilm membranes are considered.

L (cm)	b (cm)	N_{cp}	δ_{SOL} (μm)	u (cm/s)	C_{SOL}^{IN} (mol/m³)	C_{D}^{OUT} (mol/m³)
43	10	500	155	1.5	500	8.5

The model has been used to evaluate the effect of staging to desalinate seawater (500 mol/m³ NaCl, i.e. ~30 g/l) to drinking water (500 ppm NaCl, i.e., ~8.5 mol/m³ NaCl). In particular, two benchmark scenarios have been simulated: in the first scenario (i.e., "equal voltage"), the target diluate concentration is reached by applying the same voltage to the 4 stacks (i.e., 0.23 V per cell pair). Notably, this scenario corresponds to the case of a single stack with a flow path length equal to the sum of all stack lengths, and it can be considered as a reference case in the assessment of multistage operations. The second scenario ("equal current") accounts for the effect of multiple stages operating under the same overall current (2.43 A), in order to reach the target diluate concentration.

Figure 23 shows the main model results for a single cell pair along the length of the 4 stages, for both the "equal voltage" and the "equal current" cases. In particular, Figure 23 shows the cell pair voltage (Figure 23 A), current density and current efficiency (Figure 23 B), concentrations (Figure 23 C), flow rate distribution and apparent flux (Figure 23 D). Both the spatial distribution of current density (Figure 23 B) and the concentration (Figure 23 C) clearly show how the "equal voltage" case is highly inefficient compared to the "equal current" case. In the "equal voltage" scenario most of the desalination takes place in the first stage, leading to a poor ion removal in the following stages. As a consequence, the system is subjected to a large concentration difference over the membranes along most of the flow path length (i.e., after the first stage), thus causing larger water flux and salt back diffusion through the membranes, resulting in very low current efficiencies (Figure 23 B). The negative effect of water transport can be seen from the decreasing concentration of the concentrate stream (Figure 23 C), as well as from the reduced diluate flowrate (Figure 23 D).

The "equal current" scenario, instead, shows a more homogenous ion removal along the four stacks, leading to lower water transport and higher current efficiency (Figure 23 B), which decreases significantly only in the last stage, especially close to the outlet. Figure 23 B clearly shows the benefits of staging with different voltage values ("equal current") to enhance the overall current efficiency, resulting in a significant reduction of the total specific energy consumption (i.e., 1.94 kWh/m³ of product instead of 4.59 kWh/m³ required by the "equal voltage" scenario).

These results also highlight that the large concentration difference arising between diluate and concentrate is one of the main issues for desalination of concentrated streams (i.e. seawater). It is worth noting that this preliminary analysis did not include other possible scenarios, such as the use of different current, stack geometry, or membranes per stage. All of these options need to be taken into account to

properly optimise a multistage system. A more detailed analysis of the optimisation potential of multistage systems is given in chapter 0.

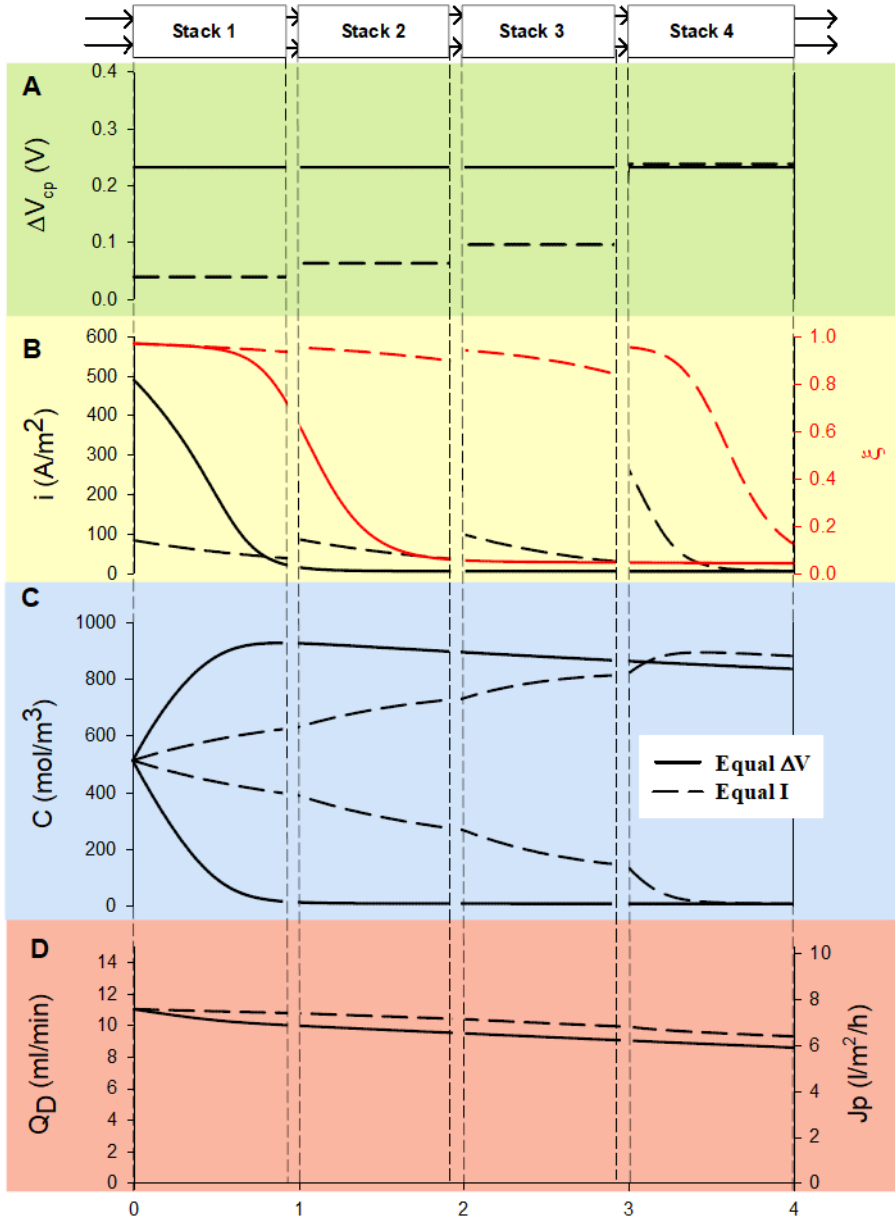

Figure 23. Model predictions for a 4-stage 10×43 cm² ED co-current system equipped with 155 µm woven spacer, Fujifilm membranes and 500 cell pairs with 5.5 l/min flowrate. Solid lines: same voltage per stage (0.23 V per cell pair). Dashed lines: same current per stage (2.43 A). A: cell pair voltage, B: current density distribution (main axis) and local current efficiency (secondary axis), C: diluate and concentrate concentration, D: flowrate (main axis) and apparent product flux per single channel (secondary axis).

2.4.2 Case II: Brackish water batch desalination

Another representative system simulated in this work is the batch ED operation for brackish water desalination (i.e., C_{SOL}^{IN}=5 g/l). In particular, a small lab scale unit has been simulated adopting the time-dependent formulation of the hierarchical model (see section 2.2). Stack features and operating conditions are reported in Table 5.

Table 5. Geometric parameters of the ED unit equipped with Fujifilm membranes simulated in batch operation.

L (cm)	b (cm)	N_{cp}	δ_{SOL} (μm)	u (cm/s)	C_{SOL}^{IN} (g/l)	C_D^{OUT} (g/l)
10	10	10	270	2	5	0.25

Fixed voltage simulations have been performed (i.e. 3, 5 or 8 V, neglecting the voltage drop at the electrodes, R_{blank}) by assuming a 2 cm/s inlet flow velocity inside each channel. Then, the solution inside the diluate tank (initially filled with a volume of 0.5 l, as for the concentrate) has been processed until its concentration reaches 250 ppm, thus accounting for a safety margin on the outlet concentration compared to the standard 500 ppm.

In Figure 24, the predicted trends of concentrations, volumes in the tanks, current and current efficiency for the three different applied voltages are reported. As expected, increasing the applied voltage reduces the time to reach the target concentration (~ 40% reduction from 3 to 8 V) as for each single pass a higher amount of salt is removed (i.e. the distance between the dashed and the continuous line is largest at the highest voltage). Reducing the operation time (i.e., the number of the recirculation cycles of the solution through the stack) decreases the impact of water transport and salt back diffusion in the system. As a result, the overall current efficiency is slightly higher at 8 V, so that ~4% less current is required to reach the target concentration compared to the 3 V case. Despite this, the overall energy consumption increases from 1 kWh/m^3 (at the minimum voltage) up to 3.6 kWh/m^3 (at the maximum voltage value). Therefore, it is clear how the voltage increase has some beneficial effects such as higher current efficiency and lower desalination times, although, from an energetic perspective, those advantages are overcome by the increase of the ohmic and non-ohmic energy dissipation, which result in a larger overall energy consumption. The competition of transport and energetic (voltage drop) phenomena suggests that, as well as for the multistage system, the batch process is particularly suitable for process optimisation. In particular, it is possible to design an optimal process where voltage (or current) changes through time, mimicking the effect of staging in time rather than in space.

Finally, it is worth noting that, in principle, a batch operation exhibits a lower energy efficiency compared to an equivalent single pass continuous operation, due to the effect of the tanks where the dilute stream exiting from the stack is concentrated again. However, the batch operation can still be considered advantageous for

specific lab experiments, in small scale productions or when an accurate control of the desalination steps is required (e.g. to minimise limiting current issues).

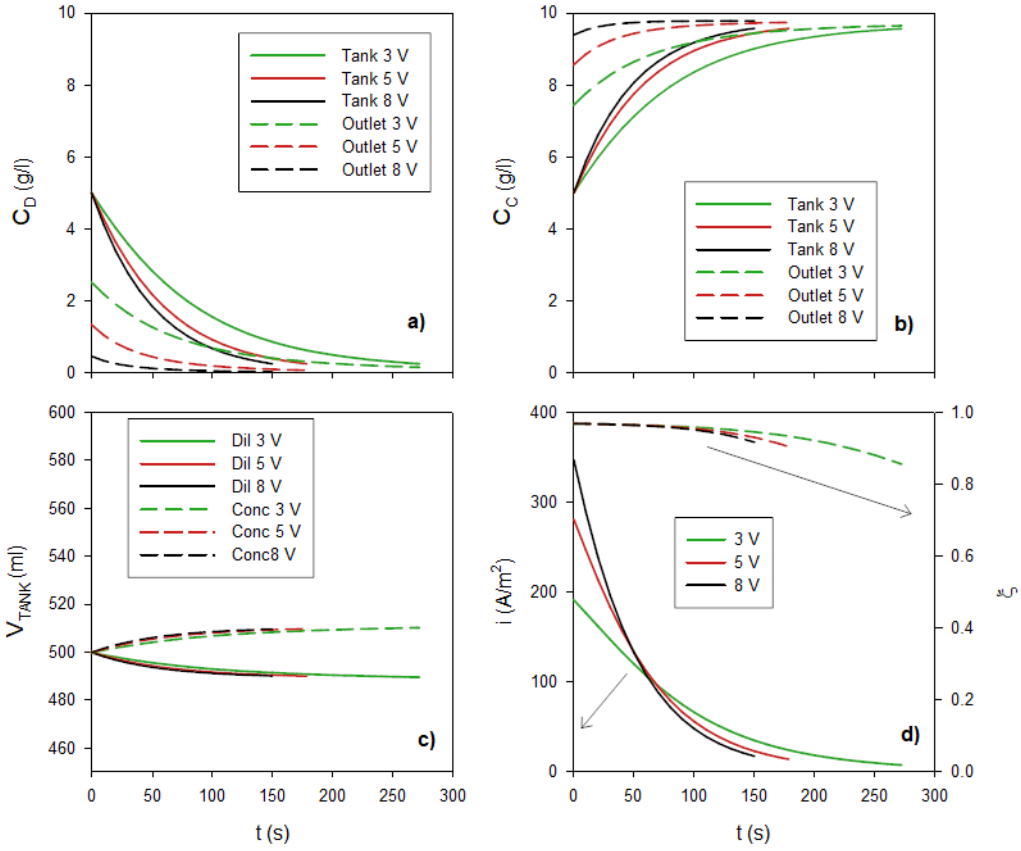

Figure 24. Results as a function of time of batch ED simulations at different applied voltage. a) Diluate and b) concentrate concentration inside the tanks and at the stack outlet. c) Diluate and concentrate volumes in the tanks, d) Current density and current efficiency. 10×10 cm² stack with 270 µm spacers, 10 cell pairs (Fujifilm membranes) and 2 cm/s inlet flow velocity.

3 Dynamic process modelling of electrodialysis and capacitive electrodialysis

In chapter 2, the problem of simulating a dynamic system (i.e. batch ED) was assessed by adopting a quasi-steady state approach. However, there are some cases in which is essential to capture the system dynamics. An effective example of the latter is represented by process control or by startup/shutdown operations. Therefore, in such cases it is necessary to consider the development of dynamic process models.

Dynamic models can be of both lumped and distributed parameter form. In the first case, a general assumption of "well mixed" system can be made, so that there are no variables with spatial distribution. Ordinary differential equations can then be written to describe the model and, once they are coupled with the algebraic constraints, a system of differential-algebraic equations is obtained. In distributed models, (as for the steady-state model presented in chapter 2) variables are also considered as a function of space. Here, the final system to be solved can be either made of parabolic or hyperbolic partial differential equations. Each of the two type of models requires different solving strategies and techniques [357] but is outside the scope of this thesis to discuss them.

From the model development perspective, a fundamental implication of considering dynamics models is the need to define the proper initial conditions for the dynamic variables. In many cases, steady state initial conditions are the most suitable for process modelling, as the transition from two different stable conditions are usually of practical interest. Nevertheless, this is not always the case and in some modelling applications the definition of initial conditions can actually be a difficult issue [357].

In the following subsections, the problem of dynamic modelling will be explored in the case of **(i)** ED with capacitive electrodes, where charge accumulation and rejection takes place over time and **(ii)** ED coupled with a dynamic power source, where the change in the available power causes the unit to go through a series of changes in process conditions.

3.1 Capacitive electrodialysis

The first example of dynamic system, namely capacitive electrodialysis (CED) process has been studied through experiments and modelling. CED couples the standard ED with capacitive electrodes and has a number of advantages such as removal of toxic products and system simplification. A novel model for this process is here presented. With a simple calibration based on macroscopic membrane properties and the characterisation of electrode behaviour, the model is able to simulate the dynamics of simple as well as more complex layouts. An original experimental characterisation of electrodes is presented, showing how the collected data can be implemented into the model. After a successful validation with experimental data, dynamic simulations of a single pass CED unit have been

performed with the aim of assessing the effect of different capacitive electrode properties on process performance.

3.1.1 Capacitive electrodes

As discussed in section 1.1.2, the ED process usually involves standard electrodes where faradic reactions occur. However, capacitive electrodes represent a promising alternative to conventional electrode systems and have been recently proposed in applications for ED and reverse ED [53,358,359]. Porous capacitive electrodes act as a means of current transport by physico-chemical mechanisms of adsorption and desorption of ions (thus ejecting/capturing electrons) instead promoting electrochemical reactions (Figure 25). There are a number of advantages associated with the use of capacitive electrodes such as the absence of unstable or toxic products (i.e. Cl_2, O_2 and acids or bases, depending on the electrode solution adopted) and the reduction of the electrode potential drop. In addition, system complexity is reduced due to the absence of the hydraulic circuit that in standard ED is used to recirculate the electrode rinse solution [53,358]. On the other hand, capacitive electrodes suffer from saturation of the carbon layer due to charge accumulation, so that the electrical polarity (as well as concentrate and diluate compartments) needs to be periodically switched in order to operate the desalination process for a long time. However, this drawback is compensated by the fact that ED plants usually operates in EDR mode, where a periodical polarity switch is already adopted to address membrane fouling issues. Therefore, such systems are already potentially suitable for the use of capacitive electrodes.

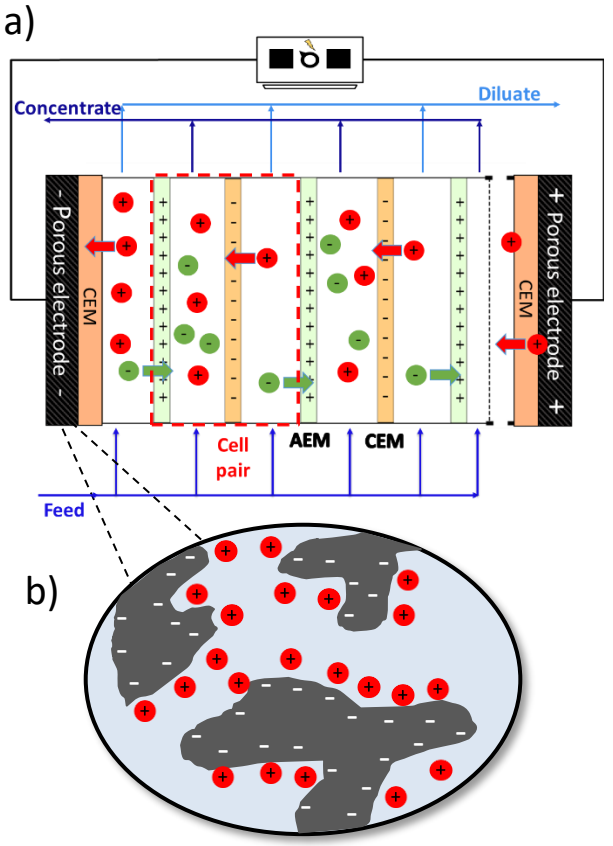

Figure 25. a) Schematic representation of the electrodialysis process with capacitive electrodes (CED), b) detail on the porous structure of the capacitive electrode.

Although a lot of complex phenomena can be involved [360,361], in principle a capacitive electrode is able to store charges in the form of ions through formation of the electric double layer (EDL) upon electrical polarisation [360,362]. As the EDL is formed on the pores' surface, the higher the specific area, the higher the amount of ions that can be stored or released. Therefore, it is imperative to use materials with high surface area in order to avoid too frequent polarity switches. Good conductivity is also desirable, in order to limit the Ohmic losses at the electrodes. For this reason, capacitive electrodes are mainly made from carbon materials [360], although alternatives such as conductive polymers have been also investigated [363]. Among the carbon materials, different authors have reported the use of graphene with various structures such as aerogels [364] multi-layer nanoribbons [365,366], nanotubes [364,367–370] and carbon onions [370,371]. In particular, Portet et al. [370] showed how carbon onions are specifically suitable for energy storage applications, due to their ability to rapidly deliver charges. Another good material is carbon black, which is able to provide a high surface area (> 1500 m^2/g) through agglomeration of nanoparticles [360,372]. However, the most common electrodes are usually made from activated carbons, characterised by randomly oriented and

highly cross-linked graphene layers [373–380]. Activated carbons are particularly attractive as they combine high surface area with low production costs, as they can be produced by natural precursors such as fruit stones [380], leaves [373] and pitch [381].

The ability of capacitive electrodes for storing and delivering ionic charges make them suitable for two fields: conversion and storage of energy, and desalination. In the first one, supercapacitors represent by far the most common application [382,383], although there are some other processes such as Reverse electrodialysis (RED) with capacitive electrodes [53] or with capacitive flow electrodes [384], capacitive cell with CO_2 solutions [385], capacitive double-layer expansion [386] and other CAPMIX technologies [360]. Among the desalination technologies, capacitive electrodes are mostly acknowledged for the capacitive deionisation (CDI) process [387–391], which was already discussed in section 1.4.3. An interesting development of CDI technology is the single module flow-electrode capacitive deionization (FCDI) [392], which allows the CDI to become a continuous process through the recirculation of an activated carbon suspension. While FCDI has the advantage to be a continuous process, compared to CED it requires a hydraulic electrode circuit. Recently, an FCDI process model was also presented [393].

Although carbon electrodes have been thoroughly studied and applied to many processes and CED is an already commercialised technology [394], the process has not been widely studied in the literature [358,359]. In addition, no CED modelling works have been published yet. In this work, the CED process has been thoroughly studied by means of modelling and experiments. A set of galvanostatic experiments on a lab scale CED stack has been performed with the aim of testing the process desalination capability and characterising a set of capacitive electrodes. In addition, a CED process model is presented. The modelling tool has been implemented by a hierarchical approach that simulates the main dynamic phenomena involved in the CED process and ensures high flexibility in simulating different scales and layouts, ranging from the simple single pass lab-unit up to complex multistage industrial installations. After a model validation by means of the aforementioned experimental data, simulations have been performed in order to present the predictive capability of the modelling tool and analyse the process performance under a variety of operating conditions.

3.1.2 Modelling of capacitive electrodes: state of the art

Despite the lack of published CED models, there are a lot of modelling works either on ED (see section 2.1) or on capacitive electrodes applied to other processes [272,361,395–400].

In particular, capacitive electrodes have been extensively modelled at different scales within the context of different applications. In the most basic approach, the electrode is represented by a simple electrical circuit composed by a capacitor and a resistor (*RC circuit model*) [272,395]. Although this approach does not take into account the physical structure of the carbon material, all the electrode characteristics are condensed into the values of the two electrical elements that are relatively easy to measure. Therefore, this simple yet effective approach is

particularly useful for process models as it requires little yet easily accessible information.

A more detailed approach to the problem is represented by the *transmission line model* [362,395,401,402]**.** In this case, the porous electrode structure is approximated through a complex circuit with electrical elements (i.e. resistor, capacitors and impedances) arranged in series and parallel. Different degrees of complexity can be found based on the assumed porous structures, ranging from simple RC transmission lines [401,402] up to a complex arrangement of hierarchical impedances where a bimodal porous structure is required [362]. This type of model can be calibrated on a specific capacitive electrode by quantifying a set of fitting parameters in the form of electrical elements by means of electrical impedance spectroscopy measurements [362].

A completely different approach is based on the theoretical description of the EDL. Traditionally, models belonging to this category are based on the Gouy-Chapman-Stern theory [361,397,398]. Alternatively, the Donnan and modified Donnan models provide a more comprehensive description, involving the dynamics of EDL formation and accounting for overlapping EDLs typical of small pores [396,400,403,404]. The latter class of models can also be extended to account for non-electrostatic ion adsorption [396] and faradic reactions [400]. Theoretical models for capacitive electrodes can predict electric potential distributions inside the pores. However, complex parameters, such as the capacitance of micropores [396], need to be estimated.

In the CED model developed in this work, the semi-empirical hierarchical ED model of chapter 2 was properly modified and extended to account for the presence of capacitive electrodes which were modelled by means of a distributed RC circuit.

3.1.3 CED model description

As stated above, the starting point for the current model formulation is the steady-state ED one-dimensional process model of chapter 2 that was adapted for the purpose of accounting for the peculiarities of the new process. Consequently, existing hierarchies were modified to take into account the intrinsic dynamic behaviour, allowing for all the variables to be also function of time (Figure 26).

Starting from the lowest scale, the model simulates mass transport and electrical behaviour of the cell pair (i.e. the ED repeating unit) and the capacitive electrodes. These two elements are coupled in the second level where the whole stack is modelled (Figure 26 c). Finally, the stack model is implemented in the plant model, i.e. the highest scale that can simulate different process layouts (i.e. single stage, multistage, batch, feed and bleed etc.).

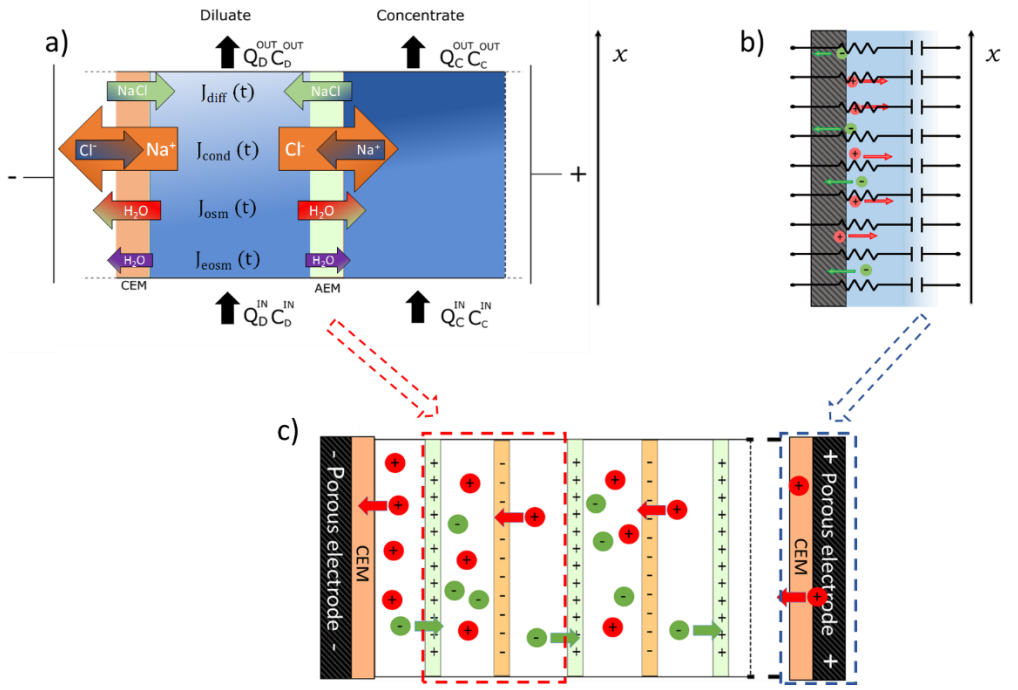

Figure 26. Schematic representation of the model hierarchies. a) Cell pair, b) capacitive electrode, c) stack.

The capacitive electrode model is a distributed entity divided into a number of discretisation intervals in the direction of the channel length (Figure 26 b). A simple RC circuit was used to model the behaviour of each interval. No contributions for unwanted faradic reactions or non-electrostatic adsorption was considered. Therefore, the time-dependent distributed electrode voltage drop (indicated as V_{el}) can be written as:

$$V_{el}^{j}(x,t) = \frac{\sigma_{el}^{j}(x,t)}{c_{el}^{j}(x,t)} + R_{el}^{j} i(x,t) \tag{57}$$

where σ_{el} is the amount of charge per unit of projected area collected by the capacitor at a given time and position, c_{el} is the electrode capacitance per unit of projected area, R_{el} the electrode areal resistance, $i = \frac{d\sigma_{el}}{dt}$ is the current density and x and t are the space and time coordinates respectively. The superscript j represents the fact that the equation is valid for both of the electrodes in the CED unit. It is worth noting that, considering a spatial distribution, each discretised electrode volume can behave differently from others, thus potentially having different values of charge, capacitance, resistance and, thus, voltage at every x. This assumption has been made in order to account for the fact that in a real unit the electrode can be subjected to a very different concentration and current density along the channel direction, thus potentially making it behave very differently from the inlet to the outlet of the stack. It is worth noting that in in the capacitive electrode model as well as in the rest of this work, the symbol V is representative of a voltage drop.

In this work, the value of c_{el} was experimentally determined as a function of the solution concentration by means of galvanostatic methods (see section 3.1.4).

The cell pair model was extensively described in section 2.2.1. In contrast to the original steady-state model, most of the variables are now intrinsically functions of time (t) as well as space (x) and salt material balances (eqs.(27)-(28)) are written in the dynamic form:

$$b\,\delta_{SOL}\frac{\partial C_{SOL}(x,t)}{\partial t}+\frac{\partial Q_{SOL}(x,t)C_{SOL}(x,t)}{\partial x}=\pm b\,J_{tot}(x,t) \tag{58}$$

The cell pair electrical terms are also computed at this scale. Interestingly, due to the discretisation of the capacitive electrodes (whose model is coupled with the cell pair model at the stack level), it is not possible to define a single voltage drop over a cell pair (V_{cp}) independent from the spatial coordinate. In fact, only in the stack, where current collectors impose an equipotential surface, is it possible to define a unique value of the voltage. Therefore, V_{cp} (as expressed in eq. (31)) is different for each single branch of the cell pair equivalent electrical circuit, thus becoming a function of x.

The stack model simulates a series of cell pairs between two capacitive electrodes which are positively or negatively polarised. Within the stack, it is possible to compute power consumption, performance parameters (e.g. current efficiency) and overall quantities such as the applied voltage [58]. At a given time, performance parameters are defined as in the classical ED process (see section 2.2.2), while the external applied voltage (V_{tot}) can be calculated by summing up the voltage drop of all cell pairs and of the two electrodes at any position (according to the system equivalent circuit shown in Figure 27):

$$V_{tot}(t)=\left(\sum_{i=1}^{Ncp}V_{cp_i}(x,t)\right)+V_{el}^{1}(x,t)+V_{el}^{2}(x,t) \tag{59}$$

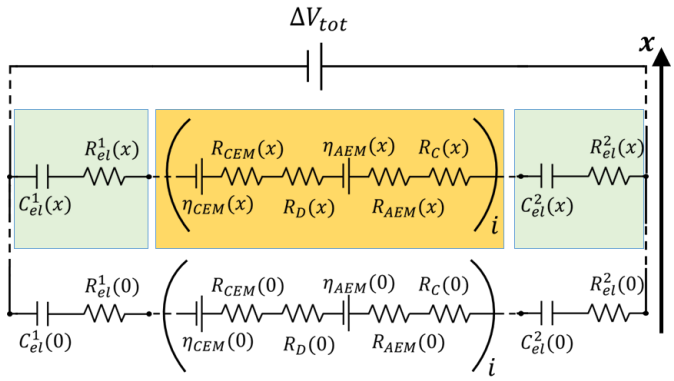

Figure 27. Scheme of the distributed equivalent electrical circuit representative of the stack model, including the cell pair circuit (in brackets) in series with the RC elements of the capacitive electrodes. For the sake of brevity, only the branches that describe the position x = 0 (channel inlet) as well as one for a generic x position have been explicitly represented.

Despite the fact that the voltage of each element (i.e. cell pairs and the two electrodes) can be different at each x position, the total voltage is a single parameter and represents the value that can be externally measured at the current collectors.

Finally, **the plant model** represents the highest hierarchy of simulation where a number of stack models can be variously arranged together with other auxiliary units.

3.1.4 Experimental CED unit setup

A 10×10 cm² bench-scale CED unit (*Deukum GmbH, Germany*), equipped with carbon capacitive electrodes with graphite current collectors (*FUJIFILM Manufacturing Europe B.V., The Netherlands*), operating in a single pass co-flow arrangement was tested. The stack was assembled with 10 cell pairs made by Type 10 ion exchange membranes (*FUJIFILM Manufacturing Europe B.V., The Netherlands*) whose main properties were already listed in Table 2, and 270 μm woven spacers (*Deukum GmbH, Germany*) [289]. CEM end-membranes have been placed in direct contact with the electrodes, so that only cations are involved in the formation of EDL at the electrodes. For this reason, during the operation one capacitor will accumulate cations while the other will desorb them. A schematic representation of the stack assembly is provided in Figure 28.

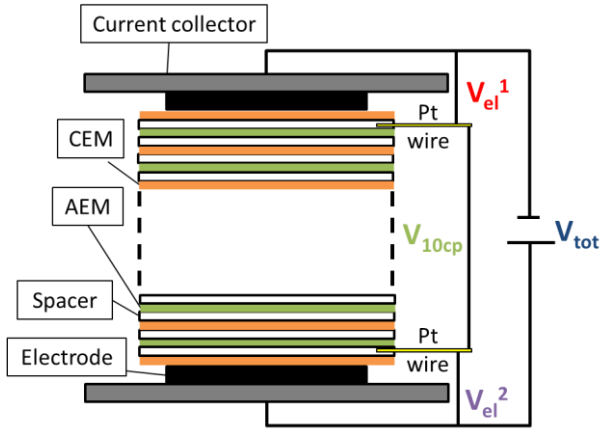

Figure 28. Schematic representation of the CED unit used for the experiments. V_{tot} ,V_{el}^1,V_{el}^2 and V_{10cp} indicates the experimentally measured voltage drops: overall voltage drop (V_{tot}), electrode 1 voltage drop (V_{el}^1), electrode 2 voltage drop (V_{el}^2), cell pairs voltage drop (V_{10cp}).

NaCl solutions at different concentrations (1, 3, 5 and 10 g/l) were pumped with a flowrate of ~ 490 ml/min (3 cm/s) through the stack using DC controlled diaphragm pumps controlled by flow meters (Krohne, Germany). Solution conductivities have been measured and continuously monitored both at the inlet and at the outlet through conductivity meters (LAQUA F-74, HORIBA *Ltd., Japan*)

The experiments were performed under galvanostatic conditions (constant current) by means of a power supply (PPS-11815, Voltcraft, *Germany*). Platinum wires of 0.2 mm diameter (Agar Scientific Ltd., UK) were used to measure the voltage drop over the membrane pile excluding the electrodes (V_{10cp}, as shown in Figure 28) and over the single electrodes (V_{el}^1 and V_{el}^2 from Figure 28). Voltages have been continuously measured and recorded through an acquisition system (M300, *Rigol Technologies Inc., U.S.*).

During a single galvanostatic test, a constant current has been maintained for a chosen time period in order to avoid complete saturation or desaturation of electrodes, and thus excessive electrode voltage and water splitting. At the end of the period, a polarity switch inverted the direction of the fixed current (Figure 29 a). The switches were repeated for a number of cycles in order to ensure the achievement of a regular periodic operation.

Figure 29 a shows an example of the electrical voltages measured during a typical experiment. Apart from V_{tot}, the graph depicts V_{el}^1, V_{el}^2 and V_{10cp}. It is worth noting that the voltages are always represented as voltage drops (so that $\sum V_i = V_{tot}$). Therefore, when a positive current (orange line) is applied, V_{el}^1 represents the voltage drop of the electrode that is adsorbing cations (and thus acting as a *passive* charging element), while the negative value of V_{el}^2 is representative of the electrode that is actively discharging and thus providing part of the current. The opposite happens when a negative current is applied.

From the V_{tot} *vs* time curves obtained from the experiments, it was possible to estimate the equivalent capacitance of the electrodes by means of equation (60):

$$\frac{dV_{tot}}{dt} = \frac{i}{c_{el}^{eq}} \tag{60}$$

where $\frac{dV_{tot}}{dt}$ is the slope of the overall voltage *vs* time curve (linear parts of V_{tot} curve as in Figure 29 b), i is the overall current and c_{el}^{eq} is the equivalent areal electrode capacitance, accounting for both capacitive electrodes. If the charging (or discharging) voltage curve of the two electrodes is almost equivalent, it can be assumed that their behaviour is the same. Consequently, the capacitance of a single electrode can be taken as twice as the value estimated from eq.(60). In the case of highly asymmetric behaviour (i.e. when two completely different electrodes are used at each side of the CED unit), the capacitance of the each electrode can be also deduced directly from the slope of each V_{el}^{j} voltage curve.

At a given feed concentration (which was assumed as the concentration inside the stack channels due to the high flowrate), the capacitance has been averaged over each value measured from positive and negative voltage curves. In addition, each experiment was repeated 2 to 3 times.

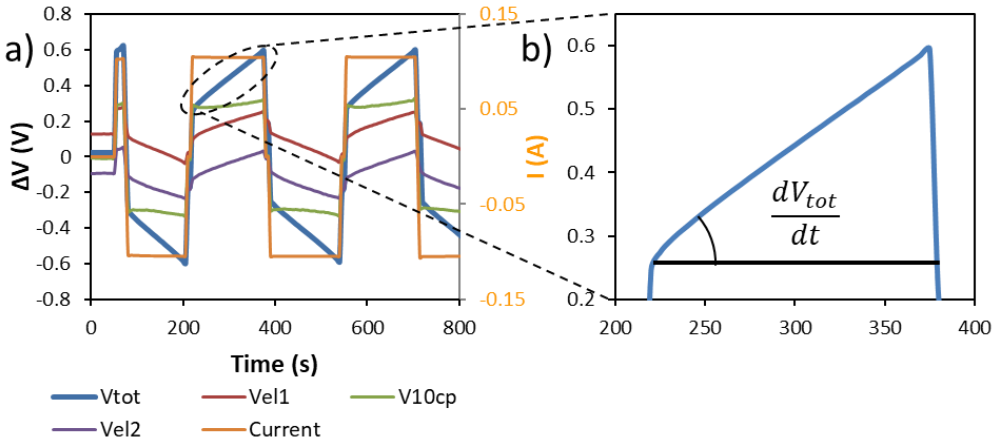

Figure 29. a) Representation of a typical experimental voltage vs time curve showing the overall voltage drop (V_{tot}), electrode 1 voltage drop (V_{el}^{1}), cell pairs voltage drop (V_{10cp}), electrode 2 voltage drop (V_{el}^{2}) and the applied current. b) Detail of a linear part of V_{tot} vs time curve used for the estimation of electrode capacitance. The graphs refer to a 1 g/l feed concentration and ±0.1 A, where positive or negative sign of the current indicates the two different polarities.

3.1.5 Experimental results and model validation

This section focuses on the experimental results from the bench scale CED units. In particular, the results from the experimental capacitance measurements and the comparison of simulation with the experimental data are shown.

i. In-situ experimental characterization of the capacitive electrodes

Figure 30 shows the specific capacitance per cm² of projected area estimated from the overall voltage versus time curves (c_{el}^{eq}) as a function of solution concentration. Error bars have been determined from the standard deviation of the outcomes of each repeated experiment. The slightly increasing trend of the capacitance can be explained by the formation of an electric double layer at the nanoscopic scale which is influenced by the amount of ions in the solution, as traditionally formulated by the Gouy-Chapman model of the diffuse EDL [405]. Given the common nature of the two electrodes of this specific unit (see section 3.1.4), the capacitance of a single electrode has been taken as twice the value reported in Figure 30 as discussed in section 3.1.4.

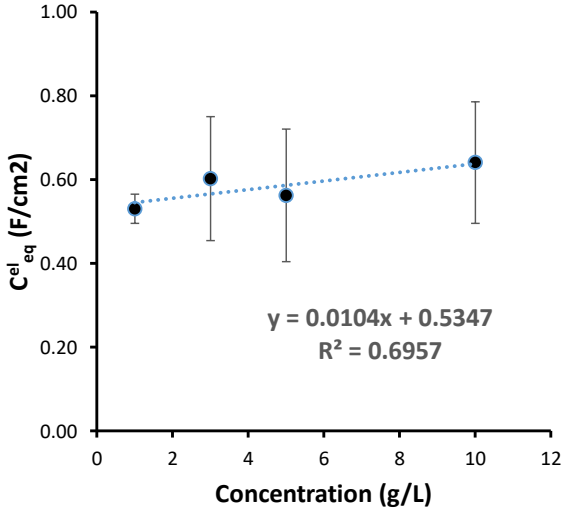

Figure 30. Measured specific overall electrodes capacitance (c_{el}^{eq}) as a function of solution concentration.

ii. Experimental characterization of the CED unit and model validation

The correlation of the capacitance *vs* the concentration obtained from the experimental results has been implemented into the capacitive electrode model of the CED process simulator in order to predict the behaviour of the experimentally characterised electrodes. Therefore, it was possible to assess the model reliability in simulating the operation of the CED unit by comparison with the experimental curves. *gProms Modelbuilde*r (*PSE, UK*) has been used as simulation platform.

Simulations were performed by applying the electrode open circuit voltages (i.e. measured when no current was flowing through the system) as initial condition. Those voltages are associated with the fact that a certain amount of charge is already

accumulated at the electrode surface. In addition, the value of the electrode ohmic resistance was calibrated from the instantaneous step voltage response of each electrode when the current is applied (Figure 31 c and Figure 32 c) and ranged from 50 to 100 Ω·m², based on solution concentration.

Figure 31 shows simulation results in comparison with the experimental data for the case of 10 g/l feed and ±0.15 A current. As shown, the process is actively desalinating one feed stream while concentrating the other (Figure 31 d). At a given polarity, the cell pair voltage stays constant as the desalination rate is kept constant by the applied current. On the other hand, the absolute value of V_{el}^{1} and V_{el}^{2} (Figure 31 c) grows in order to maintain the desired current. Interestingly, after the first two cycles the operation is quite stable and able to maintain the same performances for multiple cycles. Therefore, it seems realistic to imagine wider CED stacks (i.e. with larger active area) that can steadily desalinate a feed stream down to the drinking water concentration target.

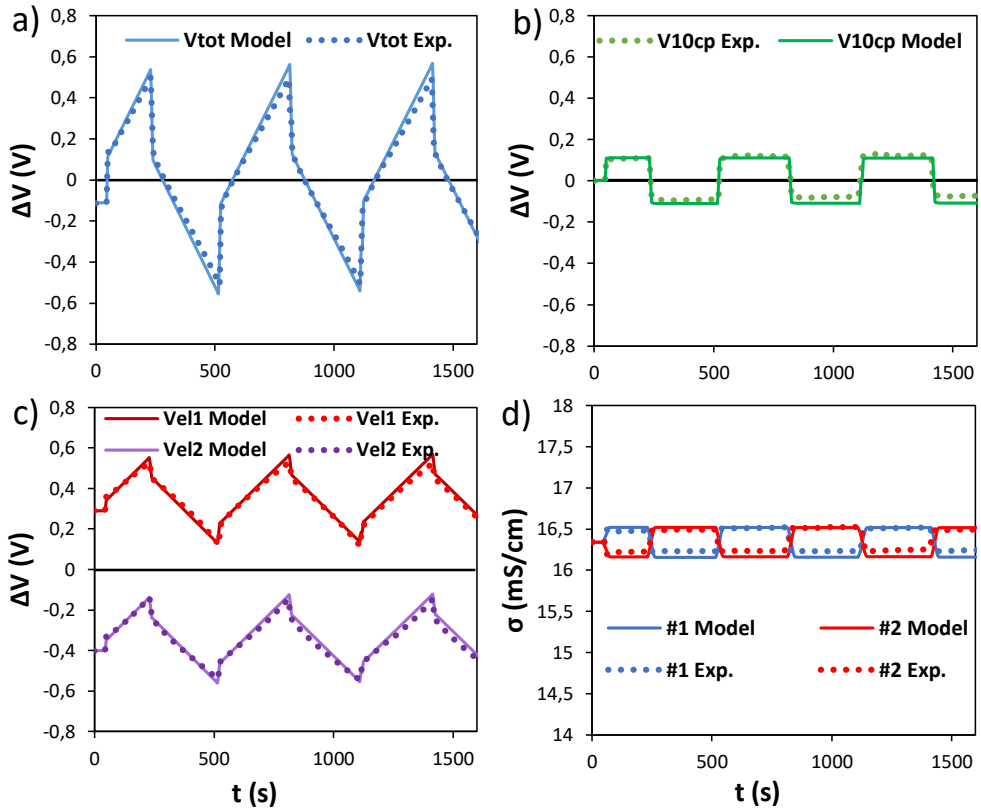

Figure 31. Model predictions compared with experimental data of a bench-scale 10×10 cm² CED stack equipped with 270 µm woven spacers and Type 10 FUJIFILM membranes. Inlet concentration of 10 g/l flowrate of 486 ml/min and applied current of ±0.15 A with polarity switches every ~280 s. a) Overall voltage drop, b) Cell pairs voltage drop, c) Electrodes voltage drop, d) outlet conductivity of the two compartments.

Other operating conditions have been tested through both experiments and simulations. For example, Figure 32 shows the case of 1 g/l of salt concentration and ±0.1 A current. Similarly to the previous case, the desalination capability has also been demonstrated for lower concentration feeds. The main difference is that in this case the cell pair voltage drop (Figure 32 b) is much higher compared to the one in Figure 31 b due to the lower solution conductivity. Consequently, shorter cycles have been performed in this case, despite the fact that the slope of the total voltage curve (Figure 32 a) is flatter due to the lower applied current.

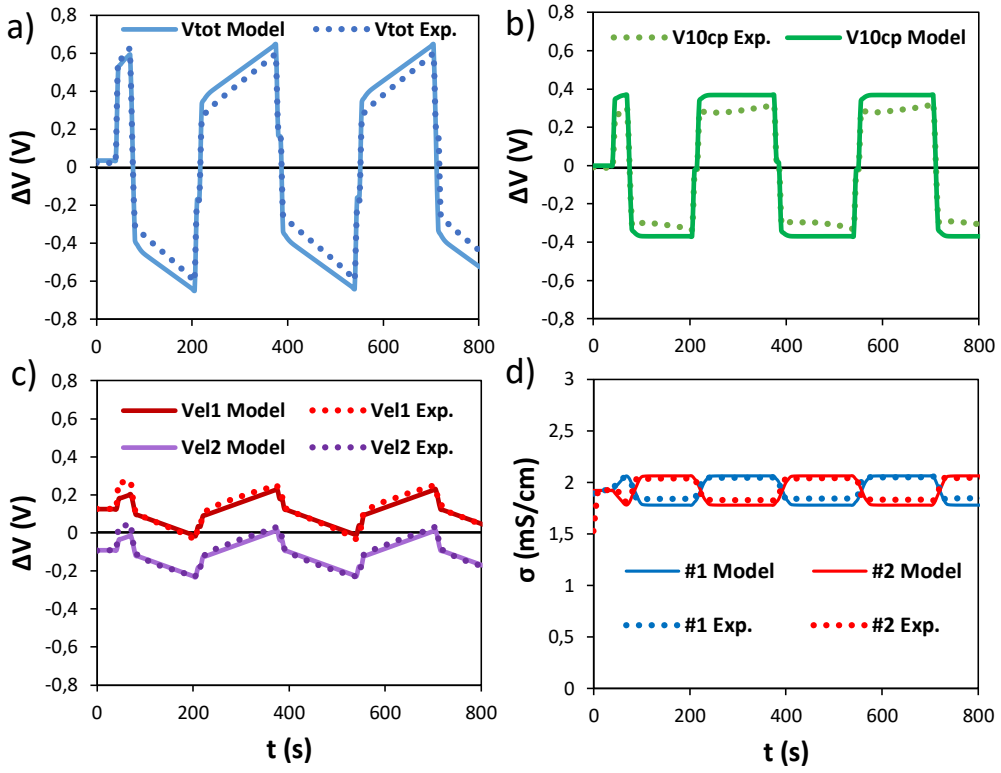

Figure 32. Model predictions compared with experimental data of a 10×10 cm² CED stack equipped with 270 µm woven spacers and Type 10 FUJIFILM membranes. Inlet concentration of 1 g/l, flowrate of 486 ml/min and applied current of ±0.1 A with polarity switches every ~180 s. a) Overall voltage drop, b) average cell pairs voltage drop, c) electrodes voltage drop, d) outlet conductivity of the two compartments.

In general, Figure 31 and Figure 32 demonstrate that the model has a good prediction capability at different operating conditions both for the voltage *vs* time curves, as well as for the outlet conductivities. However, the model shows a slight overestimation of the average cell pair voltage drop (Figure 32 b). This discrepancy can be attributed to the stack assembly. According to the scheme of Figure 28, the dimensions of the carbon electrodes are limited to the 10×10 cm² active area and no external gaskets are used to compensate for the localized increase of thickness that

takes place in the central part of the stack. Therefore, when the stack is closed, the electrodes apply a localized pressure on the active area of the membranes that are directly compressed over the spacer netting, reducing the real thickness of the channels and thus the channel Ohmic resistance. For low feed concentrations (as for the 1 g/l case) the resistance is higher and the difference between the real and the nominal value of the resistance increases the differences between the predicted and the measured voltage values.

3.1.6 Simulation of industrial scale CED

In this section, simulation results related to an industrial scale stack are reported. The aim of these simulations was to assess the influence of capacitive electrode capacitance, capacitive electrode resistance and number of cell pairs on the process performance.

i. Effect of electrode capacitance on single pass CED

In real scenarios, salty water feeds need to be desalted down to drinking water salt concentration. In order to apply the CED technology to those cases, larger units must be considered. In this context, the model is a suitable tool to analyse the process in wider and more industrially-relevant conditions.

Following the model validation, a single pass CED operation was simulated for a scaled-up configuration with 12 cell pairs and an active area of 12.5 (width) × 80 (length) cm^2. A resistance of 50 $\Omega \cdot cm^2$ has been attributed to the electrodes (see section ii). Starting from a reference case, the CED model has been used to assess the effect of the electrode features on the process performance.

The CED unit had to desalt a 2 g/l NaCl feed solution flowing with a linear velocity of 2 cm/s. This time, potentiostatic operations with a constant voltage of ±2 V have been simulated as this mode of operation is the most common in commercial applications. Multiple polarity switches were performed every 10 minutes (600 s). It is worth noting that the chosen switching time is not too far from the usual switching time of EDR plants (between 15 and 30 minutes). In order to simulate the CEM end membrane scheme, the electrode that is accumulating charge during the first cycle has a zero charge initial condition, while the opposite electrode is assumed to be pre-charged with a Q_{el} of 1 C/cm^2.

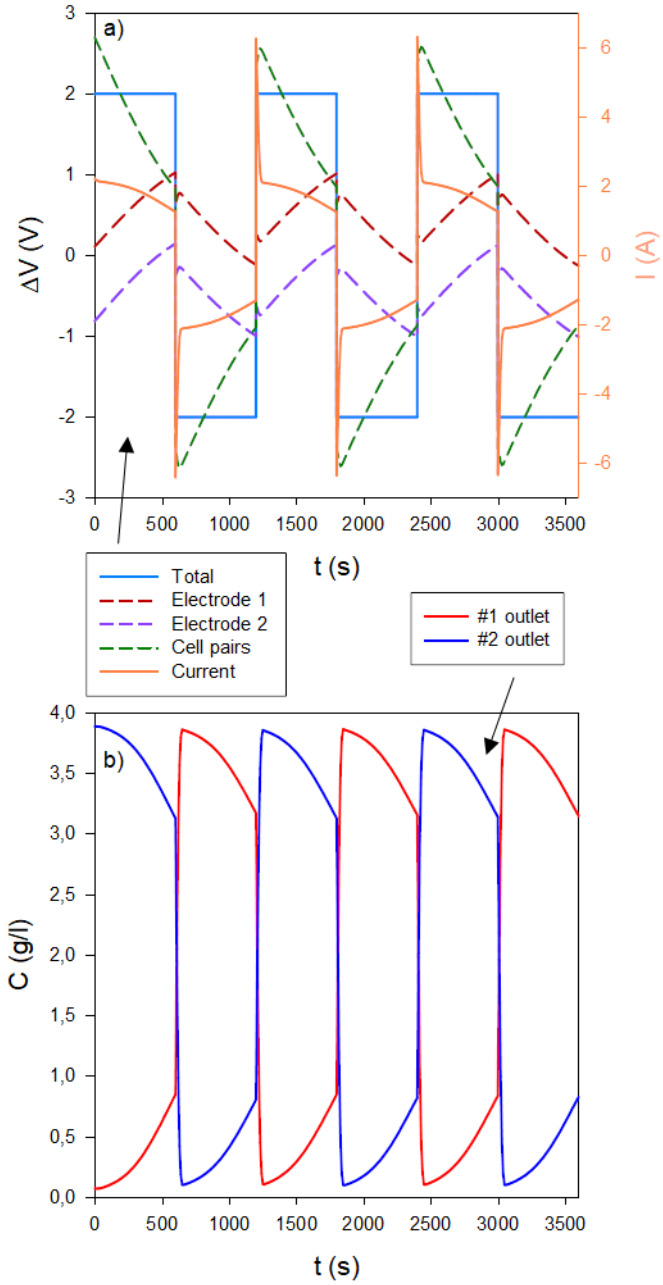

Figure 33. Simulation results of a single pass CED unit 12.5 cm wide and 80 cm long equipped with 270 µm woven spacers and FUJIFILM capacitive electrodes (RC circuit properties taken from experimental results). Inlet concentration of 2 g/l, linear velocity of 2 cm/s, and ±2 V of applied voltage with polarity switches every 600 s (10 min). a) Overall, electrodes and cell pair voltage drop and current vs time, b) outlet concentrations of the two streams vs time.

Simulation results are reported in Figure 33. In particular, Figure 33 a depicts the electrical variables as a function of time. At the beginning of a cycle, electrode 2 (i.e. the pre-charged one that is rejecting cations) is actively providing a voltage in addition to the external applied voltage (of 2V) that is higher than the actual electrode 1 voltage drop. Therefore, a voltage higher than 2 V is really applied to the cell pairs. However, during constant voltage operation, the electrodes' voltage changes, thus causing a decrease of (the absolute value of) the cell pairs' voltage. Because of this phenomenon, the overall current decreases, negatively affecting the desalination rate during a cycle and thus causing the diluate outlet concentration to increase up to 0.8 g/l at the end of the cycle, as shown in Figure 33 b.

The simulated reference case of CED operation would likely present some critical issues when replicated in a real unit. Firstly, the electrode voltage goes above 1 V in the last part of each cycle, meaning that unwanted faradic reactions (i.e. water splitting) may occur at to a large degree and damage at the electrodes may occur. In addition, the diluate outlet concentration increases well above the freshwater limit (set to 0.5 g/l, but usually taken even lower as a safety precaution). Therefore, with these electrodes shorter switching intervals would be required.

In order to avoid the aforementioned critical issues, maintaining the set switching interval or even extending it, the electrode should have an enhanced capacity. In this way, the electrodes' voltage would grow less through time, causing a slower drop in the overall current. The latter effect would also make an impact on the diluate outlet concentration slowing down its increase. In order to numerically evaluate the improvements, the effect of electrode capacitance on process performance has been assessed via simulations. In particular, the specific capacitance per electrode was increased from ~ 1.2 F/cm² for the reference case to 2 and 3.3 F/cm². In this sensitivity study, the two latter values of capacitance are taken as constant values (i.e. independent from solution concentration) for the sake of simplicity.

Simulation results are reported in Figure 34. Comparing the reference capacitance with 2 F/cm², the slope of the capacitive electrodes' voltage over time is already strongly reduced, thus not reaching the undesired 1 V threshold through the 600 s of constant polarity (Figure 34 a). In addition, desalination performances are also enhanced (Figure 34 b). At 2 F/cm², the diluate concentration goes only slightly over 0.5 g/l, achieving an acceptable result, as the outlet solution produced in the earliest part of the cycle (whose concentration was well below the limit) will be in the end mixed with the more concentrated solution exiting at the end of the cycle. Interestingly, a further increase in the capacitance up to 3.3 F/cm² does not provide a significant improvement to the voltage even though it still makes an impact on the outlet concentration.

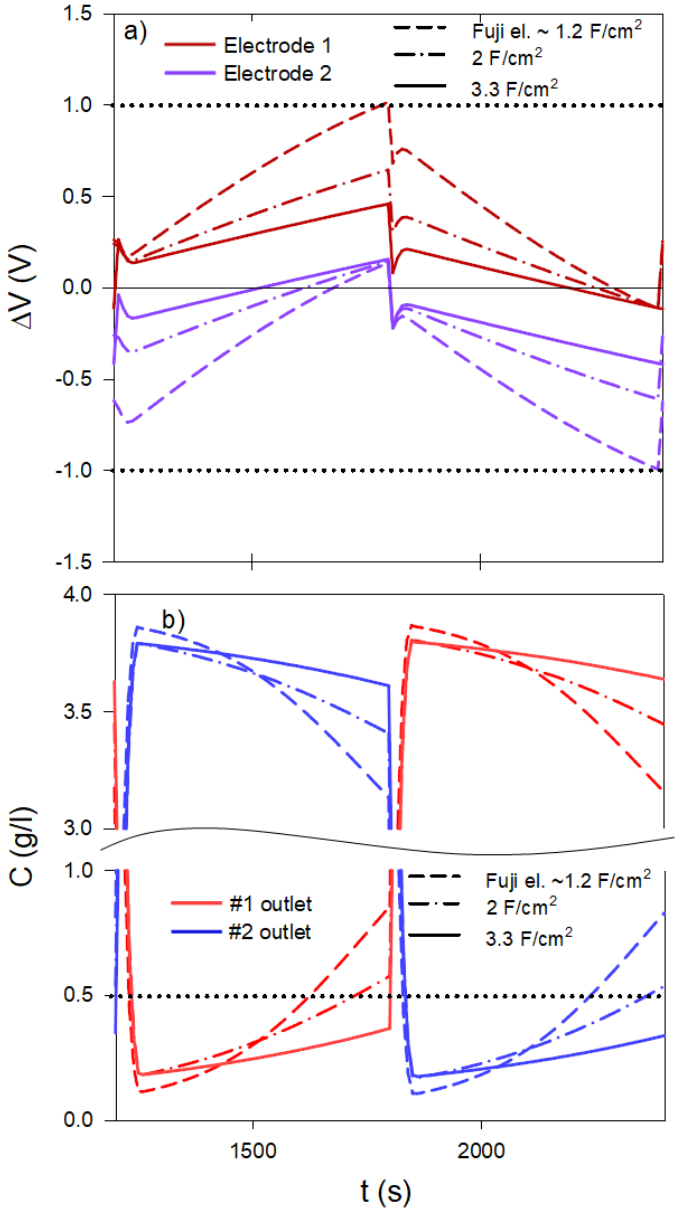

Figure 34. Simulation results for the comparison of different electrode capacitances (~ 1.2, 2 and 3.3 F/cm²) in a single pass CED unit 12.5 cm wide and 80 cm long equipped with 270 µm woven spacers and FUJIFILM capacitive electrodes (RC circuit properties taken from experimental results). Inlet concentration of 2 g/l, linear velocity of 2 cm/s, and ±2 V of applied voltage with polarity switches every 600 s (10 min). a) Electrodes voltage drop vs time, b) outlet concentrations of the two streams vs time.

ii. Effect of electrode resistance on single pass CED

The specific electrode resistance is another interesting parameter to analyse. The reference value of 50 Ω*cm² from the previous section has been compared with a doubled resistance (100 Ω*cm²) as well as with a halved one (25 Ω*cm²), maintaining the reference value of capacitance. Figure 35 shows the results in terms of electrode voltage and outlet concentration *vs* time. The increase in resistance causes a slight increase in the voltage as well as in the diluate concentration (due to a reduction in the stack current density). The reduction of the electrode resistance has the opposite effect. Nevertheless, the influence of the electrode resistance is almost negligible, as it is relatively small compared to the average Ohmic resistance of the 12 cell pairs amounting to ~ 500 Ω*cm². Consequently, a reduction in resistance does not lead to appreciable improvements of the process performance as an increase of capacitance does.

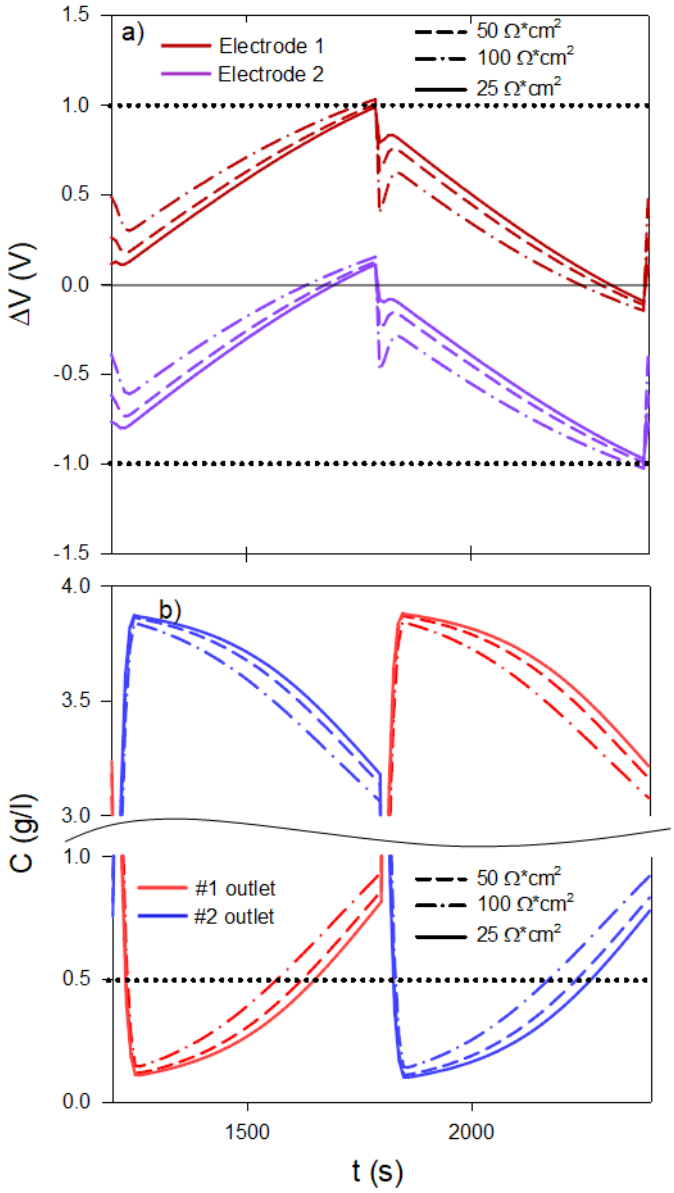

Figure 35. Simulation results for the comparison of different electrode resistances (25,50 and 100 Ω*cm²) in a single pass CED unit 12.5 cm wide and 80 cm long equipped with 270 μm woven spacers and FUJIFILM capacitive electrodes (RC circuit properties taken from experimental results). Inlet concentration of 2 g/l, linear velocity of 2 cm/s, and ±2 V of applied voltage with polarity switches every 600 s (10 min). a) Electrodes voltage drop vs time, b) outlet concentrations of the two streams vs time.

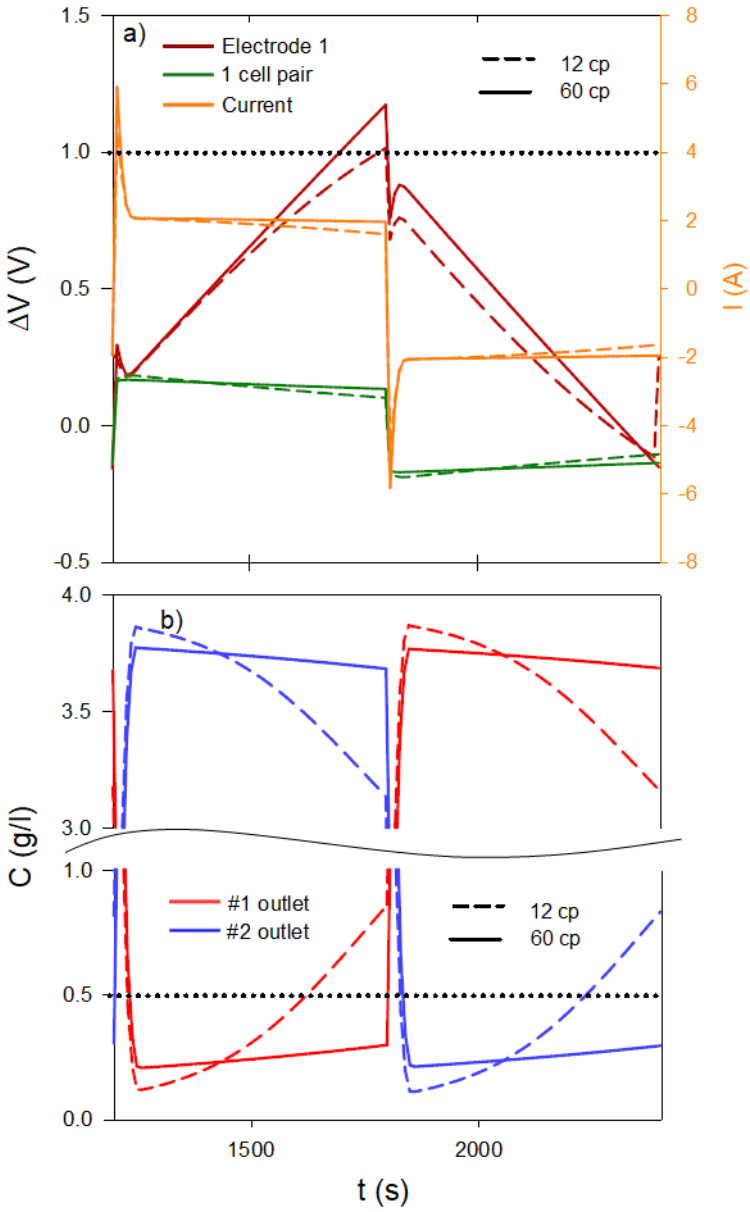

Figure 36. Simulation results showing the effect of a different number of cell pairs (12 and 60) in a single pass CED unit 12.5 cm wide and 80 cm long equipped with 270 µm woven spacers and FUJIFILM capacitive electrodes (RC circuit properties taken from experimental results). Inlet concentration of 2 g/l, linear velocity of 2 cm/s, and fixed voltage (±2 V for 12 cp, ± 9.45 V for 60 cp) with polarity switches every 600 s (10 min). a) Electrode1 and single cell pair voltage drop vs time and current vs time, b) outlet concentrations of the two streams vs time.

i. Effect of the number of cell pairs

The dynamic effects of capacitive electrodes on process performance (i.e. voltage, current and concentration *vs* time) shown in the previous subsections are also affected by the low number of cell pairs that have been simulated. In fact, an increase in the number of cell pairs can modify the impact that electrode properties have on the overall process. For this reason, the reference case has been replicated with a higher number of cell pairs.

Figure 36 shows the comparison between the reference case and a case where 60 cell pairs have been simulated. In order to set a comparable scenario, the total voltage has been fixed in a way that, at the initial condition (i.e. at 0 s), the voltage applied at each cell pair was equal for the two cases. As can be seen, the main effect of increasing the number of cell pairs is a reduction of the slope of the outlet concentration *vs* time (Figure 36 b). This trend can be explained by the fact that the more the cell pairs the smaller the electrode voltage compared to the voltage of the cell pairs. Consequently, with 60 cell pairs the electrode voltage changes through time almost does not affect the current curve that becomes flatter (orange curve from Figure 36 a) and also does the voltage drop of each cell pair (green curve from Figure 36 a). Of course, current and concentration curves would be perfectly flat for an infinite number of cell pairs. Another interesting consequence of the reduction of the current slope is the increase of the electrodes' voltage slope (only V_{el}^{1} is depicted in Figure 36 a as V_{el}^{2} is qualitatively the same) as they are subjected to a higher average current. As can be deduced from previous discussions, the two limiting factors that cause the need to reverse polarity in CED operations are the excessive salinity of the dilute stream and the reach of the threshold value of the electrode voltage. Considering the effects on the outlet concentration and on the electrode voltage it can be observed that with increasing number of cell pairs, a progressive shift from the concentration limiting condition to the voltage limiting condition occurs.

3.2 Electrodialysis as energy buffer in polygeneration systems

The second case of dynamic modelling is presented in this chapter. The presence of desalination systems in polygeneration facilities has been usually limited to either thermal processes or reverse osmosis, characterised by important difficulties in operating under non-stationary regimes. As an alternative, the possibility of using electrodialysis coupled with a hybrid photovoltaic/wind energy source was investigated in this work. In particular, while solar energy is mainly available in summer and during central hours of the day, wind energy is mainly available during night hours and winter. Therefore, the combination of photovoltaic and wind energy is very attractive in order to achieve a more stable energy production. Dynamic scenarios were analysed by means of a process model, looking at two different time scales. Quasi-steady state simulations were used to study the yearly operation, demonstrating process flexibility over a power input variation of one order of magnitude (5-45 kW). Dynamic simulations were adopted to study the daily time scale of the process, where the desalination unit control system was able to maintain a stable target value (± 10% of the outlet concentration) in the presence of

disturbances in power availability. Simulation results show how the process is particularly suitable for the integration within polygeneration systems as energy-buffer.

3.2.1 State of the art

Desalination units can generally be part of polygeneration facilities. Waste heat from thermal power plants has been used to successfully run thermal desalination plants [406] or to preheat salt water feeds [407]. In this context, polygeneration systems that use renewable sources such as photovoltaic (PV) or wind turbines represent a promising scenario [408]. In these cases, desalination technologies can be particularly attractive as means of using the excess energy that renewable sources produce during peak periods, producing drinking water instead of using energy storage devices such as batteries [409].

One of the main issues related to the use of renewable polygeneration systems consists in the unpredictability of the energy source. The unavoidable fluctuations of many renewable energy sources (wind, solar, etc.) make extremely difficult to suitably couple these systems with the cooling, heating and electrical demands of the users [410]. In this framework, many researchers investigated several storage technologies (both thermal and electrical) in order to achieve a more stable power supply profile [411]. However, such storage technologies are still too expensive for a good economic profitability. Therefore, some researchers are focusing on innovative solutions such as coupling renewables and desalination systems [412–418]. Simultaneously, many authors are focusing on specific combinations of renewable energy sources in order to mitigate the fluctuations typical of using individual renewable energy sources. For example, the combination of solar and wind energy is extremely promising. In fact, solar energy is mainly available during the summer and in the central hours of the day. Conversely, according to the weather data, wind velocity increases in winter and during the night. Therefore, combining photovoltaic solar energy and wind energy the stability of power production profile can be increased.

The possibility to couple desalination systems with renewable energy sources has been already demonstrated in the literature. Given the wider commercial diffusion of reverse osmosis (RO) among desalination technologies, a lot of works focus on this process. In particular, process feasibility has been studied and proven for PV-RO [419–427], wind-RO [428,429] and combined PV and wind-RO systems [430]. A number of these works highlight how the economic feasibility of such processes can be enhanced using battery-less power sources, as batteries are associated to a number of disadvantages such as increased capital costs, limited lifetime and increased maintenance [422,429]. Nevertheless, when desalination units are coupled with battery-less systems they are directly subjected to the fluctuation of power generation, requiring real-time adjusting. Thomson et al. [426,427] demonstrated the possibility to apply such systems to RO from both modelling and experimental perspective. However, the authors (as well as Manolakos et al. in another work [419]) highlighted that long term reliability of the system is not guaranteed due to the continuous high pressure fluctuation experienced by

membranes. An alternative to compensate for the power fluctuation, by modifying the production capacity without significantly affect the pressure, is the use a number of parallel RO plants that are switched on or off based on the amount of energy available [428]. Nevertheless, this generally implies a system oversizing and an increase in capital costs. Besides the aforementioned issues, RO systems also suffer from relatively slow and critical start-ups and shutdowns where a gradual increase/decrease in system pressure is required before reaching the steady-state [428].

On the other hand, experimental investigation on ED systems working with renewable energy sources is ongoing since few decades ago [431,432]. In general, ED can overcome most of the drawbacks that result from dynamic RO operations. A change in the available power input can be easily adjusted by changing the applied voltage and by changing the feed flowrate without the need for particular adjustments, as low pressures (usually < 1 barg) are involved in the process. Another advantage is that transient phases during start-ups and shutdowns are much shorter. Conversely, the main issue that has been highlighted refers to an increased energy consumption due to the presence of harmonic disturbances that can be mitigated through filters [428]. For these reasons, ED is particularly suitable for battery-less systems. In this context, Malek et al. [433] showed a successful experimental coupling of batch ED with direct wind energy, demonstrating how the system is insignificantly affected by moderate wind fluctuations. Similarly, Ortiz et al. [434–436] proved the operation of a batch PV-ED system through experiments and simulations in the scale of hours. In addition, from cost estimations, PV-ED resulted more convenient than PV-RO in presence of low salinity feeds [420].

As already highlighted, most of the works on ED coupled with renewable sources focus on the experimental proof of concept, on coupled process design or on economic analysis. In fact, attention to the detailed process dynamics is mostly paid only in the case of batch ED, where the effect of power fluctuations on the product quality are strongly dampened by the presence of recirculation tanks. Therefore, the aim of the present work was to study the dynamics of a single pass ED unit powered by a hybrid PV/wind power source in order to prove the flexibility of ED in maintaining drinking water specifications while changing process conditions, assessing the suitability for integration within poly-generation systems as energy-buffer. In particular, the analysis was performed by means of process simulations, focusing on two different time-scales. The first one is the yearly operational time scale, where quasi-stationary operation of ED allows for a step by step re-adaptation of working parameters in order to generate a stable output target with the available energy input. The other one is the short time scale of transient regimes of the desalination unit, where the intrinsically dynamic behaviour of the unit was modelled to predict the response to fast disturbances in energy availability. At this scale, a control system was also designed and implemented.

3.2.2 Model description

The overall simulation model was implemented by a hybrid approach combining a well-known dynamic simulation tool, TRNSYS [437] , and a user-developed model. In particular, the model for the solar/wind system is developed in TRNSYS by using weather data from Pantelleria, and conventional components included in TRNSYS library (PV panels, wind turbine, inverter, controllers, etc). The overall electrical production calculated by TRNSYS is subsequently provided as an input data to the user-developed model, simulating the ED subsystem implemented into *gPROMS Modelbuilder*. In the followings, the main algorithms of the models are briefly presented

i. PV Panels

In order to simulate the PV panels, the four parameter model was used. It assumes that the slope of the IV curve is zero at the short-circuit condition:

$$\left(\frac{dI}{dV}\right)_{v=0} = 0 \tag{61}$$

The four parameters included in the model are: $I_{L,ref}$ (module photocurrent at reference conditions), $I_{o,ref}$ (diode reverse saturation current at reference conditions), γ (empirical PV curve-fitting parameter), R_s (module series resistance). The software uses parameters values from manufacturers' data in order to generate an IV curve at each time step.

The current-voltage equation of the circuit is:

$$I = I_{L,ref}\frac{G_T}{G_{T,ref}} - I_o\left[\exp\left(\frac{q}{\gamma_{PV}kT_c}(V + IR_s)\right) - 1\right] \tag{62}$$

The diode reverse saturation current I_o is a temperature dependent function, such as:

$$\frac{I_o}{I_{o,ref}} = \left(\frac{T_c}{T_{c,ref}}\right)^3 \tag{63}$$

Once I_o is obtained, the Newton's method is employed to calculate the PV current, whereas an iterative search routine finds the current (I_{mp}) and voltage (V_{mp}) at the point of maximum power along the IV curve. To solve the four equivalent circuit characteristics, current and voltage at open-circuit, short circuit, and maximum power conditions are substituted into eq.(62), yielding, after some rearrangement, to equations (64)-(66), related to $I_{L,ref}$, $I_{o,ref}$, γ_{PV}:

$$I_{L,ref} \approx I_{sc,ref} \tag{64}$$

$$\gamma_{PV} = \frac{q\left(V_{mp,ref} - V_{oc,ref} + I_{mp,ref}R_s\right)}{kT_{c,ref}\ln\left(1 - \frac{I_{mp,ref}}{I_{sc,ref}}\right)} \tag{65}$$

$$I_{o,ref} = \frac{I_{sc,ref}}{\exp\left(\frac{qV_{oc,ref}}{\gamma_{PV} k T_{c,ref}}\right)} \tag{66}$$

A fourth equation, derived by taking the analytical derivative of voltage with respect to temperature at the reference open-circuit condition, is needed in order to determine the last unknown parameter:

$$\frac{\partial V_{oc}}{\partial T_c} = \mu_{voc} = \frac{\gamma_{PV} k}{q}\left[ln\left(\frac{I_{sc,ref}}{I_{o,ref}}\right) + \frac{T_c \mu_{isc}}{I_{sc,ref}} - \left(3 + \frac{q\varepsilon G}{\frac{\gamma_{PV}}{N_M} k T_{c,ref}}\right)\right] \tag{67}$$

This analytical value is matched to the open circuit temperature coefficient (manufactures' specification). Finally, an iterative search routine is followed to calculate the equivalent circuit characteristics.

ii. Wind turbine

The model calculates the power output P of the WT through the power coefficient of WT, c_p, multiplied by the area of the rotor and the wind power, as reported in eq.(68):

$$P = \rho c_p A_r {v_{wind}}^3 = \rho 4a(1-a)^2 A_r {v_{wind}}^3 \tag{68}$$

here, v_{wind} is the wind speed (m/s), A_r is the rotor area (m²) and ρ is the air density (kg/m³). The c_p is a function of the axial induction factor, a, and its maximum value of 59.3%, obtained for a = 1/3, was first derived by Betz in 1919 (known as Betz's limit).

The WT power calculation is based on a power versus wind speed characteristic (Figure 37), provided by the manufacturer.

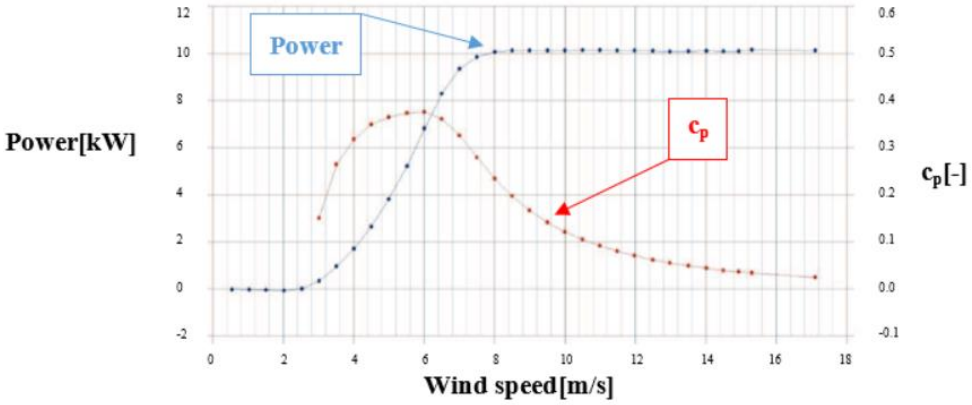

Figure 37. Power (left) and c_p (right) versus wind speed characteristic curve.

This model takes into account the air density changes and wind speed increases with height above the ground (elevation). Air density at a certain elevation is a function

of the combined effects of pressure and temperature, according to the ideal gas law, and it is calculated as:

$$\rho_{elev} = \frac{p_{elev}}{RT} \tag{69}$$

Regarding the variability of the temperature as a function of the elevation, the temperature "lapse rate" is also considered as shown in eq.(70):

$$T(z) = T_0 - Bz \tag{70}$$

where B = 6.5 K/km of altitude and T_o= 288K.

The change in wind speed per change in height above the ground is based on the theoretical work of Von Karman [438]. Here, the relation between the elevation and the wind speed is formulated as follows:

$$\frac{v_{wind,1}}{v_{wind,2}} = \left(\frac{z_1}{z_2}\right)^{\alpha_w} \tag{71}$$

A single parameter, α_w, determines the rate of wind speed increase as a function of height. Under ideal boundary layer conditions, the value of α_w is 1/7 (0.14). However, under actual conditions, the value of α_w constantly varies, and depends on a plurality of factors, affecting vertical turbulence intensity (surface roughness, mountains, buildings, atmospheric stability, etc.).

Table 6. Main design parameters of wind turbine and PV panels.

	Parameter	Description	Value	Unit
PV PANELS	$A_{module,PV}$	PV module area	1.609	m^2
	$P_{module,PV}$	Unit peak power	260	W
	$I_{sc,ref}$	Module short-circuit current at reference conditions	6.50	A
	$V_{oc,\,ref}$	Module open-circuit voltage at reference conditions	21.6	V
	$T_{c,\,ref}$	Reference temperature	298	K
	$G_{T,ref}$	Reference insolation	1000	W/m^2
	$V_{mp,ref}$	Module voltage at max power point and reference conditions	17	V
	$I_{mp,ref}$	Module current at max power point and reference conditions	5.9	A
	μ_{Isc}	Temperature coefficient of I_{sc} at (ref. condition)	0.02	A/K
	μ_{voc}	Temperature coefficient of V_{oc} (ref. condition)	-0.079	V/K
	$T_{c,\,NOCT}$	Module temperature at NOCT	313	K
	$T_{c,\,ref}$	Ambient temperature at NOCT	293	K
WIND TURBINE	z	Site elevation	205	m
	H	Data collection Height	18	m
	H_{hub}	Hub height	10.2	m
	N_{WT}	Number of turbines	1	-
	P_{WT}	Wind turbine rated power	10	kW
	v_{rated}	Wind turbine rated speed	6.5	m/s
	$v_{cut,in}$	Cut-in speed	2.6	m/s
	$v_{cut,off}$	Cut-off speed	16	m/s

iii. Electrodialysis

The ED model is the same presented in chapter 2, properly modified in its lowest hierarchy to account for process dynamics. Therefore, eqs. (27)-(28) are substituted with the dynamic mass balance (eq. (58)) that was already discussed in section 3.1.3. For the sake of this work, the overall plant model is characterised by the stack model

coupled with a variable power source and a control unit (Figure 38). The details of the controller equation, as well as its design and tuning are discussed in the control design section (3.2.4).

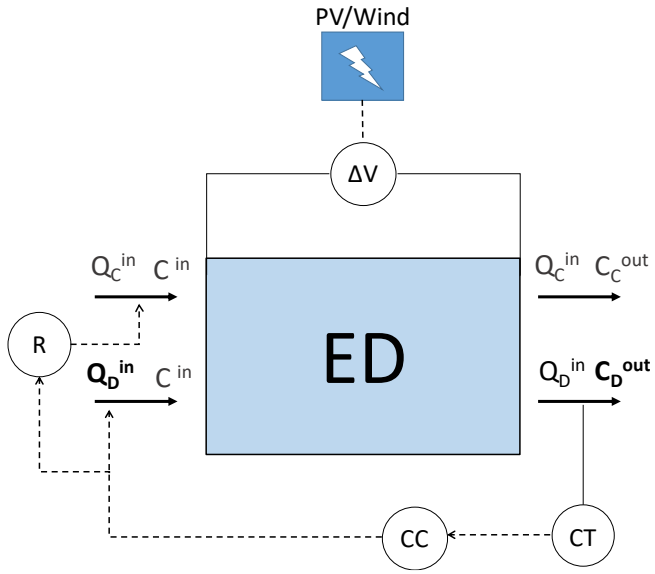

Figure 38. Block diagram of the highest hierarchy of the model (the plant) representing an ED unit powered by the PV/wind power delivery system. The concentration control system that operates on the feed flowrate is included.

3.2.3 Long timescale simulations

The aim of this work was to simulate an ED unit powered by a hybrid PV/Wind energy source. In particular, the energy system includes a 20 kW wind turbine and a PV array with a peak of power production of about 25 kW, for a total peak power production of about 45 kW. The energy supply system was simulated over an entire year.

The ED plant is composed by 4 equal stacks operating in parallel that have to desalinate a feed stream of 5g/l NaCl concentration down to 0.25 g/l with 67% recovery (i.e. the diluate to concentrate feed flowrate ratio is always kept constant to 2:1, as indicated in Figure 38) . Stacks' specifications are listed in Table 7.

Table 7.List of the main characteristics of each simulated stack.

L (cm)	b (cm)	N_{cp}	δ_{SOL} (μm)	Type of membranes	R_{blank} (Ωcm^2)
50	50	500	270	FUJIFILM Type 10	3

At nominal conditions, the plant works with ~80% of the peak power (34 kW), producing 800 m^3/d (200 per stack) of drinking water. However, the actual diluate flowrate changes according to the available power, in order to keep a constant outlet concentration. Based on feasibility conditions, upper and lower limits were set in each stack for the diluate flowrate. In particular, the maximum diluate feed flowrate was set according to the maximum allowable pressure drop that has been set to 1.2 bar, corresponding to 920 m^3/d (230 m^3/d per stack) and 43 kW of absorbed power. Conversely, the minimum allowable flowrate was set to ~ 230 m^3/d (58 m^3/d per stack) and 5 kW of absorbed power, where the current required to reach 0.25 g/l is already 90% of the estimated limiting current [237]. Further reduction in the diluate feed flowrate would cause limiting current issues and thus an impossibility to reach the target concentration.

According to the aforementioned limits, the ED system was simulated assuming that the applied voltage was changing depending on the power produced by the energy system over the entire year. The boundaries were taken into account, so that if the available power is higher than the upper limit the plant does not use all of it. Conversely, when the power is lower than the minimum the system is switched off. Given the long time scale, a quasi-steady state approach was adopted for these simulations.

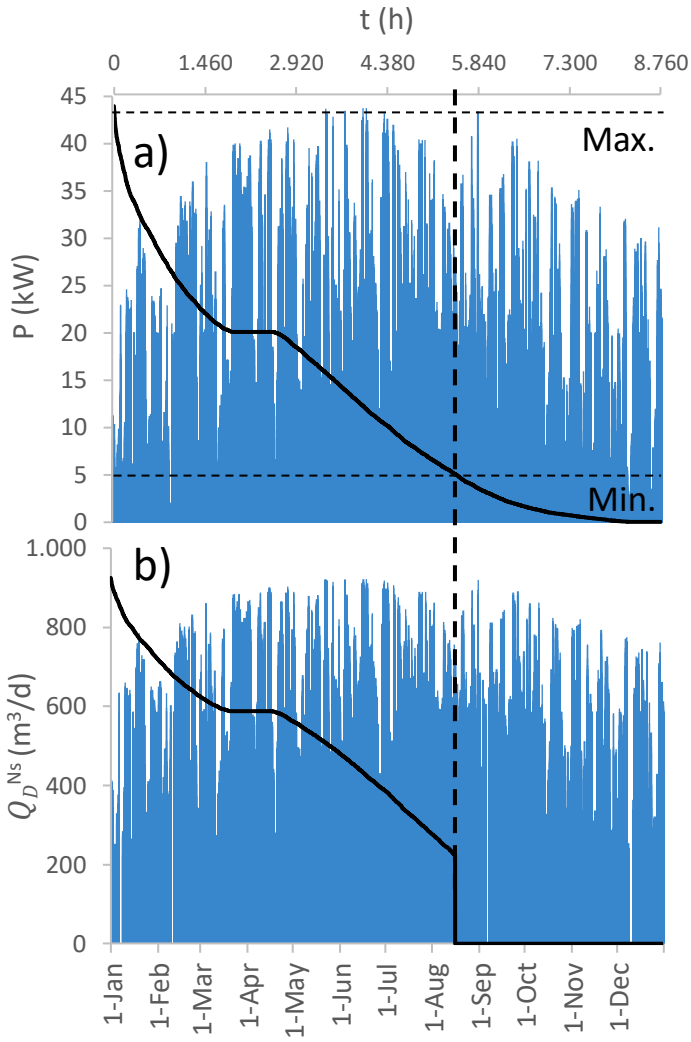

Figure 39. a) Simulated yearly power production for the coupled PV/Wind energy source, b) Simulated inlet diluate flowrate fed to 4 ED units operating in parallel. ED units specifications: 50x50 cm2, 500 cell pairs, 270 µm spacers and FUJIFILM Type 10 membranes.

Figure 39 a, shows how much the overall power can be different during the year (according to weather data from Pantelleria). In particular, peaks are clearly more frequent in summer months, when the PV system has more solar radiation available. Produced power goes slightly down in the other periods of the year, even though the wind turbine partially compensates the reduction of solar radiation.

Figure 39 b, shows the diluate feed flowrate of the ED plant (Q_D^{Ns}). As expected, the plant can adapt the feed flowrate to the produced power, and thus generating different amounts of drinking water. Interestingly, the set maximum and minimum

flowrate boundaries do not excessively influence the power utilisation on the yearly time scale. In fact, the plant never goes off for long periods except for few phases during winter months, while only very few power peaks are not entirely used during the summer. Figure 4 also shows cumulative curves (black continuous lines) that gives an estimation of the total amount of hours in which power or flowrate were maintained above a certain value. From these curves it can be seen how the plant stays on for more than 5500 (non-continuous) hours during the entire year. In addition, it is interesting to note that the specific energy consumption decreases while reducing the feed flowrate. This is to be attributed to the operating conditions that are closer to reversibility when the applied voltage is small.

3.2.4 Control system design and tuning

As the ED unit is powered by a variable power source (i.e. the coupled PV/Wind plant) the actual energy that is available for the desalination process and, thus, the external applied voltage will change over time. The desalination unit has to maintain the outlet concentration of the drinking water at the target value. Therefore, a control system is required in order to adapt continuously the feed flowrate to ensure that the outlet specifications are met. For this reason, the system dynamics was first studied with the aim of defining transfer functions, which link the inlet variables (i.e. feed flow rate and applied voltage) to the outlet variables (i.e. the product concentration) and can be assumed as simplified mathematical descriptions of the nonlinear process. The results of this analysis was then used to define the control strategies and tune the controller. For the sake of simplicity, the control loop takes into account only process dynamics, neglecting other contributions such as the regulation valve.

i. Uncontrolled process dynamics

In order to study the process dynamics, it is necessary to characterise the behaviour of the process under transient regime when the manipulation variable (i.e. the flowrate) shifts from the stationary value. Given the nature of the process under study, it is not possible to define a unique reference stationary value, as this will depend on the available power. Therefore, three reference scenarios were chosen, so that it was also possible to assess how the dynamics changes with the starting condition. In particular, the maximum and the minimum allowable flowrates (as discussed in the long time scale simulation section) as well as the average flowrate have been taken as a reference. In each scenario, the flowrate has been either increased or decreased by 20% through a step change.

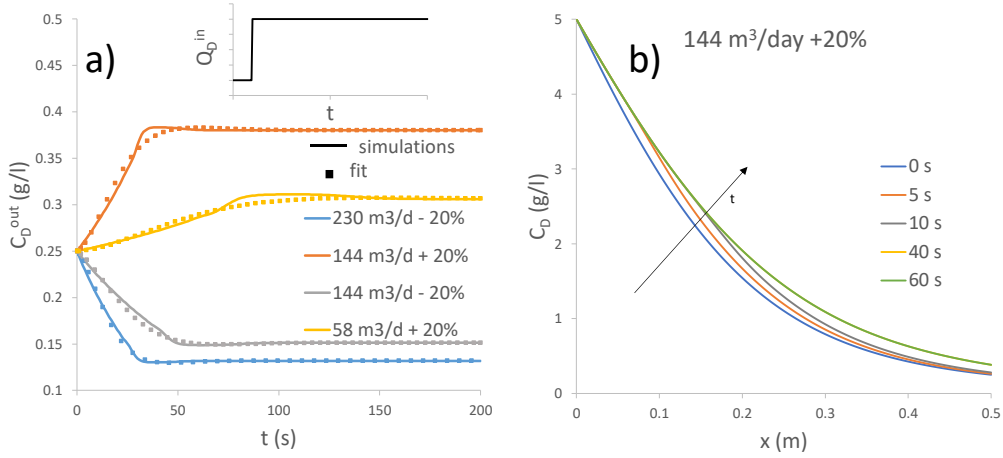

Figure 40. a) Outlet diluate concentration vs. time for a 20% step change in the feed flowrate at different initial diluate flowrates, b) Spatial profile of the outlet diluate concentration at different times for a 20% flowrate step increase starting from 144 m³/d. Results refer to a 50x50 cm² ED unit equipped with 500 cell pairs, 270 µm spacers and FUJIFILM Type 10 membranes.

Figure 40 a shows time profiles of the diluate outlet concentration after the step change. At each steady state flowrate, the voltage is set in order to reach 0.25 g/l. Therefore, when the flowrate increases or decreases, the concentration will reach a new steady state with a higher or lower concentration respectively, requiring a certain time that depends on the flowrate itself. When the flowrate is suddenly changed, the spatial concentration profile in each channel will have to adapt to the new situation (see Figure 40 b), requiring a mutual interaction between each adjacent discretisation interval, through which a certain volume of solution is flowing. Therefore, the resulting dynamic is given by a number of "virtual" processes that occur in sequence and results in a high-order behaviour. However, for the sake of simplicity, each of the curves of Figure 40 a was fitted with a second-order transfer function with a zero that, in the Laplace domain is expressed as:

$$G(s) = \frac{K\,\tau_0 s + K}{s + 2\zeta\tau s + 1} \tag{72}$$

where K is the process gain, τ_0 is the time constant of the transfer function numerator, τ is the process time constant, ζ is the damping coefficient and s is the independent variable in the Laplace domain. Each fitting curve from Figure 40 a was characterised by its own parameters according to eq. (72).

ii. Feedback control design

The aim of the feedback control is to keep the target concentration by adjusting the feed flowrate, according to equation (73):

$$Q_D^{in,tot}(t) = K_C\left(\varepsilon + \frac{1}{\tau_I}\int_0^t \varepsilon\, dt + \tau_D \frac{d\varepsilon}{dt}\right) + Q_{D,\,ss}^{in,tot}(t) \tag{73}$$

where K_C is the control gain, ε is the error (i.e. the difference between the concentration set point and the actual concentration), $Q_D^{in,tot}$ and $Q_{D,ss}^{in,tot}$ are the actual and the steady state diluate flowrate (i.e. the bias) entering inside a stack and τ_I and τ_D are the integral and derivative time constants of the controller. The controller equation written in this form includes proportional, integral and derivative actions.

In order to design an effective and robust controller for the process under study, it is required to identify the best set of parameters (i.e. K_C, τ_I and τ_D). Among the different design methods, the internal model control (IMC) was used to estimate controller parameters [439]. With the IMC method, it was possible to estimate a first set of control parameters for each reference scenario from the fitted process transfer functions previously identified (Figure 40 a). These parameters were then averaged and finely tuned with a trial and error procedure by simulating the response of the controlled system to step voltage changes on *gPROMS Modelbuilder*. The final values are reported in Table 8.

Table 8. Final values of control parameters.

K_C (m^3 l/ g s)	τ_I (s)	τ_D (s)
0.01	30	15

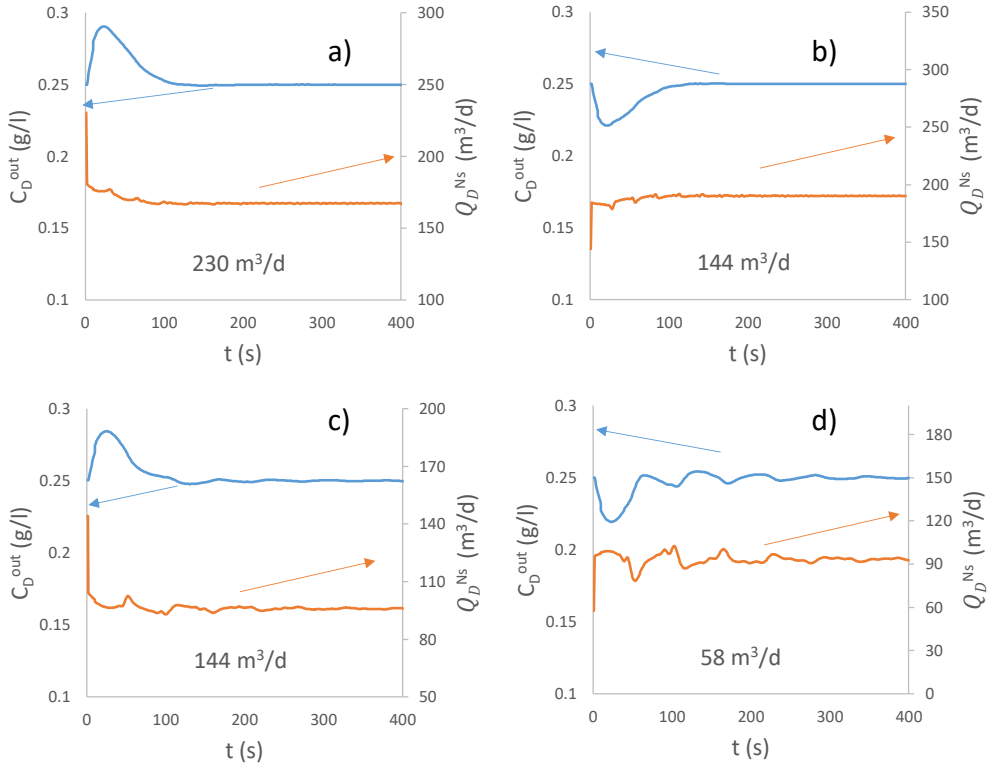

Figure 41. Dynamic ED response of the controlled and the manipulated variables (PID feedback controller) for a voltage step change at different initial diluate feed flowrates. a) 230 m³/d, 20% voltage decrease, b) 144 m³/d, 20% voltage increase, c) 144 m³/d, 20% voltage decrease, d) 58 m³/d, 20% voltage increase. Unit specifications: 50x50 cm², 500 cell pairs, 270 µm spacers and FUJIFILM Type 10 membranes.

Figure 41 shows simulation results for the controlled ED stack for each reference flowrate. At the maximum flowrate, the system is subjected to a 20% step decrease of the applied voltage (Figure 41 a), the opposite happens for the minimum flowrate (Figure 41 d), while at 144 m3/d both an increase and a decrease of the applied voltage were analysed (Figure 41 b and c). As can be observed, going from the highest to the lowest flowrate (and thus decreasing the channel velocity), the oscillations of the outlet concentration around the stationary value become more persistent and take more time to settle, even though they are still at an acceptable value. This can be explained by the transient behaviour of the system that changes significantly from high to low flowrates, according to the dynamic responses already shown in Figure 40 a. Besides, a slower response is expected at lower residence times as the process itself needs more time to adapt to the disturbance. It is worth noting that the derivative term was included in the controller in order to dampen the oscillations of the outlet concentration generated by the proportional-integral action of the controller. In particular, excessive decrease in the concentration may cause limiting current issues.

iii. Feed Forward control design

Given the measurable nature of the main disturbance to the process, namely the available power/voltage at the ED unit, also a Feed Forward (FF) and a hybrid FB-FF controller were designed and tested via simulations. In order to adapt the controller to the strong non-linear behaviour of the process, average gain and time constants were adopted for the design of the controller, leading to a unified law for the FF controller.

The same scenarios adopted for the analysis of the FB controller performance were chosen in this case and results are reported in Figure 42 for the stand-alone FF controller and in Figure 43 for the hybrid FB-FF one.

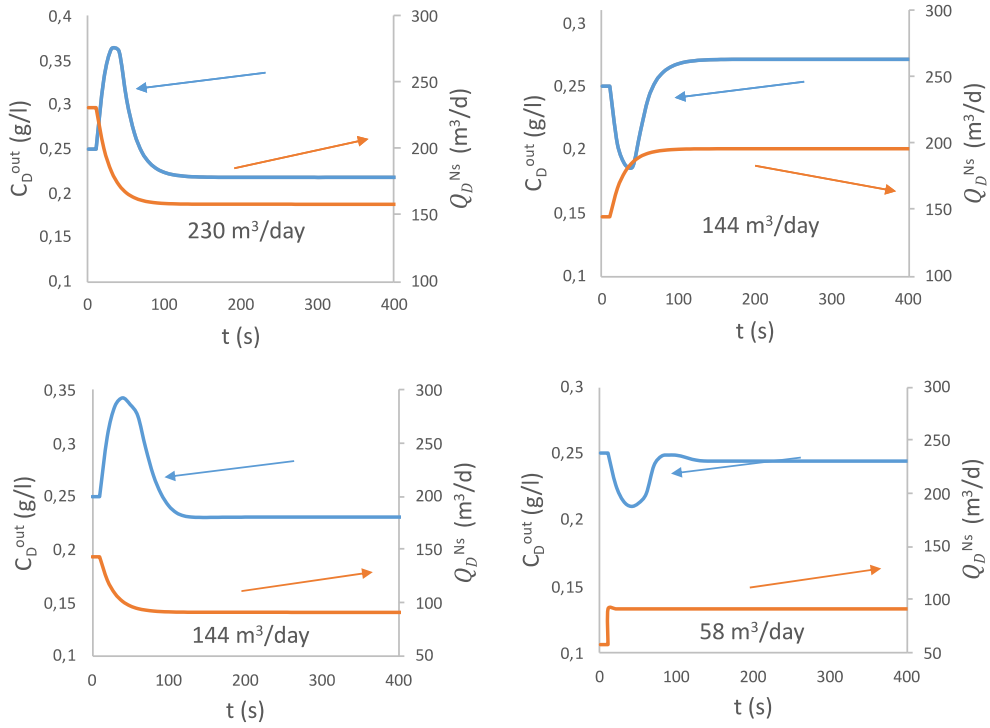

Figure 42. Dynamic ED response of the controlled and the manipulated variables in the case of a stand-alone Feed Forward controller for a voltage step change at different initial diluate feed flowrates. a) 230 m³/d, 20% voltage decrease, b) 144 m³/d, 20% voltage increase, c) 144 m³/d, 20% voltage decrease, d) 58 m³/d, 20% voltage increase. ED unit specifications: 50x50 cm², 500 cell pairs, 270 μm spacers and FUJIFILM Type 10 membranes

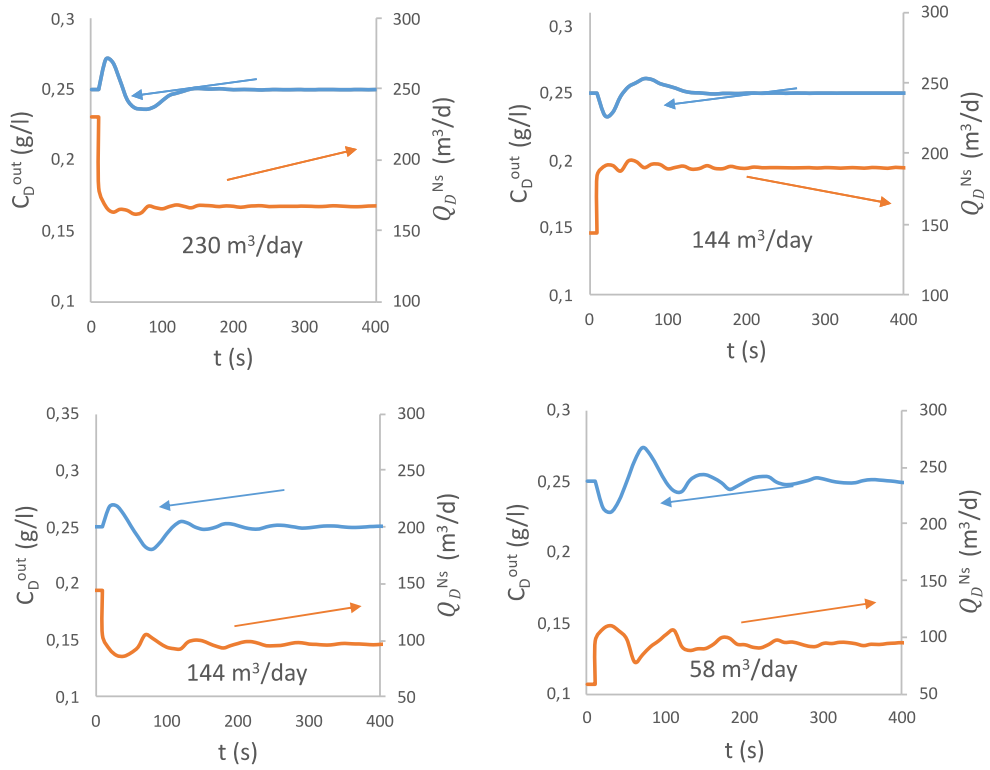

Figure 43. Dynamic ED response of the controlled and the manipulated variables in the case of a hybrid FB-FF controller for a voltage step change at different initial diluate feed flowrates. a) 230 m³/d, 20% voltage decrease, b) 144 m³/d, 20% voltage increase, c) 144 m³/d, 20% voltage decrease, d) 58 m³/d, 20% voltage increase. ED unit specifications: 50x50 cm², 500 cell pairs, 270 μm spacers and FUJIFILM Type 10 membranes.

The implementation of the stand-alone FF controller helps in minimizing the off-set restoring a concentration value close to the target. However, the control is not ideal and some transient deviation from the steady-state value of product concentration is observed.

Looking at the mostly common case of hybrid controller, the response of the system shows several small improvements compared to the simple case of FB controller, both in terms of system stability and amplitude of oscillations.

However, such improvements may have a limited interest in the real cases analysed hereafter due to the smaller and slower disturbances occurring in real operation of solar/wind-powered ED systems. Therefore, the simple FB controller has been adopted for the simulations of short-time-scale scenarios.

3.2.5 Short time scale simulations

The controlled dynamic ED model was used to simulate the operation of the controlled ED plant in 4 typical days (from 00:00 to 23:59), that were chosen as representative of the four seasons. At this scale, it is possible to observe the dynamic effect of the control system. For this reason, the voltage applied to the ED units was changed with a 3 minutes step, in order to observe discrete power changes that significantly challenge the stability of the control system.

Simulation results for the daily operations are shown in Figure 44. For each day, the available power, the voltage applied to each ED unit, the plant diluate flowrate and the outlet diluate concentration are reported. During the sample winter day (Figure 44 a), power production is very low in the very first hours (i.e. before the sunset and with almost no wind). Then, some small power peaks are observed during light hours while the power grows up to 20 kW (i.e. the maximum capacity of the wind turbine) during the night due to an increased wind speed. This means that for the first hours of the days the unit is not able to operate as the power is below the power limit, while it keeps running for the rest of the day, except for an additional short period, reaching its maximum daily production in the last quarter of the day.

On the other hand, spring and autumn days (Figure 44 b and d) present a more unstable behaviour, characterised by a similar non-operational period of about 6 hours in between the first 2 quarters of the day and a power peak in the third quarter. The main differences between the two days is that the spring day shows a higher peak power production and higher peaks in the controlled concentration.

The summer reference day (Figure 44 c) is the only one in which plant operation is never interrupted, as the power produced by the PV/Wind hybrid system is always above the minimum threshold. Despite this, the day is characterised by a high number of steep variations, especially during light hours when solar irradiation keeps changing according to weather conditions. For this reason, the highest concentration peaks are observed during this day.

In addition to the overall daily data, some dynamic details of the control system action are also shown in Figure 44. For each day, a response to a positive and a negative step disturbance as well as to a ramp are highlighted. Relatively small peaks and fast responses are found for step disturbances (as discussed in the controller tuning section). Even in the summer day, characterised by the highest peaks, the outlet concentration stays below ± 10% of the set point value. In the same way, the oscillatory responses to ramp changes shows very limited oscillations around the set point.

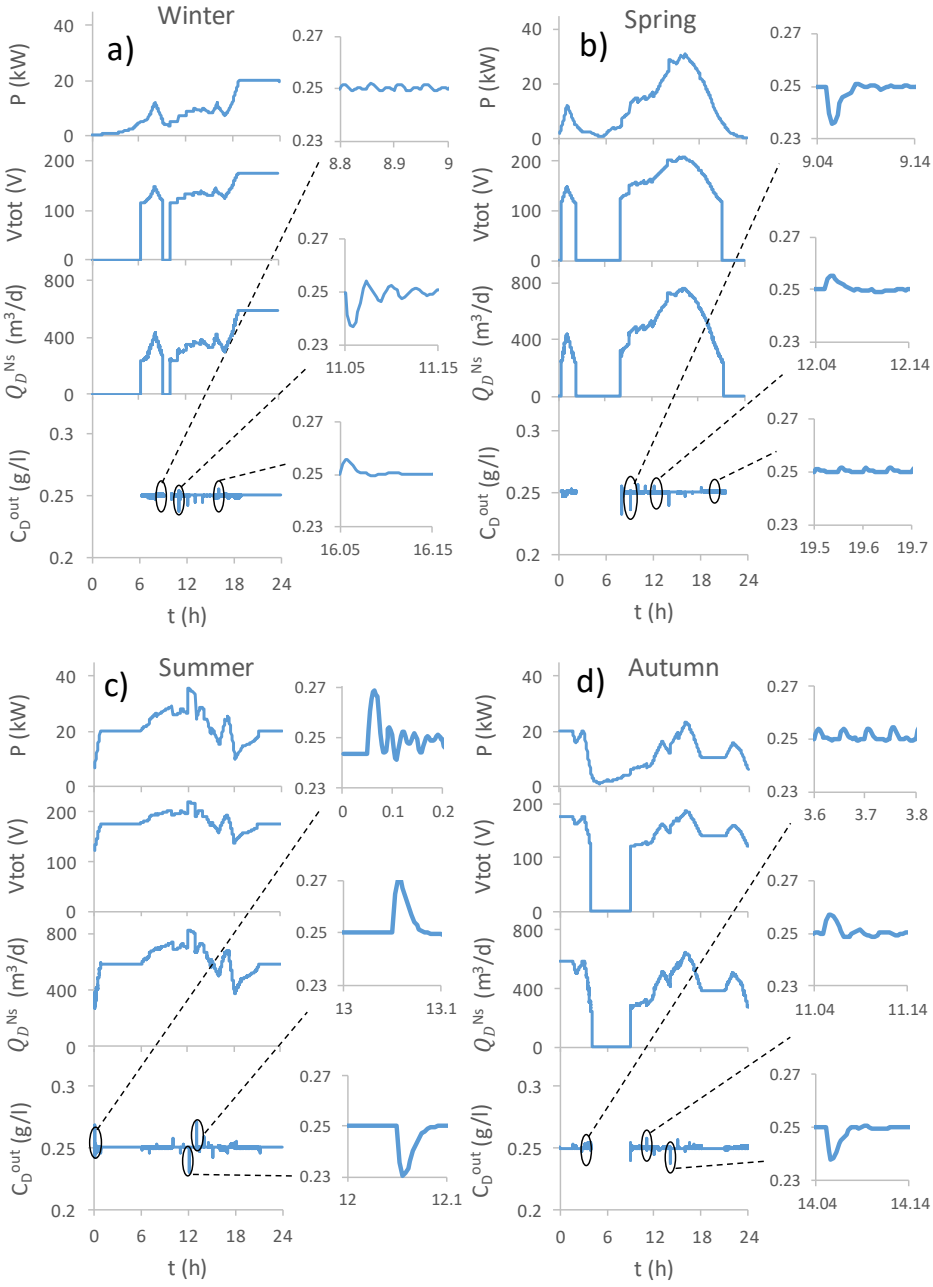

Figure 44. Results for daily simulations of the 4 ED stacks powered by a PV/Wind source. Graphs show available power, applied voltage, inlet flowrate and diluate outlet concentration (overall and dynamic details) for 4 days representative of a) Winter, b) Spring, c) Summer, d) Autumn. Units' specifications: 50x50 cm², 500 cell pairs, 270 µm spacers and FUJIFILM Type 10 membranes.

4 Electrodialysis with multi-ionic mixtures

This chapter presents the description of a hierarchical model for ED that takes into account multi-ionic feeds (here referred as multi-ionic or multicomponent ED). The model was developed following a semiempirical approach, resulting in a set of parameters that need to be experimentally determined. The nature of these parameters and their determination is discussed, identifying membrane resistance and ion membrane diffusivity as the main ones. A set of experiments for the estimation of membrane resistance in presence of different ion mixtures is presented. Finally, the model was validated against original experimental data obtained from a lab scale ED test rig with multi-ionic solutions, demonstrating that this approach can be used to mimic the behaviour of and ED stack that desalinates real seawater.

4.1 Multi-ionic ED: state of the art

As already discussed in chapter 2, in the literature is possible to find a wide number of models that describes the ED process. However, most of these models assumes that the unit is desalting a solution containing only NaCl dissolved in water. In fact, real feeds are usually characterised by the presence of additional components, such as $Mg^{2+}$and Ca^{2+}.

In general, the presence of additional ions in the feed affects the process in multiple ways. In particular, the properties of IEMs can change significantly. Membrane resistance has been found to grow in presence of divalent ions, as described in the work of Moreno et al. [440], where the stack resistance of a RED unit was compared in presence of either NaCl or $MgCl_2$ for different IEMs. In addition, uphill transport (i.e. the transport of ions against their concentration gradient) is another phenomenon typical of the presence of many ions [441], even though it is more relevant for RED than ED as in the latter the direction of the current is imposed from the outside.

All of the aforementioned changes affect the overall effectiveness of the desalination process that in the end will result less efficient (i.e. the current is used to move more ions), more troublesome (i.e. the presence of some ions can be the cause of scaling, see section 1.2.4) and more energy consuming. Hayes and Severin [442,443] experimentally investigated the effect of calcium and other cations in the treatment of concentrated brines, highlighting different practical issues such as the loss in efficiency due to scaling and the risk of suppression of sodium flux when using membranes that allow a preferential transport of other ions.

Another important phenomenon to take into account is the LCD. When there is more than one counterion in solution, the value of the LCD can change dramatically, as the limiting current is formally reached when all the ions' concentration reaches zero at the solution/membrane interface. This usually results in an increase of the LCD in presence of multi-ionic mixtures. Geraldes et al. explored the problem of concentration polarisation (and LCD) of multi-ion solutions in both RO [444] and

ED [229]. In particular, the authors developed a model for the estimation of the LCD in ED with multi-ionic solutions using a linearised form of the Nernst-Planck (NP). Model predictions matched experimental results for $MgCl_2$ + $MgSO_4$ solution successfully.

Besides the aforementioned modelling works focusing on LCD, there are only few other works that reports a partial or complete description of multicomponent ED. Firdaous et al. developed a model for multicomponent ED based on Stefan-Maxwell approach [445]. Nevertheless, this model was only used for the simulation of NaCl solutions, as it already involved 6 unknown parameters per membrane to be estimated or experimentally determined. Another attempt to describe multicomponent ion transport was made by Kodym, Filà et al. [446,447] that used the Nernst-Plank approach to model chlor-alkali electrolysis. Again, the model resulted in a set of parameters (i.e. ion diffusivities inside the membranes) that need to be estimated. Interestingly, the authors also compared the classical Donnan-NP model with the Poisson-NP model, where there is no assumption of electrochemical equilibrium, demonstrating that, at low currents, the two models predict comparable outcomes.

One of the main issues when studying multi-ionic solutions is the characterisation of the ion-membrane properties that, as was already explained in chapter 2, usually are the characterisation variables of the models. Among them, transport numbers play an important role as they indicate how much current is carried by a certain ion. As already discussed in section 1.2.3, there are different ways to estimate this quantity for membranes immersed in single salt solutions. However, it is much more complex when more than two ions are involved. Manzanares et al. [448] highlighted that the simple potentiometric method is not suitable even for a ternary system, as a single measurement of the membrane potential cannot estimate 3 transport numbers. According to this study, in some cases is possible to consider apparent transport numbers by assuming that the ternary system behaves as a binary one. However, this method generally results in erroneous predictions [448]. Another way of estimating transport numbers is through ion diffusivities inside the membranes. According to the NP approach, those two parameters are connected, as discussed in section 4.2.1. However, the estimation of IEM diffusivities presents some criticalities. While it is relatively easy to estimate the external salt permeability [449], the ionic diffusivity can only be estimated through indirect measurement that are subjected to the interpretation of the chosen approach. The main issue is related to the fact that internal membrane characteristics such as the ion concentration profile inside the membrane are required. Kamcev et al. [450] proposed a method for the estimation of the IEM diffusivities, that interprets the diffusion experiments combining the NP approach with ion sorption measurements for the estimation of the membrane side concentration and membrane resistance measurement to close the system. The disadvantage of this choice is that the result depends on membrane resistance tests, which are acknowledged to be controversial.

All the issues that have been mentioned so far makes the development and characterisation of multi-ionic ED models a difficult task that rarely results in tools of practical usefulness. For this reason, this work aims at presenting a relatively simple yet effective approach that combines the advantages of semiempirical models with the simple description of multi-ionic system given by the NP. An experimental

estimation of membrane resistance with different ions was also carried out with the aim of characterising the model. Finally, the model was validated against original experimental data using a first estimation of ion diffusivities.

4.2 Model description

The multi-ionic model was developed with the same hierarchical structure of the single salt model described in section 2.2, going from the lowest scale of the cell pair up to the plant model. In addition, the same assumptions are made, with two exceptions:

- The presence of more than two ions is now considered;
- Ion concentration is considered in the calculation of transport numbers.

In addition, as this model also involves the ion concentration at the membrane side, a linear distribution of this variable is assumed across the IEMs.

In the following text, cell pair and stack model will be discussed, while for the plant model the same description of section 2.2.3 applies.

4.2.1 Cell pair

Given the nature of the model, the main implications of considering a multicomponent solution can be seen at the cell pair scale as transport, thermodynamic and electrical features are deeply affected.

The presence of more ions does not change the type and the nature of the transport phenomena involved in the process. However, a different description is required. In order to describe the transport of each ion, it is possible to refer to a formulation of the NP equation in electroneutral solutions that involves the current rather than the electric potential [66], where the total flux of each ion across one membrane is given by the sum of a diffusive and a conductive flux:

$$J_{tot,i}^{IEM} = -\sum_{j} D_{i,j}^{IEM} \nabla C_j^{IEM} + \frac{t_{IEM,i}\, i}{z_i\, F} \tag{74}$$

in which $j = 1,2,\dots,n$ where n is the number of ions, $J_{tot,i}^{IEM}$ is the total membrane flux of the i-th ion, across each IEM, expressed in mol/m²/s¹, $D_{i,j}^{IEM}$ is the cross-diffusion coefficient in m²/s¹, C_j^{IEM} is the ion concentration in the membrane phase in mol/m³, $t_{IEM,i}$ is the membrane transport number of the i-th ion, i is the current density in A/m², z_i is the ion charge and F is the Faraday constant.

Given the assumption of the linear distribution of the ion concentration, the diffusive part of the flux can be expressed as

$$J_{diff,i}^{IEM} = -\sum_{j} \frac{D_{i,j}^{IEM}}{\delta^{IEM}} \left(C_j^{IEM,\delta^{IEM}} - C_j^{IEM,0}\right) \tag{75}$$

with the cross diffusion coefficients that are representative of the mutual interaction among the various ions:

$$D_{i,j}^{IEM} \equiv D_i^{IEM}\delta_{ij} + \frac{t_{IEM,i}}{z_i} z_j \left(D_i^{IEM} - D_j^{IEM}\right) \tag{76}$$

where D_i^{IEM} is the diffusion coefficient of the single ion and δ_{ij} is the Kronecker delta. The transport number can be related to the diffusion coefficient [66]:

$$t_{IEM,i} = \frac{{z_i}^2 D_i^{IEM} \overline{C_i^{IEM}}}{\sum_j {z_j}^2 D_j^{IEM} \overline{C_j^{IEM}}} \tag{77}$$

where $\overline{C_i^{IEM}}$ is the average concentration of the i-th ion inside the IEM.

The main advantage of this approach is that, assuming to know the ions' concentration inside the membrane, it is possible to describe the ion transport by only knowing the single ion diffusion coefficients.

In order to estimate the concentration at each side of the membrane, it is possible to make use of the Donnan equilibrium (see section 1.2.1) where the osmotic pressure term is neglected:

$$\eta_{Don} = \frac{R_G T}{z_i F} \ln\left(\frac{a_i^{SOL}}{a_i^{iem}}\right) \tag{78}$$

It is important to note that this equation stands for each ion that is present in the system. In addition, the electroneutrality condition is applied:

$$C_{fix} + \sum {C_{co}}^{IEM} = \sum {C_{ct}}^{IEM} \tag{79}$$

where C_{fix} is the fixed charge group concentration of the IEM, ${C_{co}}^{IEM}$ and ${C_{ct}}^{IEM}$ are the co-ion and counter-ion concentrations respectively.

Water transport is also taken into account in the multicomponent model, expressing osmotic and electroosmotic fluxes as follows:

$$q_{osm}^{IEM} = L_p^{IEM} \left[\nu R_G T \left(\varphi_C^{IEM} \sum_i {C_{C,i}}^{int,IEM} - \varphi_C^{IEM} \sum_i {C_{D,i}}^{int,IEM}\right)\right] \tag{80}$$

$$q_{eosm} = \sum_i \frac{w_i J_{tot,i} M_{w,i}}{\rho_{w,i}} \tag{81}$$

$$q_w = q_{osm}^{AEM} + q_{osm}^{CEM} + q_{eosm} \tag{82}$$

where *i* refers to the i-th ion in solution and $J_{tot,i} = J_{tot,i}^{CEM} - J_{tot,i}^{AEM}$, while the other symbols have the same meaning as in eq. (23) and (26) of section 2.2.1. The value of the osmotic coefficient is determined by using an external thermodynamic database (PHREEQC, USGS, US.) whose implementation will be discussed in section 4.2.3.

As for the single salt model distributions over the dimension of the channel length are computed. Bulk concentration and flowrate distributions inside the channels are described through the differential mass balance equations of section 2.2.1 (eqs. (27)-(30)). The only difference is that eq. (27) and (28) are now representative of the moles changes of the i-th ion in the system.

The electrical part of the model can be formally defined in the same way as for the single salt model. In particular, eqs. (31)-(33) are still valid. Therefore, the cell pair voltage drop is the sum of a non-ohmic and an ohmic contribution, with the latter being characterised by solution and membrane resistance.

Solution resistance can be calculated by means of eq. (33), with the solution conductivity that is estimated using the correlations by McCleskey et al. [451,452]. On the other hand, membrane resistance is highly affected by the type and the mutual amount of ions adsorbed [440]. Therefore, experimental data are used to determine the value of IEM resistance in different conditions (see section 4.4.1).

In order to estimate the membrane potential (i.e. the non ohmic contribution) a generalization of eq. (16) can be considered [453]:

$$\eta_{IEM} = \left[\frac{R_G T}{F}\sum -\frac{t_{IEM,i}}{z_i} ln\left(\frac{a_{C,i}^{int,IEM}}{a_{D,i}^{int,IEM}}\right)\right] \tag{83}$$

where $a_i = \gamma_i \ C_i$. The same thermodynamic database used for the osmotic coefficient was used to determine the activity coefficients. Also in this case, interfacial concentrations are used in order to include the effect of concentration polarisation.

4.2.2 Stack

In principle, all of the eqs. (45)-(52) from section 2.2.2 are still valid for the multicomponent model. However, the salt-specific energy consumption (eq. (50)) and the current efficiency (eq. (51)) tend to lose their original meaning. In a multi-ion system, it is not possible to talk about salts as each cation could be potentially coupled with each anion in solution. Therefore, those performance parameters can now refer to a single ion, determining the energy required to move a kg of a certain ion or the amount of current actively used to move an ion in the desired direction.

4.2.3 Thermodynamic database implementation

In order to deal with the complex thermodynamics that regulates ion-ion interaction, an open source geochemical database was involved in the model development (PHREEQC, USGS, US.). The main advantage of this tool is that it contains correlations for a wide range of ions. In addition, it is possible to choose a number of different thermodynamic methods. In particular, Pitzer's method was chosen for this model, as it is also particularly suited for high concentration solutions [346,454–456].

Given that the *PHREEQC* database is a standalone platform while the ED model is implemented in *gPROMS* Modelbuilder a problem of automating the process of sending thermodynamic data to the model arose. For this reason, a specific communication routine was implemented through *Microsoft Excel* as both *PHREEQC* and *gPROMS* can interact with it. The geochemical database has a specific COM module that allows the Excel interaction through the VBA

interface. Figure 45 shows the VBA script through which the database takes inputs from Excel and then prints the output.

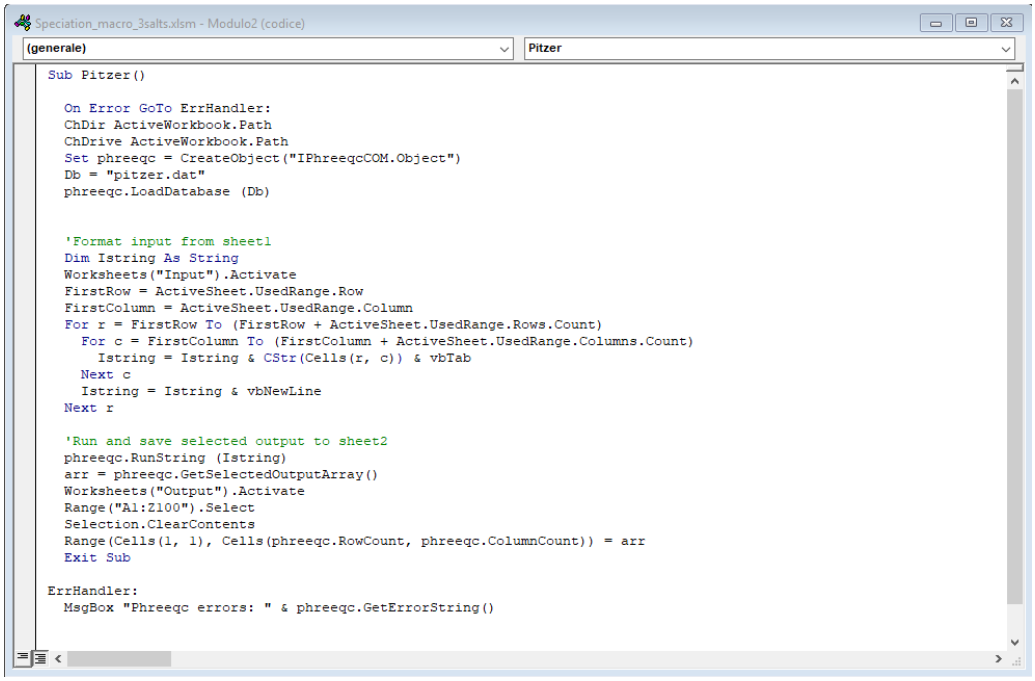

Figure 45. VBA script of the macro used for connecting *PHREEQC and Microsoft Excel.*

On the other hand, *gPROMS* has a specific port to use Excel as a foreign object, for input/output communication. Figure 46 shows how the connection is made in both *gPROMS* (Figure 46 a) and Excel (Figure 46 b). The final result is that, during a simulation, *gPROMS* communicates solution composition and state variables to PHREEQC through Excel. Then, the thermodynamic database gives back to *gPROMS* activity coefficients, the osmotic coefficient and ionic strength (used for the estimation of conductivities). This procedure is automatically repeated for each discretization interval and for each iteration. In addition, the database gives information on saturation indexes and complex ionic species that can appear in specific situations.

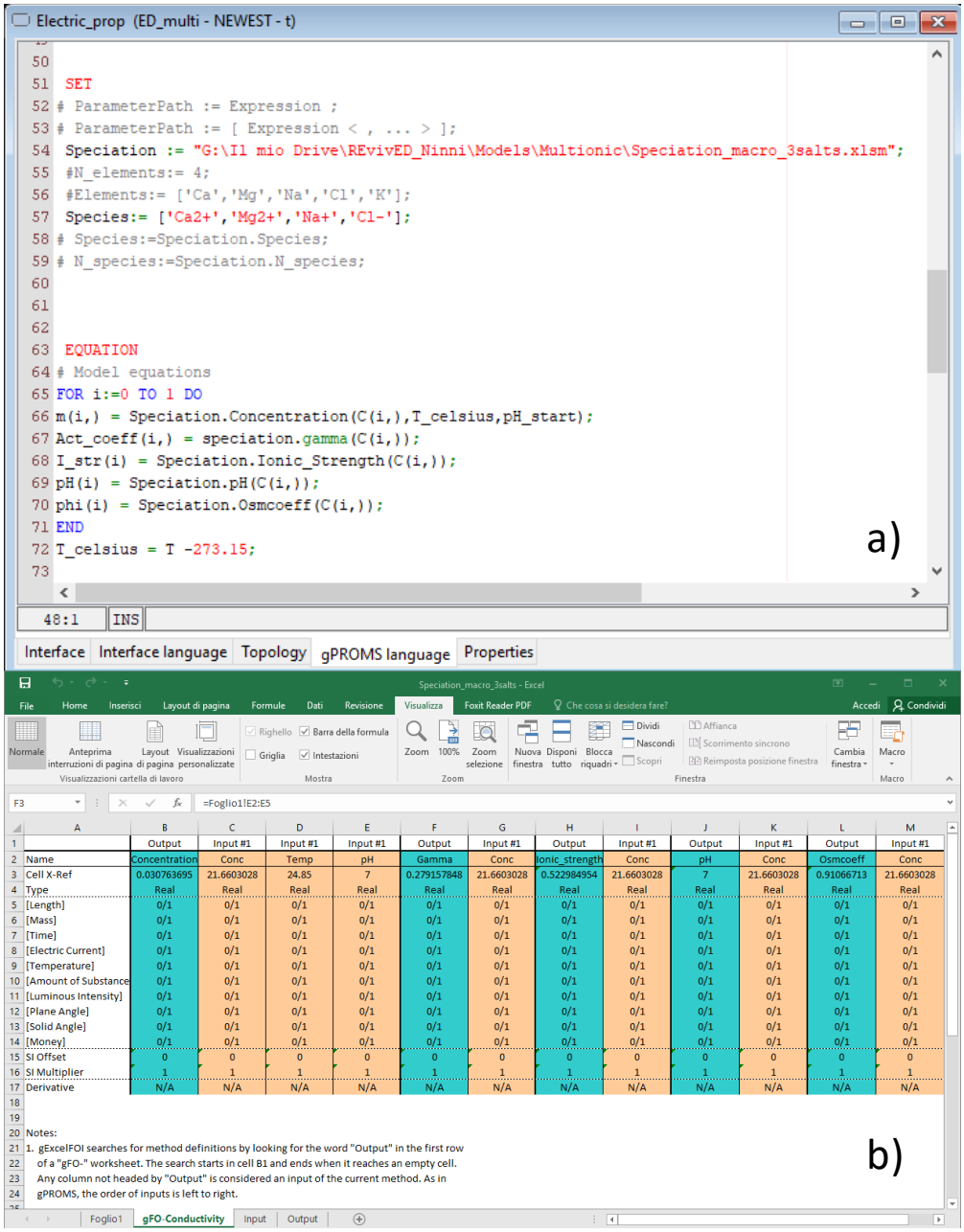

	A	B	C	D	E	F	G	H	I	J	K	L	M
1		Output	Input #1	Input #1	Input #1	Output	Input #1	Output	Input #1	Output	Input #1	Output	Input #1
2	Name	Concentration	Conc	Temp	pH	Gamma	Conc	Ionic_strength	Conc	pH	Conc	Osmcoeff	Conc
3	Cell X-Ref	0.030763695	21.6603028	24.85	7	0.279157848	21.6603028	0.522984954	21.6603028	7	21.6603028	0.91066713	21.6603028
4	Type	Real	Real	Real	Real	Real	Real	Real	Real	Real	Real	Real	Real
5	[Length]	0/1	0/1	0/1	0/1	0/1	0/1	0/1	0/1	0/1	0/1	0/1	0/1
6	[Mass]	0/1	0/1	0/1	0/1	0/1	0/1	0/1	0/1	0/1	0/1	0/1	0/1
7	[Time]	0/1	0/1	0/1	0/1	0/1	0/1	0/1	0/1	0/1	0/1	0/1	0/1
8	[Electric Current]	0/1	0/1	0/1	0/1	0/1	0/1	0/1	0/1	0/1	0/1	0/1	0/1
9	[Temperature]	0/1	0/1	0/1	0/1	0/1	0/1	0/1	0/1	0/1	0/1	0/1	0/1
10	[Amount of Substance]	0/1	0/1	0/1	0/1	0/1	0/1	0/1	0/1	0/1	0/1	0/1	0/1
11	[Luminous Intensity]	0/1	0/1	0/1	0/1	0/1	0/1	0/1	0/1	0/1	0/1	0/1	0/1
12	[Plane Angle]	0/1	0/1	0/1	0/1	0/1	0/1	0/1	0/1	0/1	0/1	0/1	0/1
13	[Solid Angle]	0/1	0/1	0/1	0/1	0/1	0/1	0/1	0/1	0/1	0/1	0/1	0/1
14	[Money]	0/1	0/1	0/1	0/1	0/1	0/1	0/1	0/1	0/1	0/1	0/1	0/1
15	SI Offset	0	0	0	0	0	0	0	0	0	0	0	0
16	SI Multiplier	1	1	1	1	1	1	1	1	1	1	1	1
17	Derivative	N/A	N/A	N/A	N/A	N/A	N/A	N/A	N/A	N/A	N/A	N/A	N/A
18													
19													
20	Notes:												
21	1. gExcelFOI searches for method definitions by looking for the word "Output" in the first row												
22	of a "gFO-" worksheet. The search starts in cell B1 and ends when it reaches an empty cell.												
23	Any column not headed by "Output" is considered an input of the current method. As in												
24	gPROMS, the order of inputs is left to right.												

Figure 46. a) *gPROMS* script to recall the *Microsoft Excel* foreign object. b) *Microsoft Excel* sheet that is connected to *gPROMS*.

4.3 Experimental setup for membrane resistance ad ED tests

Two types of experiments were performed: Estimation of Type 10 membrane resistance and ED tests for model validation. Both experiments were done in a 10×10 cm² lab-scale ED unit (*REDstack, The Netherlands*) operating in a single pass co-flow. For testing the resistance of the CEMs the stack was assembled with 13 CEMs, 4 of which were used as double shielding membranes to separate the electrode compartment from the working channels (Figure 47 a) To test the AEMs, 10 anionic membranes are placed into the stack, while maintaining the CEMs as shielding membranes (Figure 47 b). Finally, for the ED experiments 10 cell pairs were formed alternating CEMs and AEMs and using again double CEMs shielding membranes. In all cases, 270 μm woven spacers (*Deukum GmbH, Germany*) were used [289]. The tests were carried out with solutions of NaCl, MgCl2 and CaCl2, while a solution with 0.3 M $K_3Fe(CN)_6$, 0.3M $K_4Fe(CN)_6{\cdot}3H_2O$ and 0.25 M NaCl was used in the electrode compartment. Solutions under study were pumped into the system via peristaltic pumps (*Cole palmer, US*), while the system was subjected to a constant current by means of a power supply (*ES 030-10, Delta elektronika, The Netherlands*). Current and external voltage were constantly measured with digital multimeters (*87V, Fluke, US*), while the voltage of the membrane pile was measured with Ag/AgCl reference electrodes placed in the electrode compartments and a digital multimeter (*34461A, Keysight, US*). Inlet and outlet concentrations of single salt solutions were estimated through conductivity measurements (*Ph/cond 3320 WTW, US*), while the composition of the mixtures was estimated via ion chromatography (*Compact IC Flex 930, Metrohm, Switzerland*).

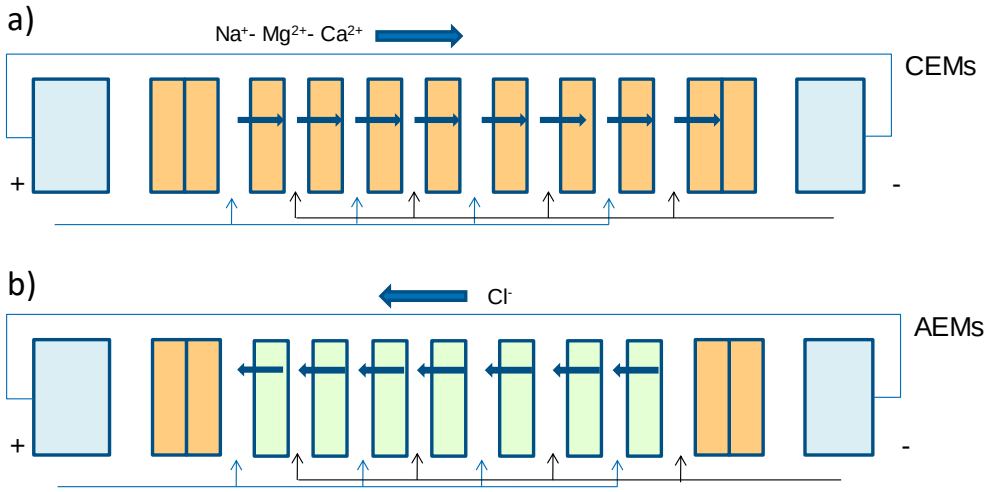

Figure 47. Scheme of the single membrane stack layout adopted to measure membrane resistance for a) CEMs and b) AEMs. It is worth noting that in the AEM configuration CEMs are still used as shielding membranes due to the characteristics of the electrode solution.

The **membrane resistance** was estimated for membranes subjected to equal solutions of 1, 2 and 3 salts, exploring concentrations from brines to almost drinking water. In the mixtures, the ratio of Na^+ to other ions was kept constant to a value typical of seawaters (43.5:1 for Ca^{2+} and 9.6:1 for Mg^{2+}, expressed in moles). The experiment aimed at measuring the stack resistance at different currents (in the 10-200 mA range) in order to measure an average resistance from the resulting curve. From the overall stack resistance, it was possible to indirectly estimate the membrane resistance by subtracting the contributions related to the channels' resistance (as from eq. (33)) and the blank resistance (i.e. the experimentally measured contribution related to electrodes, electrode compartments and shielding membranes). The stack configuration (i.e. assembled with a single type of membrane, either AEM or CEM) ensured that the concentration did not change through the channels, while a relatively high velocity of 3 cm/s (540 ml/min of feed flowrate) ensured the minimisation of polarisation phenomena. It is worth noting that, prior to the tests, IEMs were conditioned with the solution that was about to be studied imposing a constant current to the stack for about 1 hour, ensuring that a stable value of the voltage had been reached.

The **ED tests for model validation** were performed at a flow velocity of 0.5 cm/s (90 ml/min of feed flowrate). Two different type of test were performed. The first one was a classic single stage, constant current experiment, performed at different feed concentrations (5,10,20 and 30 g/l of TDS), using the same ion ratio of the membrane resistance. Different currents were applied, ranging from 20 to 80% of the LCD. The second type of test was a discontinuous multistage experiment, where the feed was consecutively processed inside the unit (i.e. concentrate and diluate exiting from the unit were fed back to the unit multiple times). 20 and 30 g/l TDS were used as initial feed concentrations. The final aim of ED tests was to measure the voltage of the unit as well as the composition of the outlet solutions in order to compare them with simulation results.

4.4 Membrane resistance results and model validation

In this section, the experimental results related to the measurement of AEM and CEM ohmic resistance are presented. In addition, the comparison between model predictions and the results of the ED tests are shown.

4.4.1 Experimental determination of membrane resistance

In Figure 48 the results of the experiments performed on the CEMs are reported both in terms of membrane resistance per unit area (Figure 48 a and b) and membrane conductivity (Figure 48 c and d). Results concerning single salt solutions as well as mixtures are reported. In general, membrane resistance is almost constant at higher concentration, while an increase can be observed in the low current range (for concentrations lower than 100 meq/l). Single salt measurements (Figure 48 a) show that CEMs are strongly affected by the type of cation in solution, as the resistance increases of almost one order of magnitude when switching from Na^+ to

divalent ions. In addition, the value of the resistance with mixtures falls slightly above the Na^+, indicating that the presence of small amount of divalent ions in solution increases the membrane resistance compared with the pure NaCl case. Of course, this increase is more when Ca^{2+} and Mg^{2+} are present at the same time rather than when only one of them is mixed with Na^+.

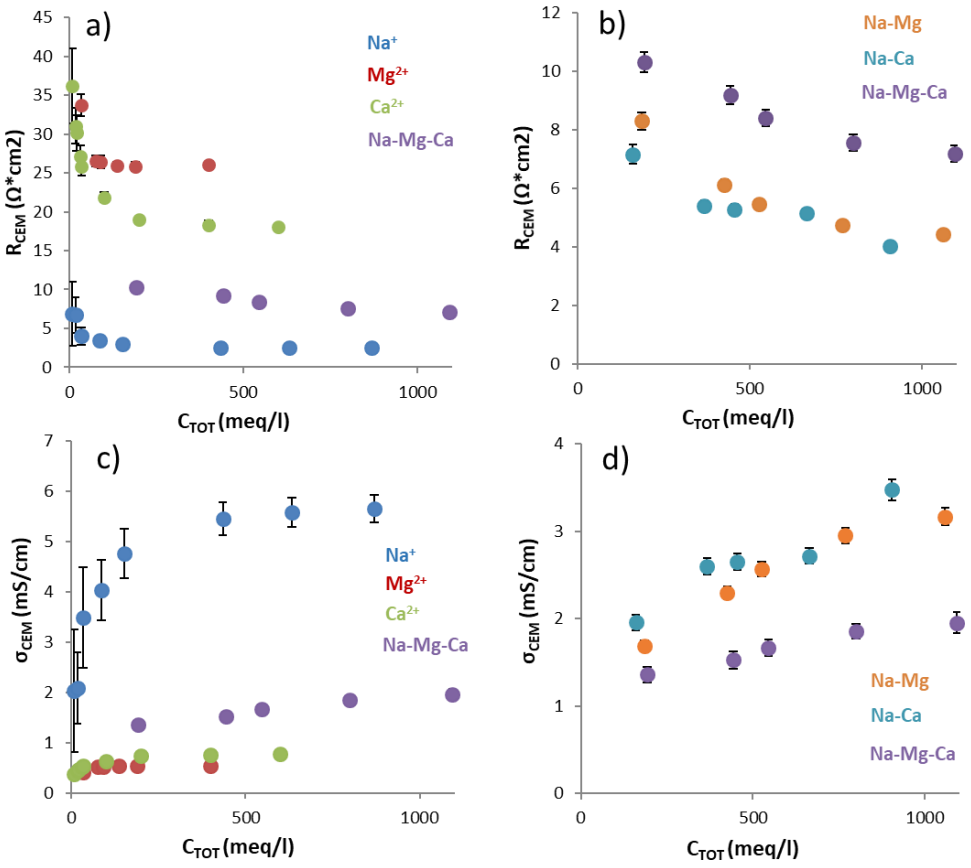

Figure 48. Experimental results of the membrane resistance measurements for the *Fujifilm* Type 10 cation exchange membrane with NaCl, MgCl2 and CaCl solutions. a) Resistance per unit area of single salt and 3-salts solutions, b) Resistance per unit area of 2-salts and 3-salts solutions, c) Membrane conductivity of single salt and 3-salts solutions, d) Membrane conductivity of 2-salts and 3-salts solutions.

By expressing the results in terms of membrane conductivity, it was possible to rearrange the data in order to find a correlation that expresses the ion conductivity of the mixture (σ_{MIX}) as a function of the single salt IEM conductivities (σ_i). In particular, the following expression was adopted:

$$\sigma_{MIX} = \sum_i \sigma_i(c_i) + \chi \tag{84}$$

where σ_i is a continuous function fitted from the experiments and valid for the analysed range of concentrations and χ represents the ion interaction coefficient that accounts for the deviation from the simple additivity of the conductivities. According to the results, the interaction coefficient varies less than 30% over more than one order of magnitude of concentrations. Therefore, as a first approximation, the value of χ was considered constant. In particular, this value was found equal to -3.23 mS/cm for NaCl-$MgCl_2$, -3.11 mS/cm for NaCl-$CaCl_2$ and -4.56 mS/cm for NaCl- $MgCl_2$-$CaCl_2$.

Figure 49 shows membrane resistance and conductivity results for the AEM in presence of the 3 different cations. Differently from what was previously observed with the CEM, lower values for the resistance (and thus higher for the conductivity) were generally found. In addition, the change in conductivity in presence of different cations is much lower. This can be explained by the fact that the AEM is mainly crossed by anions (which in this case are always Cl-) while only a small amount of cations is able to pass through due to the non-ideal selectivity. Another critical aspect of the AEM's results is that, due to the lower values of the resistance, the values estimated at low concentrations are characterised by large error bars. This is because in the low current range the channel resistance is particularly high compared to the residual membrane resistance that, according to the procedure described in section 4.3, is indirectly calculated by subtracting the channels' resistance.

The same correlation adopted for the CEM conductivity (eq. (85)) was used for the AEM case. However, given the high uncertainty related to the values estimated at low concentrations, the first points of the single salt conductivity (Figure 49 c) were ignored and concentration-independent single salt membrane conductivity was assumed. In this case, the value of χ was -8.33 mS/cm for NaCl-$MgCl_2$, -7.06 mS/cm for NaCl-$CaCl_2$ and -13.86 mS/cm for NaCl- $MgCl_2$-$CaCl_2$.

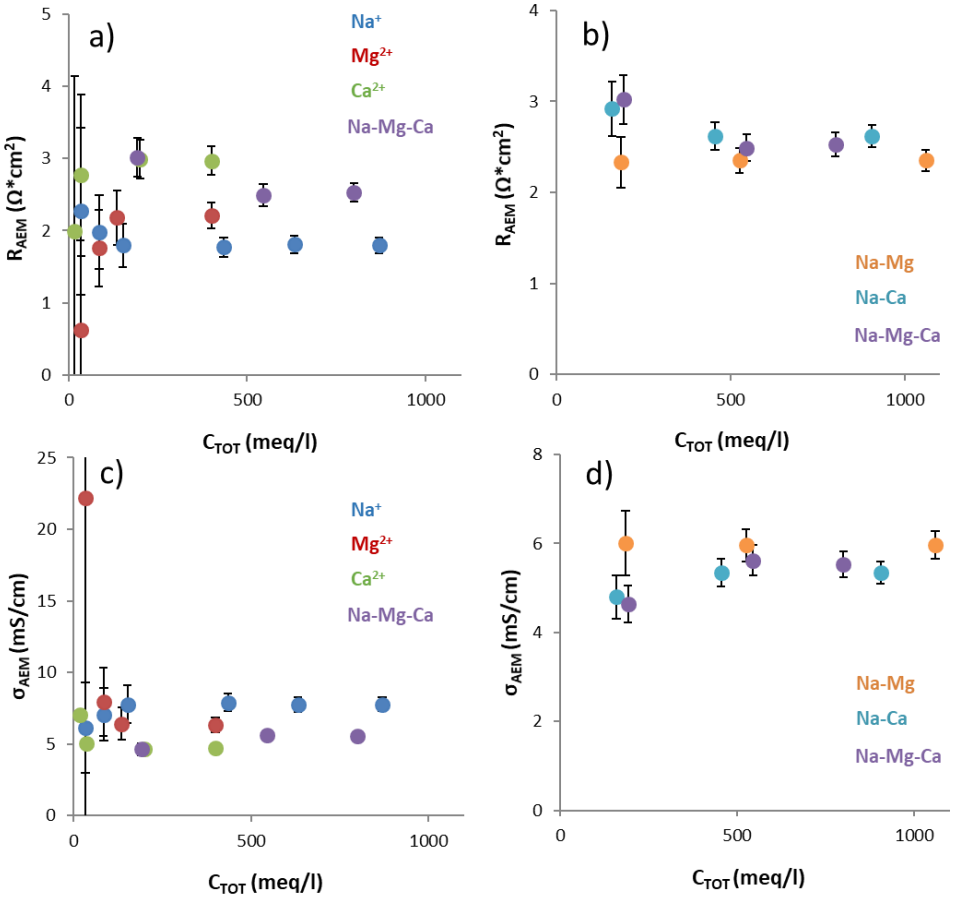

Figure 49. Experimental results of the membrane resistance measurements for the *Fujifilm* Type 10 anion exchange membrane with NaCl, MgCl2 and CaCl solutions. a) Resistance per unit area of single salt and 3-salts solutions, b) Resistance per unit area of 2-salts and 3-salts solutions, c) Membrane conductivity of single salt and 3-salts solutions, d) Membrane conductivity of 2-salts and 3-salts solutions.

4.4.2 Model validation

In order to test the reliability of the model, simulation results were compared with the experimental data of the ED tests. For the sake of brevity, only the results from single and multistage operations with 30 g/l TDS feed were reported.

It is worth noting that for all the simulations, the correlations mentioned in section 4.4.1 were used for the estimation of membrane resistance, while a first estimation of single ion diffusivities (reported in Table 9) was used.

Table 9. Values of the single ion IEM diffusivities used to perform the simulations.

D_i^{IEM} (m²/s)	**Na^+**	**Mg^{2+}**	**Ca^{2+}**	**Cl^-**
AEM	4E-12	2E-13	2E-13	4E-12
CEM	4E-12	2E-13	2E-13	4E-12

Figure 50 shows the model validation for the single stage case. In particular, the outlet concentration of the three cations (Figure 50 a, b and c) as well as the voltage at different currents (Figure 50 d) are depicted. The comparison shows a very good agreement for the concentrations and in particular for Na^+ and Mg^{2+}, while a slightly higher discrepancy is observed for Ca^{2+}, mainly due to the lower concentration values that are intrinsically more sensitive to the mismatch. On the other hand, higher errors are observed in the prediction of the voltage, with the discrepancy that increases with the current, and thus becomes higher when getting closer to the limiting current. This indicates that the model slightly underestimates the stack resistance for a reason that still needs to be identified. An explanation can be attributed to a change in the behaviour of the membrane at higher currents, although this still needs to be demonstrated.

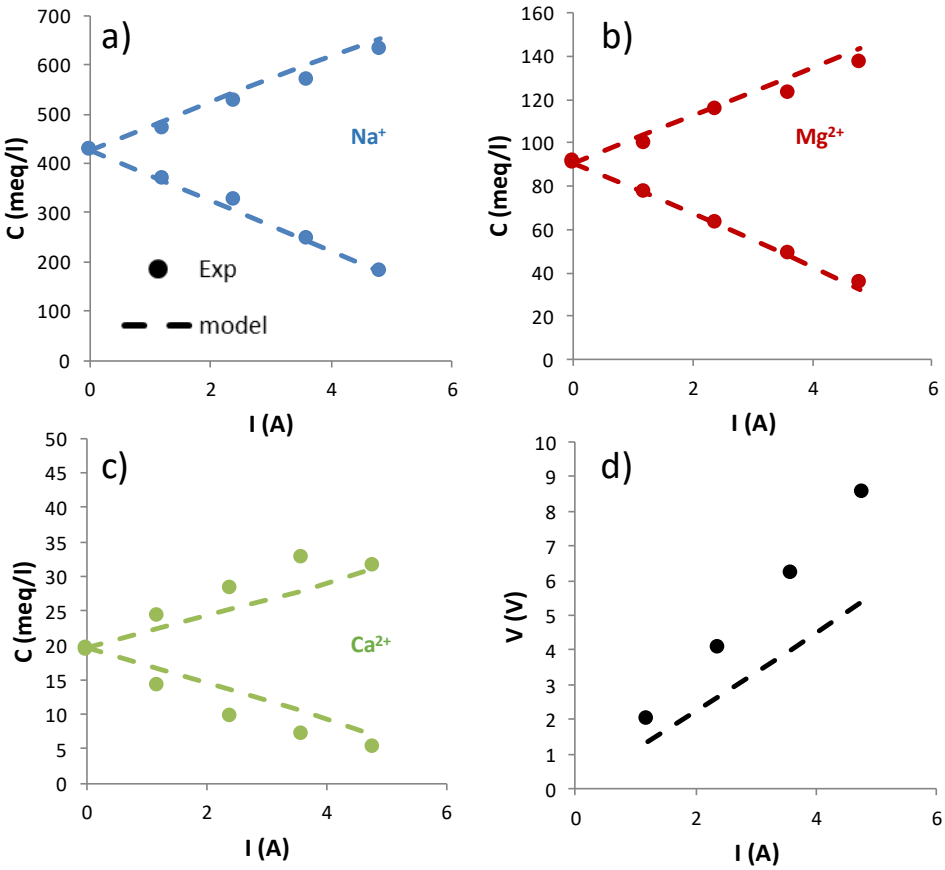

Figure 50. Comparison of experimental data with model predictions for a single stage ED process. a) Na^+ outlet concentration, b) Mg^{2+} outlet concentration, c) Ca^{2+} outlet concentration and d) applied voltage at different currents. 30 g/l TDS feed, 0.5 cm/s flow velocity, 270 µm woven spacers, 10x10 cm^2 stack area, *Fujifilm* Type 10 membranes.

Figure 51 shows the model validation for the multistage case. Here, outlet cations' concentration are reported per each stage. As for the single stage case, a very good match of simulative results with experimental data was observed for the outlet concentrations for the 3 cations. Again, the model shows an underestimation of the voltage. However, the qualitative trend is well replicated as, at each stage, the points were taken at 80% of the LCD. This indicates again that the underestimation of the voltage is related to how close to the LCD the unit is operating.

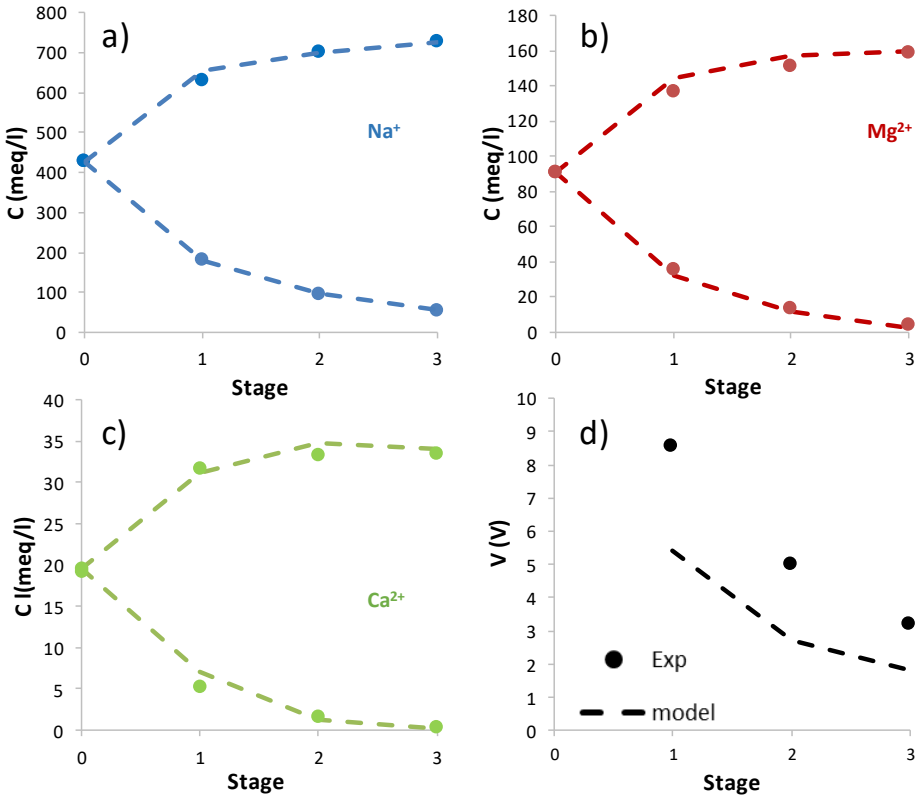

Figure 51. Comparison of experimental data with model predictions for a three-stages ED process. a) Na^+ outlet concentration, b) Mg^{2+} outlet concentration, c) Ca^{2+} outlet concentration and d) applied voltage per stage. 30 g/l TDS feed, 0.5 cm/s flow velocity, 270 µm woven spacers, 10x10 cm^2 stack area, *Fujifilm* Type 10 membranes.

5 Optimisation of hybrid schemes for low energy seawater desalination

In this section, the steady state ED model presented in chapter 2 was used to analyse possible process schemes for the treatment of seawater feeds. In this context, articulated layouts such as multistage and RED-ED integrated process are of particular interest.

The advantages of a multistage configuration were already discussed in sections 1.1.2 and 2.4.1, where the possibility of lowering the energy consumption was demonstrated. On the other hand, RED-ED process was shown in section 1.4.7, where the need for optimisation studies was highlighted. In particular, in this section the RED process as pre-treatment step was taken into account (coupling of unit I and II with reference to Figure 16).

Therefore, an optimisation study was performed on those two process schemes with the aim of producing a first assessment of their potential viability in terms of cost and energy consumption. The optimisation tool of *gPROMS Modelbuilder* was used for these studies.

5.1 Multistage electrodialysis

An optimisation study of a multistage ED system was performed. In particular, the study was focused on a 3 stages plant with fixed dimensions (i.e. length and width) that has to desalt a 30 g/l feed having a fixed production capacity of 200 m^3/d and a target concentration of the product water of 0.25 g/l. Table 10 presents a summary of the fixed variables of the problem under study.

Table 10. List of the fixed variables, control variables and constraints of the optimisation problem for the multistage system. Length and width are the same for each stage. Spacer thickness is taken as an enumerated variable where only 150, 270, 500 and 1000 μm can be chosen.

Fixed variables	C^{IN} **(g/l)**	C_D^{OUT} **(g/l)**	$Q_D^{OUT,tot}$ **(m³/d)**	L **(cm)**	b **(cm)**	**Type of membranes**
	30	0.25	200	50	50	FUJIFILM Type 10
Control variables	$Q_C^{IN,tot}$ **(m³/d)**		$V_{tot,i}$ **(V)**	$N_{cp,i}$	$\delta_{C,i}$ **(μm)**	$\delta_{D,i}$ **(μm)**
	0 - 500		0 - 1000	1 - 2000	150 - 1000	150 - 1000
Constraints	I/I_{lim}		$u_{C,i}$ **(cm/s)**	$u_{D,i}$ **(cm/s)**	Q_C^{IN}/Q_D^{IN}	
	0 - 0.9		0.5 - 5	0.5 - 5	0.5 - 2	

The optimisation problem aimed at minimising a simplified cost function that takes into account the energy of the units as well as the pumping energy (not considering efficiencies) in calculating the operating cost, while only a simplified parameter proportional to the membrane area and that accounts for IEMs, spacers and assembling was considered as fixed costs:

$$Tot.Cost = Cost_{OP} + Cost_{FIX} = En.Cost * E_{spec}^{TOT} + \frac{Stack\ Cost * 2A * \sum_{i=1}^{Ns} N_{cp,i}}{Q_D^{OUT} * Stack\ Life} \quad (85)$$

where $En.Cost$ is the cost of energy expressed in €/kWh, $Stack\ Cost$ is the cost of the stack in €/m² and was assumed proportional to the cost of the membranes. $Stack\ Life$ is the expected life of the stack that, for the sake of unit consistency is expressed in seconds. In the analysed case, $En.Cost$ was taken as 0.1 €/kWh, $Stack\ Cost$ as 30 €/m² and $Stack\ Life$ was assumed of 10 years. It is worth noting that the stack cost is relatively low as a future scenario with low cost IEMs is considered in the standard case.

In order to achieve the desired minimisation, voltage, spacer thickness, and number of cell pairs per stage were taken as control variables together with the inlet concentrate flowrate (Table 10). It is worth noting that voltages were chosen instead of currents to allow an easier solving strategy. In addition, the spacers' thickness was

taken as enumerated integer, so that only a limited number of choices (i.e. 150, 270, 500, 1000 μm) were admissible. Therefore, a proper solver (already included in of *gPROMS Modelbuilder*) had to be chosen in order to deal with mixed integer problems.

A set of constraints was also used in order to ensure the achievement of a feasible solution (Table 10). In particular, the velocity inside each channel was limited to the range between 0.5 and 5 cm/s and the ratio between the inlet flowrates was limited to the 0.5-2 range. Another essential constraint refers to the limiting current. Using the empirical correlation derived by La Cerva for the same membranes used in this study, the allowable current in each stage was limited to a maximum of 90% of the limiting current.

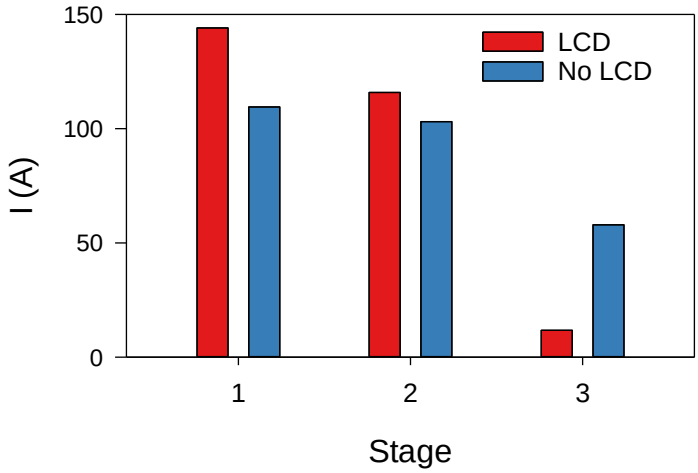

Figure 52. Current per stage with and without the LCD boundary for a 3 stages ED system where voltages were adjusted to mimimise the energy consumption. Fixed variables and constraints are the same of Table 10, with the sole exception of LCD.

In order to highlight the importance of using this constraint, a simple optimisation of the energy consumption was performed just using the voltages as control variables ($N_{cp,i}$ = 500 and $\delta_{C,D,i}$ = 270 μm) both with and without accounting for the limiting current. Figure 52 shows the current per stage in the case of the application of the LCD boundary in comparison with the case in which this boundary is not considered. Interestingly, the aforementioned boundary results in a much higher current in the first 2 stages, so that only a very small part of the desalination takes place in the last stage, giving rise to a more inefficient (but feasible) stage. Another practical consequence of considering LCD is that the system requires a higher amount of energy, going from 5.6 to 6.8 kWh/m^3. In general, the last part of the desalination is a very critical point, where working close to LCD is almost unavoidable. For this reason, in every case shown in this section the last stage always works at 90% of the limiting current.

Table 11. Summary of the main results of the cost optimisation of the 3 stage ED system with the conditions described in Table 10.

E_{spec}^{TOT} (kWh/m³)	$Total\ Cost$ (€/m³)	$Cost_{OP}$ (€/m³)	$Cost_{FIX}$ (€/m³)	J_p (l/m²/h)	$Q_C^{IN,tot}$ (m³/d)
2.4	0.35	0.24	0.11	3.5	467

Stage	I (A)	V (V)	$N_{cp,i}$	$\delta_{C,i}$ (µm)	$\delta_{D,i}$ (µm)
1	34.7	183	2000	270	150
2	51.5	323	1979	270	150
3	13.5	239	758	1000	150

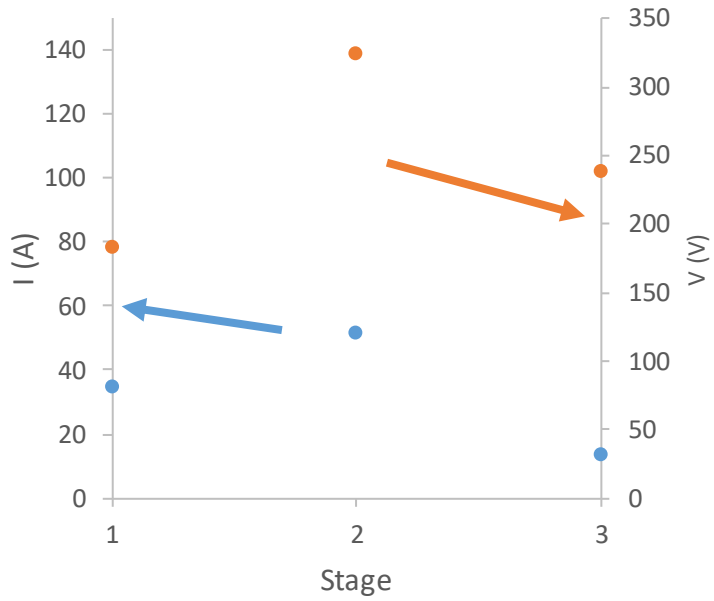

Figure 53. Voltage and current per stage of the cost optimised 3 stage ED system with the conditions described in Table 10. Cost of membranes 30 €/m², cost of energy 0.1 €/kWh.

The results of the complete optimisation problem, where the cost function (eq.(85)) was minimised by using the control variables of Table 10, are summarized in Table 11 and Figure 53. A minimum cost of 0.35 €/m³ was found for this 3 stages system. Of course, this would not be the final cost of water. However, it is a promising result that can give a good indication for comparing it with different schemes. This cost is associated with an energy consumption of 2.4 kWh/m³ which is a relatively low

energy consumption, fairly close to a typical RO consumption. Interestingly, the low energy consumption is also favoured by the high value of the inlet concentrate flowrate (corresponding to a flowrate ratio of 2), which minimises the concentration gradient throughout the stages. On the other hand, the water productivity is quite low compared to a typical value of an RO system (of about 20 l/m²/h), meaning that a larger amount of membrane area is required. The cell pair number decrease at each stage, becoming particularly low in the last one. This trend can be easily explained by the need to increase the flow velocity in order to avoid LCD issues. Unexpectedly, in the last stage the concentrate spacer thickness goes up to 1 mm. This result is a direct consequence of the velocity upper boundary constraint, as the thick spacer is used to compensate the low number of cell pairs. Finally, the diluate spacer thickness is the minimum allowed in each stage, in order to minimise the channel resistance and to increase the LCD.

In order to identify possible ways of further improvement, the optimisation was repeated for different length of the stacks and for different number of stages.

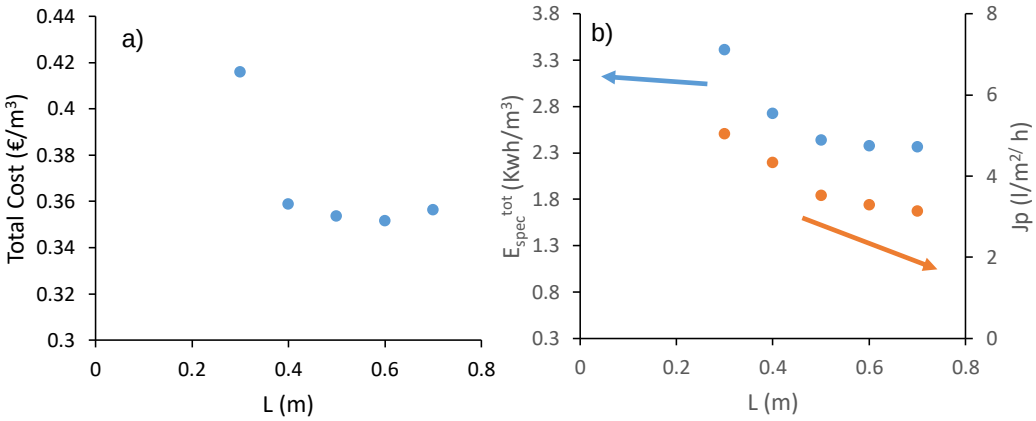

Figure 54. Cost optimisation results of the 3 stage ED system at different stacks' length. a) Total cost, b) energy consumption and water productivity. Process conditions (except for the stack length) are the ones listed in Table 10. Cost of membranes 30 €/m², cost of energy 0.1 €/kWh.

Figure 54 shows the results for the sensitivity to the stack length. The range 0.3-0.7 m was analysed. As can be seen, having very short stacks causes a significant increase in the total cost due to a significant increase in the energy consumption that is not compensated by the lower amount of membrane area (Figure 54 b). On the other hand, longer stacks allow lower cost due to lower energy consumptions, even though the water productivity decreases. After 0.6 m the decrease in energy consumption becomes negligible, water productivity prevails and the total costs start to rise. Nevertheless, the cost difference between 0.5 and 0.6 is so small that a difference can be hardly seen.

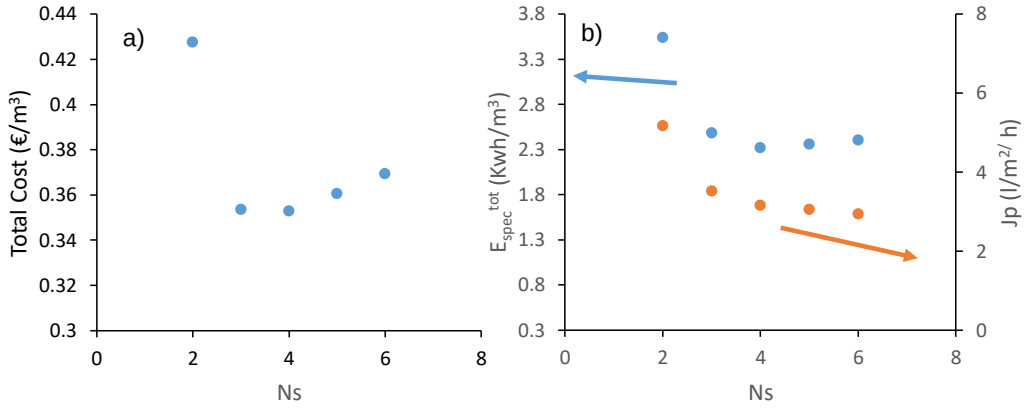

Figure 55. Cost optimisation results of the multistage ED system at different number of stages. a) Total cost, b) energy consumption and water productivity. Process conditions (except for number of stages) are the ones listed in Table 10. Cost of membranes 30 €/m², cost of energy 0.1 €/kWh.

The results for the sensitivity to the number of stages, is presented in Figure 55. Similarly to what happens when changing the stack length, going from 2 to 3 stages causes a significant reduction of the total cost, due to the reduction in the energy consumption that is almost not affected by the lower water productivity. On the other hand, longer stacks allow lower cost due to lower energy consumptions, even though the water productivity decreases. However, a further increase in the number of stages does not seem to have any advantages. In fact, with more than 4 stages the total cost increases as the membrane area increases (i.e. water productivity decreases) while the energy consumption does not get lower.

From the previous sensitivity analyses, it is clear how at the chosen stack cost (i.e. 30 €/m²) the energy consumption represents the limiting factor of the cost function. In order to have a further proof of this, the results of the cost optimisation were compared with the results of the optimisation of the energy consumption.

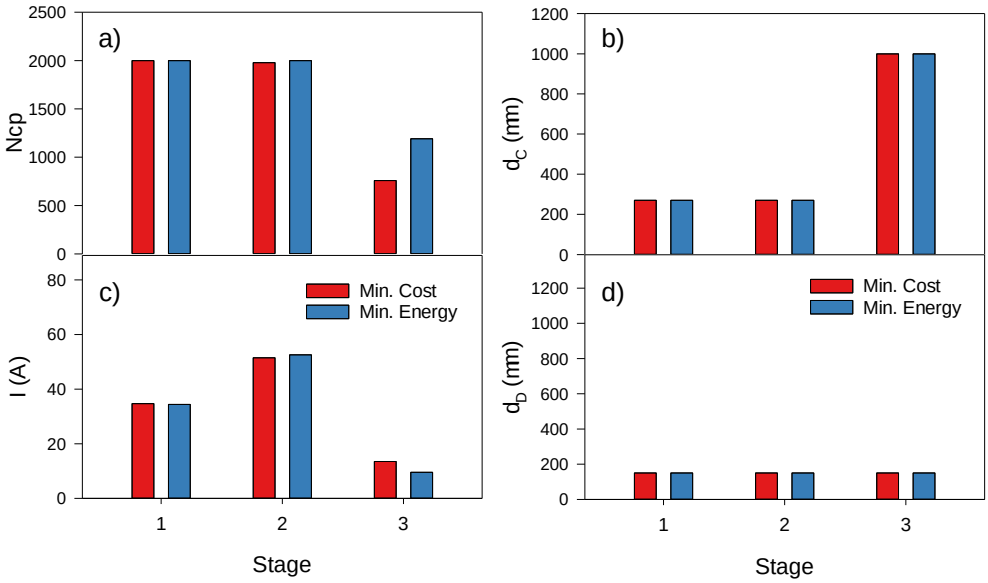

Figure 56. Cost optimisation vs energy optimisation results of the 3 stage ED system. a) Number of cell pairs per stage, b) concentrate channel thickness per stage, c) current per stage, d) diluate channel thickness per stage. Process conditions are listed in Table 10. Cost of stack 30 €/m², cost of energy 0.1 €/kWh.

Figure 56 shows the results of the comparison between cost and energy optimisation in therms of number of cell pairs, current and channels' thickness. As can be seen, the number of cell pairs is the same for the first stage, almost equal in the second one while a small different appears in the last one. The same thing applies to the current per stage. On the other hand, concentrate and diluate thickness are the same in the two scenarios. In general, a very similar optimal configuration is found when minimising the total cost and the energy consumption, confirming that the latter has the highest impact in the cost function.

Clearly, if the cost of the stack changes, the relative impact that energy and membranes have in the cost function changes. This effect is represented in Figure 57, where a sensitivity analysis on the cost of the stack was performed, analysing the range that goes from 15 to 120 €/m².

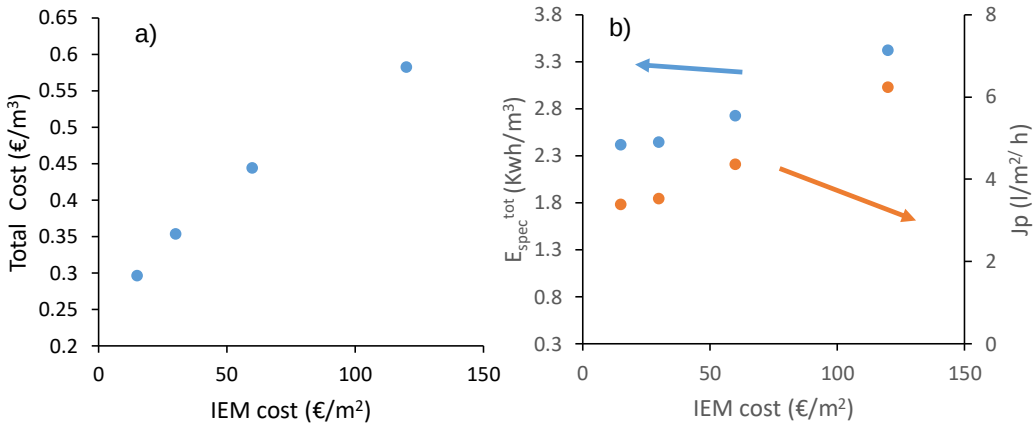

Figure 57. Cost optimisation results of the 3 stage ED system at different cost of the stack per m². a) Total cost, b) energy consumption and water productivity. Process conditions are the ones listed in Table 10. Cost of energy 0.1 €/kWh.

Besides the straightforward conclusion indicating that, increasing the stack cost the total cost increases (Figure 57 a), an important conclusion can be driven by comparing the behaviour of the specific energy consumption and the water productivity. Both of these quantities have a very similar increasing trend with the stack cost. Therefore, the higher is the membrane cost, the higher will be the optimal energy consumption. In the same way, the water productivity will also be higher, indicating a reduction in the IEM area.

At a very high stack cost, one would expect the cost and the energy optimisation to have very different outcomes. For this reason, the same detailed comparison done for the 30 €/m² case (Figure 56), was repeated for 120 €/m² and presented in Figure 58.

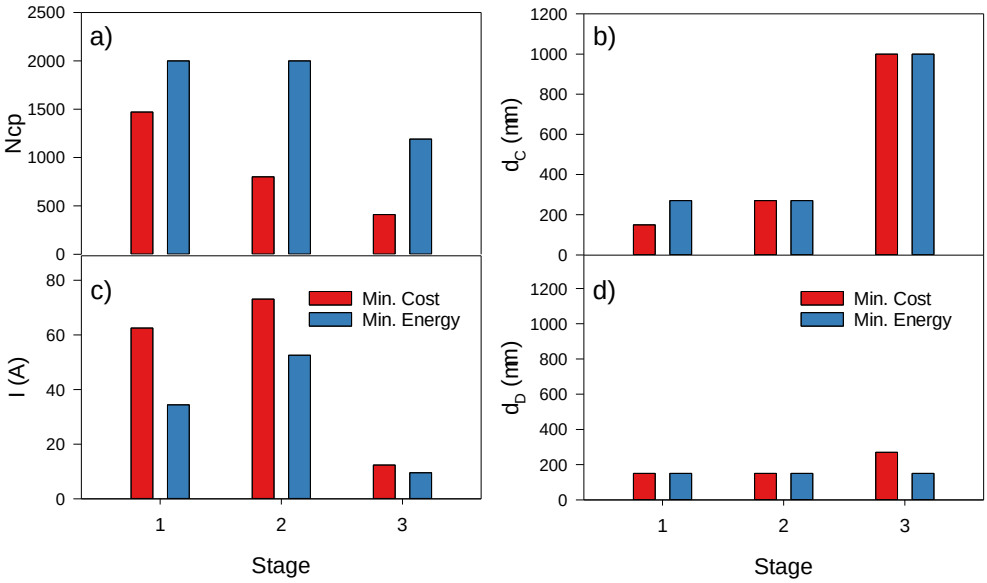

Figure 58. Cost optimisation vs energy optimisation results of the 3 stage ED system. a) Number of cell pairs per stage, b) concentrate channel thickness per stage, c) current per stage, d) diluate channel thickness per stage. Process conditions are listed in Table 10. Cost of the stack 120 €/m², cost of energy 0.1 €/kWh.

Figure 58 shows the comparison between cost and energy optimisation for the highest stack cost considered in the sensitivity analysis. Differently from the 30 €/m² case, the two optimisation have very different outcomes. Although the spacers' thickness is almost the same (except for the concentrate in the first stage and for the diluate in the last one), the number of cell pairs and the current per stage differ significantly. Interestingly, in the cost optimisation the number of cell pairs is always lower, proving that, at this stack cost, is crucial to minimise the membrane area.

5.2 RED-ED integrated process

The optimisation study shown in the previous section was also performed for the RED-ED integrated system shown in Figure 59. The RED system is used as pre-treatment step to achieve a pre-dilution of the seawater feed. In addition, the pre-treatment unit can work as RED, scRED and ARED based on the sign of V_{load}, which represent the voltage of the external load of the RED system (Figure 59). In particular, if $V_{load}>0$ a passive element is connected to the RED unit that is working with its standard configuration, if $V_{load}=0$ the unit is working in short-circuit and if $V_{load}<0$ an active element (i.e. voltage generator) is connected to the unit that is working in ARED mode.

For the sake of clarity, it should be noted that in order to simulate the RED unit, the model presented by La Cerva et al. [6,457] was used.

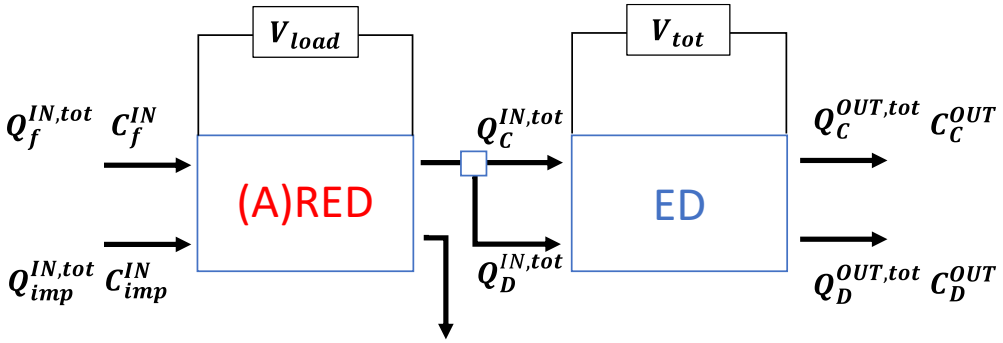

Figure 59. Schematic representation of the RED-ED plant. Symbols of flowrates and concentrations of the main streams as well as of the applied/produced voltage are reported.

As for the multistage case, the study was focused on plant with fixed dimensions (i.e. length and width) that has to desalt a 30 g/l feed having a fixed production capacity of 200 m³/d and a target concentration of the product water of 0.25 g/l. In addition, a 1 g/l impaired water is used as dilute stream in the RED unit. Table 12 presents a summary of process conditions for the optimisation problem.

Table 12. List of the fixed variables, control variables and constraints of the optimisation problem for the RED-ED system. Length and width are the same for each stage. Spacers' thickness is taken as an enumerated variable where only 150, 270, 500 and 1000 µm can be chosen.

Fixed variables	C_f^{IN} **(g/l)**	C_{imp}^{IN} **(g/l)**	C_D^{OUT} **(g/l)**	$Q_D^{OUT,tot}$ **(m³/d)**	L **(cm)**	b **(cm)**	**Type of membranes**
	30	1	0.25	200	50	50	FUJIFILM Type 10
Control variables	$Q_{imp}^{IN,tot}$ **(m³/d)**	V_{load} **(V)**	V_{tot} **(V)**	Q_{imp}^{IN}/Q_D^{IN}	$N_{cp,i}$	$\delta_{C,i}$ **(µm)**	$\delta_{D,i}$ **(µm)**
	0-500	-300 - 300	0 - 1000	0.5-2	1 - 2000	150 - 1000	150 - 1000
Constraints		I/I_{lim}		$u_{C,i}$ **(cm/s)**	$u_{D,i}$ **(cm/s)**		Q_f^{IN}/Q_{imp}^{IN}
		0 - 0.9		0.5 - 5	0.5 - 5		0.5 - 2

The optimisation study aimed at minimising the cost function of eq.(85), where E_{spec}^{TOT} has the same meaning as in eq.(53). The only difference is in the sign of the power of RED unit that is negative (i.e. produced) when working in standard RED mode and positive in the other configurations (i.e. consumed power). In order to achieve the desired minimisation, spacer thickness and number of cell pairs where taken as control variables for both RED and ED. In addition, V_{load}, ED applied voltage, the impaired water flowrate entering in the RED unit and the feed ration in ED were also considered (Table 12). Similarly to the multistage optimisation, the spacers' thickness was considered as enumerated integer, where only a limited number of choices (i.e. 150, 270, 500, 1000 μm) could have been taken.

The channel velocity of both units was limited to the range between 0.5 and 5 cm/s and the ratio between the RED inlet flowrates was limited to the 0.5-2 range. Finally, the same LCD constraint described in section 5.1 was kept for the ED unit. For the complete list of fixed, controlled and constrained variables it is possible to refer to Table 12.

Table 13. Summary of the main results of the cost optimisation of the RED-ED system with the conditions described in Table 12.

E_{spec}^{TOT} (kWh/m³)	$Total\ Cost$ (€/m³)	$Cost_{OP}$ (€/m³)	$Cost_{FIX}$ (€/m³)	J_p (l/m²/h)	$Q_{imp}^{IN,tot}$ (m³/d)
3.5	0.42	0.35	0.07	4.9	362

Stage	I (A)	V (V)	$N_{cp,i}$	$\delta_{C,i}$ (μm)	$\delta_{D,i}$ (μm)
RED	53.1	-178	2000	150	150
ED	45.3	417	1377	270	150

Table 13 summarises the cost optimisation results. A minimum cost of 0.42 €/m³ was found for this system. Despite the higher water productivity, this cost is higher than what was shown for the multistage system mainly due to the higher energy consumption of 3.5 kWh/m³. It is interesting to note that, differently from the multistage case, the impaired water inlet flowrate has a value close to the concentrate flowrate (i.e. flowrate ratio ~1). In this case, the value of the flowrate is a trade-off between maximising the dilution (for which the diluate flowrate should be as high as possible) and minimising pumping energy and channel resistance. In addition, the concentrate flowrate in ED is half of the diluate one, meaning that in this case the most advantageous thing is the maximisation of the amount of product rather than the minimisation of the concentration gradient.

An important outcome of this optimisation is that, in these conditions, the most important role of RED unit is the dilution rather than the energy production. This can be seen from Table 13 that shows a negative voltage in RED, indicating that the unit is working in assisted mode.

In order to explore the system, a sensitivity analysis on the channel length was performed.

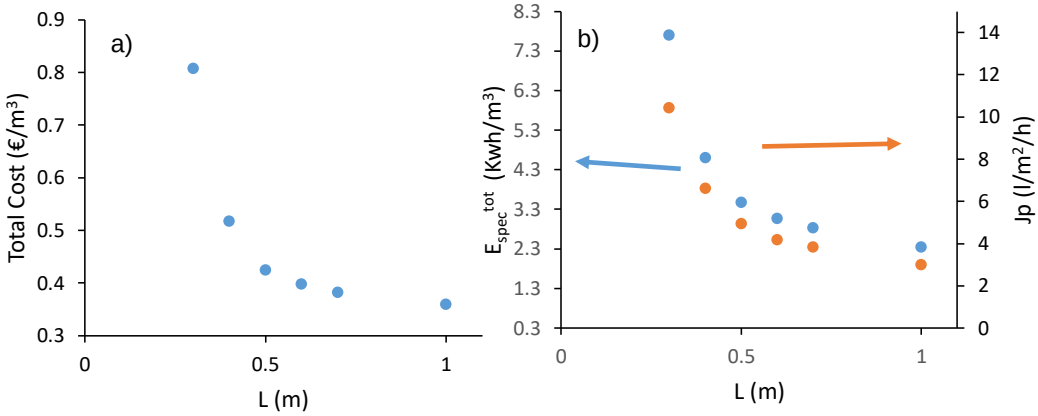

Figure 60. Cost optimisation results of the RED-ED system at different RED and ED stacks' length. a) Total cost, b) energy consumption and water productivity. Process conditions (except for the stack length) are the ones listed in Table 12. Cost of the stack 30 €/m², cost of energy 0.1 €/kWh.

Graphs in Figure 60 show what happens to the total cost, the energy consumption and the water productivity when changing the channels' length. The total cost clearly follows the energy consumption trend that decreases with the length. The drop of the water productivity does not seem to significantly affect the cost, even though the length was increased up to 1 m.

The role of the energy consumption as limiting factor in the cost function can be seen also comparing cost and energy optimisation that, as shown in Figure 61, lead to a very similar configuration.

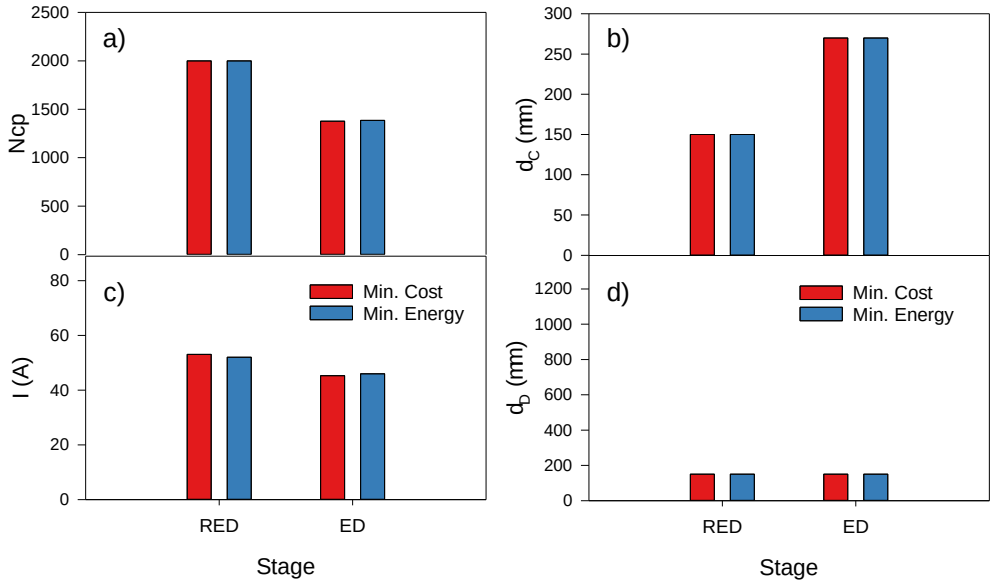

Figure 61. Cost optimisation vs energy optimisation results of the RED-ED system. a) Number of cell pairs per stage, b) concentrate channel thickness per stage, c) current per stage, d) diluate channel thickness per stage. Process conditions are listed in Table 12. Cost of the stack 30 €/m², cost of energy 0.1 €/kWh.

In order to study the system behaviour at different stack cost, a sensitivity on this parameter was carried out.

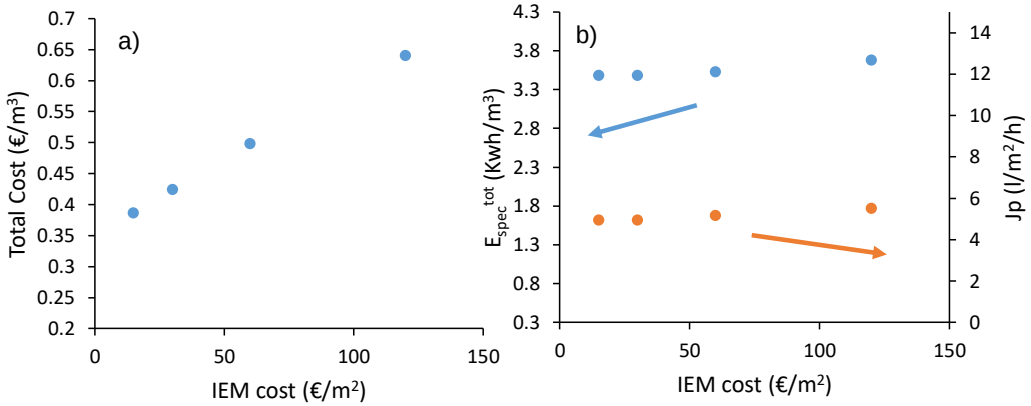

Figure 62. Cost optimisation results of RED-ED system at different cost of the stack per m². a) Total cost, b) energy consumption and water productivity. Process conditions are the ones listed in Table 12. Cost of energy 0.1 €/kWh.

Results of the stack cost sensitivity (Figure 62) shows that energy consumption remains the limiting factor even when the cost of the stack goes up to 120 €/m². This can be deduced by the fact that, although the total cost increases, the specific energy consumption and the water productivity have an almost flat trend.

This particularly strong limitations given by the specific energy consumption, suggests that the system can further improve by adding an additional stage. Therefore, a RED-ED-ED system was also studied.

The optimisation was carried out using the same process conditions as before (see Table 12), where the ED controls and constraints were applied to both stages.

Table 14. Summary of the main results of the cost optimisation of the RED-ED-ED system with the conditions described in Table 12 (same conditions apply to both ED units).

E_{spec}^{TOT} (kWh/m³)	$Total\ Cost$ (€/m³)	$Cost_{OP}$ (€/m³)	$Cost_{FIX}$ (€/m³)	J_p (l/m²/h)	$Q_{imp}^{IN,tot}$ (m³/d)
2.42	0.35	0.24	0.11	3.5	372

Stage	I (A)	V (V)	$N_{cp,i}$	$\delta_{C,i}$ (µm)	$\delta_{D,i}$ (µm)
RED	38.9	-86.4	2000	150	150
ED 1	37.2	336	2000	150	150
ED 2	13.4	241	759	500	150

Table 14 shows the results for the cost optimisation of the RED-ED-ED plant. Also in this case, the first unit works in ARED mode as shown by the value of the voltage. Adding a second ED stage, the total cost as well as the specific energy consumption drops significantly, reaching the same cost per m³ of produced water that was found in multistage ED at the same water productivity.

Whether RED-ED is more convenient than multistage ED or not depends on multiple factors such as cost and availability of seawater and impaired water. The main difference between the two configurations is that the presence of the impaired water significantly reduces the total amount of seawater that is required to produce the desired amount of drinking water (~700 m³/d for multistage vs ~400 m³/d for RED-ED), thus significantly reducing the recovery rate.

Conclusions

This thesis aimed at exploring new potentials of the electrodialysis process through the development of simulation tools, experimental investigations and process simulations, paving the way to a revival of this desalination technology by investigating poorly explored applications.

A comprehensive review on the ED process was firstly reported, critically analysing recent developments, criticalities and literature gaps.

Then, a novel ED hierarchical model was presented for both brackish water and seawater desalination. The model was validated by comparison with original experimental data showing a good agreement with experiments in a wide range of inlet concentrations, from brackish water to seawater applications. The main advantage of the hierarchical structure is the possibility to simulate complex schemes and operational strategies, allowing for higher flexibility and a wider applicability of the simulation tool. In particular, two representative examples have been presented, i.e. seawater multistage desalination and brackish water batch desalination. For the case of seawater multistage desalination, it was shown how the energy consumption could be drastically reduced by segmenting the operation, reducing the energy consumption from 4.59 kWh/m^3 to 1.94 kWh/m^3 only by changing the current distribution. Regarding the second example (brackish water batch desalination), the dynamic operation of a batch ED desalination unit was simulated. This has shown how to identify an optimal trade-off between desalination time and energy consumption and paving the way for the optimisation of the applied-voltage on a time-scale, similarly to what was shown for the multistage ED on the space-scale.

Subsequent research activities focused on specific applications that required the analysis of the dynamic behaviour.

In this context, the feasibility of the CED process has been proven with both experiments and modelling. A hierarchical dynamic model for the CED process has been presented for the first time. In particular, capacitive electrodes were modelled as an RC circuit distributed along the direction of the flowing solution. A set of experiments was performed with the aim of demonstrating the desalination capability of the CED system. In addition, an experimental characterisation of a set of capacitive electrodes was carried out and the collected data were used as input for the modelled RC circuit as well as to validate the CED model. Starting from a reference case, the model was used to assess the effect of different parameters on process performance in conditions closer to real desalination applications. By simulating the same scenario in the presence of an increased capacitance, it was possible to show that the presence of a high capacitance (i.e. 2 F/cm^2) would ensure the feasibility of longer desalination cycles prior to the occurrence of a polarity inversion, thus maintaining the electrode voltage drop below the water splitting threshold and the outlet diluate concentration below the target for a longer time. However, it has been shown that a further increase in the capacitance would unlikely lead to great improvement. A sensitivity analysis for the electrode resistance has been also carried out, demonstrating how 50 Ω*cm^2 is already a low value compared

to the Ohmic resistance of the membrane pile that is one order of magnitude higher. Finally, it has been shown how the increase in the number of cell pairs can change the effect of the electrodes, causing a shift in the limiting condition that controls the polarity switch frequency.

Another important application in which the dynamic aspect is crucial is when the ED process is combined with renewable energy sources. For this reason, the simulated behaviour of the single pass ED process powered by a hybrid PV/Wind energy source was studied. Simulations were performed through the ED process model in both a yearly and daily time scale. In the yearly time scale, a quasi-steady state approach was adopted. 4 ED units working in parallel were simulated, in order to demonstrate how the process can work over the year within a wide range of flowrates (from a total diluate flowrate of 230 to 920 m^3/d, corresponding to an absorbed power of 5 kW and 43 kW respectively, with this latter being 25% above the nominal operating condition), using the power produced by the simulated power source. The plant is able to operate for most of the year, even though it switches off for short periods during the winter due to the excessively low power, reaching a cumulative non-operational period of only 4.5 months. On the other hand, daily simulations aimed to study detailed process dynamics. Therefore, it was necessary to design a control system that is able to maintain the desired product concentration when the available power changes. By simulating the power variation over different reference days, it was shown that the controlled system works well in the entire range of flowrates, ensuring a stable operation and relatively short settling times of the outlet concentration, with maximum fluctuations of the set point lower than ± 10%. Results indicated that, given the high flexibility and the fast and controllable process dynamics, ED proved its suitability in the presence of highly non-constant power sources. Therefore, the process could be successfully implemented in battery-less polygeneration systems as a means of energy buffer.

The implications of treating real multi-ionic feeds was investigated through the development of a more advanced ED model. The model mixes the semi-empirical hierarchical approach with the Nernst-Planck-Donnan theory for the description of microscopic transport and membrane equilibrium. The modelling approach led to the presence of 2 main characterisation parameters, namely the ion diffusion coefficient and the membrane resistance. An experimental campaign aimed at the identification of the latter parameter was presented together to a set of experimental data collected from ED experiments with multi-ionic feeds. Data on IEMs' resistance showed how the membrane resistance is strongly affected by the solution composition, allowing the finding of an empirical correlation that was implemented into the model. Results from the ED experiments were involved in the model validation, where good prediction capabilities where shown, especially in the estimation of the outlet concentration of each ion.

Finally, process optimisation was used in order to explore energetic and cost potential of ED for seawater desalination. In particular, multistage and RED-ED configurations were analysed. A 3-stages ED system was optimised with the aim of minimising the cost for the production of 200 m^3/d of drinking water. The main process parameters such as stack geometry, applied voltages and feed ratio were modified during the optimisation. The final result indicated that it is possible to

reach 0.35 €/m^3 when a stack cost of 30 €/m^2 is considered, with the energy consumption being the main limiting factor. On the other hand, the RED-ED hybrid scheme can potentially reduce the overall consumption of seawater providing a pre-dilution step with RED using and impaired water stream. However, the optimisation results (performed using the same approach as per the multistage case) showed a higher final cost of water that can be potentially lowered to 0.35 €/m^3 adding an additional ED stage in the scheme.

All the presented activities showed how ED can still nowadays make an impact in the field of desalination in terms of technological development (i.e. ED with capacitive electrodes), new applications (i.e. ED as energy buffer) and novel schemes for the reduction of energy consumption (i.e. RED-ED configuration).

List of abbreviations

AC	Alternate Current
AEM	Anion-Exchange Membrane
BPM	BiPolar Membrane
CDI	Capacitive DeIonisation
CED	Capacitive electrodialysis
CEDI	Continuous ElectroDeIonisation
CEM	Cation-Exchange Membrane
DBL	Diffusion Boundary Layer
DC	Direct Current
DES	DESalination
EBPM	ElectroDialysis with Bipolar Membrane
ED	ElectroDialysis
EDI	Electro DeIonisation
EDL	Electrical Double Layer
EDM	ElectroDialysis Metathesis
EDR	ElectroDialysis Reversal
EDTA	EthyleneDiamineTetraAcetic
EIS	Electrical Impedance Spectroscopy
ER	Electrical Resistance
FCDI	Flow-electrode capacitive DeIonisation
IEC	Ion-Exchange Capacity
IEM	Ion-Exchange Membrane
IMC	Internal model control
IPN	InterPenetrating Network
LCD	Limiting current density
MV	MonoValent selective membrane
NP	Nernst-Planck
PEF	Pulsed Electrical Field
PV	PhotoVoltaic
RED	Reverse ElectroDialysis
RO	Reverse Osmosis

SED	SelElectroDialyis
SGP	Salinity Gradient Power
sIPN	Semi-InterPenetrating Network
TDS	Total dissolved solids
TMS	Teorell-Meyer-Sievers
TRL	Technological Readiness Level
WT	Wind turbine
ZLD	Zero Liquid Discharge

List of symbols

A	Membrane area (m^2)
A_r	Rotor area (m^2)
a_1	Parameter of Islam et al.' equation (A^o)
a	Activity (mol/m^3)
A_1	Debye-Huckel constant
B	Constant of WT model (K/km)
b	Membrane width (m)
b'	Constant of Pitzer's equation
B'	Parameter of Islam et al.' equation ($m^{1/2}/mol^{1/2}$)
B'_1	Parameter of Islam et al.' equation ($S\ m^3\ /\ mol^{3/2}$)
B'_2	Parameter of Islam et al.' equation ($m^{3/2}/mol^{1/2}$)
B^γ	Second virial coefficient of Pitzer's equation (kg/mol)
B^φ	Second virial coefficient of Pitzer's equation (kg/mol)
C	Concentration (mol/m^3)
C^γ	Third virial coefficient of Pitzer's equation (kg^2/mol^2)
C^φ	Third virial coefficient of Pitzer's equation (kg^2/mol^2)
c_{el}	Specific capacitance (F/m^2)
c_p	Wind turbine power coefficient
$Cost_{FIX}$	Stack cost (€/m3)
$Cost_{OP}$	Energy cost (€/m3)

D	Diffusion coefficient (m^2/s)
D_{salt}	Salt permeability coefficient of one IEM (m^2/s)
d^{eq}	Equivalent diameter (m)
E_{spec}	Specific energy consumption (J/m^3)
E_{spec}^{salt}	Salt-specific energy consumption (J/mol)
$En.Cost$	Cost of the energy (€/kWh)
f	Darcy friction coefficient
f_S	Shadow factor
G_T	Insolation (W/m^2)
I	Current (A)
I_L	Photocurrent (A)
I_o	Diode reverse saturation current (A)
i	Current density (A/m^2)
J	Flux ($mol/m^2/s$)
J_P	Apparent product flux ($l/m^2/h$)
K	Process gain ($g\ s/m^3\ l$)
k	Boltzmann constant (J/K)
k_m	Mass transfer coefficient (m/s)
K_C	Controller gain ($m^3\ l/g\ s$)
L	Channel length (m)
L_p	Water permeability ($m^3/Pa/s/m^2$)
m	Molal concentration (mol/kg)
M_w	Molecular weight (g/mol)
n_1	Constant of membrane resistance correlation
n_2	Constant of membrane resistance correlation
N_{cp}	Number of cell pairs in a stack
N_M	Number of PV module connected in series
N_s	Number of stages
P	Power consumption (W)
Δp	Pressure drop (Pa)
Q	Volumetric flow rate (m^3/s)

q	Volumetric flux ($m^3/m^2/s$)
R_G	Universal gas constant (J/mol/K)
R	Areal electrical resistance (Ωm^2)
R_s	PV module series resistance (Ω)
Re	Reynolds number
s	Independent variable in the Laplace domain
Sh	Sherwood number
$Stack\ cost$	Capital cost of the stack (€/m^2)
$Stack\ life$	Expected stack life (s)
t_{IEM}	Membrane transport number
t_{SOL}	Solution transport number
t	Time (s)
T	Temperature (K)
T_{IEM}	Integral transport number
$Tot.Cost$	Total cost (€/m^3)
u	Velocity (m/s)
V	Voltage drop (V)
$\bar{V}$	Partial molar volume (m^3/mol)
V_{cp}	Voltage drop over a cell pair (V)
${V_{el}}^{j}$	Electrode j voltage drop (V)
V_{tank}	Tank volume (m^3)
V_{tot}	Overall voltage drop (V)
V_{10cp}	Voltage drop over 10 cell pairs (V)
w	Total water transport number
x	Coordinate in the direction of the main flow (m)
y	Coordinate in the direction perpendicular to the membrane (m)
z	Altitude (km)

Greek letters

α	Permselectivity
α_w	Parameter of Von Karman correlation
$\beta^{(0)}$	Parameter of Pitzer's equation
$\beta^{(1)}$	Parameter of Pitzer's equation
γ	Activity coefficient
γ_{PV}	Empirical PV curve-fitting parameter
δ	Channel, DBL or membrane thickness (m)
ε	Error (g/l)
ε_G	Material bang gap energy
ζ	Damping coefficient
η	Non-Ohmic voltage drop (V)
$\mu_{I_{sc}}$	Temperature coefficient of I_{sc} at ref. condition (A/K)
$\mu_{V_{oc}}$	Temperature coefficient of V_{oc} at ref. condition (V/K)
Λ	Equivalent conductivity (S m²/mol)
Λ^0	Equivalent conductivity at infinite dilution (S m² / mol)
ν	Van't Hoff coefficient
ν_{wind}	Wind speed (m/s)
ξ	Current efficiency
π	Osmotic pressure (Pa)
ρ	Air density (kg/m³)
ρ_w	Density (kg/m³)
σ	Conductivity (mS/cm)
σ_{el}	Surface charge density (C/m²)
τ_D	Derivative control time constant (s)
τ_I	Integral control time constant (s)
χ	Ion interaction coefficient (mS/cm)
φ	Osmotic coefficient
ψ	Viscosity of solution (Pa s)

Subscripts and superscripts

AEM	Anion-exchange membrane
av	Average
$blank$	Blank
$bulk$	Solution bulk
C	Concentrate
CEM	Cation-exchange membrane
co	Co-ion
$cond$	Conductive
$counter$	Counter-ion
D	Dilute
$diff$	Diffusive
Don	Donnan
$elev$	Height above the ground (elevation)
$eosm$	Electroosmotic
fix	Fixed charges
el	Capacitive electrode
eq	Equivalent circuit
i	Species i (cation or anion)
IEM	Ion-exchange membrane (anion, *AEM*, or cation, *CEM*)
IN	Inlet
int	Solution-membrane interface
ion	Ion
L	Left
mp	Point of maximum power
N_s	Number of stacks
oc	Open-circuit
osm	Osmotic
OUT	Outlet
R	Right
ref	Reference condition
sc	Short-circuit

SOL	Solution (dilute, D, or concentrate, C)
ss	Steady state
$tank$	Tank
tot	Total
w	Water

References

[1] IDA, Desalination YearBook 2016-2017, Water Desalination Report, 2017.

[2] J. Veerman, M. Saakes, S.J. Metz, G.J. Harmsen, Reverse electrodialysis: A validated process model for design and optimization, Chem. Eng. J. 166 (2011) 256–268. doi:10.1016/j.cej.2010.10.071.

[3] D.A. Vermaas, M. Saakes, K. Nijmeijer, Doubled Power Density from Salinity Gradients at Reduced Intermembrane Distance, Environ. Sci. Technol. 45 (2011) 7089–7095.

[4] D.A. Vermaas, M. Saakes, K. Nijmeijer, Power generation using profiled membranes in reverse electrodialysis, J. Memb. Sci. 385–386 (2011) 234–242. doi:10.1016/j.memsci.2011.09.043.

[5] A. Daniilidis, D.A. Vermaas, R. Herber, K. Nijmeijer, Experimentally obtainable energy from mixing river water, seawater or brines with reverse electrodialysis, Renew. Energy. 64 (2014) 123–131. doi:10.1016/j.renene.2013.11.001.

[6] M. La Cerva, M. Di Liberto, L. Gurreri, A. Tamburini, A. Cipollina, G. Micale, M. Ciofalo, Coupling CFD with simplified 1-D models to predict the performance of reverse electrodialysis stacks, J. Memb. Sci. 541 (2017) 595–610. doi:10.1016/j.memsci.2017.07.030.

[7] N.Y. Yip, D.A. Vermaas, K. Nijmeijer, M. Elimelech, Thermodynamic, Energy Efficiency, and Power Density Analysis of Reverse Electrodialysis Power Generation with Natural Salinity Gradients, Environ. Sci. Technol. 48 (2014) 4925–4936. doi:10.1021/es5005413.

[8] M. Tedesco, A. Cipollina, A. Tamburini, G. Micale, Towards 1 kW power production in a reverse electrodialysis pilot plant with saline waters and concentrated brines, J. Memb. Sci. 522 (2017).

[9] E.U., REvivED water, (2016). https://www.revivedwater.eu/ (accessed November 28, 2017).

[10] H. Strathmann, Electrodialysis, a mature technology with a multitude of new applications, Desalination. 264 (2010) 268–288. doi:10.1016/j.desal.2010.04.069.

[11] T. Yamabe, Present status of electrodialysis in Japan, Desalination. 23 (1977) 195–202. doi:10.1016/S0011-9164(00)82522-9.

[12] E. Vera, J. Ruales, M. Dornier, J. Sandeaux, R. Sandeaux, G. Pourcelly, Deacidification of clarified passion fruit juice using different configurations of electrodialysis, J. Chem. Technol. Biotechnol. 78 (2003) 918–925. doi:10.1002/jctb.827.

[13] M. Fidaleo, M. Moresi, Electrodialysis Applications in The Food Industry, Adv. Food Nutr. Res. 51 (2006) 265–360. doi:10.1016/S1043-4526(06)51005-8.

[14] F. Gonçalves, C. Fernandes, P. Cameira dos Santos, M.N. de Pinho, Wine tartaric stabilization by electrodialysis and its assessment by the saturation temperature, J. Food Eng. 59 (2003) 229–235. doi:10.1016/S0260-8774(02)00462-4.

[15] F. Fu, Q. Wang, Removal of heavy metal ions from wastewaters: A review, J. Environ. Manage. 92 (2011) 407–418. doi:10.1016/j.jenvman.2010.11.011.

[16] L. Marder, A.M. Bernardes, J. Zoppas Ferreira, Cadmium electroplating wastewater treatment using a laboratory-scale electrodialysis system, Sep. Purif. Technol. 37 (2004) 247–255. doi:10.1016/j.seppur.2003.10.011.

[17] M.A. Acheampong, R.J.W. Meulepas, P.N.L. Lens, Removal of heavy metals and cyanide from gold mine wastewater, J. Chem. Technol. Biotechnol. 85 (2010) 590–613. doi:10.1002/jctb.2358.

[18] M.R. Adiga, S.K. Adhikary, P.K. Narayanan, W.P. Harkare, S.D. Gomkale, K.P. Govindan, Performance analysis of photovoltaic electrodialysis desalination plant at Tanote in Thar desert, Desalination. 67 (1987) 59–66. doi:10.1016/0011-9164(87)90232-3.

[19] J.M. Veza, B. Penate, F. Castellano, Electrodialysis desalination designed for off-grid wind energy, Desalination. 160 (2004) 211–221. doi:10.1016/S0011-9164(04)90024-0.

[20] K. Nagasubramanian, F.P. Chlanda, K.J. Liu, Use of bipolar membranes for generation of acid and base - an engineering and economic analysis, J. Memb. Sci. 2 (1977) 109–124. doi:10.1016/S0376-7388(00)83237-8.

[21] L. Bazinet, D. Ippersiel, C. Gendron, J. René-Paradis, C. Tétrault, J. Beaudry, M. Britten, B. Mahdavi, J. Amiot, F. Lamarche, Bipolar Membrane Electroacidification of Demineralized Skim Milk, J. Agric. Food Chem. 49 (2001) 2812–2818. doi:10.1021/jf000982r.

[22] X. Tongwen, Electrodialysis processes with bipolar membranes (EDBM) in environmental protection—a review, Resour. Conserv. Recycl. 37 (2002) 1–22. doi:10.1016/S0921-3449(02)00032-0.

[23] V.J. Frilette, Preparation and Characterization of Bipolar Ion Exchange Membranes, J. Phys. Chem. 60 (1956) 435–439. doi:10.1021/j150538a013.

[24] Y.C. Chiao, F.P. Chlanda, K.N. Mani, Bipolar membranes for purification of acids and bases, J. Memb. Sci. 61 (1991) 239–252. doi:10.1016/0376-7388(91)80018-2.

[25] L. Bazinet, F. Lamarche, D. Ippersiel, Bipolar-membrane electrodialysis: Applications of electrodialysis in the food industry, Trends Food Sci. Technol. 9 (1998) 107–113. doi:10.1016/S0924-2244(98)00026-0.

[26] M. Reig, C. Valderrama, O. Gibert, J.L. Cortina, Selectrodialysis and bipolar membrane electrodialysis combination for industrial process brines treatment: Monovalent-divalent ions separation and acid and base production, Desalination. 399 (2016) 88–95. doi:10.1016/j.desal.2016.08.010.

[27] Y. Zhang, S. Paepen, L. Pinoy, B. Meesschaert, B. Van der Bruggen, Selectrodialysis: Fractionation of divalent ions from monovalent ions in a novel electrodialysis stack, Sep. Purif. Technol. 88 (2012) 191–201. doi:10.1016/j.seppur.2011.12.017.

[28] A.T.K. Tran, Phosphate Pre-Concentrate from Wastewater for Phosphate Recovery by Selectrodialysis, in: Institute of Electrical and Electronics Engineers Inc., 2016: pp. 55–58. doi:10.1109/GTSD.2016.23.

[29] Y. Zhang, E. Desmidt, A. Van Looveren, L. Pinoy, B. Meesschaert, B. Van Der Bruggen, Phosphate separation and recovery from wastewater by novel electrodialysis, Environ. Sci. Technol. 47 (2013) 5888–5895. doi:10.1021/es4004476.

[30] C. Alhéritière, W.R. Ernst, T.A. Davis, Metathesis of magnesium and solium salt systems by electrodialysis, Desalination. 115 (1998) 189–198. doi:10.1016/S0011-9164(98)00037-X.

[31] R. Bond, B. Batchelor, T.A. Davis, B. Klayman, Zero liquid discharge desalination of brackish water with an innovative form of electrodialysis: Electrodialysis metathesis, in: Florida Water Resour. J., 2011: pp. 36–44.

[32] S.K. Thampy, B.S. Joshi, K.P. Govindan, Preparation of potassium bicarbonate by electrodialysis technique, Indian J. Technol. 12 (1985) 454–457.

[33] L.M. Camacho, J.A. Fox, J.O. Ajedegba, Optimization of electrodialysis metathesis (EDM) desalination using factorial design methodology, Desalination. 403 (2017) 136–143. doi:10.1016/j.desal.2016.07.028.

[34] V.A. Shaposhnik, K. Kesore, An early history of electrodialysis with permselective membranes, J. Memb. Sci. 136 (1997) 35–39. doi:10.1016/S0376-7388(97)00149-X.

[35] V.D. Grebenyuk, O. V. Grebenyuk, Electrodialysis: From an idea to realization, Russ. J. Electrochem. 38 (2002) 806–809. doi:10.1023/A:1016897224948.

[36] F.G. Donnan, The Theory of Membrane Equilibria., Chem. Rev. 1 (1924) 73–90. doi:10.1021/cr60001a003.

[37] T. Teorell, An Attempt to Formulate a Quantitative Theory of Membrane Permeability, Exp. Biol. Med. 33 (1935) 282–285. doi:10.3181/00379727-33-8339C.

[38] E.R. Reahl, Half A Century of Desalination With Electrodialysis, GE Water Process Technol. (2006) 1–5.

[39] A. Campione, L. Gurreri, M. Ciofalo, G. Micale, A. Tamburini, A. Cipollina, Electrodialysis for water desalination: A critical assessment of recent developments on process fundamentals, models and applications, Desalination. 434 (2018) 121–160. doi:10.1016/j.desal.2017.12.044.

[40] G. Belfort, G.A. Guter, An experimental study of electrodialysis hydrodynamics, Desalination. 10 (1972) 221–262. doi:10.1016/S0011-9164(00)82001-9.

[41] G. Grossman, A.A. Sonin, Experimental study of the effects of hydrodynamics and membrane fouling in electrodialysis, Desalination. 10 (1972) 157–180. doi:10.1016/S0011-9164(00)80084-3.

[42] J.M. Chiapello, M. Bernard, Improved spacer design and cost reduction in an electrodialysis system, J. Memb. Sci. 80 (1993) 251–256. doi:10.1016/0376-7388(93)85149-Q.

[43] A.H. Galama, M. Saakes, H. Bruning, H.H.M. Rijnaarts, J.W. Post, Seawater predesalination with electrodialysis, Desalination. 342 (2014) 61–69. doi:10.1016/j.desal.2013.07.012.

[44] M. Demircioglu, N. Kabay, I. Kurucaovali, E. Ersoz, Demineralization by

electrodialysis (ED) - Separation performance and cost comparison for monovalent salts, Desalination. 153 (2003) 329–333. doi:10.1016/S0011-9164(02)01119-0.

[45] E.J. Parsi, Large Electrodialysis Stack Development, Desalination. 19 (1976) 139–151. doi:10.1016/S0011-9164(00)88024-8.

[46] A. von Gottberg, New High-Performance Spacers in Electro- Dialysis Reversal (EDR) Systems, in: Proc. 1998 AWWA Anu. Conf., Dallas, Texas, 1998.

[47] O. Kedem, Reduction of polarization in electrodialysis by ion-conducting spacers, Desalination. 16 (1975) 105–118. doi:10.1016/S0011-9164(00)84095-3.

[48] O. Kedem, Y. Maoz, Ion conducting spacer for improved ed, Desalination. 19 (1976) 465–470. doi:10.1016/S0011-9164(00)88055-8.

[49] Y. Winograd, A. Solan, M. Toren, Mass transfer in narrow channels in the presence of turbulence promoters, Desalination. 13 (1973) 171–186. doi:10.1016/S0011-9164(00)82043-3.

[50] H. Strathmann, Ion-exchange membrane separation processes, First ed., Elsevier, Amsterdam, 2004.

[51] C. Larchet, V.I. Zabolotsky, N. Pismenskaya, V. V Nikonenko, A. Tskhay, K. Tastanov, G. Pourcelly, Comparison of different ED stack conceptions when applied for drinking water production from brackish waters, Desalination. 222 (2008) 489–496. doi:10.1016/j.desal.2007.02.067.

[52] B. Van der Bruggen, Advances in electrodialysis for water treatment, in: A. Basile, A. Cassano, N.K. Rastogi (Eds.), Adv. Membr. Technol. Water Treat. Mater. Process. Appl., Woodhead Publishing, 2015: pp. 185–203. doi:10.1016/B978-1-78242-121-4.00006-X.

[53] D.A. Vermaas, S. Bajracharya, B.B. Sales, M. Saakes, B. Hamelers, K. Nijmeijer, Clean energy generation using capacitive electrodes in reverse electrodialysis, Energy Environ. Sci. 6 (2013) 643–651. doi:10.1039/C2EE23562E.

[54] O.N. Demirer, R.L. Clifton, C.A.R. Perez, R. Naylor, C. Hidrovo, Characterization of Ion Transport and -Sorption in a Carbon Based Porous Electrode for Desalination Purposes, J. Fluids Eng. 135 (2013) 41201–41208. http://dx.doi.org/10.1115/1.4023294.

[55] A. Campione, A. Cipollina, E. Toet, L. Gurreri, I.D.L. Bogle, G. Micale, Water desalination by capacitive electrodialysis: Experiments and modelling, Desalination. 473 (2020) 114–150. doi:10.1016/j.desal.2019.114150.

[56] D.A. Vermaas, M. Saakes, K. Nijmeijer, Capacitive Electrodes for Energy Generation by Reverse Electrodialysis, Procedia Eng. 44 (2012) 496–497. doi:10.1016/j.proeng.2012.08.463.

[57] G.J. Doornbusch, M. Tedesco, J.W. Post, Z. Borneman, K. Nijmeijer, Experimental investigation of multistage electrodialysis for seawater desalination, Desalination. 464 (2019) 105–114. doi:10.1016/J.DESAL.2019.04.025.

[58] A. Campione, A. Cipollina, I.D.L. Bogle, L. Gurreri, A. Tamburini, M. Tedesco, G. Micale, A hierarchical model for novel schemes of electrodialysis desalination,

Desalination. 465 (2019) 79–93. doi:10.1016/j.desal.2019.04.020.

[59] Y. Tanaka, Regularity in ion-exchange membrane characteristics and concentration of sea water, J. Memb. Sci. 163 (1999) 277–287. doi:10.1016/S0376-7388(99)00169-6.

[60] A. V Demin, V.I. Zabolotskii, Model verification of limiting concentration by electrodialysis of an electrolyte solution, Russ. J. Electrochem. 44 (2008) 1058–1064. doi:10.1134/S1023193508090115.

[61] H. Strathmann, A. Grabowski, G. Eigenberger, Ion-Exchange Membranes in the Chemical Process Industry, Ind. Eng. Chem. Res. 52 (2013) 10364–10379. doi:10.1021/ie4002102.

[62] A.H. Galama, J.W. Post, M.A. Cohen Stuart, P.M. Biesheuvel, Validity of the Boltzmann equation to describe Donnan equilibrium at the membrane–solution interface, J. Memb. Sci. 442 (2013) 131–139. doi:10.1016/j.memsci.2013.04.022.

[63] J. Ran, L. Wu, Y. He, Z. Yang, Y. Wang, C. Jiang, L. Ge, E. Bakangura, T. Xu, Ion exchange membranes: New developments and applications, J. Memb. Sci. 522 (2017) 267–291.

[64] N.P. Berezina, N.A. Kononenko, O.A. Dyomina, N.P. Gnusin, Characterization of ion-exchange membrane materials: properties vs structure., Adv. Colloid Interface Sci. 139 (2008) 3–28. doi:10.1016/j.cis.2008.01.002.

[65] C. Larchet, L. Dammak, B. Auclair, S. Parchikov, V. Nikonenko, A simplified procedure for ion-exchange membrane characterisation, New J. Chem. 28 (2004) 1260. doi:10.1039/b316725a.

[66] K. Kontturi, L. Murtomäki, J.A. Manzanares, Ionic Transport Processes, Oxford University Press, New York, 2008. doi:10.1093/acprof:oso/9780199533817.001.0001.

[67] N. Lakshminarayanaiah, Transport phenomena in artificial membranes, Chem. Rev. 65 (1965) 491.

[68] A.H. Galama, J.W. Post, H.V.M. Hamelers, V. V Nikonenko, P.M. Biesheuvel, On the Origin of the Membrane Potential Arising Across Densely Charged Ion Exchange Membranes: How Well Does the Teorell-Meyer-Sievers Theory Work?, J. Membr. Sci. Res. 2 (2016) 128–140. doi:10.22079/jmsr.2016.20311.

[69] M.B. Kristensen, A. Bentien, M. Tedesco, J. Catalano, Counter-ion transport number and membrane potential in working membrane systems, J. Colloid Interface Sci. 504 (2017) 800–813. doi:10.1016/j.jcis.2017.06.010.

[70] R.K. Nagarale, G.S. Gohil, V.K. Shahi, Recent developments on ion-exchange membranes and electro-membrane processes., Adv. Colloid Interface Sci. 119 (2006) 97–130. doi:10.1016/j.cis.2005.09.005.

[71] G.E. Molau, Heterogeneous ion-exchange membranes, J. Memb. Sci. 8 (1981) 309–330. doi:10.1016/S0376-7388(00)82318-2.

[72] W. Garcia-Vasquez, L. Dammak, C. Larchet, V. Nikonenko, N. Pismenskaya, D. Grande, Evolution of anion-exchange membrane properties in a full scale electrodialysis stack, J. Memb. Sci. 446 (2013) 255–265. doi:10.1016/j.memsci.2013.06.042.

[73] C. Genies, R. Mercier, B. Sillion, N. Cornet, G. Gebel, M. Pineri, Soluble sulfonated naphthalenic polyimides as materials for proton exchange membranes, Polymer (Guildf). 42 (2001) 359–373. doi:10.1016/S0032-3861(00)00384-0.

[74] T. Sata, Studies on anion exchange membranes having permselectivity for specific anions in electrodialysis — effect of hydrophilicity of anion exchange membranes on permselectivity of anions, J. Memb. Sci. 167 (2000) 1–31. doi:10.1016/S0376-7388(99)00277-X.

[75] V.K. Shahi, S.K. Thampy, R. Rangarajan, Preparation and electrochemical characterization of sulfonated interpolymer of polyethylene and styrene–divinylbenzene copolymer membranes, React. Funct. Polym. 46 (2000) 39–47. doi:10.1016/S1381-5148(00)00031-6.

[76] Y. Woo, S.Y. Oh, Y.S. Kang, B. Jung, Synthesis and characterization of sulfonated polyimide membranes for direct methanol fuel cell, J. Memb. Sci. 220 (2003) 31–45. doi:10.1016/S0376-7388(03)00185-6.

[77] V.I. Zabolotsky, V. V. Nikonenko, Effect of structural membrane inhomogeneity on transport properties, J. Memb. Sci. 79 (1993) 181–198. doi:10.1016/0376-7388(93)85115-D.

[78] C. Larchet, S. Nouri, B. Auclair, L. Dammak, V. Nikonenko, Application of chronopotentiometry to determine the thickness of diffusion layer adjacent to an ion-exchange membrane under natural convection., Adv. Colloid Interface Sci. 139 (2008) 45–61. doi:http://dx.doi.org/10.1016/j.cis.2008.01.007.

[79] A.H. Galama, D.A. Vermaas, J. Veerman, M. Saakes, H.H.M. Rijnaarts, J.W. Post, K. Nijmeijer, Membrane resistance: The effect of salinity gradients over a cation exchange membrane, J. Memb. Sci. 467 (2014) 279–291. doi:10.1016/j.memsci.2014.05.046.

[80] J. Kamcev, R. Sujanani, E.-S. Jang, N. Yan, N. Moe, D.R. Paul, B.D. Freeman, Salt concentration dependence of ionic conductivity in ion exchange membranes, J. Memb. Sci. 547 (2018) 123–133. doi:10.1016/J.MEMSCI.2017.10.024.

[81] T. Xu, Ion exchange membranes: State of their development and perspective, J. Memb. Sci. 263 (2005) 1–29. doi:10.1016/j.memsci.2005.05.002.

[82] B.D. Gupta, A. Chapiró, Preparation of ion-exchange membranes by grafting acrylic acid into pre-irradiated polymer films-1. grafting into polyethylene, Eur. Polym. J. 25 (1989) 1137–1143. doi:10.1016/0014-3057(89)90170-5.

[83] J.-L. Gineste, J.-L. Garaud, G. Pourcelly, Grafting of acrylic acid with diethyleneglycol–dimethacrylate onto radioperoxided polyethylene, J. Appl. Polym. Sci. 48 (1993) 2113–2122. doi:10.1002/app.1993.070481206.

[84] E.-S.A. Hegazy, N.H. Taher, A.R. Ebaid, Preparation and some properties of hydrophilic membranes obtained by radiation grafting of methacrylic acid onto fluorinated polymers, J. Appl. Polym. Sci. 41 (1990) 2637–2647. doi:10.1002/app.1990.070411111.

[85] S.-H. Choi, Y.C. Nho, Radiation-induced graft copolymerization of binary monomer mixture containing acrylonitrile onto polyethylene films, Radiat. Phys. Chem. 58 (2000) 157–168. doi:10.1016/S0969-806X(99)00367-9.

[86] J.A. Horsfall, K. V Lovell, Synthesis and characterization of acrylic acid-grafted hydrocarbon and fluorocarbon polymers with the simultaneous or mutual grafting technique, J. Appl. Polym. Sci. 87 (2003) 230–243. doi:10.1002/app.11358.

[87] B. Gupta, F.N. Büchi, G.G. Scherer, A. Chapiró, Crosslinked ion exchange membranes by radiation grafting of styrene/divinylbenzene into FEP films, J. Memb. Sci. 118 (1996) 231–238. doi:10.1016/0376-7388(96)00093-2.

[88] M. V Rouilly, E.R. Kötz, O. Haas, G.G. Scherer, A. Chapiró, Proton exchange membranes prepared by simultaneous radiation grafting of styrene onto Teflon-FEP films. Synthesis and characterization, J. Memb. Sci. 81 (1993) 89–95. doi:10.1016/0376-7388(93)85033-S.

[89] M.M. Nasef, H. Saidi, A.M. Dessouki, E.M. EI-Nesr, Radiation-induced grafting of styrene onto poly(tetrafluoroethylene) (PTFE) films. I. Effect of grafting conditions and properties of the grafted films, Polym. Int. 49 (2000) 399–406. doi:10.1002/(SICI)1097-0126(200004)49:4<399::AID-PI393>3.0.CO;2-W.

[90] T. Yamaki, M. Asano, Y. Maekawa, Y. Morita, T. Suwa, J. Chen, N. Tsubokawa, K. Kobayashi, H. Kubota, M. Yoshida, Radiation grafting of styrene into crosslinked PTEE films and subsequent sulfonation for fuel cell applications, Radiat. Phys. Chem. 67 (2003) 403–407. doi:10.1016/S0969-806X(03)00075-6.

[91] H. Herman, R.C.T. Slade, J.R. Varcoe, The radiation-grafting of vinylbenzyl chloride onto poly(hexafluoropropylene-co-tetrafluoroethylene) films with subsequent conversion to alkaline anion-exchange membranes: optimisation of the experimental conditions and characterisation, J. Memb. Sci. 218 (2003) 147–163. doi:10.1016/S0376-7388(03)00167-4.

[92] W. Lee, K. Saito, S. Furusaki, T. Sugo, K. Makuuchi, Design of urea-permeable anion-exchange membrane by radiation-induced graft polymerization, J. Memb. Sci. 81 (1993) 295–305. doi:10.1016/0376-7388(93)85181-U.

[93] R.K. Nagarale, G.S. Gohil, V.K. Shahi, R. Rangarajan, Preparation and electrochemical characterization of sulfonated polysulfone cation-exchange membranes: Effects of the solvents on the degree of sulfonation, J. Appl. Polym. Sci. 96 (2005) 2344–2351. doi:10.1002/app.21630.

[94] F. Wang, M.A. Hickner, Y.S. Kim, T.A. Zawodzinski, J.E. McGrath, Direct polymerization of sulfonated poly(arylene ether sulfone) random (statistical) copolymers: candidates for new proton exchange membranes, J. Memb. Sci. 197 (2002) 231–242. doi:10.1016/S0376-7388(01)00620-2.

[95] M.-S. Kang, Electrochemical characterization of sulfonated poly(arylene ether sulfone) (S-PES) cation-exchange membranes, J. Memb. Sci. 216 (2003) 39–53. doi:10.1016/S0376-7388(03)00045-0.

[96] J. Kerres, W. Cui, S. Reichle, New Sulfonated Eengineering Polymers via the Metalation Route. II. Sulfinated/Sulfonated Poly(ether sulfone) PSU Udel via metalation-sulfination-oxidation, J. Polym. Sci. Part A Polym. Chem. 34 (1996) 2421–2438. doi:10.1002/(SICI)1099-0518(19980715)36:9<1441::AID-POLA12>3.0.CO;2-4.

[97] G.-J. Hwang, H. Ohya, Preparation of anion exchange membrane based on block

copolymers. Part II: the effect of the formation of macroreticular structure on the membrane properties, J. Memb. Sci. 149 (1998) 163–169. doi:10.1016/S0376-7388(98)00194-X.

[98] G.-J. Hwang, H. Ohya, T. Nagai, Ion exchange membrane based on block copolymers. Part III: preparation of cation exchange membrane, J. Memb. Sci. 156 (1999) 61–65. doi:10.1016/S0376-7388(98)00331-7.

[99] P. Zschocke, D. Quellmalz, Novel ion exchange membranes based on an aromatic polyethersulfone, J. Memb. Sci. 22 (1985) 325–332. doi:10.1016/S0376-7388(00)81290-9.

[100] R.K. Nagarale, V.K. Shahi, R. Rangarajan, Preparation of polyvinyl alcohol–silica hybrid heterogeneous anion-exchange membranes by sol–gel method and their characterization, J. Memb. Sci. 248 (2005) 37–44. doi:10.1016/j.memsci.2004.09.025.

[101] P. V Vyas, B.G. Shah, G.S. Trivedi, P. Ray, S.K. Adhikary, R. Rangarajan, Characterization of heterogeneous anion-exchange membrane, J. Memb. Sci. 187 (2001) 39–46. doi:10.1016/S0376-7388(00)00613-X.

[102] X. Wu, G. He, S. Gu, Z. Hu, P. Yao, Novel interpenetrating polymer network sulfonated poly (phthalazinone ether sulfone ketone)/polyacrylic acid proton exchange membranes for fuel cell, J. Memb. Sci. 295 (2007) 80–87. doi:10.1016/j.memsci.2007.02.039.

[103] C.W. Lin, Y.F. Huang, A.M. Kannan, Semi-interpenetrating network based on cross-linked poly(vinyl alcohol) and poly(styrene sulfonic acid-co-maleic anhydride) as proton exchange fuel cell membranes, J. Power Sources. 164 (2007) 449–456. doi:10.1016/j.jpowsour.2006.10.081.

[104] J. Wang, R. He, Q. Che, Anion exchange membranes based on semi-interpenetrating polymer network of quaternized chitosan and polystyrene, J. Colloid Interface Sci. 361 (2011) 219–225. doi:10.1016/j.jcis.2011.05.039.

[105] Y.-J. Choi, M.-S. Kang, S.-H. Moon, Characterization of semi-interpenetrating polymer network polystyrene cation-exchange membranes, J. Appl. Polym. Sci. 88 (2003) 1488–1496. doi:10.1002/app.11860.

[106] L. Lebrun, E. Da Silva, M. Metayer, Elaboration of ion-exchange membranes with semi-interpenetrating polymer networks containing poly(vinyl alcohol) as polymer matrix, J. Appl. Polym. Sci. 84 (2002) 1572–1580. doi:10.1002/app.10420.

[107] L. Lebrun, N. Follain, M. Metayer, Elaboration of a new anion-exchange membrane with semi-interpenetrating polymer networks and characterisation, Electrochim. Acta. 50 (2004) 985–993. doi:10.1016/j.electacta.2004.07.040.

[108] H.-P. Brack, H.G. Bührer, L. Bonorand, G.G. Scherer, Grafting of pre-irradiated poly(ethylene-alt-tetrafluoroethylene) films with styrene: influence of base polymer film properties and processing parameters, J. Mater. Chem. 10 (2000) 1795–1803. doi:10.1039/b001851l.

[109] G.K. Kostov, O. Matsuda, S. Machi, Y. Tabata, Radiation synthesis of ion-exchange carboxylic fluorine containing membranes, J. Memb. Sci. 68 (1992) 133–140. doi:10.1016/0376-7388(92)80156-E.

[110] G.K. Kostov, A.N. Atanassov, Properties of cation-exchange membranes prepared by radiation grafting of acrylic acid onto tetrafluoroethylene–ethylene copolymers, J. Appl. Polym. Sci. 47 (1993) 1269–1276. doi:10.1002/app.1993.070470715.

[111] G.K. Kostov, S.C. Turmanova, Radiation-initiated graft copolymerization of 4-vinylpyridine onto polyethylene and polytetrafluoroethylene films and anion-exchange membranes therefrom, J. Appl. Polym. Sci. 64 (1997) 1469–1475. doi:10.1002/(SICI)1097-4628(19970523)64:8<1469::AID-APP3>3.0.CO;2-F.

[112] M.M. Nasef, H. Saidi, H.M. Nor, Proton exchange membranes prepared by simultaneous radiation grafting of styrene onto poly(tetrafluoroethylene-co-hexafluoropropylene) films. I. Effect of grafting conditions, J. Appl. Polym. Sci. 76 (2000) 220–227. doi:10.1002/(SICI)1097-4628(20000411)76:2<220::AID-APP11>3.0.CO;2-M.

[113] K.A. Mauritz, D.A. Mountz, D.A. Reuschle, R.I. Blackwell, Self-assembled organic/inorganic hybrids as membrane materials, Electrochim. Acta. 50 (2004) 565–569. doi:10.1016/j.electacta.2003.09.051.

[114] J. Zou, Y. Zhao, W. Shi, Preparation and properties of proton conducting organic–inorganic hybrid membranes based on hyperbranched aliphatic polyester and phosphoric acid, J. Memb. Sci. 245 (2004) 35–40. doi:10.1016/j.memsci.2004.07.015.

[115] I. Gautier-Luneau, A. Denoyelle, J.Y. Sanchez, C. Poinsignon, Organic—inorganic protonic polymer electrolytes as membrane for low-temperature fuel cell, Electrochim. Acta. 37 (1992) 1615–1618. doi:10.1016/0013-4686(92)80122-3.

[116] L. Depre, J. Kappel, M. Popall, Inorganic–organic proton conductors based on alkylsulfone functionalities and their patterning by photoinduced methods, Electrochim. Acta. 43 (1998) 1301–1306. doi:10.1016/S0013-4686(97)10034-2.

[117] L. Depre, M. Ingram, C. Poinsignon, M. Popall, Proton conducting sulfon/sulfonamide functionalized materials based on inorganic–organic matrices, Electrochim. Acta. 45 (2000) 1377–1383. doi:10.1016/S0013-4686(99)00346-1.

[118] R.K. Nagarale, G.S. Gohil, V.K. Shahi, R. Rangarajan, Organic–Inorganic Hybrid Membrane: Thermally Stable Cation-Exchange Membrane Prepared by the Sol–Gel Method, Macromolecules. 37 (2004) 10023–10030. doi:10.1021/ma048404p.

[119] A. Walcarius, Electrochemical Applications of Silica-Based Organic–Inorganic Hybrid Materials, Chem. Mater. 13 (2001) 3351–3372. doi:10.1021/cm0110167.

[120] D.S. Kim, H.B. Park, J.W. Rhim, Y.M. Lee, Proton conductivity and methanol transport behavior of cross-linked PVA/PAA/silica hybrid membranes, Solid State Ionics. 176 (2005) 117–126. doi:10.1016/j.ssi.2004.07.011.

[121] D.S. Kim, H.B. Park, J.W. Rhim, Y.M. Lee, Preparation and characterization of crosslinked PVA/SiO2 hybrid membranes containing sulfonic acid groups for direct methanol fuel cell applications, J. Memb. Sci. 240 (2004) 37–48. doi:10.1016/j.memsci.2004.04.010.

[122] H. Ohya, R. Paterson, T. Nomura, S. McFadzean, T. Suzuki, M. Kogure,

Properties of new inorganic membranes prepared by metal alkoxide methods Part I: A new permselective cation exchange membrane based on Si/Ta oxides, J. Memb. Sci. 105 (1995) 103–112. doi:10.1016/0376-7388(95)00054-G.

[123] M. Kogure, H. Ohya, R. Paterson, M. Hosaka, J.-J. Kim, S. McFadzean, Properties of new inorganic membranes prepared by metal alkoxide methods Part II: New inorganic-organic anion-exchange membranes prepared by the modified metal alkoxide methods with silane coupling agents, J. Memb. Sci. 126 (1997) 161–169. doi:10.1016/S0376-7388(96)00289-X.

[124] J.H. Hao, C. Chen, L. Li, L. Yu, W. Jiang, Preparation of Bipolar Membranes (I), J. Appl. Polym. Sci. 80 (2001) 1658–1663. doi:10.1002/app.1260.

[125] R.Q. Fu, T.W. Xu, W.H. Yang, Z.X. Pan, Preparation of a mono-sheet bipolar membrane by simultaneous irradiation grafting polymerization of acrylic acid and chloromethylstyrene, J. Appl. Polym. Sci. 90 (2003) 572–576. doi:10.1002/app.12776.

[126] A. Jendrychowska-Bonamour, Semipermeable membranes synthesized by grafting poly (tetrafluoroethylene) films. Synthesis and study of properties. II. Anionic and cationic mixed, J. Chim. Phys. Phys. Chim. Biol. (1973).

[127] X. Zhili, G. Haifeng, Q. Mengping, Y. Ye, W. Guoxiong, C. Baokang, Preparation of bipolar membranes via radiation peroxidation grafting, Radiat. Phys. Chem. 42 (1993) 963–966. doi:10.1016/0969-806X(93)90413-O.

[128] H.H. Rachid El Moussaoui, Single-film membrane, process for obtaining it and use thereof, (1994). http://www.google.ch/patents/US5840192.

[129] M. Higa, D. Masuda, E. Kobayashi, M. Nishimura, Y. Sugio, T. Kusudou, N. Fujiwara, Charge mosaic membranes prepared from laminated structures of PVA-based charged layers1. Preparation and transport properties of charged mosaic membranes, J. Memb. Sci. 310 (2008) 466–473. doi:10.1016/j.memsci.2007.11.024.

[130] K. Wang, A.A. Abdalla, M.A. Khaleel, N. Hilal, M.K. Khraisheh, Mechanical properties of water desalination and wastewater treatment membranes, Desalination. 401 (2017) 190–205. doi:10.1016/j.desal.2016.06.032.

[131] P.W. Majsztrik, A.B. Bocarsly, J.B. Benziger, Viscoelastic Response of Nafion. Effects of Temperature and Hydration on Tensile Creep, Macromolecules. 41 (2008) 9849–9862. doi:10.1021/ma801811m.

[132] Y. Kawano, Y. Wang, R.A. Palmer, S.R. Aubuchon, Stress-Strain Curves of Nafion Membranes in Acid and Salt Forms, Polímeros. 12 (2002) 96–101. doi:10.1590/S0104-14282002000200008.

[133] E.Y. Safronova, D. V Golubenko, N. V Shevlyakova, M.G. D'yakova, V.A. Tverskoi, L. Dammak, D. Grande, A.B. Yaroslavtsev, New cation-exchange membranes based on cross-linked sulfonated polystyrene and polyethylene for power generation systems, J. Memb. Sci. 515 (2016) 196–203. doi:10.1016/j.memsci.2016.05.006.

[134] N. Liang, Y. Liu, X. Liao, Z. Luo, D. Chen, X. Liu, H. Zhang, Preparation and characterization of anion-exchange membranes derived from poly(vinylbenzyl chloride-co-styrene) and intercalated montmorillonite, Polym. Adv. Technol. 28

(2017) 728–735. doi:10.1002/pat.3959.

[135] N. Ataollahi, K. Vezzù, G. Nawn, G. Pace, G. Cavinato, F. Girardi, P. Scardi, V. Di Noto, R. Di Maggio, A Polyketone-based Anion Exchange Membrane for Electrochemical Applications: Synthesis and Characterization, Electrochim. Acta. 226 (2017) 148–157. doi:10.1016/j.electacta.2016.12.150.

[136] M. Nemati, S.M. Hosseini, M. Shabanian, Novel electrodialysis cation exchange membrane prepared by 2-acrylamido-2-methylpropane sulfonic acid; heavy metal ions removal, J. Hazard. Mater. 337 (2017) 90–104. doi:10.1016/j.jhazmat.2017.04.074.

[137] M. Tedesco, A. Cipollina, A. Tamburini, W. van Baak, G. Micale, Modelling the Reverse ElectroDialysis process with seawater and concentrated brines, Desalin. Water Treat. 49 (2012) 1–21. doi:10.1080/19443994.2012.699355.

[138] R. Lteif, L. Dammak, C. Larchet, B. Auclair, Determination du nombre de transport d'un contre-ion dans une membrane echangeuse d'ions en utilisant la methode de la pile de concentration, Eur. Polym. J. 37 (2001) 627–639. doi:10.1016/S0014-3057(00)00163-4.

[139] Y. Zhang, R. Liu, Q. Lang, M. Tan, Y. Zhang, Composite anion exchange membrane made by layer-by-layer method for selective ion separation and water migration control, Sep. Purif. Technol. 192 (2018) 278–286. doi:10.1016/j.seppur.2017.10.022.

[140] G. Ramachandraiah, P. Ray, Electroassisted Transport Phenomenon of Strong and Weak Electrolytes across Ion-Exchange Membranes: Chronopotentiometric Study on Deactivation of Anion Exchange Membranes by Higher Homologous Monocarboxylates, J. Phys. Chem. B. 101 (1997) 7892–7900. doi:10.1021/jp9701698.

[141] R. Audinos, G. Pichelin, Characterization of electrodialysis membranes by chronopotentiometry, Desalination. 68 (1988) 251–263. doi:10.1016/0011-9164(88)80059-6.

[142] J. Balster, M.H. Yildirim, D.F. Stamatialis, R. Ibañez, R.G. H Lammertink, V. Jordan, M. Wessling, Morphology and Microtopology of Cation-Exchange Polymers and the Origin of the Overlimiting Current, J. Phys. Chem. B. (2006). doi:10.1021/jp068474t.

[143] S. Pawlowski, P. Sistat, J.G. Crespo, S. Velizarov, Mass transfer in reverse electrodialysis: Flow entrance effects and diffusion boundary layer thickness, J. Memb. Sci. 471 (2014) 72–83.

[144] P. Długołęcki, B. Anet, S.J. Metz, K. Nijmeijer, M. Wessling, Transport limitations in ion exchange membranes at low salt concentrations, J. Memb. Sci. 346 (2010) 163–171. doi:10.1016/j.memsci.2009.09.033.

[145] M. Tedesco, A. Cipollina, A. Tamburini, I.D.L. Bogle, G. Micale, A simulation tool for analysis and design of reverse electrodialysis using concentrated brines, Chem. Eng. Res. Des. 93 (2015) 441–456. doi:10.1016/j.cherd.2014.05.009.

[146] A.H. Galama, N.A. Hoog, D.R. Yntema, Method for determining ion exchange membrane resistance for electrodialysis systems, Desalination. 380 (2016) 1–11. doi:10.1016/j.desal.2015.11.018.

[147] A. Elattar, A. Elmidaoui, N. Pismenskaia, C. Gavach, G. Pourcelly, Comparison of transport properties of monovalent anions through anion-exchange membranes, J. Memb. Sci. 143 (1998) 249–261. doi:10.1016/S0376-7388(98)00013-1.

[148] V.K. Shahi, S.K. Thampy, R. Rangarajan, The effect of conducting spacers on transport properties of ion-exchange membranes in electrodriven separation, Desalination. 133 (2001) 245–258. doi:10.1016/S0011-9164(01)00105-9.

[149] G.S. Gohil, V.K. Shahi, R. Rangarajan, Comparative studies on electrochemical characterization of homogeneous and heterogeneous type of ion-exchange membranes, J. Memb. Sci. 240 (2004) 211–219. doi:10.1016/j.memsci.2004.04.022.

[150] V.K. Shahi, A.P. Murugesh, B.S. Makwana, S.K. Thampy, R. Rangarajan, Comparative investigations on electrical conductance of ion-exchange membranes, Indian Joumal Chem. 39 (2000) 1264–1269.

[151] B. Auclair, V. Nikonenko, C. Larchet, M. Métayer, L. Dammak, Correlation between transport parameters of ion-exchange membranes, J. Memb. Sci. 195 (2002) 89–102. doi:10.1016/S0376-7388(01)00556-7.

[152] R.F. Silva, M. De Francesco, A. Pozio, Tangential and normal conductivities of Nafion® membranes used in polymer electrolyte fuel cells, J. Power Sources. 134 (2004) 18–26. doi:10.1016/j.jpowsour.2004.03.028.

[153] A. Alcaraz, H. Holdik, T. Ruffing, P. Ramı´rez, S. Mafé, AC impedance spectra of bipolar membranes: an experimental study, J. Memb. Sci. 150 (1998) 43–56. doi:10.1016/S0376-7388(98)00201-4.

[154] F. Valero, R. Arbós, Desalination of brackish river water using Electrodialysis Reversal (EDR): Control of the THMs formation in the Barcelona (NE Spain) area, Desalination. 253 (2010) 170–174. doi:10.1016/j.desal.2009.11.011.

[155] V. Lindstrand, G. Sundström, A.S. Jönsson, Fouling of electrodialysis membranes by organic substances, Desalination. 128 (2000) 91–102. doi:10.1016/S0011-9164(00)00026-6.

[156] J.S. Park, J.-H. Choi, K.H. Yeon, S.H. Moon, An approach to fouling characterization of an ion-exchange membrane using current-voltage relation and electrical impedance spectroscopy, J. Colloid Interface Sci. 294 (2006) 129–138. doi:10.1016/j.jcis.2005.07.016.

[157] H.-J. Lee, S.-H. Moon, S.-P. Tsai, Effects of pulsed electric fields on membrane fouling in electrodialysis of NaCl solution containing humate, Sep. Purif. Technol. 27 (2002) 89–95. doi:10.1016/S1383-5866(01)00167-8.

[158] I. Ben Salah Sayadi, P. Sistat, M.M. Tlili, Assess of physical antiscale-treatments on conventional electrodialysis pilot unit during brackish water desalination, Chem. Eng. Process. Process Intensif. 88 (2015) 47–57. doi:10.1016/j.cep.2014.11.013.

[159] W. Garcia-Vasquez, L. Dammak, C. Larchet, V. V Nikonenko, D. Grande, Effects of acid–base cleaning procedure on structure and properties of anion-exchange membranes used in electrodialysis, J. Memb. Sci. 507 (2016) 12–23. doi:10.1016/j.memsci.2016.02.006.

[160] R. Audinos, Fouling of ion-selective membranes during electrodialysis of grape

must, J. Memb. Sci. 41 (1989) 115–126. doi:10.1016/S0376-7388(00)82395-9.

[161] R.P. Allison, Electrodialysis reversal in water reuse applications, Desalination. 103 (1995) 11–18. doi:10.1016/0011-9164(95)00082-8.

[162] N. Tanaka, M. Nagase, M. Higa, Organic fouling behavior of commercially available hydrocarbon-based anion-exchange membranes by various organic-fouling substances, Desalination. 296 (2012) 81–86. doi:10.1016/j.desal.2012.04.010.

[163] E. Korngold, F. de Körösy, R. Rahav, M.F. Taboch, Fouling of anionselective membranes in electrodialysis, Desalination. 8 (1970) 195–220. doi:10.1016/S0011-9164(00)80230-1.

[164] V.D. Grebenyuk, R.D. Chebotareva, S. Peters, V. Linkov, Surface modification of anion-exchange electrodialysis membranes to enhance anti-fouling characteristics, Desalination. 115 (1998) 313–329. doi:10.1016/S0011-9164(98)00051-4.

[165] S. Mulyati, R. Takagi, A. Fujii, Y. Ohmukai, T. Maruyama, H. Matsuyama, Improvement of the antifouling potential of an anion exchange membrane by surface modification with a polyelectrolyte for an electrodialysis process, J. Memb. Sci. 417–418 (2012) 137–143. doi:10.1016/j.memsci.2012.06.024.

[166] M. Vaselbehagh, H. Karkhanechi, S. Mulyati, R. Takagi, H. Matsuyama, Improved antifouling of anion-exchange membrane by polydopamine coating in electrodialysis process, Desalination. 332 (2014) 126–133. doi:10.1016/j.desal.2013.10.031.

[167] W.E. Katz, The electrodialysis reversal (EDR) process, Desalination. 28 (1979) 31–40. doi:10.1016/S0011-9164(00)88124-2.

[168] M. Turek, P. Dydo, J. Waś, Electrodialysis reversal in high CaSO4 supersaturation mode, Desalination. 198 (2006) 288–294. doi:10.1016/j.desal.2006.01.029.

[169] N. Cifuentes-Araya, G. Pourcelly, L. Bazinet, Impact of pulsed electric field on electrodialysis process performance and membrane fouling during consecutive demineralization of a model salt solution containing a high magnesium/calcium ratio, J. Colloid Interface Sci. 361 (2011) 79–89. doi:10.1016/j.jcis.2011.05.044.

[170] C. Casademont, P. Sistat, B. Ruiz, G. Pourcelly, L. Bazinet, Electrodialysis of model salt solution containing whey proteins: Enhancement by pulsed electric field and modified cell configuration, J. Memb. Sci. 328 (2009) 238–345. doi:10.1016/j.memsci.2008.12.013.

[171] S. Suwal, J. Amiot, L. Beaulieu, L. Bazinet, Effect of pulsed electric field and polarity reversal on peptide/amino acid migration, selectivity and fouling mitigation, J. Memb. Sci. 510 (2016) 405–416. doi:10.1016/j.memsci.2016.03.010.

[172] B.A. Cooke, Concentration polarization in electrodialysis—I. The electrometric measurement of interfacial concentration, Electrochim. Acta. 3 (1961) 307–317. doi:10.1016/0013-4686(61)85007-X.

[173] K.S. Spiegler, Polarization at ion exchange membrane-solution interfaces, Desalination. 9 (1971) 367–385. doi:10.1016/0011-9164(71)80005-X.

[174] C. Forgacs, N. Ishibashi, J. Leibovitz, J. Sinkovic, K.S. Spiegler, Polarization at ion-exchange membranes in electrodialysis, Desalination. 10 (1972) 181–214. doi:10.1016/S0011-9164(00)80085-5.

[175] F. Helfferich, Ion exchange, McGraw-Hill, New York, 1962.

[176] V.G. Levich, Physicochemical Hydrodynamics, Prentice-Hall, Englewood Cliffs, N.J., 1962.

[177] V. V. Nikonenko, N.D. Pismenskaya, E.I. Belova, P. Sistat, P. Huguet, G. Pourcelly, C. Larchet, Intensive current transfer in membrane systems: Modelling, mechanisms and application in electrodialysis, Adv. Colloid Interface Sci. 160 (2010) 101–123. doi:10.1016/j.cis.2010.08.001.

[178] R.K. McGovern, S.M. Zubair, J.H. Lienhard V, The cost effectiveness of electrodialysis for diverse salinity applications, Desalination. 348 (2014) 57–65. doi:10.1016/j.desal.2014.06.010.

[179] J.J. Krol, M. Wessling, H. Strathmann, Concentration polarization with monopolar ion exchange membranes : current - voltage curves and water dissociation, J. Memb. Sci. 162 (1999) 145–154. doi:10.1016/S0376-7388(99)00133-7.

[180] J.J. Krol, M. Wessling, H. Strathmann, Chronopotentiometry and overlimiting ion transport through monopolar ion exchange membranes, J. Memb. Sci. 162 (1999) 155–164. doi:10.1016/S0376-7388(99)00134-9.

[181] R. Valerdi-Pérez, J. Ibáñez-Mengual, Current—voltage curves for an electrodialysis reversal pilot plant: determination of limiting currents, Desalination. 141 (2001) 23–37. doi:10.1016/S0011-9164(01)00386-1.

[182] J.G.D. Tadimeti, S. Chattopadhyay, Uninterrupted swirling motion facilitating ion transport in electrodialysis, Desalination. 392 (2016) 54–62. doi:10.1016/j.desal.2016.04.007.

[183] J.-H. Choi, J.-S. Park, S.-H. Moon, Direct measurement of concentration distribution within the boundary layer of an ion-exchange membrane., J. Colloid Interface Sci. 251 (2002) 311–7. doi:10.1006/jcis.2002.8407.

[184] Y. Tanaka, Concentration polarization in ion exchange membrane electrodialysis, J. Memb. Sci. 57 (1991) 217–235. doi:10.1016/S0376-7388(00)80680-8.

[185] Y. Tanaka, Concentration polarization in ion-exchange membrane electrodialysis: The events arising in an unforced flowing solution in a desalting cell, J. Memb. Sci. 244 (2004) 1–16. doi:10.1016/j.memsci.2004.02.041.

[186] C. Forgacs, J. Leibovitz, R.N. O'Brien, K.S. Spiegler, Interferometric study of concentration profiles in solutions near membrane surfaces, Electrochim. Acta. 20 (1975) 555–563. doi:10.1016/0013-4686(75)80006-5.

[187] V.A. Shaposhnik, V.I. Vasil'eva, D.B. Praslov, Concentration fields of solutions under electrodialysis with ion-exchange membranes, J. Memb. Sci. 101 (1995) 23–30. doi:10.1016/0376-7388(94)00270-9.

[188] V. Shaposhnik, Analytical model of laminar flow electrodialysis with ion-exchange membranes, J. Memb. Sci. 133 (1997) 27–37. doi:10.1016/S0376-7388(97)00063-X.

[189] V.A. Shaposhnik, O. V Grigorchuk, E.N. Korzhov, V.I. Vasil'eva, V.Y. Klimov, The effect of ion-conducting spacers on mass transfer - Numerical analysis and concentration field visualization by means of laser interferometry, J. Memb. Sci. 139 (1998) 85–96. doi:10.1016/S0376-7388(97)00247-0.

[190] V.I. Vasil 'eva, V.A. Shaposhnik, O. V Grigorchuk, I.P. Petrunya, The membrane–solution interface under high-performance current regimes of electrodialysis by means of laser interferometry, Desalination. 192 (2006) 408–414. doi:10.1016/j.desal.2005.06.055.

[191] J.G.D. Tadimeti, V. Kurian, A. Chandra, S. Chattopadhyay, Corrugated membrane surfaces for effective ion transport in electrodialysis, J. Memb. Sci. 499 (2016) 418–428. doi:10.1016/j.memsci.2015.11.001.

[192] R. Kwak, G. Guan, W.K. Peng, J. Han, Microscale electrodialysis: Concentration profiling and vortex visualization, Desalination. 308 (2013) 138–146. doi:10.1016/j.desal.2012.07.017.

[193] B. Kim, S. Choi, V.S. Pham, R. Kwak, J. Han, Energy efficiency enhancement of electromembrane desalination systems by local flow redistribution optimized for the asymmetry of cation/anion diffusivity, J. Memb. Sci. 524 (2017) 280–287. doi:10.1016/j.memsci.2016.11.046.

[194] V.M. Barragán, C. Ruíz-Bauzá, Current-voltage curves for ion-exchange membranes: A method for determining the limiting current density, J. Colloid Interface Sci. 205 (1998) 365–373. doi:10.1006/jcis.1998.5649.

[195] P. Malek, J.M. Ortiz, B.S. Richards, A.I. Schäfer, Electrodialytic removal of NaCl from water: Impacts of using pulsed electric potential on ion transport and water dissociation phenomena, J. Memb. Sci. 435 (2013) 99–109. doi:10.1016/j.memsci.2013.01.060.

[196] V. V Nikonenko, N.D. Pismenskaya, A.G. Istoshin, V.I. Zabolotsky, A.A. Shudrenko, Description of mass transfer characteristics of ED and EDI apparatuses by using the similarity theory and compartmentation method, Chem. Eng. Process. Process Intensif. 47 (2008) 1118–1127. doi:10.1016/j.cep.2007.12.005.

[197] L. Gurreri, A. Tamburini, A. Cipollina, G. Micale, M. Ciofalo, CFD prediction of concentration polarization phenomena in spacer-filled channels for reverse electrodialysis, J. Memb. Sci. 468 (2014) 133–148. doi:10.1016/j.memsci.2014.05.058.

[198] R.F. Probstein, A.A. Sonin, E. Gur-Arie, A turbulent flow theory of electrodialysis, Desalination. 11 (1972) 165–187. doi:10.1016/S0011-9164(00)80066-1.

[199] M.S. Isaacson, A.A. Sonin, Sherwood Number and Friction Factor Correlations for Electrodialysis Systems, with Application to Process Optimization, Ind. Eng. Chem. Process Des. Dev. 15 (1976) 313–321. doi:10.1021/i260058a017.

[200] G. Schock, A. Miquel, Mass transfer and pressure loss in spiral wound modules, Desalination. 64 (1987) 339–352. doi:10.1016/0011-9164(87)90107-X.

[201] A.R. Da Costa, A.G. Fane, C.J.D. Fell, A.C.M. Franken, Optimal channel spacer design for ultrafiltration, J. Memb. Sci. 62 (1991) 275–291. doi:10.1016/0376-7388(91)80043-6.

[202] F. Li, W. Meindersma, A.B. De Haan, T. Reith, Optimization of commercial net spacers in spiral wound membrane modules, J. Memb. Sci. 208 (2002) 289–302. doi:10.1016/S0376-7388(02)00307-1.

[203] M. Fidaleo, M. Moresi, Optimal strategy to model the electrodialytic recovery of a strong electrolyte, J. Memb. Sci. 260 (2005) 90–111. doi:10.1016/j.memsci.2005.01.048.

[204] C.P. Koutsou, S.G. Yiantsios, A.J. Karabelas, A numerical and experimental study of mass transfer in spacer-filled channels: Effects of spacer geometrical characteristics and Schmidt number, J. Memb. Sci. 326 (2009) 234–251. doi:10.1016/j.memsci.2008.10.007.

[205] A.J. Karabelas, M. Kostoglou, C.P. Koutsou, Modeling of spiral wound membrane desalination modules and plants – review and research priorities, Desalination. 356 (2015) 165–186. doi:10.1016/j.desal.2014.10.002.

[206] P. Sistat, G. Pourcelly, Chronopotentiometric response of an ion-exchange membrane in the underlimiting current-range. Transport phenomena within the diffusion layers, J. Memb. Sci. 123 (1997) 121–131. doi:10.1016/S0376-7388(96)00210-4.

[207] S.A. Mareev, D.Y. Butylskii, N.D. Pismenskaya, V. V. Nikonenko, Chronopotentiometry of ion-exchange membranes in the overlimiting current range. Transition time for a finite-length diffusion layer: Modeling and experiment, J. Memb. Sci. 500 (2016) 171–179. doi:10.1016/j.memsci.2015.11.026.

[208] W. Zhang, J. Ma, P. Wang, Z. Wang, F. Shi, H. Liu, Investigations on the interfacial capacitance and the diffusion boundary layer thickness of ion exchange membrane using electrochemical impedance spectroscopy, J. Memb. Sci. 502 (2016). doi:10.1016/j.memsci.2015.12.007.

[209] B. Zhang, J.G. Hong, S. Xie, S. Xia, Y. Chen, An integrative modeling and experimental study on the ionic resistance of ion-exchange membranes, J. Memb. Sci. 524 (2017). doi:10.1016/j.memsci.2016.11.050.

[210] I. Rubinstein, L. Shtilman, Voltage against current curves of cation exchange membranes, J. Chem. Soc. Faraday Trans. 2. 75 (1979) 231. doi:10.1039/f29797500231.

[211] I. Rubinstein, F. Maletzki, Electroconvection at an electrically inhomogeneous permselective membrane surface, J. Chem. Soc. Faraday Trans. 87 (1991) 2079. doi:10.1039/ft9918702079.

[212] J.-H. Choi, H.-J. Lee, S.-H. Moon, Effects of Electrolytes on the Transport Phenomena in a Cation-Exchange Membrane, J. Colloid Interface Sci. 238 (2001) 188–195. doi:10.1006/jcis.2001.7510.

[213] H.J. Lee, H. Strathmann, S.H. Moon, Determination of the limiting current density in electrodialysis desalination as an empirical function of linear velocity, Desalination. 190 (2006) 43–50. doi:10.1016/j.desal.2005.08.004.

[214] M.K. Urtenov, A.M. Uzdenova, A. V. Kovalenko, V. V. Nikonenko, N.D. Pismenskaya, V.I. Vasil 'eva, P. Sistat, G. Pourcelly, Basic mathematical model of overlimiting transfer enhanced by electroconvection in flow-through

electrodialysis membrane cells, J. Memb. Sci. 447 (2013) 190–202. doi:10.1016/j.memsci.2013.07.033.

[215] I. Rubinstein, E. Staude, O. Kedem, Role of the membrane surface in concentration polarization at ion-exchange membrane, Desalination. 69 (1988) 101–114. doi:10.1016/0011-9164(88)80013-4.

[216] F. Maletzki, H.W. Rösler, E. Staude, Ion transfer across electrodialysis membranes in the overlimiting current range: stationary voltage current characteristics and current noise power spectra under different conditions of free convection, J. Memb. Sci. 71 (1992) 105–116. doi:10.1016/0376-7388(92)85010-G.

[217] H.W. Rösler, F. Maletzki, E. Staude, Ion transfer across electrodialysis membranes in the overlimiting current range: chronopotentiometric studies, J. Memb. Sci. 72 (1992) 171–179. doi:10.1016/0376-7388(92)80197-R.

[218] R. Ibañez, D.F. Stamatialis, M. Wessling, Role of membrane surface in concentration polarization at cation exchange membranes, J. Memb. Sci. 239 (2004) 119–128. doi:10.1016/j.memsci.2003.12.032.

[219] N. Pismenskaia, P. Sistat, P. Huguet, V. V Nikonenko, G. Pourcelly, Chronopotentiometry applied to the study of ion transfer through anion exchange membranes, J. Memb. Sci. 228 (2004) 65–76. doi:10.1016/j.memsci.2003.09.012.

[220] E. Volodina, N. Pismenskaya, V. V Nikonenko, C. Larchet, G. Pourcelly, Ion transfer across ion-exchange membranes with homogeneous and heterogeneous surfaces, J. Colloid Interface Sci. 285 (2005) 247–258. doi:10.1016/j.jcis.2004.11.017.

[221] V. V. Nikonenko, A. V. Kovalenko, M.K. Urtenov, N.D. Pismenskaya, J. Han, P. Sistat, G. Pourcelly, Desalination at overlimiting currents: State-of-the-art and perspectives, Desalination. 342 (2014) 85–106. doi:10.1016/j.desal.2014.01.008.

[222] K.A. Nebavskaya, V. V Sarapulova, K.G. Sabbatovskiy, V.D. Sobolev, N.D. Pismenskaya, P. Sistat, M. Cretin, V. V Nikonenko, Impact of ion exchange membrane surface charge and hydrophobicity on electroconvection at underlimiting and overlimiting currents, J. Memb. Sci. 523 (2017) 36–44. doi:10.1016/j.memsci.2016.09.038.

[223] V. V. Nikonenko, S.A. Mareev, N.D. Pis'menskaya, A.M. Uzdenova, A. V. Kovalenko, M.K. Urtenov, G. Pourcelly, Effect of electroconvection and its use in intensifying the mass transfer in electrodialysis (Review), Russ. J. Electrochem. 53 (2017) 1122–1144. doi:10.1134/S1023193517090099.

[224] H.J. Lee, F. Sarfert, H. Strathmann, S.H. Moon, Designing of an electrodialysis desalination plant, Desalination. 142 (2002) 267–286. doi:10.1016/S0011-9164(02)00208-4.

[225] D.A. Cowan, J.H. Brown, Effect of Turbulence on Limiting Current in Electrodialysis Cells, Ind. Eng. Chem. 51 (1959) 1445–1448. doi:10.1021/ie50600a026.

[226] W.G.B. Mandersloot, R.E. Hicks, Concertration polarization on ion exchange resin membranes in electrodialytic demineralization, Ind. Eng. Chem. Process

Des. Dev. 4 (1965) 304–308. doi:10.1021/i260015a014.

[227] J. Balster, I. Pünt, D.F. Stamatialis, M. Wessling, Multi-layer spacer geometries with improved mass transport, J. Memb. Sci. 282 (2006) 351–361. doi:10.1016/j.memsci.2006.05.039.

[228] J. Balster, D.F. Stamatialis, M. Wessling, Towards spacer free electrodialysis, J. Memb. Sci. 341 (2009) 131–138. doi:10.1016/j.memsci.2009.05.048.

[229] V. Geraldes, M.D. Afonso, Limiting current density in the electrodialysis of multi-ionic solutions, J. Memb. Sci. 360 (2010) 499–508. doi:10.1016/j.memsci.2010.05.054.

[230] P. Saremirad, H.G. Gomaa, J. Zhu, Effect of flow oscillations on mass transfer in electrodialysis with bipolar membrane, J. Memb. Sci. 405–406 (2012) 158–166. doi:10.1016/j.memsci.2012.03.006.

[231] Y. Tanaka, Limiting current density of an ion-exchange membrane and of an electrodialyzer, J. Memb. Sci. 266 (2005) 6–17. doi:10.1016/j.memsci.2005.05.005.

[232] X.W. Zhong, W.R. Zhang, Z.Y. Hu, H.C. Li, Effect of characterizations of spacer in electrodialysis cells on mass transfer, Desalination. 46 (1983) 243–252. doi:10.1016/0011-9164(83)87161-6.

[233] F. Li, W. Meindersma, A.B. De Haan, T. Reith, Experimental validation of CFD mass transfer simulations in flat channels with non-woven net spacers, J. Memb. Sci. 232 (2004) 19–30. doi:10.1016/j.memsci.2003.11.015.

[234] F. Li, W. Meindersma, A.B. de Haan, T. Reith, Novel spacers for mass transfer enhancement in membrane separations, J. Memb. Sci. 253 (2005) 1–12. doi:10.1016/j.memsci.2004.12.019.

[235] C. Rodrigues, V. Geraldes, M.N. de Pinho, V. Semião, Mass-transfer entrance effects in narrow rectangular channels with ribbed walls or mesh-type spacers, Chem. Eng. Sci. 78 (2012) 38–45. doi:10.1016/j.ces.2012.04.023.

[236] C. Rodrigues, M. Rodrigues, V. Semiao, V. Geraldes, Enhancement of mass transfer in spacer-filled channels under laminar regime by pulsatile flow, Chem. Eng. Sci. 123 (2015) 536–541. doi:10.1016/j.ces.2014.11.047.

[237] M. La Cerva, L. Gurreri, M. Tedesco, A. Cipollina, M. Ciofalo, A. Tamburini, G. Micale, Determination of limiting current density and current efficiency in electrodialysis units, Desalination. 445 (2018) 138–148. doi:10.1016/J.DESAL.2018.07.028.

[238] E. V. Laktionov, N.D. Pismenskaya, V. V. Nikonenko, V.I. Zabolotsky, Method of electrodialysis stack testing with the feed solution concentration regulation, Desalination. 151 (2003) 101–116. doi:10.1016/S0011-9164(02)00988-8.

[239] P. Sistat, G. Pourcelly, Steady-state ion transport through homopolar ion-exchange membranes: an analytical solution of the Nernst–Planck equations for a 1:1 electrolyte under the electroneutrality assumption, J. Electroanal. Chem. 460 (1999) 53–62. doi:10.1016/S0022-0728(98)00339-8.

[240] A.A. Sonin, R.F. Probstein, A hydrodynamic theory of desalination by electrodialysis, Desalination. 5 (1968) 293–329. doi:10.1016/S0011-

9164(00)80105-8.

[241] Y. Kim, W.S. Walker, D.F. Lawler, Competitive separation of di- vs. mono-valent cations in electrodialysis: effects of the boundary layer properties., Water Res. 46 (2012) 2042–56. doi:10.1016/j.watres.2012.01.004.

[242] A.M. Weiner, R.K. McGovern, J.H. Lienhard V, Increasing the power density and reducing the levelized cost of electricity of a reverse electrodialysis stack through blending, Desalination. 369 (2015) 140–148. doi:10.1016/j.desal.2015.04.031.

[243] V.M. Aguilella, S. Mafe, J.A. Manzanares, J. Pellicer, Current-voltage curves for ion-exchange membranes. Contributions to the total potential drop, J. Memb. Sci. 61 (1991) 177–190. doi:10.1016/0376-7388(91)80014-W.

[244] M. Taky, G. Pourcelly, F. Lebon, C. Gavach, Polarization phenomena at the interfaces between an electrolyte solution and an ion exchange membrane Part I. Ion transfer with a cation exchange membrane, J. Electroanal. Chem. 336 (1992) 171–194. doi:10.1016/0022-0728(92)80270-E.

[245] R.Q. Fu, T.W. Xu, W.H. Yang, Z.X. Pan, A new derivation and numerical analysis of current-voltage characteristics for an ion-exchange membrane under limiting current density, Desalination. 173 (2005) 143–155. doi:10.1016/j.desal.2004.07.047.

[246] P. Sistat, A. Kozmai, N. Pismenskaya, C. Larchet, G. Pourcelly, V. V Nikonenko, Low-frequency impedance of an ion-exchange membrane system, Electrochim. Acta. 53 (2008) 6380–6390. doi:10.1016/j.electacta.2008.04.041.

[247] Y. Kim, W.S. Walker, D.F. Lawler, Electrodialysis with spacers: Effects of variation and correlation of boundary layer thickness, Desalination. 274 (2011) 54–63. doi:10.1016/j.desal.2011.01.076.

[248] M. Block, J.A. Kitchener, Polarization Phenomena in Commercial Ion-Exchange Membranes, J. Electrochem. Soc. 113 (1966) 947. doi:10.1149/1.2424162.

[249] S.J. Judd, G.S. Solt, T. Wen, Polarization and back em.f. in electrodialysis, J. Appl. Electrochem. 23 (1993) 1117–1124. doi:10.1007/BF00625584.

[250] T. Wen, G.S. Solt, D.W. Gao, Electrical resistance and coulomb efficiency of electrodialysis (ED) apparatus in polarization, J. Memb. Sci. 114 (1996) 255–262. doi:10.1016/0376-7388(96)00005-1.

[251] M. Law, T. Wen, G.S. Solt, Thickness and concentration profile of the boundary layer in electrodialysis, Desalination. 109 (1997) 95–103. doi:10.1016/S0011-9164(97)00055-6.

[252] E. Güler, R. Elizen, M. Saakes, K. Nijmeijer, Micro-structured membranes for electricity generation by reverse electrodialysis, J. Memb. Sci. 458 (2014) 136–148. doi:10.1016/j.memsci.2014.01.060.

[253] D.A. Vermaas, M. Saakes, K. Nijmeijer, Enhanced mixing in the diffusive boundary layer for energy generation in reverse electrodialysis, J. Memb. Sci. 453 (2014) 312–319.

[254] J. Liu, G.M. Geise, X. Luo, H. Hou, F. Zhang, Y. Feng, M.A. Hickner, B.E. Logan, Patterned ion exchange membranes for improved power production in microbial reverse-electrodialysis cells, J. Power Sources. 271 (2014) 437–443.

doi:10.1016/j.jpowsour.2014.08.026.

[255] J. Moreno, E. Slouwerhof, D.A. Vermaas, M. Saakes, K. Nijmeijer, The Breathing Cell: Cyclic Intermembrane Distance Variation in Reverse Electrodialysis, Environ. Sci. Technol. 50 (2016) 11386–11393. doi:10.1021/acs.est.6b02668.

[256] A.A. Moya, Electrochemical Impedance of Ion-Exchange Membranes with Interfacial Charge Transfer Resistances, J. Phys. Chem. C. 120 (2016) 6543–6552. doi:10.1021/acs.jpcc.5b12087.

[257] R. Abu-Rjal, V. Chinaryan, M.Z. Bazant, I. Rubinstein, B. Zaltzman, Effect of concentration polarization on permselectivity, Phys. Rev. E. 89 (2014) 12302. doi:10.1103/PhysRevE.89.012302.

[258] G. Pourcelly, Electrodialysis with Bipolar Membranes: Principles, Optimization, and Applications, Russ. J. Electrochem. 38 (2002) 919–926. doi:10.1023/A:1016882216287.

[259] C. Fernandez-Gonzalez, A. Dominguez-Ramos, R. Ibañez, Y. Chen, A. Irabien, Valorization of desalination brines by electrodialysis with bipolar membranes using nanocomposite anion exchange membranes, Desalination. 406 (2017) 16–24. doi:10.1016/j.desal.2016.07.033.

[260] M. Reig, S. Casas, O. Gibert, C. Valderrama, J.L. Cortina, Integration of nanofiltration and bipolar electrodialysis for valorization of seawater desalination brines: Production of drinking and waste water treatment chemicals, Desalination. 382 (2016) 13–20. doi:10.1016/j.desal.2015.12.013.

[261] S. Koter, A. Warszawski, A new model for characterization of bipolar membrane electrodialysis of brine, Desalination. 198 (2006) 111–123. doi:10.1016/j.desal.2006.09.016.

[262] V. Mavrov, H. Chmiel, B. Heitele, F. Rögener, Desalination of surface water to industrial water with lower impact on the environment Part 4: Treatment of effluents from water desalination stages for reuse and balance of the new technological concept for water desalination, Desalination. 124 (1999) 205–216. doi:10.1016/S0011-9164(99)00105-8.

[263] M. Wang, K. kai Wang, Y.-X. Jia, Q. chun Ren, The reclamation of brine generated from desalination process by bipolar membrane electrodialysis, J. Memb. Sci. 452 (2014) 54–61. doi:10.1016/j.memsci.2013.10.029.

[264] M. Badruzzaman, J. Oppenheimer, S. Adham, M. Kumar, Innovative beneficial reuse of reverse osmosis concentrate using bipolar membrane electrodialysis and electrochlorination processes, J. Memb. Sci. 326 (2009) 392–399. doi:10.1016/j.memsci.2008.10.018.

[265] R. Ibañez, A. Pérez-González, P. Gómez, A.M. Urtiaga, I. Ortiz, Acid and base recovery from softened reverse osmosis (RO) brines. Experimental assessment using model concentrates, Desalination. 309 (2013) 165–170. doi:10.1016/j.desal.2012.10.006.

[266] Y. Yang, X. Gao, A. Fan, L. Fu, C. Gao, An innovative beneficial reuse of seawater concentrate using bipolar membrane electrodialysis, J. Memb. Sci. 449 (2014) 119–126. doi:10.1016/j.memsci.2013.07.066.

[267] C. Fernandez-Gonzalez, A. Dominguez-Ramos, R. Ibañez, A. Irabien,

Electrodialysis with Bipolar Membranes for Valorization of Brines, Sep. Purif. Rev. 45 (2016) 275–287. doi:10.1080/15422119.2015.1128951.

[268] J. Wood, J. Gifford, J. Arba, M. Shaw, Production of ultrapure water by continuous electrodeionization, Desalination. 250 (2010) 973–976. doi:10.1016/j.desal.2009.09.084.

[269] L. Alvarado, A. Chen, Electrodeionization: Principles, Strategies and Applications, Electrochim. Acta. 132 (2014) 583–597. doi:10.1016/j.electacta.2014.03.165.

[270] K. Dermentzis, Continuous electrodeionization through electrostatic shielding, Electrochim. Acta. 53 (2008) 2953–2962. doi:10.1016/j.electacta.2007.11.006.

[271] K. Dermentzis, Removal of nickel from electroplating rinse waters using electrostatic shielding electrodialysis/electrodeionization, J. Hazard. Mater. 173 (2010) 647–652. doi:10.1016/j.jhazmat.2009.08.133.

[272] M. Andelman, Flow through capacitor basics, Sep. Purif. Technol. 80 (2011) 262–269. doi:10.1016/j.seppur.2011.05.004.

[273] Y. Oren, Capacitive deionization (CDI) for desalination and water treatment - past, present and future (a review), Desalination. 228 (2008) 10–29. doi:10.1016/j.desal.2007.08.005.

[274] M.A. Anderson, A.L. Cudero, J. Palma, Capacitive deionization as an electrochemical means of saving energy and delivering clean water. Comparison to present desalination practices: Will it compete?, Electrochim. Acta. 55 (2010) 3845–3856. doi:10.1016/j.electacta.2010.02.012.

[275] B. Pisarska, Transport of co-ions across ion exchange membranes in electrodialytic metathesis MgSO4 + 2KCl → K2SO4 + MgCl2, Desalination. 230 (2008) 298–304. doi:10.1016/j.desal.2007.10.021.

[276] K. Haerens, P. De Vreese, E. Matthijs, L. Pinoy, K. Binnemans, B. Van Der Bruggen, Production of ionic liquids by electrodialysis, Sep. Purif. Technol. 97 (2012) 90–95. doi:10.1016/j.seppur.2012.02.017.

[277] Y. Zhang, S. Paepen, L. Pinoy, B. Meesschaert, B. Van der Bruggen, Selectrodialysis: Fractionation of divalent ions from monovalent ions in a novel electrodialysis stack, Sep. Purif. Technol. 88 (2012) 191–201. doi:10.1016/j.seppur.2011.12.017.

[278] A.T.K. Tran, Y. Zhang, D. De Corte, J.-B. Hannes, W. Ye, P. Mondal, N. Jullok, B. Meesschaert, L. Pinoy, B. Van Der Bruggen, P-recovery as calcium phosphate from wastewater using an integrated selectrodialysis/crystallization process, J. Clean. Prod. 77 (2014). doi:10.1016/j.jclepro.2014.01.069.

[279] S. Schlumpberger, N.B. Lu, M.E. Suss, M.Z. Bazant, Scalable and Continuous Water Deionization by Shock Electrodialysis, Environ. Sci. Technol. Lett. 2 (2015) 367–372. doi:10.1021/acs.estlett.5b00303.

[280] D. Deng, E.V. Dydek, J.-H. Han, S. Schlumpberger, A. Mani, B. Zaltzman, M.Z. Bazant, Overlimiting Current and Shock Electrodialysis in Porous Media, Langmuir. 29 (2013) 16167–16177. doi:10.1021/la4040547.

[281] D. Deng, W. Aouad, W.A. Braff, S. Schlumpberger, M.E. Suss, M.Z. Bazant, Water

purification by shock electrodialysis: Deionization, filtration, separation, and disinfection, Desalination. 357 (2015) 77–83. doi:10.1016/j.desal.2014.11.011.

[282] E.V. Dydek, B. Zaltzman, I. Rubinstein, D.S. Deng, A. Mani, M.Z. Bazant, Overlimiting Current in a Microchannel, Phys. Rev. Lett. 107 (2011) 118301. doi:10.1103/PhysRevLett.107.118301.

[283] A. Yaroshchuk, Over-limiting currents and deionization "shocks" in current-induced polarization: Local-equilibrium analysis, Adv. Colloid Interface Sci. 183 (2012) 68–81. doi:10.1016/j.cis.2012.08.004.

[284] A. Mani, T.A. Zangle, J.G. Santiago, On the Propagation of Concentration Polarization from Microchannel–Nanochannel Interfaces Part I: Analytical Model and Characteristic Analysis, Langmuir. 25 (2009) 3898–3908. doi:10.1021/la803317p.

[285] D.A. Vermaas, J. Veerman, N.Y. Yip, M. Elimelech, M. Saakes, K. Nijmeijer, High Efficiency in Energy Generation from Salinity Gradients with Reverse Electrodialysis, ACS Sustain. Chem. Eng. 1 (2013) 1295–1302. doi:10.1021/sc400150w.

[286] H.-I. Jeong, H.J. Kim, D.-K. Kim, Numerical analysis of transport phenomena in reverse electrodialysis for system design and optimization, Energy. 68 (2014) 229–237. doi:10.1016/j.energy.2014.03.013.

[287] A. Tamburini, G. La Barbera, A. Cipollina, G. Micale, M. Ciofalo, CFD prediction of scalar transport in thin channels for reverse electrodialysis, Desalin. Water Treat. 55 (2015) 3424–3445. doi:10.1080/19443994.2014.959735.

[288] A.H. Avci, P. Sarkar, R.A. Tufa, D. Messana, P. Argurio, E. Fontananova, G. Di Profio, E. Curcio, Effect of Mg 2+ ions on energy generation by Reverse Electrodialysis, J. Memb. Sci. 520 (2016) 499–506. doi:10.1016/j.memsci.2016.08.007.

[289] L. Gurreri, A. Tamburini, A. Cipollina, G. Micale, M. Ciofalo, Pressure drop at low reynolds numbers in woven-spacer-filled channels for membrane processes: CFD prediction and experimental validation, Desalin. Water Treat. 61 (2017) 170–182. doi:10.5004/dwt.2016.11279.

[290] L. Gurreri, A. Tamburini, A. Cipollina, G. Micale, M. Ciofalo, Flow and mass transfer in spacer-filled channels for reverse electrodialysis: a CFD parametrical study, J. Memb. Sci. 497 (2016) 300–317. doi:10.1016/j.memsci.2015.09.006.

[291] R.E. Pattle, Production of electric power by mixing fresh and salt water in the hydroelectric pile, Nature. 174 (1954) 660.

[292] J. Veerman, M. Saakes, S.J. Metz, G.J. Harmsen, Reverse electrodialysis: Performance of a stack with 50 cells on the mixing of sea and river water, J. Memb. Sci. 327 (2009) 136–144. doi:10.1016/j.memsci.2008.11.015.

[293] REAPower, (2014). http://www.reapower.eu/.

[294] M. Tedesco, E. Brauns, A. Cipollina, G. Micale, P. Modica, G. Russo, J. Helsen, Reverse Electrodialysis with saline waters and concentrated brines: a laboratory investigation towards technology scale-up, J. Memb. Sci. 492 (2015) 9–20.

[295] J.N. Weinstein, F.B. Leitz, Electric Power from Differences in Salinity: The

Dialytic Battery, Science (80-.). 191 (1976) 557–559. doi:10.1126/science.191.4227.557.

[296] R. Audinos, Reverse electrodialysis. Study of the electric energy obtained by mixing two solutions of different salinity., J. Power Sources. 10 (1983) 203–217.

[297] J. Jagur-Grodzinski, R. Kramer, Novel process for direct conversion of free energy of mixing into electric power, Ind. Eng. Chem. Process Des. Dev. 25 (1986) 443–449. doi:10.1021/i200033a016.

[298] M. Turek, B. Bandura, Renewable energy by reverse electrodialysis, Desalination. 205 (2007) 67–74. doi:10.1016/J.DESAL.2006.04.041.

[299] M. Turek, B. Bandura, P. Dydo, Power production from coal-mine brine utilizing reversed electrodialysis, Desalination. 221 (2008) 462–466. doi:10.1016/J.DESAL.2007.01.106.

[300] J.W. Post, C.H. Goeting, J. Valk, S. Goinga, J. Veerman, H.V.M. Hamelers, P.J.F.M. Hack, Towards implementation of reverse electrodialysis for power generation from salinity gradients, Desalin. Water Treat. 16 (2010) 182–193. doi:10.5004/dwt.2010.1093.

[301] A. Cipollina, G. Micale, A. Tamburini, M. Tedesco, L. Gurreri, J. Veerman, S. Grasman, Reverse electrodialysis, in: Sustain. Energy from Salin. Gradients, Elsevier, 2016: pp. 135–180. doi:10.1016/B978-0-08-100312-1.00005-5.

[302] M. Tedesco, C. Scalici, D. Vaccari, A. Cipollina, A. Tamburini, G. Micale, Performance of the first Reverse Electrodialysis pilot plant for power production from saline waters and concentrated brines, J. Memb. Sci. 500 (2016) 33–45.

[303] B.E. Logan, M. Elimelech, Membrane-based processes for sustainable power generation using water, Nature. 488 (2012) 313–319. http://www.scopus.com/inward/record.url?eid=2-s2.0-84865125058&partnerID=40&md5=894569d02f98cb9914974d7e21305f9e.

[304] A. Tamburini, A. Cipollina, M. Papapetrou, A. Piacentino, G. Micale, Salinity gradient engines, in: Sustain. Energy from Salin. Gradients, 2016: pp. 219–256. doi:10.1016/B978-0-08-100312-1.00007-9.

[305] M. Bevacqua, A. Tamburini, M. Papapetrou, A. Cipollina, G. Micale, A. Piacentino, Reverse electrodialysis with NH4HCO3 -water systems for heat-to-power conversion, Energy. 137 (2017) 1293–1307. doi:10.1016/j.energy.2017.07.012.

[306] K. Kwon, B.H. Park, D.H. Kim, D. Kim, Parametric study of reverse electrodialysis using ammonium bicarbonate solution for low-grade waste heat recovery, Energy Convers. Manag. 103 (2015) 104–110. doi:10.1016/j.enconman.2015.06.051.

[307] A. Tamburini, M. Tedesco, A. Cipollina, G. Micale, M. Ciofalo, M. Papapetrou, W. Van Baak, A. Piacentino, Reverse electrodialysis heat engine for sustainable power production, Appl. Energy. 206 (2017) 1334–1353. doi:10.1016/j.apenergy.2017.10.008.

[308] W.J. van Egmond, M. Saakes, S. Porada, T. Meuwissen, C.J.N. Buisman, H.V.M. Hamelers, The concentration gradient flow battery as electricity storage system: Technology potential and energy dissipation, J. Power Sources. 325 (2016) 129–

139. doi:10.1016/J.JPOWSOUR.2016.05.130.

[309] W.J. van Egmond, M. Saakes, I. Noor, S. Porada, C.J.N. Buisman, H.V.M. Hamelers, Performance of an environmentally benign acid base flow battery at high energy density, Int. J. Energy Res. (2017). doi:10.1002/er.3941.

[310] M. Vanoppen, G. Blandin, S. Derese, P. Le Clech, J. Post, A.R.D. Verliefde, Salinity gradient power and desalination, in: Sustain. Energy from Salin. Gradients, Elsevier, 2016: pp. 281–313. doi:10.1016/B978-0-08-100312-1.00009-2.

[311] Y.A.C. Jande, W.S. Kim, Integrating reverse electrodialysis with constant current operating capacitive deionization, J. Environ. Manage. 146 (2014) 463–469. doi:10.1016/j.jenvman.2014.07.039.

[312] W. Li, W.B. Krantz, E.R. Cornelissen, J.W. Post, A.R.D. Verliefde, C.Y. Tang, A novel hybrid process of reverse electrodialysis and reverse osmosis for low energy seawater desalination and brine management, Appl. Energy. 104 (2013) 592–602. doi:10.1016/j.apenergy.2012.11.064.

[313] Y. Mei, C.Y. Tang, Co-locating reverse electrodialysis with reverse osmosis desalination: Synergies and implications, J. Memb. Sci. 539 (2017) 305–312. doi:10.1016/J.MEMSCI.2017.06.014.

[314] K. Kwon, J. Han, B.H. Park, Y. Shin, D. Kim, Brine recovery using reverse electrodialysis in membrane-based desalination processes, Desalination. 362 (2015) 1–10. doi:10.1016/j.desal.2015.01.047.

[315] B.J. Feinberg, G.Z. Ramon, E.M. V Hoek, Thermodynamic Analysis of Osmotic Energy Recovery at a Reverse Osmosis Desalination Plant, Environ. Sci. Technol. 47 (2013) 2982–2989. doi:10.1021/es304224b.

[316] Q. Wang, X. Gao, Y. Zhang, Z. He, Z. Ji, X. Wang, C. Gao, Hybrid RED/ED system: Simultaneous osmotic energy recovery and desalination of high-salinity wastewater, Desalination. 405 (2017) 59–67. doi:10.1016/j.desal.2016.12.005.

[317] C. Tortajada, P. van Rensburg, Drink more recycled wastewater, Nature. 577 (2020) 26–28. doi:10.1038/d41586-019-03913-6.

[318] M. La Cerva, L. Gurreri, A. Cipollina, A. Tamburini, M. Ciofalo, G. Micale, Modelling and cost analysis of hybrid systems for seawater desalination: Electromembrane pre-treatments for Reverse Osmosis, Desalination. 467 (2019) 175–195. doi:10.1016/J.DESAL.2019.06.010.

[319] J. Kim, M. Park, S.A. Snyder, J.H. Kim, Reverse osmosis (RO) and pressure retarded osmosis (PRO) hybrid processes: Model-based scenario study, Desalination. 322 (2013) 121–130. doi:10.1016/j.desal.2013.05.010.

[320] G. Blandin, A.R.D. Verliefde, C.Y. Tang, P. Le-Clech, Opportunities to reach economic sustainability in forward osmosis-reverse osmosis hybrids for seawater desalination, Desalination. 363 (2015) 26–36. doi:10.1016/j.desal.2014.12.011.

[321] T.Y. Cath, N.T. Hancock, C.D. Lundin, C. Hoppe-Jones, J.E. Drewes, A multi-barrier osmotic dilution process for simultaneous desalination and purification of impaired water, J. Memb. Sci. 362 (2010) 417–426. doi:10.1016/j.memsci.2010.06.056.

[322] V. Yangali-Quintanilla, Z. Li, R. Valladares, Q. Li, G.L. Amy, Indirect desalination of Red Sea water with forward osmosis and low pressure reverse osmosis for water reuse, Desalination. 280 (2011) 160–166. doi:10.1016/j.desal.2011.06.066.

[323] V. Yangali-Quintanilla, L. Olesen, J. Lorenzen, C. Rasmussen, H. Laursen, E. Vestergaard, K. Keiding, Lowering desalination costs by alternative desalination and water reuse scenarios, Desalin. Water Treat. 55 (2015) 2437–2445. doi:10.1080/19443994.2014.940660.

[324] M. Sadrzadeh, A. Kaviani, T. Mohammadi, Mathematical modeling of desalination by electrodialysis, Desalination. 206 (2007) 538–546. doi:10.1016/j.desal.2006.04.062.

[325] Z. Zourmand, F. Faridirad, N. Kasiri, T. Mohammadi, Mass transfer modeling of desalination through an electrodialysis cell, Desalination. 359 (2015) 41–51. doi:10.1016/j.desal.2014.12.008.

[326] K. Tado, F. Sakai, Y. Sano, A. Nakayama, An analysis on ion transport process in electrodialysis desalination, Desalination. 378 (2016) 60–66. doi:10.1016/j.desal.2015.10.001.

[327] R. Enciso, J.A. Delgadillo, O. Domínguez, I. Rodríguez-Torres, Analysis and validation of the hydrodynamics of an electrodialysis cell using computational fluid dynamics, Desalination. 408 (2017) 127–132. doi:10.1016/j.desal.2017.01.015.

[328] M. Tedesco, H.V.M. Hamelers, P.M. Biesheuvel, Nernst-Planck transport theory for (reverse) electrodialysis: I. Effect of co-ion transport through the membranes, J. Memb. Sci. 510 (2016) 370–381.

[329] M. Tedesco, H.V.M. Hamelers, P.M. Biesheuvel, Nernst-Planck transport theory for (reverse) electrodialysis: II. Effect of water transport through ion-exchange membranes, J. Memb. Sci. 531 (2017) 172–182. doi:10.1016/j.memsci.2017.02.031.

[330] L. Gurreri, G. Battaglia, A. Tamburini, A. Cipollina, G. Micale, M. Ciofalo, Multi-physical modelling of reverse electrodialysis, Desalination. 423 (2017) 52–64. doi:10.1016/j.desal.2017.09.006.

[331] P.N. Pintauro, D.N. Bennion, Mass transport of electrolytes in membranes. 1. Development of mathematical transport model, Ind. Eng. Chem. Fundam. 23 (1984) 230–234. http://www.scopus.com/inward/record.url?eid=2-s2.0-0021425029&partnerID=tZOtx3y1.

[332] G. Kraaijeveld, V. Sumberova, S. Kuindersma, H. Wesselingh, Modelling electrodialysis using the Maxwell-Stefan description, Chem. Eng. J. Biochem. Eng. J. 57 (1995) 163–176. doi:10.1016/0923-0467(94)02940-7.

[333] J.A. Wesselingh, P. Vonk, G. Kraaijeveld, Exploring the Maxwell-Stefan description of ion exchange, Chem. Eng. J. Biochem. Eng. J. 57 (1995) 75–89. doi:10.1016/0923-0467(94)02932-6.

[334] K.M. Chehayeb, J.H. Lienhard, Entropy generation analysis of electrodialysis, Desalination. 413 (2017) 184–198. doi:10.1016/j.desal.2017.03.001.

[335] J.M. Ortiz, J.A. Sotoca, E. Expósito, F. Gallud, V. García-García, V. Montiel, A. Aldaz, Brackish water desalination by electrodialysis: Batch recirculation

operation modeling, J. Memb. Sci. 252 (2005) 65–75. doi:10.1016/j.memsci.2004.11.021.

[336] P. Tsiakis, L.G. Papageorgiou, Optimal design of an electrodialysis brackish water desalination plant, Desalination. 173 (2005) 173–186. doi:10.1016/j.desal.2004.08.031.

[337] N.A.A. Qasem, B.A. Qureshi, S.M. Zubair, Improvement in design of electrodialysis desalination plants by considering the Donnan potential, Desalination. 441 (2018) 62–76. doi:10.1016/j.desal.2018.04.023.

[338] B.A. Qureshi, S.M. Zubair, Design of electrodialysis desalination plants by considering dimensionless groups and variable equivalent conductivity, Desalination. 430 (2018) 197–207. doi:10.1016/j.desal.2017.12.030.

[339] R.K. McGovern, A.M. Weiner, L. Sun, C.G. Chambers, S.M. Zubair, J.H. Lienhard V, On the cost of electrodialysis for the desalination of high salinity feeds, Appl. Energy. 136 (2014) 649–661. doi:10.1016/j.apenergy.2014.09.050.

[340] K.M. Chehayeb, D.M. Farhat, K.G. Nayar, J.H. Lienhard, Optimal design and operation of electrodialysis for brackish-water desalination and for high-salinity brine concentration, Desalination. 420 (2017) 167–182. doi:10.1016/j.desal.2017.07.003.

[341] K.M. Chehayeb, K.G. Nayar, J.H. Lienhard, On the merits of using multi-stage and counterflow electrodialysis for reduced energy consumption, Desalination. 439 (2018) 1–16. doi:10.1016/j.desal.2018.03.026.

[342] S. Pawlowski, V. Geraldes, J.G. Crespo, S. Velizarov, Computational fluid dynamics (CFD) assisted analysis of profiled membranes performance in reverse electrodialysis, J. Memb. Sci. 502 (2016) 179–190.

[343] N.C. Wright, S.R. Shah, S.E. Amrose, A.G. Winter, A robust model of brackish water electrodialysis desalination with experimental comparison at different size scales, Desalination. 443 (2018) 27–43. doi:10.1016/J.DESAL.2018.04.018.

[344] S.R. Shah, N.C. Wright, P.A. Nepsky, A.G. Winter, Cost-optimal design of a batch electrodialysis system for domestic desalination of brackish groundwater, Desalination. 443 (2018) 198–211. doi:10.1016/j.desal.2018.05.010.

[345] S.R. Shah, S.L. Walter, A.G. Winter, Using feed-forward voltage-control to increase the ion removal rate during batch electrodialysis desalination of brackish water, Desalination. 457 (2019) 62–74. doi:10.1016/j.desal.2019.01.022.

[346] K.S. Pitzer, Thermodynamics of electrolytes. I. Theoretical basis and general equations, J. Phys. Chem. 77 (1973) 268–277. doi:10.1021/j100621a026.

[347] C.F. Weber, Calculation of Pitzer Parameters at High Ionic Strengths, Ind. Eng. Chem. Res. 39 (2000) 4422–4426. doi:10.1021/ie0004110.

[348] J.R. Wilson, Demineralization by electrodialysis, Butterworths Scientific Publications, 1960.

[349] A. Despić, G.J. Hills, Electro-osmosis in charged membranes. The determination of primary solvation numbers, Discuss. Faraday Soc. 21 (1956) 150. doi:10.1039/df9562100150.

[350] S.S. Islam, R.L. Gupta, K. Ismail, Extension of the Falkenhagen-Leist-Kelbg equation to the electrical conductance of concentrated aqueous electrolytes, J. Chem. Eng. Data. 36 (1991) 102–104. doi:10.1021/je00001a031.

[351] V. V Wagholikar, H. Zhuang, Y. Jiao, N.E. Moe, H. Ramanan, L.M. Goh, J. Barber, K.S. Lee, H.P. Lee, J.Y.H. Fuh, Modeling cell pair resistance and spacer shadow factors in electro-separation processes, J. Memb. Sci. 543 (2017) 151–162. doi:10.1016/J.MEMSCI.2017.08.054.

[352] S. Mehdizadeh, M. Yasukawa, T. Abo, Y. Kakihana, M. Higa, Effect of spacer geometry on membrane and solution compartment resistances in reverse electrodialysis, J. Memb. Sci. 572 (2019) 271–280. doi:10.1016/J.MEMSCI.2018.09.051.

[353] P. Długołęcki, P. Ogonowski, S.J. Metz, M. Saakes, K. Nijmeijer, M. Wessling, On the resistances of membrane, diffusion boundary layer and double layer in ion exchange membrane transport, J. Memb. Sci. 349 (2010) 369–379. doi:10.1016/j.memsci.2009.11.069.

[354] S. Zhu, R.S. Kingsbury, D.F. Call, O. Coronell, Impact of solution composition on the resistance of ion exchange membranes, J. Memb. Sci. 554 (2018) 39–47. doi:10.1016/J.MEMSCI.2018.02.050.

[355] L. Gurreri, M. Ciofalo, A. Cipollina, A. Tamburini, W. Van Baak, G. Micale, CFD modelling of profiled-membrane channels for reverse electrodialysis, Desalin. Water Treat. 55 (2015) 1–20. doi:10.1080/19443994.2014.940651.

[356] A.M. Lopez, M. Williams, M. Paiva, D. Demydov, T.D. Do, J.L. Fairey, Y.P.J. Lin, J.A. Hestekin, Potential of electrodialytic techniques in brackish desalination and recovery of industrial process water for reuse, Desalination. 409 (2017) 108–114. doi:10.1016/j.desal.2017.01.010.

[357] K.M. (Katalin M.. Hangos, I.T. Cameron, Process modelling and model analysis, Academic Press, 2001.

[358] J.H. Barber, R. MacDonald, H. Yang, W. Lu, Capacitive carbon electrodes for electrodialysis reversal applications, in: American Water Works Association, 2014.

[359] C. Wei, Y. Du, W. Cai, R. Xiong, L. Cao, Non-faraday based systems, devices and methods for removing ionic species from liquid, US20110042219A1, 2011. https://patents.google.com/patent/US20110042219 (accessed June 25, 2018).

[360] P. Ratajczak, M.E. Suss, F. Kaasik, F. Béguin, Carbon electrodes for capacitive technologies, Energy Storage Mater. 16 (2019) 126–145. doi:10.1016/j.ensm.2018.04.031.

[361] P.M. Biesheuvel, M.Z. Bazant, Nonlinear dynamics of capacitive charging and desalination by porous electrodes, Phys. Rev. E. 81 (2010) 031502. doi:10.1103/PhysRevE.81.031502.

[362] M.E. Suss, T.F. Baumann, M.A. Worsley, K.A. Rose, T.F. Jaramillo, M. Stadermann, J.G. Santiago, Impedance-based study of capacitive porous carbon electrodes with hierarchical and bimodal porosity, J. Power Sources. 241 (2013) 266–273. doi:10.1016/J.JPOWSOUR.2013.03.178.

[363] G. Wang, L. Zhang, J. Zhang, A review of electrode materials for electrochemical

supercapacitors, Chem. Soc. Rev. 41 (2012) 797–828. doi:10.1039/C1CS15060J.

[364] E. Frackowiak, F. Béguin, Carbon materials for the electrochemical storage of energy in capacitors, Carbon N. Y. 39 (2001) 937–950. doi:10.1016/S0008-6223(00)00183-4.

[365] Y. Ding, J. Zhu, C. Wang, B. Dai, Y. Li, Y. Qin, F. Xu, Q. Peng, Z. Yang, J. Bai, W. Cao, Y. Yuan, Y. Li, Multifunctional three-dimensional graphene nanoribbons composite sponge, Carbon N. Y. 104 (2016) 133–140. doi:10.1016/J.CARBON.2016.03.058.

[366] E. Castillo-Martínez, J. Carretero-González, J. Sovich, M.D. Lima, High temperature structural transformations of few layer graphene nanoribbons obtained by unzipping carbon nanotubes, J. Mater. Chem. A. 2 (2014) 221–228. doi:10.1039/C3TA13292G.

[367] X. Zhou, L. Yu, X.-Y. Yu, X.W.D. Lou, Encapsulating Sn Nanoparticles in Amorphous Carbon Nanotubes for Enhanced Lithium Storage Properties, Adv. Energy Mater. 6 (2016) 1601177. doi:10.1002/aenm.201601177.

[368] G. Xiong, P. He, Z. Lyu, T. Chen, B. Huang, L. Chen, T.S. Fisher, Bioinspired leaves-on-branchlet hybrid carbon nanostructure for supercapacitors, Nat. Commun. 9 (2018) 790. doi:10.1038/s41467-018-03112-3.

[369] E.S. Snow, F.K. Perkins, E.J. Houser, S.C. Badescu, T.L. Reinecke, Chemical Detection with a Single-Walled Carbon Nanotube Capacitor, Science (80-.). 307 (2005) 1942–1945. doi:10.1126/science.1109128.

[370] C. Portet, G. Yushin, Y. Gogotsi, Electrochemical performance of carbon onions, nanodiamonds, carbon black and multiwalled nanotubes in electrical double layer capacitors, Carbon N. Y. 45 (2007) 2511–2518. doi:10.1016/J.CARBON.2007.08.024.

[371] M.E. Plonska-Brzezinska, L. Echegoyen, Carbon nano-onions for supercapacitor electrodes: recent developments and applications, J. Mater. Chem. A. 1 (2013) 13703. doi:10.1039/c3ta12628e.

[372] J. García-Martínez, K. Li, Mesoporous Zeolites, Wiley-VCH Verlag GmbH & Co. KGaA, Weinheim, Germany, 2015. doi:10.1002/9783527673957.

[373] N. Boukmouche, N. Azzouz, L. Bouchama, J.P. Chopart, Y. Bouznit, Activated carbon derived from marine Posidonia Oceanica for electric energy storage, Arab. J. Chem. 7 (2014) 347–354. doi:10.1016/j.arabjc.2012.12.010.

[374] F. Béguin, V. Presser, A. Balducci, E. Frackowiak, Carbons and Electrolytes for Advanced Supercapacitors, Adv. Mater. 26 (2014) 2219–2251. doi:10.1002/adma.201304137.

[375] H.F. Stoeckli, F. Kraehenbuehl, The external surface of microporous carbons, derived from adsorption and immersion studies, Carbon N. Y. 22 (1984) 297–299. doi:10.1016/0008-6223(84)90174-X.

[376] T. Alencherry, N. A.R., S. Ghosh, J. Daniel, V. R., Effect of increasing electrical conductivity and hydrophilicity on the electrosorption capacity of activated carbon electrodes for capacitive deionization, Desalination. 415 (2017) 14–19. doi:10.1016/J.DESAL.2017.04.001.

[377] L. Zou, G. Morris, D. Qi, Using activated carbon electrode in electrosorptive deionisation of brackish water, Desalination. 225 (2008) 329–340. doi:10.1016/J.DESAL.2007.07.014.

[378] C.-H. Hou, C.-Y. Huang, A comparative study of electrosorption selectivity of ions by activated carbon electrodes in capacitive deionization, Desalination. 314 (2013) 124–129. doi:10.1016/J.DESAL.2012.12.029.

[379] J.Y. Hwang, M. Li, M.F. El-Kady, R.B. Kaner, Next-Generation Activated Carbon Supercapacitors: A Simple Step in Electrode Processing Leads to Remarkable Gains in Energy Density, Adv. Funct. Mater. 27 (2017) 1605745. doi:10.1002/adfm.201605745.

[380] M. Olivares-Marín, J.A. Fernández, M.J. Lázaro, C. Fernández-González, A. Macías-García, V. Gómez-Serrano, F. Stoeckli, T.A. Centeno, Cherry stones as precursor of activated carbons for supercapacitors, Mater. Chem. Phys. 114 (2009) 323–327. doi:10.1016/J.MATCHEMPHYS.2008.09.010.

[381] I. Villar, S. Roldan, V. Ruiz, M. Granda, C. Blanco, R. Menéndez, R. Santamaría, Capacitive Deionization of NaCl Solutions with Modified Activated Carbon Electrodes †, Energy & Fuels. 24 (2010) 3329–3333. doi:10.1021/ef901453q.

[382] C. Vix-Guterl, E. Frackowiak, K. Jurewicz, M. Friebe, J. Parmentier, F. Béguin, Electrochemical energy storage in ordered porous carbon materials, Carbon N. Y. 43 (2005) 1293–1302. doi:10.1016/J.CARBON.2004.12.028.

[383] A.G. Pandolfo, A.F. Hollenkamp, Carbon properties and their role in supercapacitors, J. Power Sources. 157 (2006) 11–27. doi:10.1016/J.JPOWSOUR.2006.02.065.

[384] F. Liu, O. Coronell, D.F. Call, Electricity generation using continuously recirculated flow electrodes in reverse electrodialysis, J. Power Sources. 355 (2017) 206–210. doi:10.1016/J.JPOWSOUR.2017.04.061.

[385] J.M. Paz-Garcia, O. Schaetzle, P.M. Biesheuvel, H.V.M. Hamelers, Energy from CO2 using capacitive electrodes – Theoretical outline and calculation of open circuit voltage, J. Colloid Interface Sci. 418 (2014) 200–207. doi:10.1016/J.JCIS.2013.11.081.

[386] D. Brogioli, Extracting Renewable Energy from a Salinity Difference Using a Capacitor, Phys. Rev. Lett. 103 (2009) 058501. doi:10.1103/PhysRevLett.103.058501.

[387] Y.A.C. Jande, W.S. Kim, Desalination using capacitive deionization at constant current, Desalination. 329 (2013) 29–34. doi:10.1016/J.DESAL.2013.08.023.

[388] Y. Salamat, C.H. Hidrovo, A parametric study of multiscale transport phenomena and performance characteristics of capacitive deionization systems, Desalination. 438 (2018) 24–36. doi:10.1016/J.DESAL.2018.03.022.

[389] Z. Chen, H. Zhang, C. Wu, L. Luo, C. Wang, S. Huang, H. Xu, A study of the effect of carbon characteristics on capacitive deionization (CDI) performance, Desalination. 433 (2018) 68–74. doi:10.1016/J.DESAL.2017.11.036.

[390] O.N. Demirer, R.M. Naylor, C.A. Rios Perez, E. Wilkes, C. Hidrovo, Energetic performance optimization of a capacitive deionization system operating with transient cycles and brackish water, Desalination. 314 (2013) 130–138.

doi:10.1016/J.DESAL.2013.01.014.

[391] J. Ma, C. He, D. He, C. Zhang, T.D. Waite, Analysis of capacitive and electrodialytic contributions to water desalination by flow-electrode CDI, Water Res. 144 (2018) 296–303. doi:10.1016/J.WATRES.2018.07.049.

[392] A. Rommerskirchen, Y. Gendel, M. Wessling, Single module flow-electrode capacitive deionization for continuous water desalination, Electrochem. Commun. 60 (2015) 34–37. doi:10.1016/J.ELECOM.2015.07.018.

[393] A. Rommerskirchen, B. Ohs, K.A. Hepp, R. Femmer, M. Wessling, Modeling continuous flow-electrode capacitive deionization processes with ion-exchange membranes, J. Memb. Sci. 546 (2018) 188–196. doi:10.1016/J.MEMSCI.2017.10.026.

[394] SUEZ, Carbon Electrodes for EDR, (2013). https://my.suezwatertechnologies.com/WTSCustomerPortal/s/content-download?DN=%2Fdocuments%2FFact+Sheets_Cust%2FAmericas%2FEnglish%2FFSelEDRCarbonElectrode_EN.pdf (accessed July 29, 2019).

[395] Y. Qu, P.G. Campbell, L. Gu, J.M. Knipe, E. Dzenitis, J.G. Santiago, M. Stadermann, Energy consumption analysis of constant voltage and constant current operations in capacitive deionization, Desalination. 400 (2016) 18–24. doi:10.1016/J.DESAL.2016.09.014.

[396] A. Hemmatifar, M. Stadermann, J.G. Santiago, Two-Dimensional Porous Electrode Model for Capacitive Deionization, J. Phys. Chem. C. 119 (2015) 24681–24694. doi:10.1021/acs.jpcc.5b05847.

[397] J. Newman, W. Tiedemann, Porous-electrode theory with battery applications, AIChE J. 21 (1975) 25–41. doi:10.1002/aic.690210103.

[398] A.M. Johnson, J. Newman, Desalting by Means of Porous Carbon Electrodes, J. Electrochem. Soc. 118 (1971) 510. doi:10.1149/1.2408094.

[399] J.S. Newman, Electrochemical Systems, second, Prentice Hall, Englewood Cliffs, 1991.

[400] P.M. Biesheuvel, Y. Fu, M.Z. Bazant, Diffuse charge and Faradaic reactions in porous electrodes, Phys. Rev. E. 83 (2011) 061507. doi:10.1103/PhysRevE.83.061507.

[401] R. de Levie, On porous electrodes in electrolyte solutions: I. Capacitance effects, Electrochim. Acta. 8 (1963) 751–780. doi:10.1016/0013-4686(63)80042-0.

[402] R. Kötz, M. Carlen, Principles and applications of electrochemical capacitors, Electrochim. Acta. 45 (2000) 2483–2498. doi:10.1016/S0013-4686(00)00354-6.

[403] P.M. Biesheuvel, H.V.M. Hamelers, M.E. Suss, Theory of Water Desalination by Porous Electrodes with Immobile Chemical Charge, Colloids Interface Sci. Commun. 9 (2015) 1–5. doi:10.1016/J.COLCOM.2015.12.001.

[404] E.N. Guyes, A.N. Shocron, A. Simanovski, P.M. Biesheuvel, M.E. Suss, A one-dimensional model for water desalination by flow-through electrode capacitive deionization, Desalination. 415 (2017) 8–13. doi:10.1016/J.DESAL.2017.03.013.

[405] D.L. Chapman, LI. A contribution to the theory of electrocapillarity, London,

Edinburgh, Dublin Philos. Mag. J. Sci. 25 (1913) 475–481. doi:10.1080/14786440408634187.

[406] E. Cardona, S. Culotta, L. Mangiaracina, R. Terranova, Multi-flash desalination and cogeneration to solve the water supply problems in southeastern Sicily, Desalination. 106 (1996) 121–130. doi:10.1016/S0011-9164(96)00100-2.

[407] I. Kamal, Cogeneration desalination with reverse osmosis: A means of augmenting water supplies in Southern California, Desalination. 88 (1992) 355–369. doi:10.1016/0011-9164(92)80127-U.

[408] E.U. Khan, A.R. Martin, Optimization of hybrid renewable energy polygeneration system with membrane distillation for rural households in Bangladesh, Energy. 93 (2015) 1116–1127. doi:10.1016/J.ENERGY.2015.09.109.

[409] S. Usón, J. Uche, A. Martínez, A. del Amo, L. Acevedo, Á. Bayod, Exergy assessment and exergy cost analysis of a renewable-based and hybrid trigeneration scheme for domestic water and energy supply, Energy. 168 (2019) 662–683. doi:10.1016/J.ENERGY.2018.11.124.

[410] F. Calise, G. de Notaristefani di Vastogirardi, M. Dentice d'Accadia, M. Vicidomini, Simulation of polygeneration systems, Energy. 163 (2018) 290–337. doi:10.1016/J.ENERGY.2018.08.052.

[411] K. Jana, A. Ray, M.M. Majoumerd, M. Assadi, S. De, Polygeneration as a future sustainable energy solution – A comprehensive review, Appl. Energy. 202 (2017) 88–111. doi:10.1016/J.APENERGY.2017.05.129.

[412] F. Calise, M. Dentice d'Accadia, R. Vanoli, M. Vicidomini, Transient analysis of solar polygeneration systems including seawater desalination: A comparison between linear Fresnel and evacuated solar collectors, Energy. 172 (2019) 647–660. doi:10.1016/J.ENERGY.2019.02.001.

[413] U. Sahoo, R. Kumar, P.C. Pant, R. Chaudhary, Development of an innovative polygeneration process in hybrid solar-biomass system for combined power, cooling and desalination, Appl. Therm. Eng. 120 (2017) 560–567. doi:10.1016/J.APPLTHERMALENG.2017.04.034.

[414] M. Esrafilian, R. Ahmadi, Energy, environmental and economic assessment of a polygeneration system of local desalination and CCHP, Desalination. 454 (2019) 20–37. doi:10.1016/J.DESAL.2018.12.004.

[415] F. Calise, A. Macaluso, A. Piacentino, L. Vanoli, A novel hybrid polygeneration system supplying energy and desalinated water by renewable sources in Pantelleria Island, Energy. 137 (2017) 1086–1106. doi:10.1016/J.ENERGY.2017.03.165.

[416] F. Calise, M. Dentice d'Accadia, A. Macaluso, L. Vanoli, A novel solar-geothermal trigeneration system integrating water desalination: Design, dynamic simulation and economic assessment, Energy. 115 (2016) 1533–1547. doi:10.1016/J.ENERGY.2016.07.103.

[417] F. Calise, M. Dentice d'Accadia, A. Piacentino, Exergetic and exergoeconomic analysis of a renewable polygeneration system and viability study for small isolated communities, Energy. 92 (2015) 290–307. doi:10.1016/J.ENERGY.2015.03.056.

[418] F. Calise, A. Cipollina, M. Dentice d'Accadia, A. Piacentino, A novel renewable polygeneration system for a small Mediterranean volcanic island for the combined production of energy and water: Dynamic simulation and economic assessment, Appl. Energy. 135 (2014) 675–693. doi:10.1016/J.APENERGY.2014.03.064.

[419] D. Manolakos, E.S. Mohamed, I. Karagiannis, G. Papadakis, Technical and economic comparison between PV-RO system and RO-Solar Rankine system. Case study: Thirasia island, Desalination. 221 (2008) 37–46. doi:10.1016/J.DESAL.2007.01.066.

[420] L. Karimi, L. Abkar, M. Aghajani, A. Ghassemi, Technical feasibility comparison of off-grid PV-EDR and PV-RO desalination systems via their energy consumption, Sep. Purif. Technol. 151 (2015) 82–94. doi:10.1016/j.seppur.2015.07.023.

[421] M.C. Garg, H. Joshi, A Review on PV-RO Process: Solution to Drinking Water Scarcity due to High Salinity in Non-Electrified Rural Areas, Sep. Sci. Technol. 50 (2015) 1270–1283. doi:10.1080/01496395.2014.951725.

[422] H.A. Shawky, A.A. Abdel Fatah, M.M.S. Abo ElFadl, A.H.M. El-Aassar, Design of a small mobile PV-driven RO water desalination plant to be deployed at the northwest coast of Egypt, Desalin. Water Treat. 55 (2015) 3755–3766. doi:10.1080/19443994.2015.1080447.

[423] A.M. Helal, S.A. Al Malek, E.M. Al Hammadi, H.A. Al-Thani, Economic feasibility of grid-connected PV-RO and PV-MVC small desalination units for remote areas in The United Arab Emirates — A comparative study, Desalin. Water Treat. 3 (2009) 241–251. doi:10.5004/dwt.2009.466.

[424] M.A.I. El-Shaarawi, H. Al Awjan, D. Al Ramadhan, M. Hussain, Effect of thermodynamic limitations on PV initial cost estimations for solar-powered RO desalination, Desalination. 276 (2011) 28–37. doi:10.1016/J.DESAL.2011.03.021.

[425] D.P. Clarke, Y.M. Al-Abdeli, G. Kothapalli, The effects of including intricacies in the modelling of a small-scale solar-PV reverse osmosis desalination system, Desalination. 311 (2013) 127–136. doi:10.1016/J.DESAL.2012.11.006.

[426] M. Thomson, D. Infield, A photovoltaic-powered seawater reverse-osmosis system without batteries, Desalination. 153 (2003) 1–8. doi:10.1016/S0011-9164(03)80004-8.

[427] M. Thomson, D. Infield, Laboratory demonstration of a photovoltaic-powered seawater reverse-osmosis system without batteries, Desalination. 183 (2005) 105–111. doi:10.1016/J.DESAL.2005.03.031.

[428] J.A. Carta, J. González, V. Subiela, The SDAWES project: An ambitious R and D prototype for wind-powered desalination, Desalination. 161 (2004) 33–48. doi:10.1016/S0011-9164(04)90038-0.

[429] L. García-Rodríguez, Desalination by Wind Power, Wind Eng. 28 (2005) 453–463. doi:10.1260/0309524042886405.

[430] U. Caldera, D. Bogdanov, C. Breyer, Local cost of seawater RO desalination based on solar PV and wind energy: A global estimate, Desalination. 385 (2016) 207–

216. doi:10.1016/J.DESAL.2016.02.004.

[431] J.E. Lundstrom, Water desalting by solar powered electrodialysis, Desalination. 31 (1979) 469–488. doi:10.1016/S0011-9164(00)88551-3.

[432] N. Ishimaru, Solar photovoltaic desalination of brackish water in remote areas by electrodialysis, Desalination. 98 (1994) 485–493. doi:10.1016/0011-9164(94)00175-8.

[433] P. Malek, J.M. Ortiz, H.M.A. Schulte-Herbrüggen, Decentralized desalination of brackish water using an electrodialysis system directly powered by wind energy, Desalination. 377 (2016) 54–64. doi:10.1016/j.desal.2015.08.023.

[434] J.M. Ortiz, E. Expósito, F. Gallud, V. García-García, V. Montiel, A. Aldaz, Photovoltaic electrodialysis system for brackish water desalination: Modeling of global process, J. Memb. Sci. 274 (2006) 138–149. doi:10.1016/j.memsci.2005.08.006.

[435] J.M. Ortiz, E. Expósito, F. Gallud, V. García-García, V. Montiel, A. Aldaz, Electrodialysis of brackish water powered by photovoltaic energy without batteries: direct connection behaviour, Desalination. 208 (2007) 89–100. doi:10.1016/J.DESAL.2006.05.026.

[436] J.M. Ortiz, E. Expósito, F. Gallud, V. García-García, V. Montiel, V.A. Aldaz, Desalination of underground brackish waters using an electrodialysis system powered directly by photovoltaic energy, Sol. Energy Mater. Sol. Cells. 92 (2008) 1677–1688. doi:10.1016/j.solmat.2008.07.020.

[437] Sa. Klein, W.A. Beckman, J.W. Mitchell, J.A. Duffie, N.A. Duffie, T.L. Freeman, Solar energy laboratory, TRNSYS, A Transient Syst. Simul. Program. Univ. Wisconsin, Madison. (2006).

[438] Koeppl, G.W., Putnam's power from the wind, Van Nostrand Reinhold Company,New York, NY, 1982. https://www.osti.gov/biblio/5488696 (accessed May 27, 2019).

[439] D.E. Seborg, T.F. Edgar, D.A. Mellichamp, F.J. Doyle, Process dynamics and control, Wiley, 2016. https://www.wiley.com/en-us/Process+Dynamics+and+Control%2C+4th+Edition-p-9781119285915 (accessed April 30, 2019).

[440] J. Moreno, V. Díez, M. Saakes, K. Nijmeijer, Mitigation of the effects of multivalent ion transport in reverse electrodialysis, J. Memb. Sci. 550 (2018) 155–162. doi:10.1016/j.memsci.2017.12.069.

[441] J.W. Post, H.V.M. Hamelers, C.J.N. Buisman, Influence of multivalent ions on power production from mixing salt and fresh water with a reverse electrodialysis system, J. Memb. Sci. 330 (2009) 65–72. doi:10.1016/j.memsci.2008.12.042.

[442] T.D. Hayes, B.F. Severin, Electrodialysis of highly concentrated brines: Effects of calcium, Sep. Purif. Technol. 175 (2017) 443–453. doi:10.1016/J.SEPPUR.2016.10.035.

[443] B.F. Severin, T.D. Hayes, Electrodialysis of concentrated brines: Effects of multivalent cations, Sep. Purif. Technol. 218 (2019) 227–241. doi:10.1016/J.SEPPUR.2019.02.039.

[444] V. Geraldes, M.D. Afonso, Prediction of the concentration polarization in the nanofiltration/reverse osmosis of dilute multi-ionic solutions, J. Memb. Sci. 300 (2007) 20–27. doi:10.1016/J.MEMSCI.2007.04.025.

[445] L. Firdaous, T. Saheb, A mathematical model of multicomponent mass transfer in electrodialysis, Pap. Present. Scand. Conf. Simul. Model. Trondheim, Norw. (2005). http://www.scansims.org/sims2005/SIMS2005_82.pdf.

[446] V. Fíla, K. Bouzek, A mathematical model of multiple ion transport across an ion-selective membrane under current load conditions, J. Appl. Electrochem. 33 (2003) 675–684. doi:10.1023/A:1025018726112.

[447] R. Kodým, V. Fíla, D. Šnita, K. Bouzek, Poisson–Nernst–Planck model of multiple ion transport across an ion-selective membrane under conditions close to chlor-alkali electrolysis, J. Appl. Electrochem. 46 (2016) 679–694. doi:10.1007/s10800-016-0945-1.

[448] J.A. Manzanares, G. Vergara, S. Mafé, K. Kontturi, P. Viinikka, Potentiometric Determination of Transport Numbers of Ternary Electrolyte Systems in Charged Membranes, J. Phys. Chem. B. 102 (1998) 1301–1307. doi:10.1021/jp970216w.

[449] J. Kamcev, D.R. Paul, G.S. Manning, B.D. Freeman, Predicting Salt Permeability Coefficients in Highly Swollen, Highly Charged Ion Exchange Membranes, ACS Appl. Mater. Interfaces. 9 (2017) 4044–4056. doi:10.1021/acsami.6b14902.

[450] J. Kamcev, D.R. Paul, G.S. Manning, B.D. Freeman, Ion Diffusion Coefficients in Ion Exchange Membranes: Significance of Counterion Condensation, Macromolecules. 51 (2018) 5519–5529. doi:10.1021/acs.macromol.8b00645.

[451] R.B. McCleskey, D.K. Nordstrom, J.N. Ryan, J.W. Ball, A new method of calculating electrical conductivity with applications to natural waters, Geochim. Cosmochim. Acta. 77 (2012) 369–382. doi:10.1016/j.gca.2011.10.031.

[452] R.B. McCleskey, D.K. Nordstrom, J.N. Ryan, Comparison of electrical conductivity calculation methods for natural waters, Limnol. Oceanogr. Methods. 10 (2012) 952–967. doi:10.4319/lom.2012.10.952.

[453] Y. Tanaka, Ion Exchange Membranes: Fundamentals and applications, Elsevier, 2007. doi:10.1016/S0927-5193(07)12021-0.

[454] C.A.J. Appelo, Principles, caveats and improvements in databases for calculating hydrogeochemical reactions in saline waters from 0 to 200°C and 1 to 1000atm, Appl. Geochemistry. 55 (2015) 62–71. doi:10.1016/j.apgeochem.2014.11.007.

[455] C.E. Harvie, N. Møller, J.H. Weare, The prediction of mineral solubilities in natural waters: The Na-K-Mg-Ca-H-Cl-SO4-OH-HCO3-CO3-CO2-H2O system to high ionic strengths at 25°C, Geochim. Cosmochim. Acta. 48 (1984) 723–751. doi:10.1016/0016-7037(84)90098-X.

[456] N. Plummer, D.L. Parkhurst, G.W. Fleming, S.A. Dunkle, A computer program incorporating Pitzer's equations for calculation of geochemical reactions in brines, Water-Resources Investig. Rep. (1988). https://pubs.er.usgs.gov/publication/wri884153 (accessed June 14, 2018).

[457] M. La Cerva, L. Gurreri, A. Cipollina, A. Tamburini, M. Ciofalo, G. Micale, Modelling and cost analysis of hybrid systems for seawater desalination: Electromembrane pre-treatments for Reverse Osmosis, Desalination. 467 (2019)

175–195. doi:10.1016/J.DESAL.2019.06.010.

Aknowledgments

First of all, I would like to thank Giorgio, Andrea and David for their support during the work carried out in these three years.

In addition, I would like to acknowledge all my colleagues for making this experience so special, with a special mention to Luigi for the great scientific contribution and to Mariagiorgia for being there most times.

Finally, I would like to say thank you to my parents and to Tiziana for their presence in the good and the bad moments and for giving me the strength to pursue the completion of this work.